Wrinkling and folding induced pattern formation in elastic thin sheets

Ignacio Javier Andrade Silva

▶ **To cite this version:**

Ignacio Javier Andrade Silva. Wrinkling and folding induced pattern formation in elastic thin sheets. Soft Condensed Matter [cond-mat.soft]. Université de Lyon, 2019. English. NNT : 2019LYSEN065 . tel-02476368

HAL Id: tel-02476368
https://theses.hal.science/tel-02476368

Submitted on 12 Feb 2020

HAL is a multi-disciplinary open access archive for the deposit and dissemination of scientific research documents, whether they are published or not. The documents may come from teaching and research institutions in France or abroad, or from public or private research centers.

L'archive ouverte pluridisciplinaire **HAL**, est destinée au dépôt et à la diffusion de documents scientifiques de niveau recherche, publiés ou non, émanant des établissements d'enseignement et de recherche français ou étrangers, des laboratoires publics ou privés.

N° d'ordre NNT : 2019LYSEN065

THÈSE DE DOCTORAT DE L'UNIVERSITÉ DE LYON
opérée par
l'École Normale Supérieure de Lyon

École Doctorale N°52
Physique et Astrophysique de Lyon (PHAST)

Spécialité de doctorat : PHYSIQUE

Soutenue publiquement le 29/11/2019, par :
Ignacio Javier ANDRADE SILVA

Wrinkling and folding induced pattern formation in elastic thin sheets

Formation de motifs induits par le froissement et le pliage dans de films minces élastiques

---

Devant le jury composé de :

Bico José, Maître de conférences, ESPCI	Rapporteur
Müller Martin Michael, Maître de conférences, Université de Lorraine	Rapporteur
Ben Amar Martine, Professeur des Universités, ENS Paris	Examinatrice
Géminard Jean-Christophe, DR CNRS, ENS de Lyon	Examinateur
Adda-Bedia Mokhtar, DR CNRS, ENS de Lyon	Directeur de thèse
Dias Marcelo A., Professeur, Université d'Aarhus	Invité

Résumé

Cette thèse explore deux mécanismes de formation de motifs dans des feuilles minces élastiques : la formation de rides et des plis. La première partie de la thèse aborde le rôle des conditions aux limites dans l'analyse des instabilités de rides dans des films minces tendus. Les instabilités de rides ont été largement étudiées dans des géométries simples, où la direction des rides est connue à priori. Par exemple, le problème de Lamé, consistant en une feuille annulaire radialement étirée, a servi de modèle pour la formation de rides en traction dans des géométries axiales. Nous étudions les effets de la modification des conditions de charge et de la géométrie. Premièrement, nous considérons une feuille annulaire étirée vers l'intérieur dont le bord extérieur est fixé et comparons l'analyse du motif ridé avec le cas du problème de Lamé. Deuxièmement, nous étudions le problème élastique d'une feuille élastique infinie perforée d'un trou elliptique et soumise à une tension différentielle uniforme entre son bord extérieur et intérieur. Nous calculons le champ de contraintes dans l'état pré-déformé et leurs composantes principales et directions correspondantes. Nous obtenons un diagramme de phase montrant les différents états de contrainte de la membrane et discutons des résultats possibles au-delà de l'instabilité de flambement.

La deuxième partie de la thèse aborde la forme à l'équilibre des motifs d'origami non rigide à sommet unique dans des feuilles élastiques. La conception de métamatériaux mécaniques inspirés de l'origami est généralement axée sur la cinématique d'assemblages de plaques planaires rigides reliées par des charnières (origami rigide). Lorsque les panneaux sont flexibles (origami non rigide), de nouveaux comportements apparaissent, tels que le cas des cônes pliables (f-cones), des feuilles circulaires décorées de plis radiaux. Ces structures sont toujours bistables, en ce sens qu'elles peuvent passer d'une configuration métastable à une autre. Nous avons proposé un modèle général de f-cones composés de feuilles inextensibles qui démontre la nature bistable de ces systèmes. De plus, le modèle est capable de prédire les formes d'équilibre pour toutes les déflexions en fonction des angles de plis et leur réponse. En outre, nous avons testé la validité de l'hypothèse d'inextensibilité au moyen d'une étude numérique d'éléments finis, dans laquelle les plis sont modélisés sous forme de tranches continues de la plaque qui se plient en raison d'un gradient de dilatation thermique.

Summary

This thesis explores two mechanisms for pattern formation in elastic thin sheets : wrinkling and folding. The first part of the thesis discusses the role of boundary conditions in the analysis of tensional wrinkling of thin films. Wrinkling phenomena have been widely studied in simple geometries, where the direction of wrinkles is known a priori. For instance, the Lamé problem, consisting of a radially stretched annular sheet, has served as a prototypical model for theoretical and experimental studies in axial geometries. We study the effect of changing the loading conditions and geometry of the Lamé problem. First, we consider an inwardly stretched annular sheet whose outer edge is clamped and compare the analysis of the wrinkled pattern with the Lamé case. Second, we study the elastic problem of an infinite elastic sheet perforated by an elliptic hole and subjected to a uniform differential tension between its outer and inner edges. We compute the stress field in the pre-buckled state and its corresponding principal components and directions. We obtain a phase diagram showing different stress states of the membrane and discuss the possible outcomes beyond the buckling instability.

The second part of the thesis discusses the equilibrium shape of nonrigid single-vertex origami patterns in elastic sheets. The designing of origami-inspired mechanical metamaterials usually focuses on the kinematics of assemblies of rigid flat plates connected by hinges (rigid origami). When the panels are allowed to bend (nonrigid origami), novel behaviors emerge, such as the case of foldable cones (f-cones), circular sheets decorated by radial creases. These structures are generically bistable, in the sense that they can snap-through from one metastable configuration to another. We propose a model for f-cones made of inextensible sheets that demonstrates the bistable nature of these systems. Moreover, the model is able to predict the equilibrium shapes for any deflections as a function of the folding angles and crease mechanics. Furthermore, we test the validity of the inextensible hypothesis by means of an FEA study, where the creases are modeled as continuous slices of the plate that fold due to a nonuniform thermal field.

Remerciements

Les travaux de recherche présentés dans ce manuscrit ont débuté en octobre 2016 sous la direction de Mokhtar Adda-Bedia, au Laboratoire de Physique ENS de Lyon, où j'ai profité des bonnes amitiés et d'une ambiance scientifiquement stimulant. Je tiens à remercier tous les membres du laboratoire de m'avoir accueilli.

Je voudrais spécialement remercier Mokhtar Adda-Bedia pour ses conseils, sa patiente et son soutien durant cette trois années de doctorat. Je remercie Marcelo Dias de m'avoir accueilli à Aarhus et pour sa précieuse contribution au développement de cette recherche. Merci à Théo Jules pour les discussions enrichissantes sur ses expériences. Je remercie aux membres de jury, Jose Bico, Martin Micheal Müller, Martine Ben Amar et Jean Christophe Géminard pour leur lecture attentive de ce manuscrit.

Merci à tous les amis que je me suis fait à Lyon : les chiliens Yeraldinne Carrasco, Cristobal Oliver et Marcelo Guzmán, les italiennes Alex Fontana, Alex Amato, Marco Marciani, Dario Lucente, mes collègues de bureau, Jeremy Vessaire, Matthias Droth, Jorge Pereda, Richard Pedurand, Lavi Upreti, Hadi Kabalane et les doctorants du Laboratoire de Physique. Merci à tous pour votre amitié et soutien.

Enfin, je remercie ma famille au Chili qui m'a soutenu au loin et mon épouse Valentina Villalobos de m'avoir accompagné dans cette aventure.

Contents

Résumé iii

Summary v

Remerciements vii

1 Introduction 1

1.1 Patterns and elasticity 1
1.1.1 Why thin sheets? 2
1.1.2 Folding sheets: Origami and applications 5

2 Conceptual review 7

2.1 Elasticity: basic notions 7
2.1.1 Defining strain 8
2.1.2 Constitutive relations and equilibrium equations 10
2.1.3 Linear vs. nonlinear 12
2.2 2D linear elasticity 13
2.3 Elastic theory of thin sheets 14
2.3.1 Bending vs. stretching 15
2.3.2 Geometry of a surface: curvature 16
2.3.3 Constitutive relations for plates 17
2.3.4 The FvK equations 19
2.4 Theorema egregium 21
2.4.1 Developable surfaces 22
2.5 Conical Defects 23
2.5.1 Developable cones 23
2.5.2 Other conical dislocations 24
2.6 Origami 25
2.6.1 Flat foldability 25
2.6.2 Rigid foldability 27

I Physics of Wrinkling 31

3 Wrinkle formation in elastic thin sheets 33
3.1 Wrinkling phenomena . . . 33
3.1.1 Tension-field theory . . . 35
3.1.2 NT and FFT regimes . . . 35
3.1.3 The Lamé problem . . . 36
3.1.4 The role of geometry and boundary conditions . . . 37
3.2 Annular sheet with clamped boundaries . . . 38
3.2.1 Setup . . . 38
3.2.2 Base state solution . . . 39
3.2.3 Near-threshold analysis . . . 41
3.2.4 Far-from-threshold analysis . . . 42
3.2.5 Discussion: the effect of clamping an edge . . . 44
3.3 Lamé problem for an elliptic hole . . . 45
3.3.1 Setup . . . 46
3.3.2 Equilibrium equations and boundary conditions . . . 46
3.3.3 The Kolosoff-Inglis solution . . . 47
3.3.4 Solution of the problem and stress field analysis . . . 48
3.3.5 Phase diagram . . . 51
3.3.6 Crack-limit . . . 54
3.3.7 Discussion: the role of geometry . . . 56
3.4 General conclusions . . . 58

II Folding induced patterns 59

4 Nonrigid origami 61
4.1 Rigid vs nonrigid origami . . . 61
4.2 Physics of folding . . . 62
4.3 Foldable Cones . . . 64
4.3.1 Previous works . . . 65
4.3.2 Summary of the linear model . . . 66
4.4 Elastic theory of conical singularities . . . 70
4.4.1 Geometry of a developable cone . . . 71
4.4.2 Elastic energy of a conical surface . . . 72
4.4.3 Conserved quantity . . . 74
4.4.4 Shape reconstruction . . . 75
4.5 Elastic theory of foldable cones . . . 76
4.5.1 Geometry of a foldable cone . . . 76
4.5.2 Nonlinear model for f-cones . . . 77
4.5.3 Euler's *Elastica* . . . 79

4.5.4 Boundary conditions . . . 80
4.6 Solving the *Elastica* . . . 83
4.6.1 Generic bistability . . . 83
4.6.2 Solutions for symmetrical *f*-cones . . . 85
4.6.3 Snap-through dynamics . . . 89
4.7 Continuous elastic model of origami structures . . . 90
4.7.1 Temperature-induced hingelike creases . . . 90
4.8 Numerical analysis of foldable cones . . . 92
4.8.1 Snap-through dynamics . . . 92
4.8.2 Numerical results . . . 93
4.9 General conclusions . . . 96

5 Perspectives **99**
5.1 Loss of bistability of foldable cones . . . 99
5.1.1 Elastic ribbon theory . . . 99
5.1.2 Equilibrium equations and boundary conditions . . . 102
5.1.3 Phase field like model of creases for origami networks . . . 103
5.2 The complexity of crumpled paper . . . 103

A Appendix A **107**
A.1 Corrections to the linear model of the developable cone . . . 107
A.1.1 Inextensibility condition . . . 107
A.1.2 Bending energy . . . 108
A.1.3 Lagrangian . . . 109
A.2 Determination of the folding angle . . . 110
A.3 Frame virtual rotations and Euler-like angles . . . 111

B Appendix B **113**
B.1 Solution for alternate crease *f*-cone . . . 113

C Appendix C **115**
C.1 Theory of elastic ribbons . . . 115
C.1.1 Edge function for an annular ribbon . . . 115
C.1.2 Derivation of equilibrium equations . . . 116

D Appendix D **119**
D.1 Published articles . . . 119

Bibliography **139**

List of Figures

1.1 Patterns in nature triggered by mechanical instabilities. (a) Basalt columns at the Giant's Causeway in Northern Ireland (taken from [49]). (b) Self-similar buckling cascade in the edges of leaves [110]. (c) Three common patterns of human fingerprints: whorl, loop and arc [74]. (d) Differential growth induced buckling of the gut of a chick embryo [102]. 2

1.2 Some instabilities in elastic thin sheets. (a) Buckling pattern in an axially compressed cylinder (adapted from [106]). (b) Wrinkled pattern obtained from a rubber curtain due to the action of gravity (taken from [123]). (c) Triangular buckling pattern in a twisted elastic ribbon (image from [73]). (d) Localized deformations in shells under indentation [124]. (e) Wrapping of an adhesive sphere with a flat elastic sheet [63]. 4

1.3 Origami and origami-based materials. (a) *Orizuru* (paper crane) and its crease network. (b) Miura fold (taken from [91, 92]). (c) Origami-inspired deployable array [141]. (d) Shape programmed motifs using origami tessellations [45]. 5

2.1 (a) An object being stretched. The deformed object has a length $L' = L + \Delta L$ and a cross section area $S' = S + \Delta S$. (b) Reference (dashed line) and deformed (solid line) configurations of an object. A material point at $\mathbf{r}$ moves to a new position $\mathbf{r}'(\mathbf{r})$. 8

2.2 Scheme showing stretching (a) and bending (b) deformations of a plate. (c) Stress profile across the thickness of the plate in pure bending. The material underneath the middle surface is under compression while the material that is above the middle surface is stretched. 16

2.3 Examples of surfaces with negative Gaussian curvature (hyperboloid), zero Gaussian curvature (cylinder), and positive Gaussian curvature (sphere) (image adapted from [34]). 17

2.4 Examples of developable surfaces: (a) conical, (b) cylindrical and (c) tangent developable. 23

2.5 (a) Emergence of d-cones in a uniaxially compressed cylinder [51]. (b) Isolated d-cone: a circular piece of paper is pushed into a cylinder by a point force [9]. (e) e-cone with a surplus angle [93]. 24

2.6 (a) Definitions of mountain and valley creases. (b) Miura crease pattern. 25

2.7 A flat foldable vertex of four creases. $\alpha_1 + \alpha_3 = \alpha_2 + \alpha_4 = \pi$. . . . 26

2.8 (a) Rigid origami as rigid panels connected by hinges. (b) A 4-creases vertex seen as a rigid frame. 27

2.9 Venn diagram of flat foldable, rigid foldable and not foldable crease patterns. The examples correspond to the square twist fold [112], the Miura-fold, the 3-D corner origami. 28

3.1 (a) Wrinkles in the skin of a shriveled apple and (b) on the back of one's hand by bunching up the skin substrate (figures taken from [24]). (c) Wrinkles in a stretched polyethylene sheet (taken from [26]). The dimensions of the sheet are: length, $L = 20$ cm; width, $W = 12$ cm; thickness, $h = 0.01$ cm. (d) "Drop-on-sheet" experiment: Capillary-induced wrinkling of a thin floating polymer film on which a drop is placed [59]. Notice that the inward tension is mainly caused by capillary forces rather than the weight of the drop. The thickness of the sheet is 41 nm and the radius of the drop is 0.5 mm. 34

3.2 (a) The Lamé configuration. (b) Theoretical phase diagram of wrinkling patterns in the Lamé configuration. The dimensionless parameters ϵ^{-1}, τ represent, respectively, the bendability and confinement. The inset shows the evolution of the hoop stress $\sigma_{\theta\theta}(r)$ for different points in the phase diagram. Both figures were taken from reference [38]. 36

3.3 Annular sheet subjected to inward tension T in its inner edge while its outer edge is clamped. L denotes the extent of wrinkles. 39

3.4 Mechanical energy U (normalized by $R_{\text{in}}^2 T^2/Y$) as a function of the wrinkle extent L (normalized by R_{in}) for $\rho = 2$ and $\nu = 1/3$. An inflection point exists at $L_{\text{NT}} = \sqrt{(1-\nu)/(1+\nu)}R_{\text{out}}$. 43

3.5 Comparison between the Classical Lamé problem and the modified Lamé problem with a clamped edge. 45

3.6 Schematics of the modified Lamé problem. Lines on the sheet illustrate the elliptic coordinate system (ξ, η). 46

3.7 Three-dimensional profiles of $\sigma_{\xi\xi}$, $\sigma_{\eta\eta}$ and $\sigma_{\xi\eta}$ for $\tau = 3.5$ and $\delta = 0.4$. 48

3.8 Tension Lines: maximum (——) and minimum (- - -) principal stress directions. 49

3.9 Representation of six possible states, where taut, UT, and slack regions are plotted on the sheet. The coordinates at each figure stand for the values (δ, τ). 50

3.10 Diagram showing different states in the parameter space (δ, τ). The critical curves $\tau_c(\delta)$, $\tau_1(\delta)$, $\tau_2(\delta)$ and $\tau_s(\delta)$ separate the different regions. The state S1s exists for values of τ greater than 50. 51

3.11 Profile of σ_{rr} along the x–axis close to the hole for $\delta = 0.01$ and $\tau = 1.1$. The linear and crack approximation given, respectively, by Eqs. (3.60) and (3.64) are shown for comparison. The shaded area represents the region where the crack approximation fails. 54

4.1 Examples of nonrigid origami. (a) The square twist fold (taken from [112]). (b) The accordionlike origami (taken from [39]). (b) Curved crease origami (taken from [44]). 62

4.2 (a) The geometry of a single straight crease can be described by its length L and the three unit vectors $(\mathbf{u}, \mathbf{v}, \mathbf{w})$. (Figure adapted from [18]). (b) Experimental setup to test the mechanical response of a creased sheet and (c) applied moment M as function of the folding angle ψ (Figures (a) and (b) adapted from Ref. [79]). 63

4.3 Experimental, mechanically stable f-cones in mylar-sheet disks (350 μm thick, 15 cm in radius (figure taken from reference [79]). . . . 64

4.4 Representations of a convex (a) and a concave (b) vertex terminating a mountain crease appearing in Huffman's paper [61] and corresponding to, respectively, the rest and the snapped states of a single crease f-cone. The figures at the left represent the contours around the vertex, where + (−) signs denote "convexity" ("concavity") of edges, regions or vertices, as defined by the author. The figures at the right represent the trace in the Gaussian sphere, where L and R stand for the left and right side of the crease. 66

4.5 Bistable creased strips, which are equivalent to a $n = 2$ f-cone. (a) Metallic creased strips with and without a hole in their initial and inverted states. (b) A snapped strip compared to a dent in a vehicle body. The figures were adapted from [131]. 66

4.6 Lagrange multipliers $\bar{\lambda}_n^{\mathrm{R}}$ and $\bar{\lambda}_n^{\mathrm{S}}$ as a function of the number of faces n (Figure taken from [78]). 69

4.7 The cone geometry. A closed curve $\Gamma(s)$ on the unit sphere describes the entire conical surface. The Euler-like angles $\{\theta(s), \varphi(s), \phi(s)\}$ are shown. 71

4.8 (a) Imprinted crease pattern on a flat plate. (b) Deformed state of the ith panel of a f- cone. The curve Γ, the material frame and the Euler-like angles are defined. 77

4.9 Definition of a mountain and a valley crease. The vectors $\mathbf{t}_i^{\pm}$, $\mathbf{n}_i^{\pm}$ and the crease angle ψ_i are defined. 78

4.10 The Lagrange multiplier c as function of the folding angle ψ for (a) rest states and (b) snapped states for all-mountain f-cones with 1, 2 and 4 creases. 86

4.11 Solutions of (a-b) $1^{\mathrm{R,S}}$ and (c-d) $4^{\mathrm{R,S}}$ f-cones with prescribed folding angles $\psi = 0°$ and $\psi = 90°$. The arrows indicate the J-vector direction, but not its magnitude. 87

4.12 (a) Schematic definition of the polar angle θ_c for $n^{\mathrm{R,S}}$ f-cones ($n > 1$). (b) Case $1^{\mathrm{R,S}}$: the angle $\beta(\psi) = \pi - \cos^{-1}(\mathbf{u}(0) \cdot \mathbf{u}(\pi))$ that describes the deviation from the flat configuration. (c) Case $2^{\mathrm{R,S}}$: the polar angle $\theta_c(\psi)$ at the creases compared with the prediction of the linear model for the snapped state. (d) Case $4^{\mathrm{R,S}}$: the polar angle $\theta_c(\psi)$ at the creases. 88

4.13 Comparison of $\theta(\varphi)$ between the nonlinear and the linear model. For small ψ the linear model fails to predict the entire shape of the structure. 88

4.14 (a-c) Equilibrium shapes for $\bar{k} = 1$ and $\psi_0 = \pi/2$. (d) Final crease angles ψ as function of $\bar{k}$ for $\psi_0 = \pi/2$. Rest (blue lines) and snapped (red lines) states for all-mountain f-cones with 1, 2 and 4 creases (respectively dashed, dotted and plain lines). 89

4.15 (a) Energy landscape of an all-mountain f-cone with 4 creases as function of θ_c for $\bar{k} = 1$ and $\psi_0 = \pi/2$. The blue and red curves correspond to the bending energy of the facets for the rest and snapped states, respectively. The plain gray curve is the crease energy given by Eq. (4.47). The black curve is the total elastic energy. (b) Normalized moment $M(\theta_c)$ applied on the creases. The black dots correspond to the rest and snapped states of the f-cone. 89

4.16 Transverse view of a plate with a narrow slice whose thermal and mechanical properties differ from those of the rest of the plate. (a) Reference configuration. (b) Curvature induced equilibrium configuration due to a linear thermal gradient across the thickness. 91

4.17 Schematics of the indentation protocol. Equal moments M are applied on each crease such that the center rim moves vertically in the downward direction, while the end points of the symmetry planes (denoted by red dots) are free to move in the xy-plane. The average displacement of the center rim is imposed and the moment M is computed as a function of the polar angle θ_c. 92

4.18 (a-b) Indentation paths $\theta_c(\psi)$ as computed by the numerical model for $h_c/h = 1, 1/4$ and $E_c/E = 2, 1, 1/2, 1/10$. The theoretical curves $\theta_c(\psi)$ for a $4^{R,S}$ f-cone are reproduced from Fig. 4.12. The dots correspond to the rest and snapped states of each indentation path. 93

4.19 Lines of smallest principal curvature of a symmetric foldable cone with four creases. The upper (resp. lower) row corresponds to a stiff (resp. soft) crease case. The equilibrium rest (left column) and snapped (right column) states are shown. The boxes show zoomed regions next to the vertex. The black dotted line indicates the location of the crease and the color code corresponds to the elastic energy density. 95

4.20 (a) Moment M as function of θ_c during the indentation of a stiff crease with $h_c = h$, $E_c = 2E$, and a soft crease, with $h_c = h/4$, $E_c = E/2$. (b) The corresponding total stretching energy. Inset. Normalized bending energy of the facets compared to the theoretical result of Fig. 4.15(a). 96

5.1 Geometry of a developable annular ribbon. The shape is parametrized by a family of straight generators that make an angle γ with $\mathbf{d}_3$. The outer edge is chosen as the directrix $\mathbf{x}(S)$ of the parametrization. . . 100

5.2 (a) A crumpled aluminum foil revealing a network of polygonal ridges. Ridges meet at vertices which are tips of conical defects (adapted from [9]). (b) Ridge network reconstruction from a real paper sheet (adapted from [7]). 104

5.3 Plot of the degree distribution $p(k)$ as a function of node degree k obtained from real ridge networks. The inset shows the same data plotted on log-log scale. Note that $p(k)$ has a peak at $k = 4$. (figure adapted from [7]). 105

B.1 (a) Family of solutions found numerically represented by the polar angles $\{\theta_m, \theta_v\}$ as function of the two folding angles $\{\psi_m, \psi_v\}$. The capital R and S denotes rest and snapped states, respectively. (b) Schematics showing the angles $\{\psi_m, \psi_v, \theta_m, \theta_v\}$. 113

C.1 Schematics of the mapping Φ between the flat configuration and the deformed configuration. 116

1 Introduction

1.1 Patterns and elasticity

Patterns, spatially ordered structures, are abundant in the natural world attracting the interest of researchers from different fields such as physics, biology, mathematics and engineering [35]. They are studied not only because of their beauty or by mere curiosity but also to understand the mechanisms that produce such instabilities. The field of pattern formation usually deals with macroscopic dissipative systems that self-organize into periodic structures. However, many patterns we observe in nature are often triggered by mechanical instabilities in elastic continuous media.

Many examples of such patterns can be found in the field of fracture mechanics, where cracks can undergo several instabilities. For instance, traveling cracks in cooling glass plates can be destabilized in such a way that the tip of the crack follows an oscillatory path leaving a wavy trace [140, 4]. In brittle materials, cracks can branch into two subsequent cracks [65]. Cracks in drying or cooling media fragment the material forming a network pattern of polygonal pieces, where two types of pattern are commonly observed [48]. The first one is a rectilinear pattern in which later cracks tend to intersect earlier cracks at 90 degrees (T-junctions) as frequently seen in old pottery surface or drying mud. A second kind of pattern happens when new cracks form in 120 degree joints (Y-junctions) such as the cracks formed in cooling lava flows which form prismatic columns that are mostly hexagonal [115], like the basalt columns at the Giant's Causeway in Northern Ireland shown in Fig. 1.1(a). Hexagonal crack patterns have also been found in sandstone, mud, coal, glass, starch, and ice.

Another class of patterns in elastic media emerges as the result of buckling instabilities of elastic thin sheets, where nonlinearities become relevant. A widely studied case is the buckling instability of thin sheets induced by differential growth which occurs when parts of a sheet, or coupled sheets, grow at different rates. Differential growth can cause some tree leaves to develop a buckling cascade at their edges [111, 110]. Fig. 1.1(b) shows this phenomenon in the leaves of an ornamental cabbage and the inset shows the profile of a beet leaf edge. Here, the in-plane lengthening of the sheet results in an excess of length such that the sheet has to buckle. Surprisingly, the equilibrium shape of the edge consists of a self-similar profile of waves upon waves. The same buckling cascade is found at the edges of some torn elastic sheets (like garbage bags). Differential growth is usually the basic ingredient that explains the

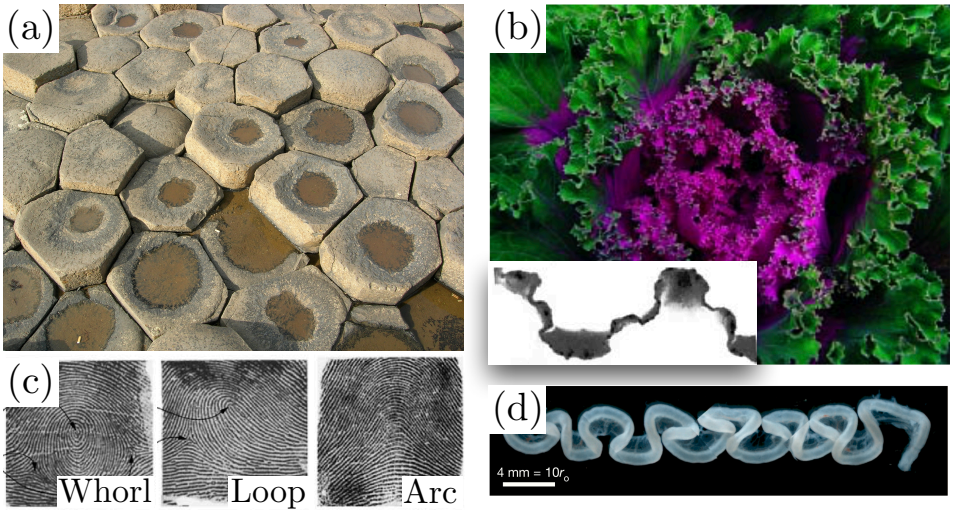

Figure 1.1 Patterns in nature triggered by mechanical instabilities. (a) Basalt columns at the Giant's Causeway in Northern Ireland (taken from [49]). (b) Self-similar buckling cascade in the edges of leaves [110]. (c) Three common patterns of human fingerprints: whorl, loop and arc [74]. (d) Differential growth induced buckling of the gut of a chick embryo [102].

buckling of sheets in many morphogenesis processes. The resulting patterns can be exceptionally rich and complex as in our fingerprints (see Fig. 1.1(c)). Researchers have identified the basic mechanisms for the development of epidermal ridges in fingerprints by applying principles of elasticity theory [74]. The differential growth between the basal layer of the epidermis with respect to the innermost and outermost layers of the skin yields an in-plane compressive stress triggering a buckling instability of the basal layer. This results in the emergence of ridges that arrange in a distinctive pattern. Based on an elastic model, researchers could reproduce numerically the characteristic shape of the three most frequent types of fingerprints: whorl, loop and arc. Another example of a differential growth induced instability is the formation of loop patterns in the developing vertebrate gut [102] (Fig. 1.1(d)). The gut buckles due to the difference in growth rates between the gut tube and the dorsal mesentery, a tissue to which the gut is anchored. These works show that many phenomena in morphogenesis processes can be explained by applying basic principles of elasticity instead of complex genetic coding.

1.1.1 Why thin sheets?

Elastic slender structures, objects whose size is much greater than their typical thickness, have received particular attention for exhibiting peculiar mechanical responses. Rods, ribbons, plates and shells are examples of slender structures. To be precise, one can define the *slenderness* ratio of an object as

$$\lambda = \frac{l}{h}, \tag{1.1}$$

where l is its typical size and h is its characteristic thickness. Let us give some examples and orders of magnitudes. For a typical commercial airplane $l \sim 80$ m and $h \sim 50$ cm, giving a slenderness $\lambda \sim 10^2$. The skin of an apple is about 50 μm thick while its diameter is typically about 8 cm, then $\lambda \sim 10^3$, the same slenderness as a disk-shaped red blood cell, where $l \sim 10$ μm and $h \sim 10$ nm. The slenderness of a human hair ranges between $\lambda \sim 10^3$–10^4. Examples of extremely slender objects are carbon nanotubes which have been made with a length-to-diameter ratio of about $\lambda \sim 10^8$ [134]. In all these examples, moderate forces can trigger large deformations due to the large extension of the objects compared to their thickness. Here, nonlinearities, which are of geometrical origin, can arise even when the material properties remain linear. In order to illustrate how slenderness affects the mechanics of an object consider the Euler buckling failure criterion in which the critical stress before buckling is given by [20]

$$\sigma_{cr} = \frac{\pi^2 E}{\lambda^2}, \tag{1.2}$$

where E is the so called Young's modulus. As $\lambda \to 0$, the structure is more likely to suffer a buckling failure, such as the deformations we observe in collapsed silos, crashed cars, rail stressing buckling or in the crumpling of cell membranes. Researchers usually perform experiments that allow us to understand how such instabilities occur and under which conditions, with the interest to prevent failure of materials or to take advantage of such instabilities to develop novel materials with unusual mechanical properties and new functionalities. Therefore, the goal is to study the behavior of slender structures subjected to different loading configurations and boundary conditions.

Plates and thin films under in-plane compression can develop several types of buckling modes. It has been shown that strips under lateral compression can show various buckling motifs [8]. Diamond-like buckling patterns have been observed in axially compressed cylinders where the inward radial displacement is constrained by a smaller cylindrical core [58, 106] (see Fig. 1.2(a)). Notice that the latter example can be considered as an extension of the former case with periodic boundary conditions. In-plane compressive stress can also be achieved in sheets on compliant soft substrates. For example, vapor deposited metal thin films can develop patterns due to the mismatch between the substrate and the film produced when the system is cooled [29] as well as stiff films adhered to soft substrates by delamination [126]. These buckling patterns usually result in a wavy periodic texture referred to as wrinkles. Fig. 1.2(b) shows a wrinkled pattern obtained from a rubber curtain due to the action of gravity [26]. The elastic sheet develops wrinkles due to the transversal Poisson effect. Wrinkling instabilities have been widely studied in recent years due to their appearance in many instances of our daily life such as the wrinkles in our skin, clothes or fruits peels [24, 125, 60, 38, 123]. An entire chapter of this thesis is devoted to the physics of wrinkling instabilities.

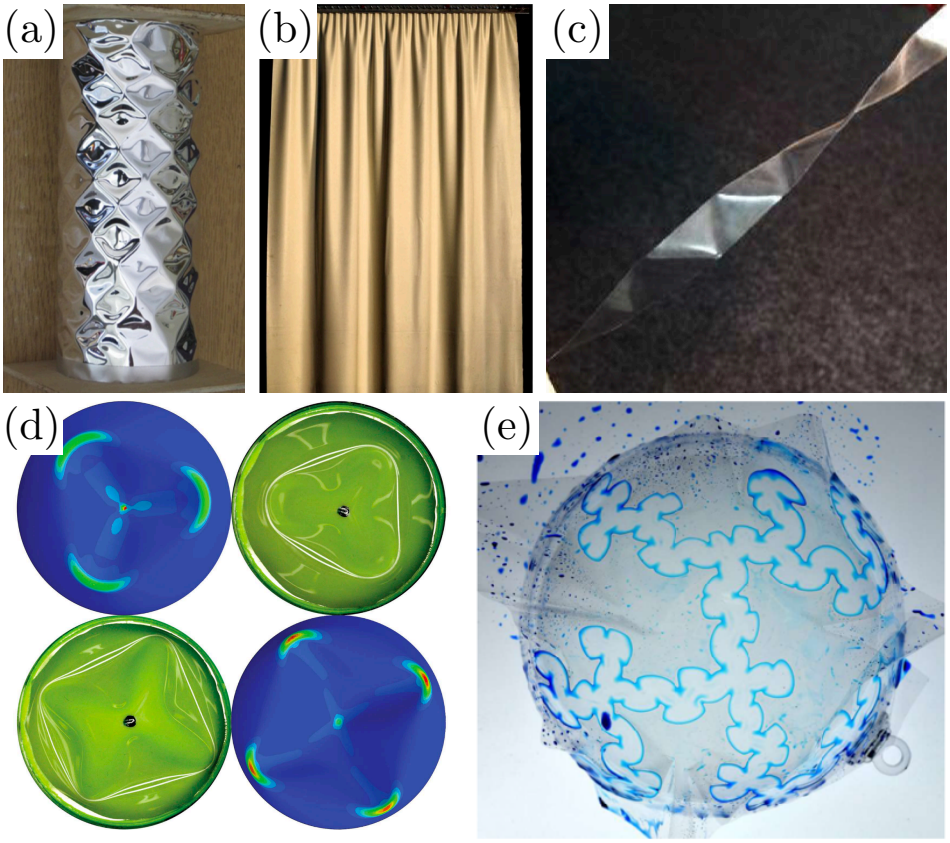

Figure 1.2 Some instabilities in elastic thin sheets. (a) Buckling pattern in an axially compressed cylinder (adapted from [106]). (b) Wrinkled pattern obtained from a rubber curtain due to the action of gravity (taken from [123]). (c) Triangular buckling pattern in a twisted elastic ribbon (image from [73]). (d) Localized deformations in shells under indentation [124]. (e) Wrapping of an adhesive sphere with a flat elastic sheet [63].

We can also mention patterns induced by energy localization in thin plates or shells. Fig. 1.2(b) shows the triangular pattern that thin elastic ribbons develop when twisted [73]. Here, the elastic energy is localized at the edges and the vertices of the triangles. Fig. 1.2(c) shows various sharp motifs of energy localization in thin shells during indentation [124]. There are other mechanisms for pattern formation such as the draping of clothes [25] and wrapping. Fig. 1.2(e) shows the adhesion patterns of an elastic sheet on a rigid spherical substrate [63]. There is a wide variety of buckling modes and instabilities in elastic thin sheets. Their study could lead to applications in graphene [95, 14] or deformable electronics [85], among others.

So far, we have mentioned examples of patterns in thin sheets that emerge spontaneously through different load conditions as a result of buckling instabilities and/or elastic energy localization. A different mechanism to obtain patterns in elastic sheets is by folding them.

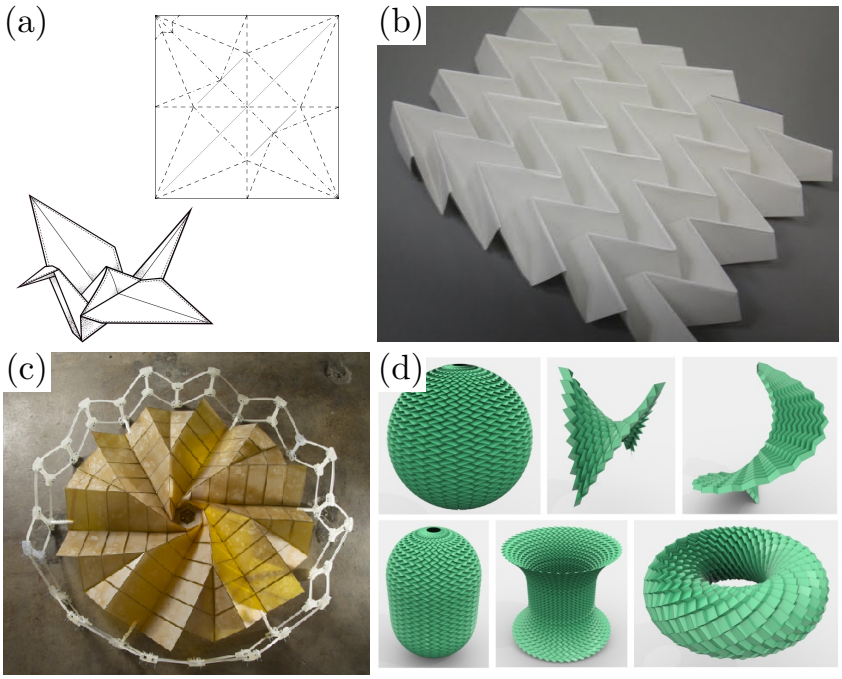

Figure 1.3 Origami and origami-based materials. (a) *Orizuru* (paper crane) and its crease network. (b) Miura fold (taken from [91, 92]). (c) Origami-inspired deployable array [141]. (d) Shape programmed motifs using origami tessellations [45].

1.1.2 Folding sheets: Origami and applications

When a piece of paper is folded, a plastic permanent deformation is produced along the crease [11]. If many folds are made in the sheet, very complex shapes can be achieved and the system can behave in unexpected ways. For instance, a paper plane created by a series of folds acquires new mechanical properties that allow it to fly and at the same time to maintain its shape.

Origami, the ancient Japanese art of folding a piece of paper, is about crafting paper sculptures, often, of high complexity. Its basic premise is to obtain a 3-dimensional structure from a 2-dimensional sheet to which a crease network is imprinted. Then, the final shape is obtained by folding the creases following a given step sequence. Figure 1.3(a) shows an *Orizuru*, a classic origami model representing a Manchurian crane that has a special meaning in Japanese culture. The figure also shows its corresponding crease pattern drawn in a square paper.

Originally thought purely as an art, origami has been a source of inspiration for the design of mechanical metamaterials [103, 135], man-made structures whose mechanical properties depend on their structure rather than their composition. The so-called origami-inspired mechanical metamaterials consist of assemblies of rigid panels connected by hinges. The most known example is the famous *Miura fold*, invented in the 80s by the Japanese astrophysicist Koryo Miura [91, 92] designed to be implemented in space exploration as a deployable structure (see Fig. 1.3(b)).

The crease pattern of the Miura fold forms a periodic tessellation on the flat sheet based on a zigzag pattern of folds forming parallelograms. Using such a design, a large membrane (e.g., a solar array) could be folded compactly and sent into space inside a rocket to be deployed once it is in space (see Fig. 1.3(b)). In recent years, the field of mechanical metamaterials has sought inspiration from origami [103, 135] in the search of smart materials with a vast range of functionality such as deployability of large membranes [92], shape changing structures [44, 45, 139] (see Fig. 1.3(c)), and tunable mechanical and thermal properties [113, 130, 15, 99], among others. Many of these designs are based on the Miura fold or modifications of it. Besides applications, origami has served to understand how tree-leaves fold and how insects [70], notably beetles, fold their wings inside the elytra [56]. For these reasons, origami has been studied by physicists and mathematicians, however, it presents several challenges from the point of view of its theoretical description.

2 Conceptual review

In this chapter, I dedicate a few pages to review some basic concepts on the theory of elasticity, classical differential geometry and origami. The contents about elasticity presented here can be found in any standard book on the subject [76, 121, 84, 94]. References [114, 119] are useful guides for concepts on classical differential geometry and their application to elasticity is well covered in reference [9]. For an overview of concepts related to origami, references [77, 132, 62, 40] are suggested. This chapter aims to provide the elementary tools needed to develop the main results of the thesis.

2.1 Elasticity: basic notions

The theory of elasticity deals with deformations of elastic solids produced by forces. Here, the term *elastic* refers to the property of an object to return to its original state once the forces are removed. The main goal of the theory is to set a relation between the deformations a body experiences and the forces that cause them. First of all, we should begin by giving a precise way to measure deformations. Consider an object of length L and cross section area S in its rest state (or *reference configuration*) to which a force F is applied along its length (see Fig. 2.1(a)). The object is deformed to a new state (*actual configuration*) of length $L' = L + \Delta L$. A natural way to measure such deformation is through the strain ε defined as the ratio between the length change and its original size:

$$\varepsilon = \frac{\Delta L}{L}. \tag{2.1}$$

According to this definition, the strain does not depend on the object size (if the dimensions of the object are amplified by a factor, the strain remains the same).

Let us assume that the solid is constituted by many equal microscopic springs that behave according to the usual Hooke's law for springs. One expects, at least for small deformations, a spring-like behavior of the form $F \propto k\Delta L$, where k is an effective elastic constant. We can think that the small springs act like a chain of springs in series along the direction of the applied force. Then, one expects that $k \propto 1/L$ because the effective elastic constant of a chain of equal springs in series is inversely proportional to the number of springs. On the other hand, the springs respond in parallel along directions transversal to the applied force. Their effective elastic constant is directly

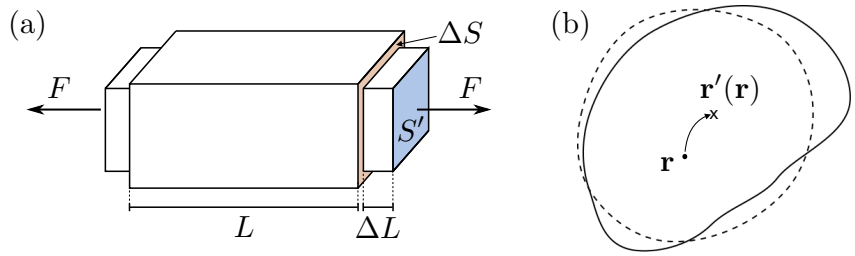

Figure 2.1 (a) An object being stretched. The deformed object has a length $L' = L + \Delta L$ and a cross section area $S' = S + \Delta S$. (b) Reference (dashed line) and deformed (solid line) configurations of an object. A material point at $\mathbf{r}$ moves to a new position $\mathbf{r}'(\mathbf{r})$.

proportional to the number of springs which in turn is proportional to S, thus, one expects that $k \propto S$. These two effects combined lead to the following relation

$$F = E\frac{S}{L}\Delta L, \tag{2.2}$$

where E is a constant of proportionality known as *Young's modulus*. This parameter depends on the material properties and has units of pressure. Eq. (2.2) sets a linear relation between the applied force and the strain. Defining the *stress* as $\sigma = F/S$, one has a linear relation between the stress and the strain:

$$\sigma = E\varepsilon. \tag{2.3}$$

When an elastic object is compressed, it tends to expand transversally to the direction of compression. Conversely, an object being stretched tends to contract transversally to the direction of stretching. This phenomenon is known as the *Poisson effect*. The same object considered previously will experience a change of its cross section area ΔS (see Fig. 2.1(a)). For small enough strain, one has that $\Delta S/S \propto \Delta L/L$. The convention is to write this relation as follows

$$\frac{\Delta S}{S} = -2\nu\frac{\Delta L}{L}, \tag{2.4}$$

where ν is known as *Poisson's ratio*.

In the following sections, we formalize the notions of stress and strain in the continuum limit to be able to apply them to objects of any geometry in three dimensions.

2.1.1 Defining strain

When a solid is deformed, the material point of the solid at position $\mathbf{r}$ in the reference configuration moves to a new position $\mathbf{r}'(\mathbf{r})$ in the actual configuration (see Fig. 2.1(b)). We define the *displacement field* as $\mathbf{u}(\mathbf{r}) = \mathbf{r}' - \mathbf{r}$.

We would like to measure distances between material points within the solid to compare the reference and the actual configurations. To do this we should look for the metric tensor, which defines distances in a particular set of coordinates. As the vector $\mathbf{r}$ spans the space occupied by the solid in the reference configuration, we define the *metric tensor* (or simply *metric*) as $g_{ij} = \partial_i \mathbf{r} \cdot \partial_j \mathbf{r}$, with $\partial_i \equiv \partial/\partial x_i$, where x_i are the material coordinates chosen to describe the body. Notice that components of the metric tensor depend on the set of coordinates chosen to describe the solid. In Cartesian coordinates, the metric of the reference configuration is simply given by the Kronecker's symbol $g_{ij} = \delta_{ij}$. The length element $dr = \sqrt{g_{ij}\, dx_i dx_j}$ defines distances between neighboring points in the solid. The metric tensor of the actual configuration reads $g'_{ij} = \partial_i \mathbf{r}' \cdot \partial_j \mathbf{r}'$. In Cartesian coordinates, the actual position can be written as

$$\mathbf{r}'(x_j) = (x_i + u_i(x_j))\mathbf{e}_i. \tag{2.5}$$

where x_i are Cartesian coordinates, $\mathbf{e}_i$ are the vectors of the Cartesian frame and Einstein summation is assumed. Using Eq. (2.5) one finds that

$$g'_{ij} = g_{ij} + 2\varepsilon_{ij}, \tag{2.6}$$

where

$$\varepsilon_{ij} = \frac{1}{2}\left(\frac{\partial u_i}{\partial x_j} + \frac{\partial u_j}{\partial x_i} + \frac{\partial u_k}{\partial x_i}\frac{\partial u_k}{\partial x_j}\right) \tag{2.7}$$

is called the *strain tensor* which is the tensorial generalization of the scalar strain (2.1) which depends on gradients of the displacement field. The diagonal terms are associated with isotropic expansion/contraction while the off-diagonal terms of the strain tensor are related to *shear* deformations. Notice that the strain tensor is symmetrical, i.e., $\varepsilon_{ij}(\mathbf{r}) = \varepsilon_{ji}(\mathbf{r})$, thus, it is diagonalizable and its eigenvectors are orthogonal. Its diagonalization defines the *principal strain values*, which are the eigenvalues of the strain tensor, and the *principal directions of strain*, given by the eigenvectors. The principal directions define a local frame in which the strain tensor is diagonal and, thus, shear-free. The strain tensor contains information about how material lengths and material angles inside the deformed body changed with respect to the reference configuration.

In the limit of small displacement, i.e., $\mathbf{r}'(\mathbf{r}) \approx \mathbf{r}$, the nonlinear terms in Eq. (2.7) become negligible and, thus, the strain tensor can be approximated by

$$\varepsilon_{ij} \approx \frac{1}{2}\left(\frac{\partial u_i}{\partial x_j} + \frac{\partial u_i}{\partial x_j}\right), \tag{2.8}$$

where the right-hand side is usually called the *linearized strain*.

2.1.2 Constitutive relations and equilibrium equations

Let us consider an isotropic elastic solid occupying a volume Ω and surface $\partial\Omega$. The total potential energy stored in the solid is given by

$$E_{\text{Tot}} = E_{\text{el}} - \int_{\Omega} \rho \mathbf{g} \cdot \mathbf{u}\, dV - \int_{\partial\Omega} \mathbf{P} \cdot \mathbf{u}\, dS. \tag{2.9}$$

where, E_{el} is the elastic energy stored in the body while the two last terms account for the work exerted by external forces: $\rho\mathbf{g}$ is the density of *body forces* from external sources (e.g. gravitational force) and $\mathbf{P}$ is the *surface force* density per unit area applied at the boundary $\partial\Omega$. The stored elastic energy in the body can be written as

$$E_{\text{el}} = \int_{\Omega} W(\partial_j u_i)\, dV, \tag{2.10}$$

where, $W(\partial_j u_i)$ is the internal work per unit volume, which is assumed to be a function of displacement field gradients only.

Stress tensor and Hooke's law: Being a scalar quantity, W can be expanded in powers of invariants built from the strain tensor. Up to second order in strain, this expansion reads

$$W = \frac{\lambda}{2}\varepsilon_{ii}\varepsilon_{kk} + \mu\varepsilon_{ij}\varepsilon_{ij} + O(\varepsilon^3), \tag{2.11}$$

where λ is known as *Lamé's first parameter* and μ is *Lamé's second parameter*, *shear modulus*, or *modulus of rigidity* (also denoted G). In the expansion, there is no linear term proportional to ε_{ii} because it is only relevant in thermo-elastic problems. We formally define the *stress tensor* as

$$\sigma_{ij} \equiv \frac{\partial W}{\partial(\partial_j u_i)}. \tag{2.12}$$

Using Eq. (2.11) and the linearized version of the strain (2.8) (valid for small displacements), the stress tensor reads

$$\sigma_{ij} = 2\mu\varepsilon_{ij} + \lambda\varepsilon_{kk}\delta_{ij}. \tag{2.13}$$

Equation (2.13) is known as *Hooke's law* which sets a linear relation between the stress and the strain and it corresponds to the generalization of Eq. (2.3). Notice that $W = \sigma_{ij}\varepsilon_{ij}/2$, so that the stored elastic energy can be written as

$$E_{\text{el}} = \frac{1}{2}\int_{\Omega} \sigma_{ij}\varepsilon_{ij}\, dV. \tag{2.14}$$

Young's modulus is defined by $E = \mu(3\lambda + 2\mu)/(\lambda + \mu)$ and *Poisson's ratio* by $\nu = \lambda/(2(\lambda + \mu))$. Young's modulus measures the stiffness of a solid material. Poisson's ratio is the amount of transversal expansion divided by the amount of axial compression

and it can only take values in the range $-1 < \nu \leq 1/2$. Although ordinary materials have $\nu < 0$, some materials such as certain foams or man-made materials exhibit negative Poisson's ratio, in which case they are called *auxetic materials* [46].

With these definitions Eq. (2.13) takes its more common form:

$$\sigma_{ij} = \frac{E}{1+\nu}\left[\varepsilon_{ij} + \frac{\nu}{1-2\nu}\varepsilon_{kk}\delta_{ij}\right]. \tag{2.15}$$

The inverse relation reads

$$\varepsilon_{ij} = \frac{1}{E}\left[(1+\nu)\sigma_{ij} - \nu\sigma_{kk}\delta_{ij}\right]. \tag{2.16}$$

Equations of equilibrium. The actual configuration of the solid is determined by the *Principle of virtual work* which states that, at equilibrium, the virtual work given by the body deformations equals the work applied by external forces. This principle is equivalent to impose $\delta E_{\text{Tot}} = 0$ at equilibrium. The variation of energy (2.9) reads

$$\delta E_{\text{tot}} = -\int_\Omega \left[\frac{\partial}{\partial x_j}\left(\frac{\partial W}{\partial(\partial_j u_i)}\right) - \rho g_i\right]\delta u_i \, dV + \int_{\partial\Omega}\left(\frac{\partial W}{\partial(\partial_j u_i)}n_j - P_i\right)\delta u_i \, dS. \tag{2.17}$$

The equilibrium condition $\delta E_{\text{Tot}}/\delta u_i = 0$ leads to the following set of equations

$$\frac{\partial \sigma_{ij}}{\partial x_j} = \rho g_i, \tag{2.18}$$

plus the following boundary conditions

$$\sigma_{ij} n_j = P_i, \tag{2.19}$$

where we have used the definition of stress Eq. (2.12). In the absence of external volume forces, the equilibrium condition simply reads

$$\frac{\partial \sigma_{ij}}{\partial x_j} = 0. \tag{2.20}$$

To interpret the stress tensor, consider a volume V in a body and its boundary ∂V. The net interior force $\mathbf{F}$ acing on V is given by the integral of the left-hand side of Eq. (2.20). Using the divergence theorem, one finds that the components of the force $F_i = \mathbf{F}\cdot\mathbf{e}_i$ are given by

$$F_i = \int_{\partial V} \sigma_{ij}(\mathbf{r}) n_j(\mathbf{r}) \, dA, \tag{2.21}$$

where $\mathbf{n}$ is the normal vector to ∂V. The number σ_{ij} represents the ith component of the interior force per unit area acting along the jth component of the normal $\mathbf{n}$ to the surface ∂V. If V is a small cube oriented along the Cartesian axis, σ_{ij} represents

the ith component of the interior force per unit area acting in a plane whose normal points in the j-direction.

Diagonalizing the stress tensor. The diagonal terms of the stress tensor are associated to an all-around pressure. Indeed, in the case of pure hydrostatic pressure $p(\mathbf{r})$, one has that $\sigma_{ij} = -p(\mathbf{r})\delta_{ij}$. On the other hand, the off-diagonal terms are related to *shear* stress. Likewise to the strain tensor, the stress tensor is symmetrical, i.e., $\sigma_{ij} = \sigma_{ji}$, thus, it is diagonalizable. The eigenvalues are called *principal stresses* and its eigenvectors define the *principal directions of stress*. The eigenvectors define a local frame such that the stress tensor is diagonal and such that there is no shear. In two dimensions, given a stress tensor with components σ_{xx}, σ_{yy} and σ_{xy} ($\sigma_{xy} = \sigma_{yx}$) in Cartesian coordinates, the two principal stresses are given by

$$\sigma_{1,2} = \frac{\sigma_{xx} + \sigma_{yy}}{2} \pm \sqrt{\left(\frac{\sigma_{xx} + \sigma_{yy}}{2}\right)^2 + \sigma_{xy}^2}, \tag{2.22}$$

where σ_1 and σ_2 are called, respectively, the *largest and smallest principal stresses*. It can be shown that the angle β between the direction of the maximum principal stress σ_1 and x–axis is given by

$$\tan 2\beta = \frac{2\sigma_{xy}}{\sigma_{xx} - \sigma_{yy}}. \tag{2.23}$$

How many equations do we need to solve? Summing up, in linear elasticity one has 3 unknowns from the displacement field $\mathbf{u}(\mathbf{r})$, 6 unknowns from the stress tensor σ_{ij} (recall it is symmetric) and 6 unknowns from the strain tensor ε_{ij}, giving in total 15 unknowns. Thus, one needs 15 equations of which 6 come from the strain-displacement relation (2.7), 3 from the equilibrium equations (2.18), and 6 equations from the constitutive law (2.15). Some of these equations are partial differential equations, therefore, they should be supplemented with boundary conditions which can be set by prescribing at the boundaries the displacement field, the stress tensor or a combination of both.

2.1.3 Linear vs. nonlinear

The linearized version of the strain tensor given by Eq. (2.8) is a valid approximation as long as $|\partial u_i/\partial x_j| \ll 1$ for all i and j. Here, one should emphasize the distinction between small displacement and small strain. Indeed, although small displacements imply small strain, the converse is not true. There are some situations in which the nonlinear terms in Eq. (2.7) are of the same order of magnitude as the linear terms and even then the total strain remains small. This happens when pieces of material undergo rigid body rotations by finite angles and in such cases, the nonlinear terms can not be neglected. This often occurs in slender objects such as rods and plates, where large deformations can take place and even then the strain remains small. The

nonlinearities are of geometrical origin and they arise from the definition of the strain given by Eq. (2.8). In this thesis, we study how the elasticity of slender bodies usually leads to important nonlinear effects such as buckling or energy localization.

2.2 2D linear elasticity

In this section, we focus on two-dimensional linear elasticity. In what follows, we shall assume small displacements only and, thus, the linearized strain approximation is valid. There are two types of two-dimensional problems: *plane stress* and *plane strain*. A material is said to be under plane stress if the stress is zero across a particular plane. This happens in thin plates under in-plane loads at its boundaries, then, the stress components σ_{iz} for all i are zero in both faces of the plate, where the z-axis is normal to the plate. If the plate is thin enough, one may assume that $\sigma_{iz} = 0$ for all i across the thickness of the plate and that no component of the stress varies through the thickness. On the other hand, a plane strain situation occurs for very thick objects, where the length of the object is much greater than its other two dimensions and, thus, one can assume that $\varepsilon_{iz} = 0$ for all i, where z is the coordinate along its length. In this thesis, we shall focus on plane stress problems although the results presented in this section apply for both situations.

In 2D plane stress elasticity, the three relevant components of the strain are ε_{xx}, ε_{yy} and ε_{xy} which are built upon two components of the displacement field. This implies that the strain components are not independent. Using Eq. (2.8) one can show that

$$\partial_{yy}\varepsilon_{xx} + \partial_{xx}\varepsilon_{yy} - 2\partial_{xy}\varepsilon_{xy} = 0. \tag{2.24}$$

The above equation is known as *compatibility condition*. As $\sigma_{iz} = 0$ for all i in plane stress, the equilibrium equations in the absence of body forces read:

$$\partial_x\sigma_{xx} + \partial_y\sigma_{xy} = 0 \tag{2.25a}$$
$$\partial_y\sigma_{yy} + \partial_x\sigma_{xy} = 0. \tag{2.25b}$$

Using Hooke's law (2.15) with $\sigma_{iz} = 0$, the condition of compatibility (2.24) and the equilibrium equations (2.25), it is possible to show that

$$\Delta(\sigma_{xx} + \sigma_{yy}) = 0. \tag{2.26}$$

Equations (2.25) and (2.26) together with the boundary conditions (2.19) form a closed system of equations. This is why Eq. (2.26) is usually referred to as a closure relation. In the case of plane strain, one can derive the same equation.

Airy function. In two dimensional problems, it is convenient to introduce the *Airy function* ϕ (also called *stress function*) defined such that

$$\sigma_{xx} = \partial_{yy}\phi, \quad \sigma_{yy} = \partial_{xx}\phi, \quad \sigma_{xy} = -\partial_{xy}\phi \tag{2.27}$$

In this way, the equilibrium equations (2.25) are automatically satisfied. Substituting relations (2.27) into Eq. (2.26) we find that the Airy function must be biharmonic:

$$\nabla^4\phi = 0. \tag{2.28}$$

Complex potentials. In some cases, it is useful to work in the complex plane and use complex variables by introducing the complex coordinate $z = x + iy$ (z no longer designates the vertical coordinate). In can be shown that any Airy function ϕ satisfying Eq. (2.28) is expressible in the following general form [121]

$$\phi = \mathrm{Re}[\bar{z}\psi(z) + \chi(z)], \tag{2.29}$$

where $\psi(z)$ and $\chi(z)$ are analytical functions called *complex stress functions* (Re means real part, the overline denotes complex conjugate, $\bar{z} = x - iy$). Given $\psi(z)$ and $\chi(z)$, the stresses are obtained by the following relations:

$$\sigma_{xx} + \sigma_{yy} = 4\,\mathrm{Re}\{\psi'(z)\} \tag{2.30a}$$

$$\sigma_{xx} - \sigma_{yy} - 2i\sigma_{xy} = 2(\bar{z}\psi''(z) + \chi''(z)). \tag{2.30b}$$

The displacement field for plane stress is obtained via the following formula

$$u_x + iu_y = \frac{1}{2\mu}\left[\frac{3-\nu}{1+\nu}\psi(z) - z\bar{\psi}'(\bar{z}) - \bar{\chi}'(\bar{z})\right], \tag{2.31}$$

where ν is the shear modulus. In practice, the functions $\psi(z)$ and $\chi(z)$ can be found by inspecting the symmetries of a problem and the behavior of the stress components as dictated by the boundary conditions. Then, formulas (2.30) and (2.31) provide the solution of the problem. The present approach allows to solve many two-dimensional problems in plane stress or plane strain situations and is especially useful for geometries that require to work in curvilinear coordinates.

2.3 Elastic theory of thin sheets

As we pointed out, geometric nonlinearity in slender objects plays an important role in their mechanical behavior. Plates that are initially flat can deform into three-dimensional shapes. Thus, they are not described by two-dimensional linear elasticity in which out-of-plane deformations are not allowed. To account for out-of-plane

deformations, one can derive an effective two-dimensional nonlinear elastic theory for plates from three-dimensional elasticity.

2.3.1 Bending vs. stretching

Plates can undergo basically two deformation modes: stretching and bending (see Fig. 2.2(a)). Let us explore the consequences of the competition between stretching and bending in thin plates. Bending corresponds to out-of plane deformations in which the displacement is normal to the reference configuration of the plate. On the other hand, stretching corresponds to in-plane deformations that change the material lengths on the surface of the plate. We shall see that, for very thin plates, the contributions of both stretching and bending to the total elastic energy can be separated. To estimate the energetic cost of bending and stretching consider a plate of characteristic size L and thickness h, where $h \ll L$. The in-plane stress components can be expanded in powers of the coordinate z across the thickness of the plate, where $z = 0$ corresponds to the middle surface of the plate. At zero order in z, one has that $\sigma^{(0)} \sim E\varepsilon^{(0)}$, where $\sigma^{(0)}$ and $\varepsilon^{(0)}$ are the in-plane stress and the in-plane strain associated with stretching of the middle surface. Then, using the definition (2.14), the stretching energy E_s scales as

$$E_s = \frac{1}{2}\int \sigma^{(0)}\varepsilon^{(0)} dV \sim Eh\left(\varepsilon^{(0)}\right)^2 L^2. \tag{2.32}$$

When the plate undergoes pure bending as shown in Fig. 2.2, the regions that are above middle surface experience stretching while the regions that are below the middle surface experience compression. Thus, the strain associated with bending is a function of z. At first order in z, this strain reads $\varepsilon^{(1)} = z/R$, where R is the radius of curvature of the plate, and the stress scales as $\sigma^{(1)}(z) \sim E\varepsilon^{(1)}(z)$. Then, the bending energy E_b scales as

$$E_b = \frac{1}{2}\int \sigma^{(1)}\varepsilon^{(1)} dV \sim Eh^3\frac{1}{R^2}L^2. \tag{2.33}$$

Comparing the two energies one has that

$$\frac{E_b}{E_s} \sim \left(\frac{h}{L}\right)^2. \tag{2.34}$$

Therefore, in the limit of very thin sheets $h \ll L$ stretching becomes energetically costly compared to bending. When the sheet is subjected to loads, bending deformations are energetically preferable whenever possible. This means that the lengths on the surface of the plate remain practically constant during deformation, that is, the sheet undergoes isometric deformations. In the next sections, we explore the consequences of this result.

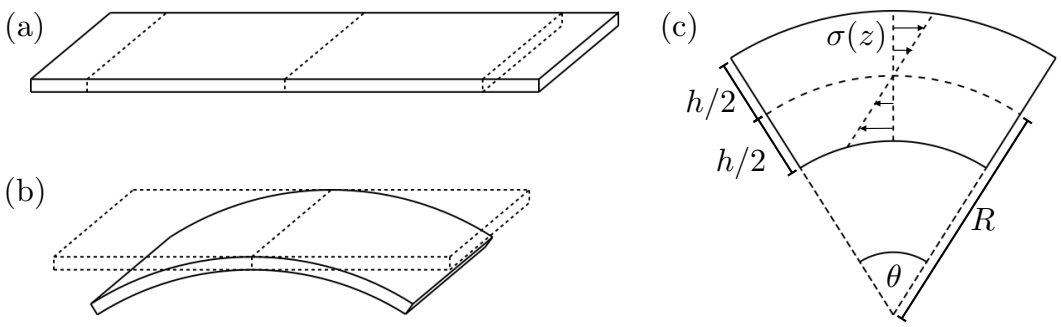

Figure 2.2 Scheme showing stretching (a) and bending (b) deformations of a plate. (c) Stress profile across the thickness of the plate in pure bending. The material underneath the middle surface is under compression while the material that is above the middle surface is stretched.

2.3.2 Geometry of a surface: curvature

To measure the deformations of a surface, one should first formalize the concept of curvature. Let us consider a surface in space for which one wants to quantify its curvature. The middle surface of the sheet admits a general parametrization of the form $\mathbf{r}(x_\alpha, x_\beta)$, where x_α and x_β are material coordinates. Here, Greek indices run over the two dimensions along the middle surface, $\alpha, \beta = 1, 2$. To formalize the notion of curvature, we define the *curvature tensor* as

$$K_{\alpha\beta} = \mathbf{n} \cdot (\partial_\alpha \partial_\beta \mathbf{r}), \tag{2.35}$$

where

$$\mathbf{n} = \frac{\partial_\alpha \mathbf{r} \times \partial_\beta \mathbf{r}}{\|\partial_\alpha \mathbf{r} \times \partial_\beta \mathbf{r}\|} \tag{2.36}$$

is the normal of the middle surface. Similarly to the stress tensor, the curvature tensor is symmetric and, then, it can always be diagonalized. The eigenvectors of the curvature tensor define the *principal directions of curvature* and the eigenvalues correspond to the *principal curvatures* k_1 and k_2. The *mean curvature* of the surface is defined as

$$K_M \equiv \frac{1}{2} \mathrm{tr}\, K_{\alpha\beta} = \frac{k_1 + k_2}{2}. \tag{2.37}$$

The mean curvature is an *extrinsic* measure of curvature because it depends on how the surface is embedded in space. Alternatively, we define the *Gaussian curvature* (or *Gauss curvature*) as the product between the two principal curvatures:

$$K_G = \det K_{\alpha\beta} = k_1 k_2. \tag{2.38}$$

Figure 2.3 shows examples of surfaces with negative, zero and positive Gauss curvature. The Gauss curvature is an *intrinsic* property of the surface, that is, it is a property of the surface itself and not of the particular embedding (see Section 2.4). A particular case of our interest is when a surface has zero Gaussian curvature, in which case the

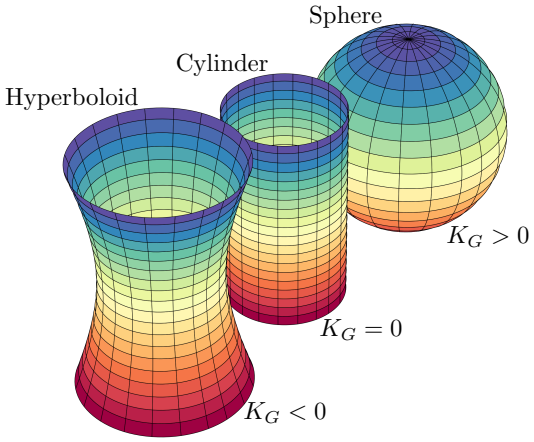

Figure 2.3 Examples of surfaces with negative Gaussian curvature (hyperboloid), zero Gaussian curvature (cylinder), and positive Gaussian curvature (sphere) (image adapted from [34]).

surface is said to be *developable*. Both quantities K_M and K_G are necessary concepts to describe deformations of an elastic plate.

2.3.3 Constitutive relations for plates

The constitutive relations in 3D linear elasticity can be reduced to 2D equations for thin elastic plates. Consider an initially flat plate of length L, width W and thickness h, with $h \ll W, L$. In the reference configuration, each point of the plate is described by the vector $(x, y, 0)$, where $z = 0$ corresponds to the middle surface of the plate, with z being the coordinate across the thickness. In the actual configuration, each point of the middle surface moves to a new position $(x + u_x(x,y), y + u_y(x,y), w(x,y))$, where $(u_x(x,y), u_y(x,y), w(x,y))$ is the displacement field. In what follows, we assume that the in-plane displacements are much smaller than normal displacements, that is, $u_x, u_y \ll w$. As we pointed out before, for plane stress problems, one has $\sigma_{iz} = 0$ for $i = x, y, z$ at the boundaries and across the thickness of the plate. Under this assumption, one can show using Eqs. (2.15) that the horizontal displacements admits the following decomposition:

$$u_\alpha(x,y,z) = u_\alpha^{(0)}(x,y) - z\partial_\alpha w(x,y). \tag{2.39}$$

Eq. (2.39) is a kinematical condition indicating that the in-plane displacement components are the sum of the displacement of the middle surface $u_\alpha^{(0)}$ (zero-order term) plus a linear function of z proportional to gradients of the normal displacement. Eq. (2.39) implies that the strain tensor can be decomposed in a similar way:

$$\varepsilon_{\alpha\beta} = \varepsilon_{\alpha\beta}^{(0)} - zK_{\alpha\beta}. \tag{2.40}$$

Here, the zero order term corresponds to the middle surface strain tensor given by

$$\varepsilon^{(0)}_{\alpha\beta} = \frac{1}{2}\left(\frac{\partial u_\alpha}{\partial x_\beta} + \frac{\partial u_\beta}{\partial x_\alpha} + \frac{\partial w}{\partial x_\alpha}\frac{\partial w}{\partial x_\beta}\right). \tag{2.41}$$

and the first order term is the curvature tensor of the middle surface given by $K_{\alpha\beta} = \partial_\alpha \partial_\beta w$. Comparing Eq. (2.40) with Eq. (2.7), one notices that the quadratic terms of u_α have disappeared. This is because we assumed $u_x, u_y \ll w$. Moreover, the middle surface strain scales as $\varepsilon \sim u/L + (w/L)^2$, meaning that there is a contribution due to stretching and a contribution due to bending.

2D constitutive laws. Using Hooke's law (2.15) and Eq. (2.39), the stress tensor can also be decomposed as follows

$$\sigma_{\alpha\beta} = \sigma^{(0)}_{\alpha\beta} - z m_{\alpha\beta}. \tag{2.42}$$

The zero order term in Eq. (2.42) corresponds to the middle surface stress tensor given by:

$$\sigma^{(0)}_{\alpha\beta} = \frac{E}{1-\nu^2}\left[(1-\nu)\varepsilon^{(0)}_{\alpha\beta} + \nu\varepsilon^{(0)}_{\gamma\gamma}\delta_{\alpha\beta}\right]. \tag{2.43}$$

The above equation corresponds to an effective Hooke's law for plates that relates in-plane stresses with the in-plane components of the strain. The first order term in Eq. (2.42) is the moment density tensor given by

$$m_{\alpha\beta} = \frac{E}{1-\nu^2}\left[(1-\nu)K_{\alpha\beta} + \nu\delta_{\alpha\beta}K_{\gamma\gamma}\right]. \tag{2.44}$$

Eq. (2.44) it is a constitutive law that relates the moment per unit of length across the plate thickness to the curvature of the middle-surface. The moment quantifies the amount of bending of plates. Integrating Eq. (2.42) through the plate thickness, one obtains the total moment tensor $M_{\alpha\beta} = \int_{-h/2}^{+h/2} z\sigma_{\alpha\beta}\, dz$, then,

$$M_{\alpha\beta} \;=\; B\left[(1-\nu)K_{\alpha\beta} + \nu\delta_{\alpha\beta}K_{\gamma\gamma}\right], \tag{2.45}$$

where

$$B = \frac{Eh^3}{12(1-\nu^2)}, \tag{2.46}$$

is the *Bending modulus* (also called *Flexural rigidity*). The greater the value of the bending modulus the harder it is to bend a plate. In the limit of zero flexural rigidity, the so-called *membrane limit*, the sheet cannot support in-plane compressive stress so that it has to buckle out-of-the plane.

2.3.4 The FvK equations

Equations (2.40) and (2.42) allow us to separate the total elastic energy into stretching and bending parts. Using this decomposition and the formula for the total elastic energy Eq. (2.14), one has that

$$\begin{aligned} E_{\text{el}} &= \frac{1}{2}\int_V \sigma_{ij}\varepsilon_{ij}\,dV \\ &\simeq \underbrace{\frac{h}{2}\int_S \sigma^{(0)}_{\alpha\beta}\varepsilon^{(0)}_{\alpha\beta}\,dA}_{E_s} + \underbrace{\frac{h^3}{24}\int_S m_{\alpha\beta}K_{\alpha\beta}\,dA}_{E_b}, \end{aligned} \tag{2.47}$$

where V is the volume and S the surface area of the plate, where E_s and E_b are the stretching and bending energies, respectively. In particular, the bending energy can be written as follows

$$E_b = \frac{h^3}{24}\int_S m_{\alpha\beta}K_{\alpha\beta}\,dA = \frac{B}{2}\int_S \left[K_M^2 - 2(1-\nu)K_G\right], \tag{2.48}$$

where

$$K_M = \partial_{xx}w + \partial_{yy}w, \quad \text{and} \quad K_G = (\partial_x\partial_y w)^2 - \partial_{xx}w\,\partial_{yy}w, \tag{2.49}$$

are, respectively, the mean and Gauss curvatures of the middle surface. The total energy (2.47) is a functional of the coordinates w and $u^{(0)}_\alpha$. Following the Principle of Virtual Work, the conditions of equilibrium $\delta E_{\text{Tot}}/\delta w = 0$ and $\delta E_{\text{Tot}}/\delta u^{(0)}_\alpha = 0$ lead, respectively, to the following equations:

$$B\,\nabla^4 w - h\frac{\partial}{\partial x_\alpha}\left(\sigma^{(0)}_{\alpha\beta}\frac{\partial w}{\partial x_\beta}\right) = 0, \tag{2.50a}$$

$$\frac{\partial \sigma^{(0)}_{\alpha\beta}}{\partial x_\beta} = 0, \tag{2.50b}$$

known as *Föppl–von Kármán* (FvK) equations. They are a set of nonlinear partial differential equations describing the large deflection of plates. Eq. (2.50a) can be seen as a balance of out-of-plane forces describing the normal deflection $w(x,y)$ of the plate while Eq. (2.50b) corresponds to the equilibrium condition for the in-plane stresses. In the presence of an external force, the right-hand side of Eqs. (2.50) must be replaced by, respectively, $-h\rho g_z$ and $-\rho g_\alpha$, where $\rho\mathbf{g}$ is the density of volume external forces.

Similarly to the case of 2D linear elasticity, one can introduce an Airy function ϕ such that Eq (2.50b) is satisfied:

$$\sigma^{(0)}_{xx} = \partial_{yy}\phi, \quad \sigma^{(0)}_{yy} = \partial_{xx}\phi, \quad \text{and} \quad \sigma^{(0)}_{xy} = -\partial_{xy}\phi. \tag{2.51}$$

Using the Airy function, Eq. (2.50a) one obtains

$$B\nabla^4 w = h\left(\partial_{xx}w\partial_{yy}\phi + \partial_{yy}w\partial_{xx}\phi - 2\partial_{xy}w\partial_{xy}\phi\right),. \tag{2.52}$$

There are now two unknowns w and ϕ, therefore, an additional equation is needed. One can derive an equation that is analogous to the compatibility condition (2.24) for 2D equation. Following the same method as before, the components $\varepsilon^{(0)}_{xx}$,$\varepsilon^{(0)}_{yy}$ and $\varepsilon^{(0)}_{xy}$ given by Eq. (2.41) can be differentiated and added in such a way that the gradients of u_x and u_y are eliminated. Then, one obtains

$$2\partial_{xy}\varepsilon^{(0)}_{xy} - \partial_{yy}\varepsilon^{(0)}_{xx} - \partial_{xx}\varepsilon^{(0)}_{yy} = \partial_{xx}w\,\partial_{yy}w - (\partial_{xy}w)^2. \tag{2.53}$$

Using the constitutive relations (2.43) and the definition of the Airy function, one obtains the following equation

$$\nabla^4\phi = -E\left(\partial_{xx}w\,\partial_{yy}w - (\partial_{xy}w)^2\right), \tag{2.54}$$

Equations (2.56) and (2.56b) form a closed system which can be written in a more compact form by introducing the differential operator $[f,g]$ acting on arbitrary functions $f(x,y)$ and $g(x,y)$, where

$$[f,g] = \partial_{xx}f\,\partial_{yy}g + \partial_{xx}g\,\partial_{yy}f - 2\partial_{xy}f\,\partial_{xy}g. \tag{2.55}$$

Then, equations (2.56a) and (2.56b) take the form

$$B\nabla^4 w - h[w,\phi] = 0, \tag{2.56a}$$

$$\nabla^4\phi + \frac{E}{2}[w,w] = 0. \tag{2.56b}$$

Notice that $[w,w] = 2K_G$, thus, Eq. (2.56b) has the following form

$$\nabla^4\phi = -EK_G. \tag{2.57}$$

Compare the above equation with its 2D linear elastic counterpart (2.28): the right-hand side has been replaced by a source-type term $-EK_G$. As gradients of the function ϕ are related to in-plane stresses, the Gauss curvature can be interpreted as a source of stretching. Any region on the plate where $K_G \neq 0$ experiences stretching. This observation reveals a connection between Gauss curvature and the change of material lengths on a surface, which is formally stated by the well-known Gauss's *Theorema egregium*. Moreover, Eq. (2.57) provides a formula for the Gauss curvature in terms of the strain tensor:

$$K_G = 2\frac{\partial^2\varepsilon^{(0)}_{xy}}{\partial x\partial y} - \frac{\partial^2\varepsilon^{(0)}_{yy}}{\partial x^2} - \frac{\partial^2\varepsilon^{(0)}_{xx}}{\partial y^2}. \tag{2.58}$$

The above equation indicates that to change the Gauss curvature of a flat sheet, gradients of the in-plane strain must take place (homogenous in-plane strains results in dilation or contraction of the sheet while remaining flat).

2.4 Theorema egregium

Deformations that preserve lengths and angles on a surface are called *isometrical* deformations. Specifically, an *isometry* is a transformation that maps a surface to another while preserving the metric of the original surface. The famous Gauss's *Theorema egregium* (meaning "remarkable theorem") states that the Gaussian curvature is an invariant under local isometries. This theorem is especially important in the description of very thin sheets, where stretching becomes costly. In the limit when stretching becomes infinitely costly, the sheet can only undergo isometrical deformations and, thus, K_G is preserved and the sheet can be considered as *inextensible*. Theorema egregium explains why mapping the earth surface to a flat map is impossible without distorting areas and angles or why it is impossible to wrap a sphere with a flat piece of paper without tearing it.

The theorem tells us that the Gauss curvature is an intrinsic property of a surface, that is, can be measured without knowing how the surface is embedded in space. Indeed, let $\gamma(P,r)$ be the set of points on a surface at distance r measured along the surface from point P and let $\mathcal{P}_\gamma(P,r)$ be the perimeter of this curve. One can show that the Gauss curvature of S at the point P is given

$$K(P) = -6 \lim_{r\to 0} \left[\frac{1}{r^2} \left(\frac{\mathcal{P}_\gamma(P,r)}{2\pi r} - 1 \right) \right]. \tag{2.59}$$

This formula means that the Gauss curvature can be computed by measuring the perimeters of small circles drawn on the surface. This proves the *Theorema egregium* since these perimeters depend only on the surface metric and, therefore, are invariant under isometric deformations.

A more general result is the *Gauss-Bonet* theorem which takes into account the topology of the manifold. This theorem states that for any closed curve ∂S embedded on a surface and enclosing an area S, the integral of K_G on S is given by [119]

$$\int_S K_G \, dA = 2\pi\chi(S) - \int_{\partial S} k_g(s) \, ds. \tag{2.60}$$

Here, $\chi(S)$ is the *Euler characteristic* of the surface, $k_g(s)$ is the *geodesic curvature* of the curve ∂S and s is its arc-length. The Euler characteristic is a topological quantity that counts the number of "holes" in a manifold. For a simply connected surface, $\chi(S) = 1$. The geodesic curvature k_g is the curvature of the surface when computed intrinsically on the surface, therefore, it measures how far a curve is from being a

geodesic on the surface, As the geodesic curvature is an intrinsic measure of curvature (it does not depend on the particular embedding of the surface), it is invariant under isometric deformations of the surface.

2.4.1 Developable surfaces

One frequently is interested in sheets which are initially flat such as a sheet of paper (as is normally used for origami). By the Theorema egregium, if the sheet is inextensible, then the Gauss curvature is zero at any stage of the deformations. Surfaces with zero Gaussian curvature are called *developable surfaces*. This means that, by deforming a flat inextensible sheet without tearing it, we can only obtain developable surfaces. Conversely, any developable surface can be isometrically mapped to a flat surface.

Every developable surface is *ruled*, which means that it is generated by moving a straight line in space. Every ruled surface admits the following parametrization:

$$\mathbf{r}(u,v) = \mathbf{x}(u) + v\,\mathbf{g}(u), \tag{2.61}$$

where, $\mathbf{x}(u)$ and $\mathbf{g}(u)$ are smooth curves in space. The curve $\mathbf{x}(u)$ is called the *directrix* of the parametrization and any curve $\mathbf{r}(u_0, v)$ with fixed u_0 is a *generatrix* (or *generator*) of the surface, which are tangent to the surface [119, 9]. There are many ways to choose $\mathbf{x}(u)$ and $\mathbf{g}(u)$ that yield equivalent parametrizations. To avoid this indeterminacy, one can impose without loss of generality some additional conditions. First, we can freely choose $\mathbf{g}$ to have unit length: $|\mathbf{g}(u)| = 1$. Then, one can enforce the parameter u to be the arc-length of the directrix, implying that $|\mathbf{x}'(u)| = 1$. Finally, one can impose the generatrices to be orthogonal to the tangent of the directrix: $\mathbf{x}'(u) \cdot \mathbf{g}(u) = 0$.

For a ruled surface to be developable, the Gauss curvature vanishes. It can be shown that this condition is fulfilled when

$$(\mathbf{g} \times \mathbf{g}') \cdot \mathbf{x}' = 0. \tag{2.62}$$

This means that any ruled surface is developable when the vectors $\{\mathbf{g}, \mathbf{g}', \mathbf{x}'\}$ lie in a plane which is tangent to the surface. In this case, the normal vector to the surface does not depend on v, so, it does not vary along a generator. According to condition (2.62), developable surfaces can be classified into three types:

Cylinders: Cylinders and *generalized* cylinders which are surfaces traced out by a one-dimensional family of parallel lines. They are a particular case of the parametrization (2.61) when $\mathbf{g}(u) = \mathbf{g}_0$, with $\mathbf{g}_0$ constant. Flat surfaces can be seen as a particular case of cylindrical surfaces.

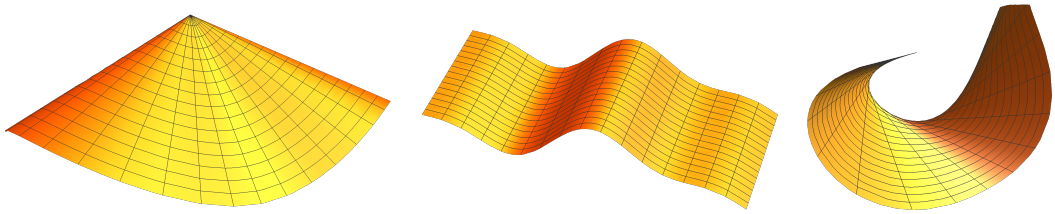

Figure 2.4 Examples of developable surfaces: (a) conical, (b) cylindrical and (c) tangent developable.

Cones: Cones and conical surfaces are a particular case of the parametrization (2.61) for $\mathbf{x}(u) = \mathbf{x}_0$, where $\mathbf{x}_0$ is the apex of the cone where all the generators meet.

Tangent developable surfaces: Surfaces which are constructed by extending the tangent lines of a curve in space. Any tangent developable surface can be parametrized by Eq. (2.62) with $\mathbf{g}(u) = \mathbf{x}'(u)$, in which case, the curve $\mathbf{x}(u)$ is called the *striction curve*.

Every three-dimensional shape made from a flat inextensible sheet may be formed by gluing together pieces of these three types of developable surfaces.

2.5 Conical Defects

When we crumple a sheet of paper, we see at the beginning the emergence of point defects of maximum curvature. These defects are points of energy localization where usually plastic deformation or damage take place. Inextensible sheets are very likely to exhibit such defects when they are deformed. As the sheet is inextensible, it will be developable everywhere except at the singularities. Thus, the resulting shape around a defect will be that of a developable cone, where the generators meet at the vertex. These defects usually lead to plastic deformations or damage if the deformations are large. As the sheet forms a developable surface, the resulting shape around the defects will be that of a developable cone where the generators of the surface meet at the vertex. In the literature, these defects have received the name of conical disclinations, developable cones, or simply d-cones [10]. A big part of this thesis concerns the study of elastic conical defects.

2.5.1 Developable cones

A single conical defect can be isolated by performing the following simple experiment [21]. A circular elastic sheet is placed on the rim of a hard cylinder of smaller radius and, then, the sheet is pushed into the cylinder by a vertical point force applied at its center (see Fig. 2.5). The indentation produces an excess of material that bends

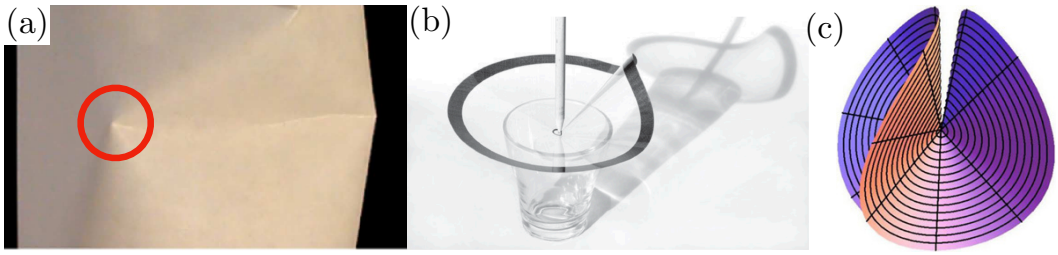

Figure 2.5 (a) Emergence of d-cones in a uniaxially compressed cylinder [51]. (b) Isolated d-cone: a circular piece of paper is pushed into a cylinder by a point force [9]. (e) e-cone with a surplus angle [93].

as a fold and loses contact with the cylinder rim. The final shape is conical but loses the axial symmetry of a perfect cone. Any circle drawn on the sheet at a distance r from the vertex preserve its length, thus, one can guess that the final shape is determined only by geometrical parameters such as the dimension of the sheet and the indentation depth. Thus, the resulting shape of d-cones is universal in the sense that it does not depend on the specific material properties.

Notice that in an ideal d-cone, the curvature is undefined at the tip. If we introduce a cut of radius $r_0 \ll R$, where R is the radius of the disk, one can show that $E_b \sim \ln(R/r_0)$, which diverges logarithmically as $r_0 \to 0$. This divergence is a characteristic feature of d-cones and other conical defects. In real situations, this divergence is regularized so that the stretching energy becomes comparable to the bending energy.

2.5.2 Other conical dislocations

Developable cones have motivated the study of other types of conical dislocations such as the *excess–cone*, or simply e-cone, which consists of a circular sheet to which a circular sector of material is either removed or introduced yielding a deficit or surplus angle [93] (see Fig. 2.5(c)). In the first case, a circular sector of the flat sheet is cut out and then the two remaining edges are glued together: the equilibrium shape will be a circular cone, as expected. In the case of a surplus angle, the circular sheet is cut radially once, and then, a circular sector previously cut out from other sheet is inserted and then glued. The resulting shape breaks the axial symmetry and can exhibit several instabilities. The e-cone has been inspired by morphogenesis processes in certain plant tissues which lead to conical shapes [42, 109, 69]. As the flat sheet is not subjected to any stretching, one expects the Gaussian curvature to be zero (indeed, the surface along the radial direction remains flat). However, there is a subtlety: circles drawn around the vertex lengthen (shorten) depending on the angular surplus (deficit), indicating a non-zero Gauss curvature according to Eq. 2.59. Indeed, an e-cone has a non-zero Gauss curvature, but it is localized at the tip. We can mention other conical defects such as the c-cone [133], k-cone [108], p-cone [107] and the foldable cone, or f-cone [78, 61] which are variations of the d-cone which combine cutting, gluing and

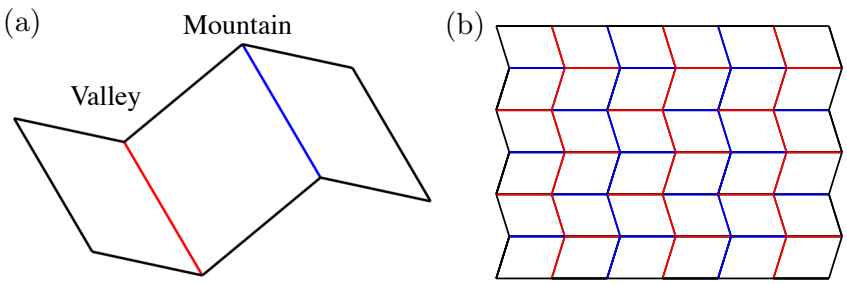

Figure 2.6 (a) Definitions of mountain and valley creases. (b) Miura crease pattern.

folding a circular sheet in different ways. The latter example, the *f*-cone is made by folding a sheet such that the creases meet at a single point. This system combines the elasticity of flexible inextensible sheets and origami. The second part of this thesis is devoted to the study of f-cones as a framework for nonrigid origami. In the next section, we review some key concepts concerning the study of origami from a technical viewpoint.

2.6 Origami

An origami design is based on a crease pattern, a network of creases and vertices drawn in a flat sheet of paper. From the point of view of applications, an origami is any 3-dimensional structure obtained by folding a 2-dimensional plate made of any solid material (from membranes to rigid thick plates), instead of just paper. Then, instead of folding paper, the creases can be any mechanism similar to a hinge.

Once the crease pattern is defined, each crease is folded to a certain folding angle $\psi \in [0, 2\pi]$ defined as the dihedral angle between the two facets connected by the crease (see Fig. 2.6.). The folding angles can be imposed as a fixed parameter of the final shape or they can be a result of a prescribed hingelike mechanism at the creases and the loading conditions to which the structure is subjected. Depending on its orientation, each crease can be either a *mountain* (if the ridge points upwards) or a *valley* (if the ridge points downwards) (see Fig. 2.6(a)). Each fold can be assigned to mountain or valley before folding, and if so, the mountain-valley assignment must guarantee the foldability of the structure. If there is no mountain-valley pre-assignment, then each fold chooses to be a mountain or a valley depending on the way the crease network deforms when subjected to loads.

2.6.1 Flat foldability

A classical problem in origami is whether a given crease pattern can be folded to a flat state such that it lies in a plane, and if so, what is the mountain-valley assignment of the crease network. Thus, flat foldability means that there exists a continuous mapping

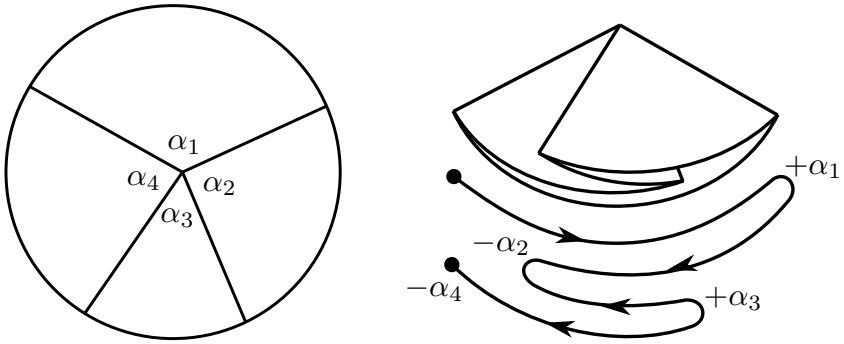

Figure 2.7 A flat foldable vertex of four creases. $\alpha_1 + \alpha_3 = \alpha_2 + \alpha_4 = \pi$.

from the unfolded state (reference configuration) to a configuration in which each crease is folded completely (each folding angle is either 0 or 2π).

To begin, we focus on *local flat foldability*, that is, what are the conditions for a single-vertex origami to be flat-foldable. Figure 2.7(a) shows a four-creases vertex origami. There are some conditions that must be met for a single-vertex origami to be flat foldable. Consider a disk with n radial creases meeting at its center. A result from Jun Maekawa [62] relates the number of mountain and valley creases around a flat single-vertex origami.

Maekawa's theorem: Let M be the number of mountain creases and V the number of valley creases flat foldable single-vertex origami, then [62, 12], $|M - V| = 2$.

This theorem is a necessary condition but it is not sufficient to characterize local flat foldability. As a corollary of Maekawa's theorem, the number of creases around the vertex must be even. Another theorem from Kawasaki relates the angles between consecutive creases (sector angles) in the unfolded configuration.

Kawasaki's theorem: Consider now a disk with $2n$ radial creases and let $\alpha_1, \alpha_2, \ldots, \alpha_{2n}$, with $\sum_{i=1}^{2n} \alpha_i = 2\pi$ denote the consecutive angles between the creases in the unfolded state, then [66],

$$\alpha_1 - \alpha_2 + \alpha_3 - \ldots + \alpha_{2n-1} - \alpha_{2n} = 0. \tag{2.63}$$

To see why this happens it is enough to observe that, in the folded state, the orientation of the paper is reversed at each crease. If one follows the path left by the edge of the paper starting from a crease, one notices that the first crease is rotated by an angle α_1, then by $-\alpha_2$ and so on (see 2.7(b)). Therefore, the paper meets back up with itself if Kawasaki's condition is met (2.63). Alternatively, the theorem states that the sum of the alternate angles about the vertex is π. Figure 2.7 shows Kawasaki's theorem applied to a 4-creases vertex. The Kawasaki theorem is a necessary and sufficient condition for local flat foldability.

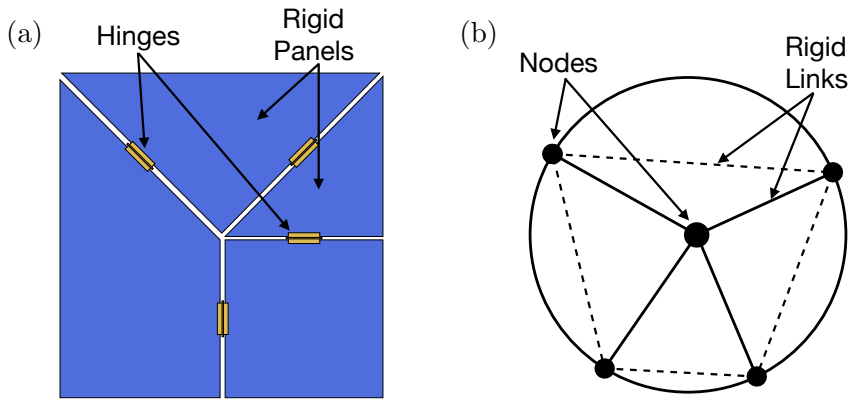

Figure 2.8 (a) Rigid origami as rigid panels connected by hinges. (b) A 4-creases vertex seen as a rigid frame.

Global foldability, that is, given a crease pattern, can be folded flat, is a much harder problem. It has been proved that testing global foldability is an NP-hard problem, which means that the problem can not be solved by a computer in polynomial time [12]. In particular, what was proven is that, given a crease pattern, finding a mountain-valley assignment that folds flat is NP-hard. Even if a mountain-valley assignment that folds flat is given, finding the overlap order of a flat folded state is NP-hard.

2.6.2 Rigid foldability

Rigid foldability is the property of a crease pattern to continuously transform from an unfolded state to an intermediate folded state by keeping its facets rigid. Most of the research about origami and its applications deal with materials based on *rigid origami* which consists of rigid panels connected by hingelike creases (see Fig. 2.8(a)). Notice that the folding process must satisfy the geometrical constraints imposed by the rigidity and the inextensibility of the plates. Therefore, one needs suitable conditions to characterize rigid foldability of a crease pattern.

We focus first on local rigid foldability, that is, what happens about a single-vertex. Consider a single-vertex origami with n radial creases and sector angles $\{\alpha_i\}_n$. It is clear that the case $n = 1$ cannot fold. The $n = 2$ case can fold only if $\alpha_1 = \alpha_2 = \pi$, which is a trivial case. For $n > 2$, it is easy to note that if one of the sector angles α_i is larger than π, then the vertex cannot fold. A rigid n-creases single-vertex origami can be seen as a rigid frame made of $n + 1$ nodes connected by $2n$ rigid links (see Fig. 2.8(b)). The nodes correspond to the ends of the creases plus the vertex and the links correspond to the n creases plus n virtual links lying on the facets connecting the ends of consecutive creases. A necessary condition to have local rigid foldability is to

have at least one degree of freedom. One can compute the degrees of freedom using the Maxwell formula for rigid frames [90, 77]:

$$\frac{d(d+1)}{2} + N_0 - N_S = dN - N_B. \tag{2.64}$$

Here, d is the number dimensions, N the number of nodes, N_0 the number of degrees of freedom, N_S the states of self-stress and N_B the number of constraints (rigid bonds). As this linkage system is constituted only by triangles there are no self-stress states. In order to have rigid foldability, one must have at least one degree of freedom. Using $d = 3$, $N = n + 1$, $N_B = 2n$ and $N_S = 0$ one obtains that $N_0 = n - 3$, thus, rigid-foldability requires $n > 3$.

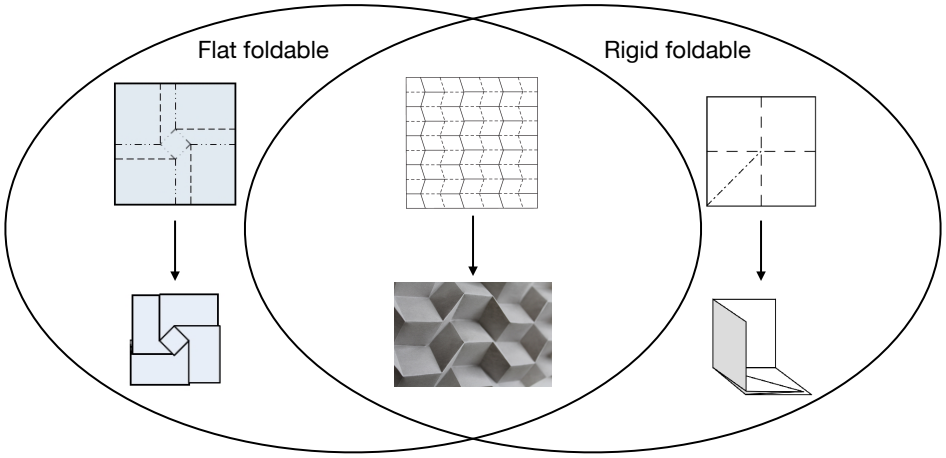

Figure 2.9 Venn diagram of flat foldable, rigid foldable and not foldable crease patterns. The examples correspond to the square twist fold [112], the Miura-fold, the 3-D corner origami.

Necessary and sufficient conditions for a single-vertex crease pattern to be rigidly foldable were determined in reference [1] for the case where the creases are pre-assigned to be mountains and valleys as well as in the unassigned case. However, similarly to flat foldability, characterizing global rigid foldability of any crease pattern is a hard problem. Recently, it has been proved that testing global rigid-foldability is NP-hard [6].

Rigid foldability and flat foldability are unrelated concepts. Indeed, some rigid foldable crease patterns are not flat foldable such as the 3D corner origami (see Fig. 2.9). Also, there are examples of crease patterns that are flat-foldable, but to access to this folded state the facets necessarily have to bend. For instance, the square twist fold can reach a flat folded state, but the facets have to bend during the transition to a folded state [112].

Flat-foldable and rigid-foldable origamis require many and complex restrictions on the crease patterns. However, these constraints are relaxed when the facets are allowed to bend as in the case of the square twist fold. We will refer to this case as nonrigid

origami. In the second part of this thesis, we study foldable cones as a framework for nonrigid origami.

I

Physics of Wrinkling

3 Wrinkle formation in elastic thin sheets

In this chapter we provide a brief introduction into wrinkling instabilities in elastic thin sheets focusing on tensional wrinkling. Then, we explore the role of boundary conditions in the analysis of wrinkled patterns in thin elastic sheets by studying the consequences of modifying the geometry and loading conditions of the paradigmatic Lamé problem.

3.1 Wrinkling phenomena

Elastic thin sheets subjected to in-plane compressive or tensile stresses can undergo several buckling instabilities, so that the out-of-plane deflection forms periodic wavy structures called *wrinkles*. Examples of wrinkled patterns can be observed in many instances of daily life: from wrinkles in human skin or the peel of drying fruits to curtains or clothes [22] (see Figs. 3.1(a-b)). Also, wrinkle phenomena has aroused great interest due to its applications [16, 19, 24, 75, 47, 22, 38, 37, 41]. In condensed matter physics, pre-wrinkled conductive films have been proposed as stretchable electric contacts [75] and wrinkles in graphene sheets are believed to modify its electronic properties [41]. In biophysics, traction forces involved in cell motility on elastic substrates can be studied via the emerging wrinkling patterns [19]. For medical purposes, a better understanding of wrinkle formation would be helpful for the treatment of post-surgery scars [22, 16]. Finally, wrinkle formation can be used for a metrology of the elastic properties and thickness of ultrathin sheets [59].

Wrinkles triggered by compressive in-plane stresses and those triggered by in-plane tension usually exhibit different properties. In the first case, compression occurs when the film adheres to a substrate and there is a mismatch between both. Fig. 3.1(a) shows this situation in the wrinkling of the skin of a shriveled apple where compression is induced by the shrinkage of the flesh due to the loss of moisture. The fine features of the final pattern are a result of the competition between the flexural stiffness of the sheet membrane and the stiffness of the foundation [22]. Thin sheets on compliant soft substrates can result in complex wrinkling patterns with varying degrees of orientational ordering [29, 122, 5]. A balance between these forces yields universal scaling laws for the fine features of the wrinkling pattern: the wavelength scales as $\lambda \sim (B/K)^{1/4}$, where B is the bending stiffness of the sheet (measured in N·m) and K

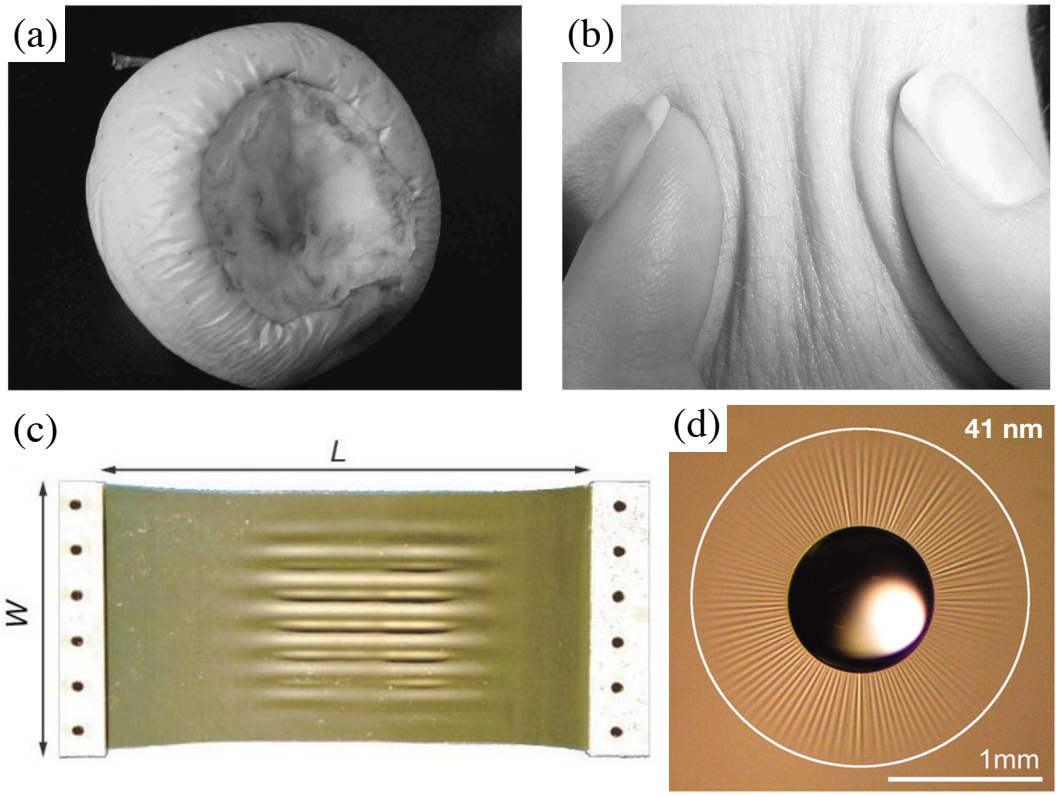

Figure 3.1 (a) Wrinkles in the skin of a shriveled apple and (b) on the back of one's hand by bunching up the skin substrate (figures taken from [24]). (c) Wrinkles in a stretched polyethylene sheet (taken from [26]). The dimensions of the sheet are: length, $L = 20$ cm; width, $W = 12$ cm; thickness, $h = 0.01$ cm. (d) "Drop-on-sheet" experiment: Capillary-induced wrinkling of a thin floating polymer film on which a drop is placed [59]. Notice that the inward tension is mainly caused by capillary forces rather than the weight of the drop. The thickness of the sheet is 41 nm and the radius of the drop is 0.5 mm.

is the substrate stiffness (measured in $\mathrm{N/m^3}$), while the amplitude scales linearly with the wavelength. On the other hand, wrinkles induced by tension exhibit a well-defined direction. Fig. 3.1(c) shows a rectangular sheet with clamped boundaries subjected to uniaxial stretching. When the longitudinal stretching strain is large enough, the sheet develops wrinkles that are parallel to the direction of tension. The transverse stress is tensile near the clamped boundary but compressive slightly further from it, where wrinkles appear. In this region, the sheet buckles to accommodate the in-plane strain incompatibility generated by the Poisson effect. The out-of-plane deformations form an oscillatory structure whose wavelength scales as $\lambda \sim (B/T)^{1/4} L^{1/2}$, where T is the tension to which the sheet is subjected and L is its length. Fig. 3.1(d) shows the analogous axisymmetric version of this experiment: the "drop-on-sheet" experiment. A drop of water is placed on a circular ultrathin polymer film floating in liquid [59]. The surface tension of the liquid produces an outward radial tension while the drop produces an inward tension due to capillary forces. The radial tensions produce a Poisson effect in the azimuthal direction yielding radial wrinkles of finite length around the drop. The weight of the drop is marginal compared to the capillary forces

which are exerted by the surface tension at the air-water-sheet contact line, hence the inward tension is produced due to capillarity and not gravity. The number of wrinkles and their extension are functions of the involved capillary forces and the flexural stiffness of the film.

3.1.1 Tension-field theory

In 1929, Wagner noticed that a stretched membrane buckles so that loads are transmitted along one of the principal axes of stress defining "tension rays" [129]. The membrane develops wrinkles whose direction coincides with the trajectories of tensile stress. Reissner first formulated in 1938 a "tension-field theory" (TFT) capturing these tension rays in the wrinkled regions [100]. The theory assumes that the smallest principal stress, whose principal direction is perpendicular to the wrinkles, collapses to zero [88]. This assumption is based on the fact that a sheet with zero flexural rigidity[1] cannot bear compressive stresses, that is, it buckles as soon as one component of the stress becomes negative. Subsequent works continued investigating into the wrinkling of membranes until presently [72, 118, 87, 96, 117, 26, 24, 86]. Tension field theory has been applied successfully in some specific geometries [87, 36], however, the theory as originally formulated focuses on predicting the direction of the tension lines and the magnitude of the tensile stress rather than the fine features of the wrinkles such as their amplitude, wavelength, and extension.

3.1.2 NT and FFT regimes

When the flexural stiffness is small but finite, the sheet buckles when a stress component exceeds a critical compressive load. TFT is only valid far from the buckling threshold. Nevertheless, recent studies have put attention on complementing the theory by incorporating an analysis of the Föppl-von Karman equations at the onset of the instability [22, 38, 37]. These works emphasized the differences between near-threshold (NT) and far-from-threshold (FFT) wrinkling patterns, suggesting that the underlying mechanisms governing these two regimes are different [38, 37]. In the NT regime, the wrinkling pattern can be characterized by a perturbative analysis of the FvK equations over the flat state assuming that the stresses are those of the flat state and the out-of-plane deflection is infinitesimal. Then, a balance of the dominant forces yields scaling laws for the wavelength and extension of the wrinkles, while the amplitude follows a square root law as expected for supercritical bifurcations [37, 35]. On the other hand, the FFT regime is characterized by a collapse of the stress component in the direction of compression. Upon this assumption, the extension of the wrinkles and their wavelength can be obtained by minimizing an energy functional.

[1] Equivalent to a sheet with zero thickness since $B \sim h^3$. This regime is commonly called the "membrane limit"

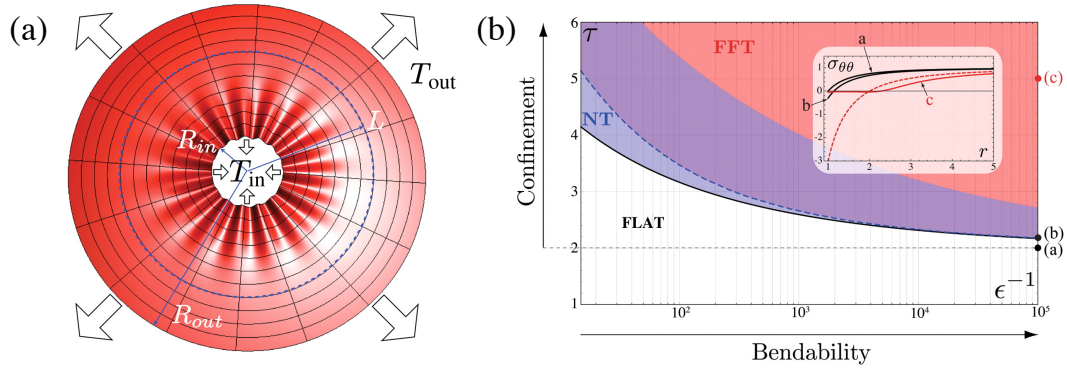

Figure 3.2 (a) The Lamé configuration. (b) Theoretical phase diagram of wrinkling patterns in the Lamé configuration. The dimensionless parameters ϵ^{-1}, τ represent, respectively, the bendability and confinement. The inset shows the evolution of the hoop stress $\sigma_{\theta\theta}(r)$ for different points in the phase diagram. Both figures were taken from reference [38].

Thus, the FFT analysis can be considered as a tension field theory for membranes with finite flexural rigidity.

3.1.3 The Lamé problem

With regard to the "drop-on-sheet" experiment, wrinkling formation in axisymmetric geometries can be theoretically studied by means of the Lamé configuration consisting of an annular elastic sheet under planar axisymmetric loading[1]. The Lamé problem is a paradigmatic model that has served as a prototypical model for the analysis of wrinkling instabilities in several systems with axial symmetry [47, 32, 31, 38, 37, 59, 125, 127, 105]. This configuration is depicted in Fig. 3.2(a): an annular sheet of inner radius R_{in} and outer radius R_{out} is subjected to differential tensions T_{out} at $r = R_{\text{out}}$ and $T_{\text{in}} > T_{\text{out}}$ at $r = R_{\text{in}}$. This problem is characterized by two dimensionless parameters: the confinement (τ) and the bendability (ϵ^{-1}), where

$$\tau \equiv \frac{T_{\text{in}}}{T_{\text{out}}}; \qquad \epsilon \equiv \frac{B}{R_{\text{in}}^2 T_{\text{in}}}. \tag{3.1}$$

Using the Lamé solutions for the stress field of the flat state, one finds that the hoop stress becomes compressive for $\tau > 2$ in a region $R_{\text{in}} < r < L_{\text{NT}}$, where $L_{\text{NT}}/R_{\text{in}} = \sqrt{\tau - 1}$. Then, for a given ϵ, buckling is expected for a critical value $\tau_c(\epsilon) > 2$. As the sheet gets thinner, the energetic cost of bending becomes smaller, hence one expects $\tau_c(\epsilon) \to 2$ as $\epsilon \to 0$. Fig. 3.2(b) presents a phase diagram showing the NT and FFT regimes in the parameter space (ϵ^{-1}, τ). The NT regime exists in a region above the curve $\tau_c(\epsilon)$ that shrinks as $\epsilon \to 0$. By performing perturbative analysis of the FvK equations in the NT regime, one can find scaling laws for the critical confinement $\tau_c(\epsilon)$, the number of wrinkles of the emerging pattern $m_c(\epsilon)$ and the wrinkle extent L_{NT}. A balance of the dominant forces appearing in the FvK equations yields: $\tau_c(\epsilon) - 2 \sim \epsilon^{1/4}$,

[1] This system was apparently first studied by Lamé [121].

$m_c(\epsilon) \sim \epsilon^{-3/8}$ and $L_{\mathrm{NT}}/R_{\mathrm{in}} - 1 \sim \epsilon^{1/4}$. Well above the curve $\tau_c(\epsilon)$, the hoop stress collapses in the wrinkled region, as assumed in TFT, and the system enters into the FFT regime. The perturbative analysis is no longer valid here because of the finite amplitude of the wrinkles and the abrupt change in stress in the wrinkled region. Nevertheless, one can show that a winkled state is energetically favorable compared to that of a flat membrane. The wrinkles extent L_{FFT} in the FFT regime is obtained through energy minimization, yielding $L_{\mathrm{FFT}}/R_{\mathrm{in}} = \tau/2$. In this regime, the number of wrinkles scales as $m_{\mathrm{FFT}} \sim \epsilon^{-1/4}$. Therefore, the number of wrinkles and their extent follows different scaling laws than those of the near-threshold regime.

Unfortunately, both NT and FFT analysis can be performed only when the direction of the subsequent wrinkles is known a priori, which is the case of simple geometries such as rectangular and annular sheets. Little is known when the lines of tension in the pre-buckled state of a sheet are not straight. Slight changes on the boundary conditions, such as nonuniform tensions or asymmetric geometries would lead to curved tension lines in the flat state. The characterization of the wrinkling instability for general geometrical and loading conditions remains an open problem [5]. The main goal of this chapter is to explore the consequences of changing boundary conditions of the Lamé configuration by modifying the load conditions and the geometry of the Lamé configuration.

3.1.4 The role of geometry and boundary conditions

The present work explores the role of boundary conditions on the tensional wrinkling instabilities. As a natural extension of the Lamé configuration studied in reference [38], we study two modified versions of it. First, we consider an annular sheet subjected to inward tension in its inner edge while its outer edge is clamped. In this configuration, we analyze the wrinkling patterns in both NT and FFT regimes and examine the similarities and differences with the usual Lamé case. Second, we consider the elastic problem of an infinite elastic sheet with an elliptic hole and subjected to a uniform differential tension between its outer boundary and inner edge. We obtain the stress field in the pre-buckled state and compute both its principal components and principal directions as function of the eccentricity of the hole and the ratio between the inward and outward tensions. Depending on these control parameters, regions around the membrane can be either in a taut, slack or unidirectionally tensional state. This yields a rich phase diagram of different global stress states depending on the topology of the compressed regions and on the presence (or absence) of slack regions. Finally, we compute the lines of tensions and show that as one moves away from the circular hole case towards the crack limit, lines of tensions bent considerably, making it difficult to predict wrinkling patterns beyond the buckling instability.

3.2 Annular sheet with clamped boundaries

In this section, we analyze the tensional wrinkling instability of an inwardly stretched annular sheet whose outer edge is clamped.

3.2.1 Setup

We study the tensional wrinkling instability of an annular sheet of inner radius R_{in} and outer radius R_{out} subjected to an inward tension T (force per unit length) applied at $r = R_{\text{in}}$ while the outer edge is clamped (see Fig. 3.3). For this configuration, we use polar coordinates, where σ_{rr}, $\sigma_{\theta\theta}$, $\sigma_{r\theta}$ are the components of the two-dimensional stress tensor (force per unit length) and u_r, u_θ are the components of the in-plane displacement field. Then, the boundary conditions can be written as follows

$$\sigma_{rr}(r = R_{\text{in}}) = T, \qquad u_r(r = R_{\text{out}}) = 0. \tag{3.2}$$

The equilibrium equations (2.25) for the stress components in polar coordinates read [76]

$$\partial_r(r\sigma_{rr}) - \sigma_{\theta\theta} + \partial_\theta\sigma_{r\theta} = 0, \tag{3.3a}$$
$$\partial_r(r\sigma_{r\theta}) + \sigma_{r\theta} - \partial_\theta\sigma_{\theta\theta} = 0. \tag{3.3b}$$

The stress tensor is related to the strain tensor via Hooke's law,

$$\varepsilon_{ij} = \frac{1}{Y}\left((1+\nu)\sigma_{ij} - \nu\sigma_{kk}\delta_{ij}\right), \tag{3.4}$$

where $Y = Eh$ is the stretching modulus, E is the Young's modulus, h is the thickness of the plate and ν is the Poisson ratio. Notice that this expression is similar to Eq. (2.16) except for the prefactor $1/h$ because the stress components in the present case have units of length per unit length. In the large deflection regime, the components of the strain tensor read

$$\varepsilon_{rr} = \frac{\partial u_r}{\partial r} + \frac{1}{2}\left(\frac{\partial w}{\partial r}\right)^2, \tag{3.5a}$$
$$\varepsilon_{\theta\theta} = \frac{u_r}{r} + \frac{1}{r}\frac{\partial u_\theta}{\partial \theta} + \frac{1}{2r^2}\left(\frac{\partial w}{\partial \theta}\right)^2, \tag{3.5b}$$
$$\varepsilon_{r\theta} = \frac{1}{2r}\frac{\partial u_r}{\partial \theta} + \frac{1}{2}\frac{\partial u_\theta}{\partial r} + \frac{1}{2r^2}\frac{\partial w}{\partial \theta}\frac{\partial w}{\partial r}, \tag{3.5c}$$

where $w(r,\theta)$ is the vertical deflection of the sheet.

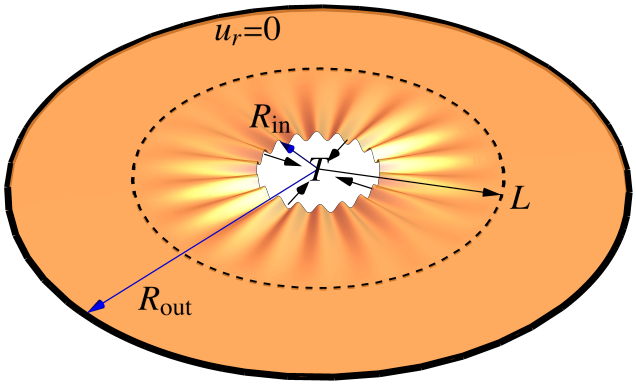

Figure 3.3 Annular sheet subjected to inward tension T in its inner edge while its outer edge is clamped. L denotes the extent of wrinkles.

3.2.2 Base state solution

Before studying the buckling instability, we compute the stress field of the base state: the planar, axisymmetrical state, where $u_\theta = \partial_\theta u_r = w = 0$. We introduce an Airy function $\phi(r,\theta)$ defined such that

$$\sigma_{rr} = \frac{1}{r}\frac{\partial \phi}{\partial r} + \frac{1}{r^2}\frac{\partial^2 \phi}{\partial \theta^2}, \tag{3.6a}$$

$$\sigma_{\theta\theta} = \frac{\partial^2 \phi}{\partial r^2}, \tag{3.6b}$$

$$\sigma_{r\theta} = -\frac{\partial}{\partial r}\left(\frac{1}{r}\frac{\partial \phi}{\partial \theta}\right). \tag{3.6c}$$

In this way Eq. (3.3) is automatically satisfied. In the planar state, the condition of equilibrium is that the Airy function is biharmonic, that is, $\nabla^4 \phi = 0$ (recall that Eq. (2.28) in two dimensional elasticity is equivalent to the second FvK Eq. (2.56b) for $w = 0$). In polar coordinates, the Laplacian operator is given by

$$\nabla^2 = \frac{\partial^2}{\partial r^2} + \frac{1}{r}\frac{\partial}{\partial r} + \frac{1}{r^2}\frac{\partial^2}{\partial \theta^2}. \tag{3.7}$$

Since we are looking for axisymmetrical solutions, the Airy function is a function of r only and, thus, the biharmonic equation reduces to

$$r\frac{\partial}{\partial r}\left(\frac{1}{r}\frac{\partial}{\partial r}\left(r\frac{\partial \phi}{\partial r}\right)\right) = 0, \tag{3.8}$$

whose solution is given by

$$\phi(r) = \frac{A}{2}r^2 + B\ln(r) + C, \tag{3.9}$$

where A, B and C are constants to be determined by imposing the boundary conditions (3.2). The constant C can be freely chosen since it does not have an effect on the stress field. Using Eqs. (3.6), one finds that the stress components have the form

$$\sigma_{rr} = A + \frac{B}{r^2}, \tag{3.10a}$$

$$\sigma_{\theta\theta} = A - \frac{B}{r^2}, \tag{3.10b}$$

$$\sigma_{r\theta} = 0. \tag{3.10c}$$

Imposing the first condition in Eq. (3.2), one obtains that

$$\sigma_{rr}(R_{\text{in}}) = A + \frac{B}{R_{\text{in}}^2} = T. \tag{3.11}$$

To impose the second boundary condition in (3.2) one needs to compute the radial displacement which can be obtained by using Eqs. (3.5b) (with $u_\theta = w = 0$), the Hooke's law (3.4) and Eqs. (3.10), yielding

$$u_r(R_{\text{out}}) = \frac{1}{Y}\left((1-\nu)AR_{\text{out}} - (1+\nu)\frac{B}{R_{\text{out}}}\right) = 0. \tag{3.12}$$

The constants A and B are obtained from Eqs. (3.11,3.12). Then, the stress components are given by

$$\sigma_{rr} = \left(\frac{\frac{1+\nu}{1-\nu} + \left(\frac{R_{\text{out}}}{r}\right)^2}{\frac{1+\nu}{1-\nu} + \left(\frac{R_{\text{out}}}{R_{\text{in}}}\right)^2}\right)T, \qquad \sigma_{\theta\theta} = \left(\frac{\frac{1+\nu}{1-\nu} - \left(\frac{R_{\text{out}}}{r}\right)^2}{\frac{1+\nu}{1-\nu} + \left(\frac{R_{\text{out}}}{R_{\text{in}}}\right)^2}\right)T. \tag{3.13}$$

The radial stress is tensile everywhere but the hoop stress becomes compressive for $R_{\text{in}} < L_{\text{NT}}$, where

$$L_{\text{NT}} \equiv \sqrt{\frac{1-\nu}{1+\nu}}R_{\text{out}}. \tag{3.14}$$

Notice that the existence of compressed regions depends on the geometry of the sheet and not on T. The present problem is characterized by two dimensionless parameters: the ratio between the two radii (ρ) and the bendability (ϵ^{-1}), where

$$\rho \equiv \frac{R_{\text{out}}}{R_{\text{in}}}; \qquad \epsilon \equiv \frac{B}{R_{\text{in}}^2 T}. \tag{3.15}$$

By defining

$$\rho^* \equiv \sqrt{\frac{1+\nu}{1-\nu}}, \tag{3.16}$$

the condition for existence of compression can be expressed as $\rho > \rho^*$. For a fixed value of ϵ, buckling is expected if $\rho > \rho_c(\epsilon) > \rho^*$, where $\rho_c(\varepsilon)$ is the critical geometrical ratio. As the sheet gets thinner, the energetic cost of bending decreases, hence, in the

high bendability regime, $\epsilon \to 0$, one expects that this critical value $\rho_c(\epsilon) \to \rho^*$, which means that the membrane buckles as soon as compressive regions appear around the hole.

3.2.3 Near-threshold analysis

To predict the critical value $\rho_c(\epsilon)$ for the buckling threshold one needs to account for the out-of-plane deflections of the plate which are described by the FvK equations. In polar coordinates, Eq. (2.50a) reads [88]

$$B\nabla^4 w = \sigma_{rr}\frac{\partial^2 w}{\partial r^2} + 2\sigma_{r\theta}\frac{\partial}{\partial r}\left(\frac{1}{r}\frac{\partial w}{\partial \theta}\right) + \sigma_{\theta\theta}\left(\frac{1}{r}\frac{\partial w}{\partial r} + \frac{1}{r^2}\frac{\partial^2 w}{\partial \theta^2}\right). \tag{3.17}$$

where $B = Eh^3/12(1-\nu^2)$ is the bending modulus. The stress components have been rescaled by a factor h. The buckling instability in the NT regime can be studied by performing a stability analysis of the flat solution using Eq. (3.17). We assume the out-of-plane displacement has the form

$$w = f(r)\cos(m\theta), \tag{3.18}$$

where $f(r)$ is the amplitude of the pattern and m accounts for the number of wrinkles. Then, at dominant order, Eq. (3.17) reduces to

$$B\left[\frac{1}{r}\frac{d}{dr}\left(r\frac{d}{dr}\right) - \frac{m^2}{r^2}\right]^2 f = \sigma_{\theta\theta}\left(-\frac{m^2}{r^2} + \frac{1}{r}\frac{d}{dr}\right)f + \sigma_{rr}\frac{d^2 f}{dr^2}. \tag{3.19}$$

A detailed derivation of the above equation, which takes into account dominant and sub-dominant order terms, can be found in reference [37]. A stability analysis of Eq. (3.19) (assuming $f(r)$ is infinitesimal) yields the critical value $\rho_c(\epsilon)$ and the number of wrinkles $m_c(\epsilon)$ of the emerging pattern. Focusing on the high bendability regime ($\epsilon \ll 1$), an estimation of the dominant forces involved in Eq. (3.19) yields scaling laws for $\rho_c(\epsilon)$ and $m_c(\epsilon)$. At the onset of the buckling instability, thus close to the inner radius $r \sim R_{\text{in}}$, the stress components (3.13) can be approximated by $\sigma_{rr} \approx T$ and $\sigma_{\theta\theta} \approx -\tilde{\rho}_c(\epsilon)T/\rho^*$, where $\tilde{\rho}_c(\epsilon) \equiv \rho_c(\epsilon) - \rho^*$ (recall $\tilde{\rho}_c(\epsilon) \to 0$ in this limit). For $m_c \gg 1$, the three dominant forces in Eq. (3.19) are azimuthal bending ($\approx Bm_c^4 f/R_{\text{in}}^4 = \epsilon m_c^4 Tf/R_{\text{in}}^2$), azimuthal compression ($\approx \tilde{\rho}_c T m_c^2 f/R_{\text{in}}^2$) and radial tension ($\approx Tf/\tilde{\rho}_c^2 R_{\text{in}}^2$), were we have used that the radial derivatives d/dr scale as $1/(L_{\text{NT}} - R_{\text{in}}) \approx 1/R_{\text{in}}\tilde{\rho}_c$. Balancing these three forces we obtain the following scaling laws

$$\tilde{\rho}_c(\varepsilon) \sim \epsilon^{1/4}, \quad m_c(\epsilon) \sim \epsilon^{-3/8}, \tag{3.20}$$

$$\frac{L_{\text{NT}}}{R_{\text{in}}} - 1 \approx \frac{\tilde{\rho}_c(\epsilon)}{\rho^*} \sim \epsilon^{1/4}. \tag{3.21}$$

These scaling laws are the analogous to those found in the Lamé problem [33, 38], where the parameter ρ plays an analogous role as the ratio between the outer and inner tensions (τ in Fig. 3.2).

3.2.4 Far-from-threshold analysis

Let us analyze the far-from-threshold regime for very thin sheets ($\epsilon \ll 1$). Expecting the NT analysis is valid for a zone of the parameter space (ϵ, ρ) just above the critical curve $\rho_c(\epsilon)$, we assume now a fixed value of ρ well above the buckling threshold and consider the limit $\epsilon \to 0$ by keeping ρ constant. We assume that the sheet is composed of two parts: a wrinkled region in $R_{\text{in}} < r < L$ (region I) where the shear and hoop stresses collapsed $\sigma_{r\theta}$, $\sigma_{\theta\theta} \to 0$, and an outer annulus $L < r < R_{\text{out}}$ (region II) where the sheet remains flat. In region I, Eq. (3.3a) and the first boundary condition in (3.2) and Hooke's law imply that

$$\sigma_{rr}^{I} = \frac{R_{\text{in}} T}{r}; \qquad \varepsilon_{rr} = \frac{\sigma_{rr}}{Y}; \qquad \varepsilon_{\theta\theta} = -\nu \varepsilon_{rr}. \tag{3.22}$$

In region II, the computation of the stresses and the radial displacement follows a similar procedure as for the base state solution. Imposing continuity of the radial stress, $\sigma_{rr}^{I}(L) = \sigma_{rr}^{II}(L)$, and zero displacement at the outer edge, $u_r^{II}(R_{\text{out}}) = 0$, one finds that

$$\sigma_{rr}^{II}(r) = \frac{\left(\frac{1+\nu}{1-\nu} + \frac{R_{\text{out}}^2}{r^2}\right)}{\left(\frac{1+\nu}{1-\nu} + \frac{R_{\text{out}}^2}{L^2}\right)} \frac{R_{\text{in}} T}{L}, \qquad \sigma_{\theta\theta}^{II}(r) = \frac{\left(\frac{1+\nu}{1-\nu} - \frac{R_{\text{out}}^2}{r^2}\right)}{\left(\frac{1+\nu}{1-\nu} + \frac{R_{\text{out}}^2}{L^2}\right)} \frac{R_{\text{in}} T}{L}. \tag{3.23}$$

The radial displacement in region II is given by

$$u_r^{II}(r) = \frac{(1+\nu) R_{\text{in}} T \left(r - \frac{R_{\text{out}}^2}{r}\right)}{Y L \left(\frac{1+\nu}{1-\nu} + \frac{R_{\text{out}}^2}{L^2}\right)}. \tag{3.24}$$

The radial displacement in region I can be obtained by using relation (3.5b), the Hooke's law and the stress in Eq. (3.22). After imposing continuity in the displacements at $r = L$, we obtain

$$u_r^{I}(r) = \frac{R_{\text{in}} T}{Y} \ln\left(\frac{r}{L}\right) + u_r^{II}(L). \tag{3.25}$$

This particular solution implies certain conditions on the wrinkling pattern. In region I, where the hoop stress collapses, Eqs. (3.22) indicates that the sheet is in radial pure traction which produces a Poisson effect $\varepsilon_{\theta\theta} = -\nu \varepsilon_{rr} < 0$ in the azimuthal direction. This causes that a circle of radius r reduce its perimeter by a length $-2\pi\nu R_{\text{in}} T/Y$. However, this local contraction is not compatible with the shortening of the perimeter $2\pi u_r^{I}(r)$ generated by the inwardly radial displacement ($u_r^{I} < 0$). This incompatibility

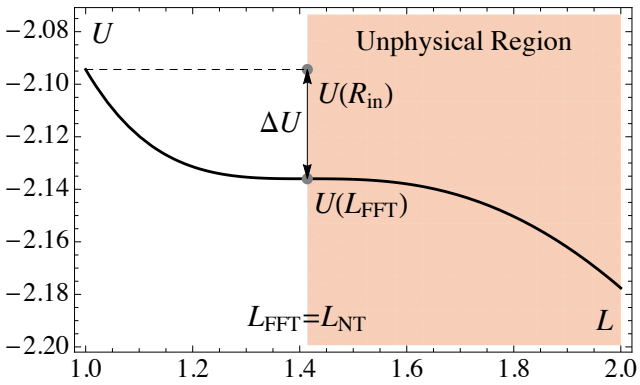

Figure 3.4 Mechanical energy U (normalized by $R_{\text{in}}^2 T^2/Y$) as a function of the wrinkle extent L (normalized by R_{in}) for $\rho = 2$ and $\nu = 1/3$. An inflection point exists at $L_{\text{NT}} = \sqrt{(1-\nu)/(1+\nu)}R_{\text{out}}$.

yields an excess of length that is relieved by out-of plane deformations which are oscillatory. Using relations (3.5b) and (3.5b) and Fourier integrating $\int_0^{2\pi} d\theta\,(.)$, one finds that

$$\begin{aligned}\frac{m^2 f^2}{4r^4} &= -\frac{u_r^I}{r} - \nu\frac{du_r^I}{dr} \\ &= \frac{R_{\text{in}}T}{Yr}\left[\ln\left(\frac{L}{r}\right) - \nu - (1+\nu)\left(\frac{L^2 - R_{\text{out}}^2}{\frac{1+\nu}{1-\nu} + \frac{R_{\text{out}}^2}{L^2}}\right)\right].\end{aligned} \tag{3.26}$$

The above equation indicates that wrinkling is only possible if the right-hand side is positive in the region $R_{\text{in}} < r < L$. Notice that the left-hand side of the above equation implies that the right-hand side must be positive for wrinkling to be possible. The positivity of the left-hand side of the above equation implies that wrinkling for $R_{\text{in}} < r < L$ is only posible if $L \leq L_{\text{NT}}$. This bound is usually referred to as the "slaving" condition. Interestingly, this upper bound coincides with the actual wrinkle extent in the near-threshold regime, in sharp contrast to the usual Lamé case [38].

The extent of wrinkles in the FFT regime

One can characterize the wrinkling pattern of the FFT regime by following an energetic approach. We shall show that, for $\epsilon \ll 1$, a wrinkled state in a region $R_{\text{in}} < r < L$ is energetically favorable compared to the flat state. Moreover, we shall derive the extent of wrinkles by minimizing the elastic energy with respect to L. We start by computing the elastic energy $U_E = \frac{1}{2}\int_A dA(\sigma_{rr}\varepsilon_{rr} + \sigma_{\theta\theta}\varepsilon_{\theta\theta})$ of the FFT stress field. The integral over the area can be separated in regions I and II. After straightforward calculations, one finds that the elastic energy at dominant order reads

$$U_E = \frac{\pi(R_{\text{in}}T)^2}{Y}\left\{\ln\left(\frac{L}{R_{\text{in}}}\right) + \frac{(1-\nu)\left(R_{\text{out}}^2 - L^2\right)}{L^2 + L_{NT}^2}\right\}. \tag{3.27}$$

This energy does not include the cost of bending and out-of-plane stretching of the sheet, which are of subdominant order. Indeed, one can show that the energy contributions involving out-of-plane deformations scale as $\epsilon^{1/2}$ and, thus can be neglected in the high bendability regime [37]. In order to find the extent of wrinkles L, one must minimize the total mechanical energy $U = U_E - W$, where $W = -2\pi T R_{\text{in}} u_r^I(R_{\text{in}})$ is the exerted work. Coincidentally, we find that $W = 2U_E$, hence one must minimize $U(L) = -U_E(L)$ with respect to L. The first derivative of U with respect to L gives

$$\frac{\partial U}{\partial L} = -\frac{\pi(R_{\text{in}}T)^2}{YL}\frac{(L^2 - L_{NT}^2)^2}{\left(L^2 + L_{NT}^2\right)^2} \leq 0. \tag{3.28}$$

The above equation indicates that $L = L_{\text{NT}}$ is an inflection point of $U(L)$ and not a local minimum (see Fig. 3.4). However, the slaving condition given by Eq. (3.26) implies that the actual length of wrinkles is bounded by $L \leq L_{\text{NT}}$. Surprisingly, this upper bound coincides with the inflection point of $U(L)$ and hence, the possible state of minimum energy occurs for $L = L_{\text{NT}}$. Moreover, one has that $U(R_{\text{in}}) > U(L_{\text{FFT}})$, which indicates that, in the FFT regime, a wrinkled state has a lower energetic cost than that of the flat solution (see Fig. 3.4).

In this system, we found that, in the FFT regime, $L_{\text{FFT}} = L_{\text{NT}}$, in sharp contrast with the Lamé problem studied in reference [38], where $L_{\text{FFT}} > L_{\text{NT}}$.

Number of wrinkles in the FFT regime

Although the extension of the wrinkles is determined by the dominant part of the total energy, which does not depend on ϵ, the number of wrinkles in the FFT regime is given by the subdominant part of the elastic energy, which scales as $\epsilon^{1/2}$. The analysis in the FFT regime is performed by taking the limit $\epsilon \to 0$ while keeping ρ at a fixed value (and hence, by equation (3.14), fixing $L_{\text{FFT}}/R_{\text{in}}$) and allowing $\sigma_{\theta\theta}$ to vary. The three dominant forces involved in equation (3.19) are the azimuthal bending ($\approx Bm^4 f/L_{\text{FFT}}^4$), azimuthal compression ($\approx \sigma_{\theta\theta} m^2 f/L_{\text{FFT}}^2$) and radial tension ($\approx \sigma_{rr} f/L_{\text{FFT}}^2$, with σ_{rr} given by (3.22)). Balancing these three forces we find that the azimuthal compression scales as $\sigma_{\theta\theta}/T \sim \epsilon^{1/2}$, whereas the NT analysis yields, by Eq. (3.21), $\sigma_{\theta\theta}/T \sim \epsilon^{1/4}$. This result shows that the hoop stress collapses faster in the FFT regime than in the NT regime. We also find that the number of wrinkles scales as $m_{\text{FFT}} \sim \epsilon^{-1/4}$. The scaling laws for the hoop stress and the number of wrinkles in the FFT regime are the same as the ones found in the usual Lamé problem [38].

3.2.5 Discussion: the effect of clamping an edge

Fig. 3.5 summarizes the differences of the wrinkling analysis between the classical Lamé problem and the modified clamped Lamé problem. The scaling laws found

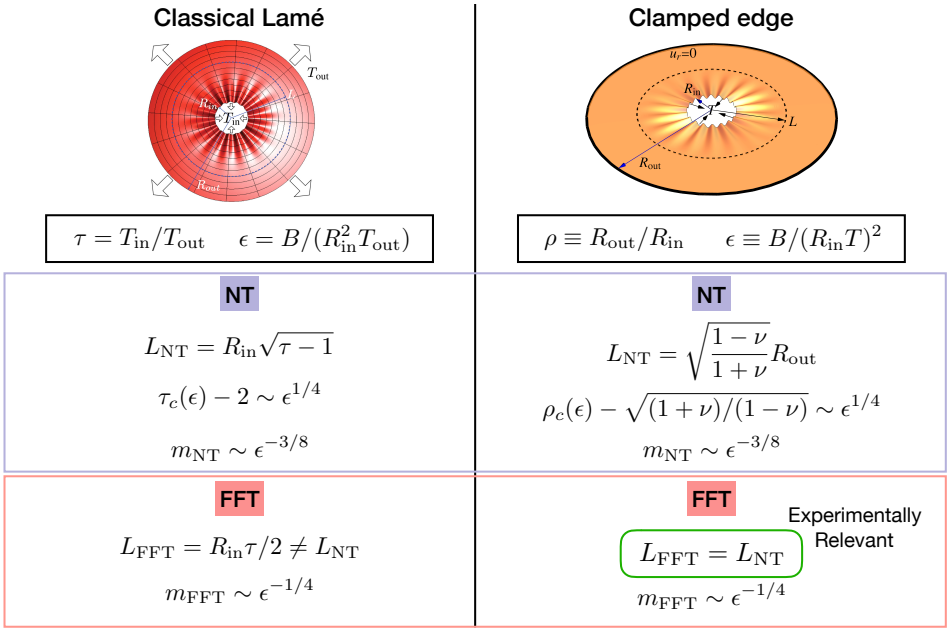

Figure 3.5 Comparison between the Classical Lamé problem and the modified Lamé problem with a clamped edge.

in the clamped case are essentially analogous to those of the classical Lamé case, where ρ plays the role of the ratio between the inward and outward tensions (τ) [38]. Nevertheless, when characterizing the NT regimes and the FFT regimes we found important differences with the Lamé case regarding the extent of wrinkles.

The Lamé configuration is more sensitive to the extension of wrinkles rather than their number [38]. Recall that the extent is determined by the leading energy while the number of wrinkles by the subleading energy. The small ratio between the subleading and leading energies suggests that the wrinkle extent is more robust than the wavelength. This means that for experimental analysis, the length of wrinkles is a better tool to distinguish between the NT and FFT regimes than the number of wrinkles. However, we showed that with a slight modification of the load conditions of the Lamé problem–by clamping the outer edge–this feature is lost. When the outer edge is clamped, the extension of the wrinkling pattern in the NT and the FFT regimes coincide, thus hindering a clear distinction between both regimes. These observations are crucial to correctly interpret experimental results such as that shown in reference [47], where the authors studied a similar system with clamped boundaries.

3.3 Lamé problem for an elliptic hole

In this section, we study a natural generalization of the classical Lamé problem by changing the geometry from an annular sheet to an infinite sheet with an elliptical hole, while keeping the same load conditions.

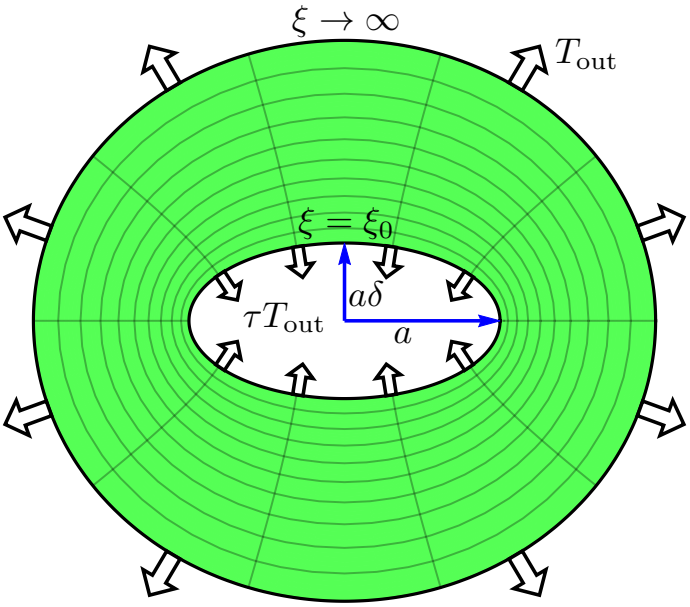

Figure 3.6 Schematics of the modified Lamé problem. Lines on the sheet illustrate the elliptic coordinate system (ξ, η).

3.3.1 Setup

We consider an infinite sheet with an elliptic hole of semi axes a and $a\delta$, with $\delta < 1$, that is stretched through uniform tensions applied at its boundaries, as shown in Fig. 3.6. For this configuration, it is suitable to use the elliptic coordinates $\xi > 0$ and $\eta \in [0, 2\pi]$ given by

$$(x, y) = (c \cosh \xi \cos \eta, c \sinh \xi \sin \eta), \tag{3.29}$$

where (x, y) are the Cartesian coordinates whose origin is at the centre of the hole and the boundary of the inner hole corresponds to the ellipse $\xi = \xi_0 = \tanh^{-1} \delta$ whose foci are located at a distance $c = a\sqrt{1 - \delta^2}$ from the center. The sheet is subjected to tensions applied at the boundaries: a uniform all-around tension T_{out} at an infinite distance from the hole and an inward tension τT_{out}, with $\tau > 0$, at the inner edge while keeping the edges shear-free.

3.3.2 Equilibrium equations and boundary conditions

In the absence of out of plane deformations, the so called-pre-buckled state, the linear elastic response of the plate is given by the following equilibrium equations

$$\nabla \cdot \overline{\overline{\sigma}} = 0, \tag{3.30a}$$
$$\Delta \left(\operatorname{Tr} \overline{\overline{\sigma}} \right) = 0, \tag{3.30b}$$

where ∇ and Δ are, respectively, the divergence and Laplacian operators and $\overline{\overline{\sigma}}$ is the two-dimensional stress tensor. Thus, the boundary conditions can be written as follows

$$\text{at } \xi \to \infty : \sigma_{\xi\xi} = \sigma_{\eta\eta} = T_{\text{out}}, \tag{3.31a}$$

$$\text{at } \xi = \xi_0 : \sigma_{\xi\xi} = \tau T_{\text{out}}, \text{ and } \sigma_{\xi\eta} = 0. \tag{3.31b}$$

3.3.3 The Kolosoff-Inglis solution

Instead of solving the problem posed by Eqs. (3.30) and (3.31) directly, we shall make use of the well-known Kolosoff-Inglis solution [71]: an infinite sheet with an elliptic hole subjected to an all-around uniform tension S at infinity while the boundary of the hole is traction-free. These boundary conditions can be written as follows

$$\sigma_{xx} = \sigma_{yy} = S \qquad \text{at } \xi \to \infty, \tag{3.32a}$$

$$\sigma_{\xi\xi} = \sigma_{\xi\eta} = 0 \qquad \text{at } \xi = \xi_0. \tag{3.32b}$$

We now explain the Kolosoff-Inglis solution to apply it afterwards to our problem. This problem can be solved using the method of complex stress functions for two-dimensional linear elasticity as explained in Section 2.2. One must find suitable analytic functions $\psi(z)$ and $\chi(z)$, with $z = x + iy$, such that the stress field given by Eqs. (2.30) and the displacement field given by Eq. (2.31) satisfy the boundary conditions. As our problem requires elliptic coordinates, we introduce the complex coordinate ζ such that $z = c \cosh \zeta$, where $\zeta = \xi + i\eta$. In order to use Eqs. (2.30) we need to transform the stress components in Cartesian to elliptic coordinates. Such transformation can be expressed through the following formula

$$\sigma_{\xi\xi} + \sigma_{\eta\eta} = \sigma_{xx} + \sigma_{yy} \tag{3.33a}$$

$$\sigma_{\xi\xi} - \sigma_{\eta\eta} - 2i\sigma_{\xi\eta} = e^{2i\alpha}(\sigma_{xx} - \sigma_{yy} - 2i\sigma_{xy}), \tag{3.33b}$$

where α is the angle between the x–axis and the tangent to a curve η =constant (in the direction ξ–increasing). It can be shown that the factor $e^{2i\alpha}$ is given by the following formula

$$e^{2i\alpha} = \frac{\sinh \zeta}{\sinh \bar{\zeta}}. \tag{3.34}$$

The components of the displacement in elliptic coordinates are related to the Cartesian components via

$$u_\xi + iu_\eta = e^{-i\alpha}(u_x + iu_y). \tag{3.35}$$

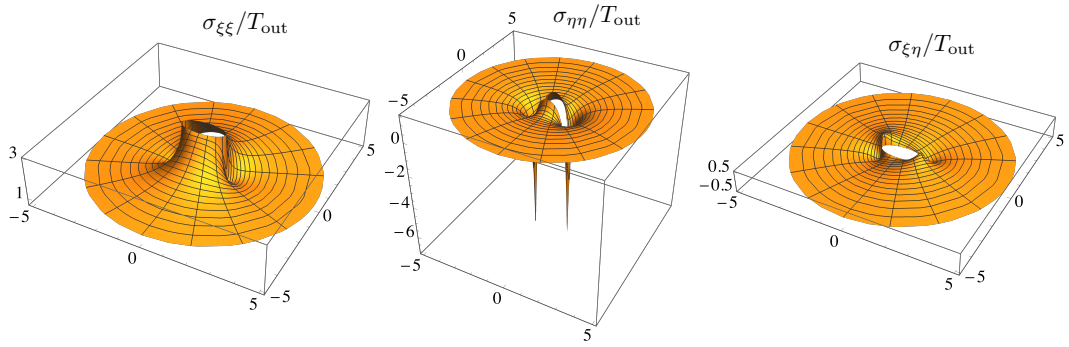

Figure 3.7 Three-dimensional profiles of $\sigma_{\xi\xi}$, $\sigma_{\eta\eta}$ and $\sigma_{\xi\eta}$ for $\tau = 3.5$ and $\delta = 0.4$.

The solution is given by the following stress functions [121]

$$\psi(z) = \frac{1}{2} S c \sinh \zeta, \quad \chi(z) = -\frac{1}{2} S c^2 \cosh 2\xi_0 \cdot \zeta. \tag{3.36}$$

Replacing these stress functions in Eqs. (2.30) and Eq. (2.31) yields the stress fields and the displacement in Cartesian coordinates which can be transformed to elliptic coordinates using Eqs. (3.33) and Eq. (3.35).

3.3.4 Solution of the problem and stress field analysis

Our elastic problem defined by the boundary conditions (3.31) can be solved using the *superposition principle*: taking advantage of the linearity of the system, we can add two already known solutions to obtain the solution of the problem defined by (3.31). First, we consider the Kolosoff-Inglis solution of a sheet subjected to a uniform pressure $-\Delta T$, with $\Delta T = (\tau - 1)T_{\text{out}}$, at infinity while the boundary of the hole is traction-free. The associated stress field of this problem is given by the stress functions (3.36), with $S = -\Delta T$. Then, to satisfy the boundary conditions (3.31), we add to the latter solution a homogeneous stressed state of the sheet given by $\sigma_{\xi\xi} = \sigma_{\eta\eta} = \tau T_{\text{out}}$ and $\sigma_{\xi\eta} = 0$. The solution is given by the following stress functions

$$\begin{aligned} \psi(z) &= \frac{T_{\text{in}}}{2} z - \frac{1}{2} \Delta T c \sinh \zeta, \\ \chi(z) &= \frac{1}{2} \Delta T c^2 \cosh 2\xi_0 \cdot \zeta. \end{aligned} \tag{3.37}$$

Then, the components of the resulting stress tensor are given by

$$\sigma_{\xi\xi} + \sigma_{\eta\eta} = 2\tau T_{\text{out}} - 2\Delta T \,\text{Re}\{\coth \zeta\}, \tag{3.38a}$$

$$\sigma_{\eta\eta} - \sigma_{\xi\xi} + 2i\sigma_{\xi\eta} = \Delta T \frac{\cosh \bar{\zeta} - \cosh 2\xi_0 \cosh \zeta}{\sinh \bar{\zeta} \sinh^2 \zeta}. \tag{3.38b}$$

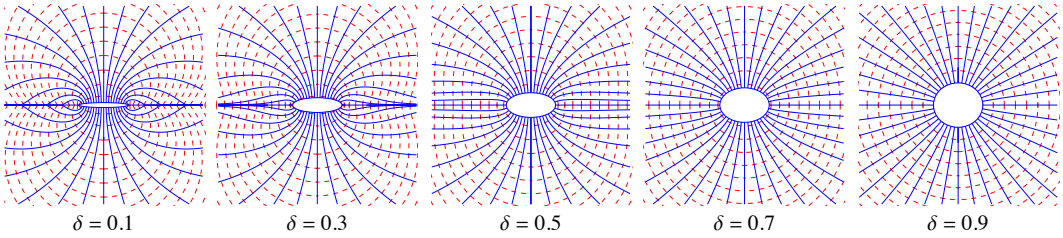

Figure 3.8 Tension Lines: maximum (——) and minimum (- - -) principal stress directions.

The displacement field, given by Eq. (2.31) and (3.35), has no discontinuities, thus the stress functions (3.37) yield a valid solution. Fig. 3.7 shows three-dimensional profiles of $\sigma_{\xi\xi}$, $\sigma_{\eta\eta}$ and $\sigma_{\xi\eta}$ given by Eqs. (3.38).

Since we are interested in the subsequent wrinkling pattern, we focus on the regions under compression around the hole. To do this, one should first compute the principal stresses and their associated principal directions. The largest and smallest principal stresses, σ_1 and σ_2, are given by

$$\begin{aligned}\sigma_{1,2} &= \tau T_{\text{out}} - \frac{\Delta T \sinh 2\xi}{\cosh 2\xi - \cos 2\eta} \\ &\quad \pm|\Delta T| \frac{\sqrt{(\cosh 2\xi - \cosh 2\xi_0)^2 \sin^2 2\eta + (\cosh 2\xi_0 - \cos 2\eta)^2 \sinh^2 2\xi}}{(\cosh 2\xi - \cos 2\eta)^2}.\end{aligned} \tag{3.39}$$

The directions of the principal stresses are defined by Eq. (2.23). In elliptic coordinates, the directions of the principal stresses are given by

$$\tan 2\beta = \frac{(\sigma_{\xi\xi} - \sigma_{\eta\eta}) \sinh 2\xi \sin 2\eta + 4\sigma_{\xi\eta}(\sinh^2 \xi - \sin^2 \eta)}{2(\sigma_{\xi\xi} - \sigma_{\eta\eta})(\sinh^2 \xi - \sin^2 \eta) - 2\sigma_{\xi\eta} \sinh 2\xi \sin 2\eta}, \tag{3.40}$$

where β is the angle between the direction of the largest principal stress and the x-axis [3]. The directions of the tension lines do not depend on the parameter τ. Fig. 3.8 shows tension lines for several values of δ. For $\delta \to 1$ the lines of tension are radial rays coming from the center. As δ approaches zero, the lines of tension of the largest principal stress curve towards the x-axis. In the crack limit case, $\delta = 0$, the tension lines intersect the x-axis at 45°, as shown in reference [136].

The perturbative analysis of tensional wrinkling usually focuses on the pre-buckled planar state of the membrane to define the regions of the membrane where a single component of the stress tensor is compressive. In the present case, both principal stresses can be either negative or positive in different regions. Hence, when σ_1 reaches negative values, the membrane becomes slack. In order to analyze in detail the stress

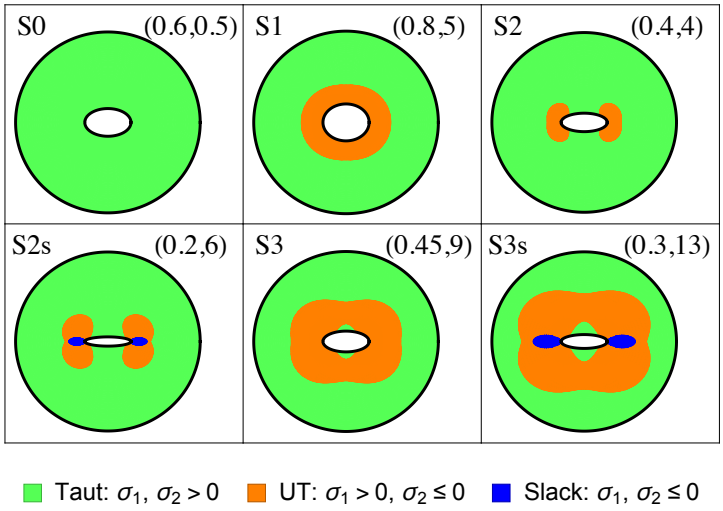

Figure 3.9 Representation of six possible states, where taut, UT, and slack regions are plotted on the sheet. The coordinates at each figure stand for the values (δ, τ).

state on the membrane, we classify regions on the sheet according to the signs of their principal stresses:

- Taut region: $\sigma_1 > 0$, $\sigma_2 > 0$.
- Unidirectional stretched (UT) region: $\sigma_1 > 0$, $\sigma_2 \leq 0$.
- Slack region: $\sigma_1 \leq 0$, $\sigma_2 \leq 0$.

Fig. 3.9 shows all the possible states of the membrane for different values of the parameters (δ, τ). Far enough from the hole, the sheet is always in a taut state. However, depending on the values of the control parameters, regions of compressive stress(es) will appear around the hole. UT regions can either concentrate at the ends of the major axis of the elliptic hole or surround it entirely (as in the Lamé case). Slack regions can also appear as small elliptical spots around the tips of the ellipse. A relevant question for a wrinkling stability analysis is whether the regions under compression that surround the hole are connected or disconnected. According to Fig. 3.9, one can identify six possible global states depending on the topology of taut, UT and slack regions:

- S0: the entire sheet is taut, i.e, $\sigma_2(\xi_0, \eta) > 0$, $\forall\, \eta \in [0, 2\pi]$.
- S1: a single UT region surrounding the hole such that each point at the edge is under compression, i.e, $\sigma_2(\xi_0, \eta) < 0$, $\forall\, \eta \in [0, 2\pi]$ and $\sigma_1 > 0$ everywhere.
- S1s: similar to S1 but with the presence of slack regions around the tips of the ellipse.
- S2: there are two disconnected UT regions at both ends of the major axis of the hole, without slack regions, i.e, $\sigma_2(\xi_0, 0) < 0$ and $\sigma_2(\xi, \pi/2) > 0$, $\forall \xi \geq \xi_0$.

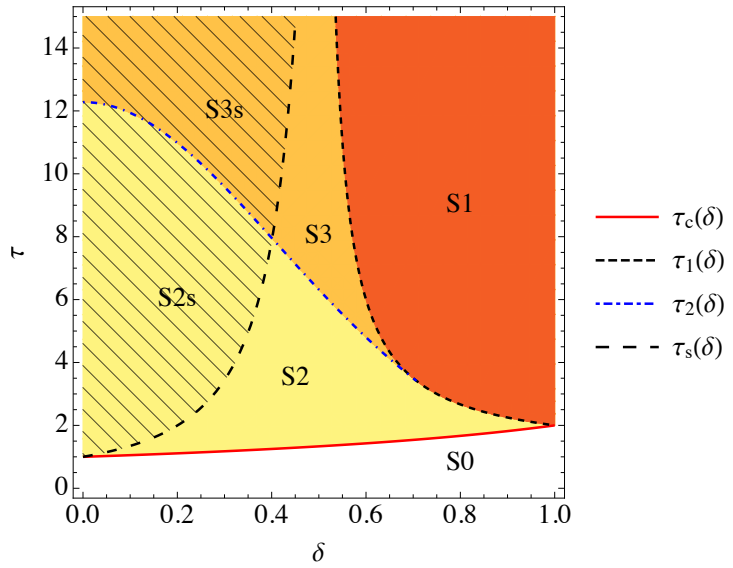

Figure 3.10 Diagram showing different states in the parameter space (δ, τ). The critical curves $\tau_c(\delta)$, $\tau_1(\delta)$, $\tau_2(\delta)$ and $\tau_s(\delta)$ separate the different regions. The state S1s exists for values of τ greater than 50.

- S2s: similar to S2 but with the presence of slack regions around the tips of the ellipse.
- S3: a single connected UT region around the ellipse without slack regions and with taut regions touching both ends of the minor axis of the hole, i.e, $\sigma_2(\xi, \pi/2) \leq 0$ in a finite interval $\xi_0 < \xi_{\min} \leq \xi \leq \xi_{\max}$ and $\sigma_2(\xi, \pi/2) > 0$ elsewhere.
- S3s: similar to S3 but with the presence of slack regions around the tips of the ellipse.

3.3.5 Phase diagram

The states of stress exist for different values of δ and τ which can be plotted in a phase diagram in the parameter space (δ, τ). Fig. 3.10 shows where these states are located in the parameter space and the critical curves that separate them. These separation curves can be computed analytically as explained below.

Due to the symmetries of the states shown in Fig. 3.9, the phase diagram can be retrieved by examining the principal stresses along $\eta = 0$ and $\eta = \pi/2$ only. Using Eqs. (3.39), one has for $\tau > 1$

$$\sigma_{1,2}(\xi, 0) = \tau T_{\text{out}} - \Delta T \coth \xi \left[1 \mp \frac{\sinh^2 \xi_0}{\sinh^2 \xi} \right], \tag{3.41}$$

$$\sigma_{1,2}(\xi, \pi/2) = \tau T_{\text{out}} - \Delta T \tanh \xi \left[1 \mp \frac{\cosh^2 \xi_0}{\cosh^2 \xi} \right]. \tag{3.42}$$

Recall that $\delta = \tanh \xi_0$ and $\Delta T = (\tau - 1)T_{\text{out}}$. At the hole edge, one has $\sigma_1(\xi_0, 0) = \sigma_1(\xi_0, \pi/2) = \tau T_{\text{out}}$, while $\sigma_2(\xi_0, 0) \leq \sigma_2(\xi_0, \pi/2)$. Therefore, compressive stresses around the hole appear when $\sigma_2(\xi_0, 0) < 0$. Using Eq. (3.41), this condition yields

$$\tau > \tau_c(\delta) = \frac{2}{2 - \delta}. \tag{3.43}$$

The region S0 is defined by the condition $\tau < \tau_c(\delta)$ for which no compressive stresses occur. Notice that one recovers the threshold $\tau_c(1) = 2$ corresponding to the Lamé problem [38]. For a crack-like problem, $\delta = 0$, one has that $\tau_c(0) = 1$. Region S1 is characterized by the existence of a compressive region all around the hole. Thus the curve $\tau_1(\delta)$ bounding S1 is found by imposing the condition $\sigma_2(\xi_0, \pi/2) < 0$. Using Eq. (3.42), this conditions reads

$$\tau > \tau_1(\delta) = \frac{2\delta}{2\delta - 1}. \tag{3.44}$$

As expected from the Lamé case, one has $\tau_1(1) = \tau_c(1) = 2$. Moreover, Eq. (3.44) shows that τ_1 diverges as $\delta \to 1/2$.

To discriminate between the regions S2 [S2s] and S3 [S3s], one should explore the behaviour of σ_2 along the y-axis. In these regions, one has $\sigma_2(\xi_0, \pi/2) > 0$ and $\sigma_2(\infty, \pi/2) > 0$ but $\sigma_2(\xi, \pi/2)$ may reach negative values for $\xi \geq \xi_0$. The critical curve $\tau_2(\delta)$ separates a region S2 [S2s] in which $\sigma_2(\xi, \pi/2) > 0$ for all $\xi \geq \xi_0$ from a region S3 [S3s] where $\sigma_2(\xi^*, \pi/2) \leq 0$ where $\xi^* \geq \xi_0$ is a local minimum such that

$$\frac{d\sigma_2}{d\xi}(\xi^*, \pi/2) = 0,. \tag{3.45}$$

Then, the transition is given by

$$\sigma_2(\xi^*, \pi/2) = 0. \tag{3.46}$$

Using Eq. (3.42), Eq. (3.45) gives

$$\xi^* = \cosh^{-1} \sqrt{\frac{3}{1 + \delta^2}}. \tag{3.47}$$

The solution given by Eq. (3.47) should satisfy $\xi^* \geq \xi_0$. This condition holds for $\cosh \xi_0 \leq \sqrt{2}$, which is equivalent to require that $\delta \leq \delta^* = 1/\sqrt{2}$. The curve $\tau_2(\delta)$ is found by imposing condition (3.46). Using Eqs. (3.42,3.47) one finds

$$\tau_2(\delta) = \frac{2\sqrt{3}(2 - \delta^2)^{3/2}}{2\sqrt{3}(2 - \delta^2)^{3/2} - 9(1 - \delta^2)}, \text{ with } 0 \leq \delta \leq \frac{1}{\sqrt{2}}. \tag{3.48}$$

One can show that the curves $\tau_2(\delta)$ and $\tau_1(\delta)$ intersect at (δ^*, τ^*) where $\tau^* \equiv \tau_1(\delta^*) = 2 + \sqrt{2}$. Hence, (δ^*, τ^*) corresponds to a triple point in the phase dia-

gram linking the states S1, S2 and S3 (see Fig. 3.10). Furthermore, notice that he slopes of $\tau_1(\delta)$ and $\tau_2(\delta)$ coincide at the triple point ($\tau_2'(\delta^*) = \tau_1'(\delta^*)$). At the crack limit, τ_2 reaches a finite value $\tau_2(0) = 4\sqrt{6}/(4\sqrt{6} - 9)$.

The critical curve $\tau_s(\delta)$ defines the transition from the states S2 and S3 to the states with slack regions S2s and S3s. As the slack regions concentrate close to the major axis of the elliptic hole (see Fig. 3.9), it is sufficient to inspect the behavior of $\sigma_1(\xi \geq \xi_0, 0)$ as given by Eq. (3.41). This curve can be computed using the same methodology as for the determination of $\tau_2(\delta)$. A local minimum of $\sigma_1(\xi \geq \xi_0, 0)$ exists for $\delta < 1/3$, which is reached at

$$\bar{\xi}^* = \frac{1}{2}\cosh^{-1}\left(\frac{1+3\delta^2}{1-3\delta^2}\right). \tag{3.49}$$

This solution satisfies $\bar{\xi}^* \geq \xi_0$. The curve $\tau_s(\delta)$ is defined by the condition $\sigma_1(\bar{\xi}^*, 0) = 0$, yielding

$$\tau_s(\delta) = \frac{2\sqrt{3}}{2\sqrt{3} - 9\delta(1-\delta^2)}, \text{ with } 0 \leq \delta < \frac{1}{\sqrt{3}}. \tag{3.50}$$

Eq. (3.50) shows that $\tau_s(\delta)$ diverges as $\delta \to 1/\sqrt{3}$ and $\tau_s(0) = \tau_c(0) = 1$. The curves $\tau_s(\delta)$ and $\tau_1(\delta)$ intersect at (δ^{**}, τ^{**}), where

$$\delta^{**} = \sqrt{\frac{1 - \sqrt{1 - \frac{4}{3\sqrt{3}}}}{2}}, \tag{3.51}$$

$$\tau^{**} = \frac{\sqrt{1 - \sqrt{1 - \frac{4}{3\sqrt{3}}}}}{-\frac{1}{\sqrt{2}} + \sqrt{1 - \sqrt{1 - \frac{4}{3\sqrt{3}}}}}. \tag{3.52}$$

This intersection defines the bounds of the region S1s, which is only observed for very large values of $\tau > \tau^{**} \simeq 50.98$ in the range $1/2 < \delta < 1/\sqrt{3}$.

One can compute the typical extension ΔL_{slack} of the slack regions, measured from the end of the hole along the x-axis. Writing $\sigma_1(\xi \geq \xi_0, 0)$ in Cartesian coordinates along the x-axis yields

$$\frac{\sigma_1(x,0)}{T_{\text{out}}} = \tau - (\tau - 1)\left(1 - \frac{\delta^2 a^2}{\left(x^2 - a^2(1-\delta^2)\right)}\right)\frac{x}{\sqrt{x^2 - a^2(1-\delta^2)}}. \tag{3.53}$$

For $\delta \ll 1$, the two zeros of $\sigma_1(x,0)$ are well approximated, up to second order in δ, by

$$x_1 = a + O(\delta^3); \quad x_2 = a\frac{\tau}{\sqrt{2\tau - 1}}\left(1 - \frac{3\delta^2}{2}\right) + O(\delta^4), \tag{3.54}$$

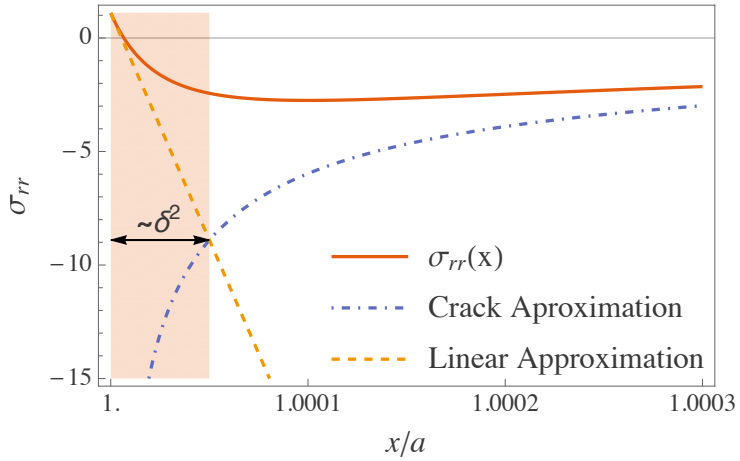

Figure 3.11 Profile of σ_{rr} along the x–axis close to the hole for $\delta = 0.01$ and $\tau = 1.1$. The linear and crack approximation given, respectively, by Eqs. (3.60) and (3.64) are shown for comparison. The shaded area represents the region where the crack approximation fails.

hence, the typical extension of the slack regions scale as

$$\frac{\Delta L_{\text{slack}}}{a} \simeq \frac{\tau}{\sqrt{2\tau - 1}}\left(1 - \frac{3\delta^2}{2}\right) - 1. \tag{3.55}$$

Recall that the above equation is defined for $\delta < 1/\sqrt{3}$ and $\tau > 1$. This latter result motivates the analysis of the stress field of the membrane in the crack-like limit.

3.3.6 Crack-limit

As $\delta \to 0$ the elliptic hole becomes slender and tends to a straight cut of length $2a$, resembling a crack in a stretched membrane [86]. In this case the stress field close to the elliptic hole is better represented in polar coordinates (r, θ) with origin $r = 0$ at the crack tip $x = a$. We are interested in the asymptotic behavior of the stress field in the vicinity of the crack tip.

The components of the stress field in polar coordinates (r, θ) can be obtained from Eqs. (3.38) by using the following transformations

$$\sigma_{rr} + \sigma_{\theta\theta} = \sigma_{\xi\xi} + \sigma_{\eta\eta}, \tag{3.56a}$$

$$\sigma_{rr} - \sigma_{\theta\theta} - 2i\sigma_{r\theta} = e^{2i(\theta-\alpha)}(\sigma_{\xi\xi} - \sigma_{\xi\eta} - 2i\sigma_{\xi\eta}). \tag{3.56b}$$

We focus on the stress close to one of the tips by writing

$$z = a + re^{i\theta}. \tag{3.57}$$

Using Eq. (3.29) and the stress field given by Eqs. (3.38), one obtains

$$\sigma_{rr}+\sigma_{\theta\theta} = 2\tau T_{\text{out}} - 2\Delta T\,\text{Re}\left[\frac{a+re^{i\theta}}{\sqrt{r^2e^{2i\theta}+2rae^{i\theta}+a^2\delta^2}}\right], \tag{3.58a}$$

$$\sigma_{rr}-\sigma_{\theta\theta}-2i\sigma_{r\theta} = \Delta T\,\frac{2a^3\delta^2e^{2i\theta}-\left((1-\delta^2)e^{i\theta}-(1+\delta^2)e^{3i\theta}\right)a^3r}{\left(r^2e^{2i\theta}+2rae^{i\theta}+a^2\delta^2\right)^{3/2}}. \tag{3.58b}$$

The asymptotic expansion of the stress field in the vicinity of the tip of the slender ellipse can be performed in two ways: either by assuming a finite δ and taking $r\to 0$ or by taking first $\delta=0$ in and then $r\to 0$. We shall show that the limits $r\to 0$ and $\delta\to 0$ do not commute.

Let us first consider the asymptotic expansion of the stress field in powers of r/a for a given nonzero value of δ. Using Eqs. (3.58), the stress components, expanded up to order r/a, read

$$\begin{aligned}
\sigma_{rr}^{(1)} &= \tau T_{\text{out}} - \frac{\Delta T}{\delta}\left(1-\cos 2\theta\right) + \frac{\Delta T}{2\delta^3}\frac{r}{a}\left(\left(1-\delta^2\right)\cos\theta - \left(5-\delta^2\right)\cos 3\theta\right),\\
\sigma_{\theta\theta}^{(1)} &= \tau T_{\text{out}} - \frac{\Delta T}{\delta}\left(1+\cos 2\theta\right) + \frac{\Delta T}{2\delta^3}\frac{r}{a}\left(3\left(1-\delta^2\right)\cos\theta + \left(5-\delta^2\right)\cos 3\theta\right),\\
\sigma_{r\theta}^{(1)} &= -\frac{2\Delta T}{\delta}\cos\theta\sin\theta + \frac{\Delta T}{\delta^3}\frac{r}{a}\left(3-\delta^2+\left(5-\delta^2\right)\cos 2\theta\right)\sin\theta.
\end{aligned}$$

Therefore, as one approaches the crack tip ($r\to 0$) the radial stress component along the x-axis admits an expansion of the form

$$\sigma_{rr}(r,0) = \tau T_{\text{out}} - \frac{2\Delta T}{\delta^3}\frac{r}{a} + O\left((r/a)^2\right). \tag{3.60}$$

We will refer to this expression as the linear approximation of the radial stress profile (see Fig.3.11). Notice that $\sigma_{rr}(0,0)=\tau T_{\text{out}}$, as dictated by the boundary conditions. At higher orders, we noticed that the stress components in polar coordinates admit a general expansion of the form

$$\sigma_{ij}(r,\theta) = T_{\text{in}}\delta_{ij} + \Delta T\sum_{n=0}^{\infty}\left(\frac{r}{a}\right)^n\sum_{m=p_n}^{n}\frac{f_{ijnm}(\theta)}{\delta^{2m+1}}, \tag{3.61}$$

where δ_{ij} is the Kronecker delta (indices take the values $i,j=r,\theta$), $f_{ijmn}(\theta)$ are functions of the polar angle and

$$p_n = \begin{cases} \frac{n}{2} & \text{if } n \text{ even},\\ \frac{n-1}{2} & \text{if } n \text{ odd}. \end{cases} \tag{3.62}$$

Notice that each group of terms of order $(r/a)^n$ are a sum in powers of $\delta^{-(2m+1)}$, with $m=p_n,\dots,n$. When $\delta\to 0$, the dominant terms in each of these groups goes with the

power $\delta^{-(2n+1)}$. In order to guarantee the convergence of (3.61), it is necessary that at least $r/a < \delta^2$. Therefore, this power expansion is valid in a region bounded by the radius of curvature $a\delta^2$ of the ellipse at its tip.

On the other hand, taking the crack limit first ($\delta = 0$), the asymptotic expansion of Eqs. (3.58) read

$$\sigma_{rr}|_{\delta=0} = \tau T_{\text{out}} - \frac{\Delta T}{2\sqrt{2}}\sqrt{\frac{a}{r}}\cos\frac{\theta}{2}(3-\cos\theta) + O\left(\sqrt{\frac{r}{a}}\right), \tag{3.63a}$$

$$\sigma_{\theta\theta}|_{\delta=0} = \tau T_{\text{out}} - \frac{\Delta T}{\sqrt{2}}\sqrt{\frac{a}{r}}\cos^3\frac{\theta}{2} + O\left(\sqrt{\frac{r}{a}}\right), \tag{3.63b}$$

$$\sigma_{r\theta}|_{\delta=0} = -\frac{\Delta T}{2\sqrt{2}}\sqrt{\frac{a}{r}}\cos\frac{\theta}{2}\sin\theta + O\left(\sqrt{\frac{r}{a}}\right). \tag{3.63c}$$

The radial component of the stress tensor reads, up to order $\sqrt{a/r}$,

$$\sigma_{rr}|_{\delta=0}(r,0) = \tau T_{\text{out}} - \frac{\Delta T}{\sqrt{2}}\sqrt{\frac{a}{r}} + O\left(\sqrt{\frac{r}{a}}\right). \tag{3.64}$$

Excepting the term τT_{out}, Eq. (3.64) corresponds to the asymptotic expansion of the radial stress component of a stationary crack [136]. Notice that this expansion violates the original boundary conditions (3.31b) at the hole. For small $\delta \neq 0$, the crack limit approximation looses validity as one moves closer to the tip (see Fig. 3.11). The crack approximation breaks down inside a cohesive zone-like region of typical size r_c. The radius r_c can be estimated either as the radial distance at the intersection of the linear approximation (3.60) with the crack approximation (3.64) or as the radial distance of the local minimum of $\sigma_1(r,0)$. The two criteria yield $r_c \sim a\delta^2$ which coincides, up to proportionality factors, both with the radius of curvature at the tip of the elliptic hole and with the radius of convergence of series expansion for finite δ (3.61).

3.3.7 Discussion: the role of geometry

Fig. 3.10 shows the phase diagram of the different accessible global stress configurations of a stretched sheet prior to any out-of-plane deformation. To release compressive stresses, a sheet with zero flexural rigidity buckles as soon as $\tau > \tau_c(\delta)$, implying that the states S3 and S3s of the phase diagram would not be accessible. However, a sheet with finite flexural rigidity should overcome a critical compressive stress to buckle and thus, one expects the whole phase diagram to be relevant. The present study shows that a slight deviation from the original Lamé problem (in our case, a change of the geometry of the perforated hole) gives rise to a phase diagram with different global stress states that might induce a rich variety of wrinkled patterns. Our study motivates the realization of experiments to answer fundamental questions such as: Do wrinkled

regions exhibit topologies similar to those of UT regions shown in Fig. 3.9? To what extent the phase diagram computed in Fig. 3.10 remains relevant as τ is increased?

From a theoretical point of view, the difficulties of predicting the state of the sheet beyond the pre-buckled one are due to three main observations:

- UT regions exhibit complex, possibly disconnected, contours. Indeed, Fig. 3.10 shows that the Lamé case $\delta = 1$ is peculiar as a small eccentricity modifies the nature of the transition to the wrinkled state. While for $\delta = 1$ a single symmetrical wrinkled state S1 exists, a new intermediate state S2 (or S2s) emerges for $\delta \neq 1$.
- The eccentricity of the hole may generate slack regions whose effect on the post-wrinkling process is not documented neither experimentally nor theoretically.
- The tension lines are not straight, curving considerably as the hole becomes slender (see Fig. 3.8). This feature hinders any prediction about the shape of wrinkles from the pre-buckled state.

These ascertainments prevent from performing classical NT or FFT analysis. Due to the loss of axial symmetry, it is not obvious how to perform a perturbation analysis around the planar state or to find the regions of the sheet where only tensile forces take place. We believe that an accurate description of a general wrinkling problem should be considered as a step-by-step dynamical-like problem, in the sense that once the buckling threshold is exceeded, the stress landscape on the whole membrane is modified and the buckled regions of the membrane are reshaped accordingly. In our specific problem, for $\delta < 1$ and $\tau \gtrsim \tau_c(\delta)$, compressed regions occur mainly at the tips of the ellipse, consequently, the buckling instability will be preferably located around the tips of the ellipse, much as a crack-like problem.

Specifically, wrinkles, as wavy periodic structures, could be peculiar patterns observed exclusively in symmetric configurations while the generic buckling instability would induce in the first place folded patterns—localized out-of-plane excursions of the sheet separated by flat regions under pure tension [68]. This assumption opens alternative approaches for the description of the post-buckling behavior. For example, if one considers the folding mechanism as a mean to suppress both normal and shear tractions along folds, one can envision the resulting pattern as traction-free crack lines. In this sense, one expects the physics underlying the selection of the folds pattern to be analogous to that of cracks and then must be treated as a dynamical process. The extension of a single fold should satisfy the principle of local symmetry [50] and a Griffith energy criterion [17] with vanishing fracture energy. Thus, the "equations of motion" of the fold can be written as $K_{II} = 0$ and $K_I = 0$, where K_I (respectively, K_{II}) is the mode I (respectively, mode II) stress intensity factor associated to the square root singularity of the stress field at the tip of the fold. These conditions ensure that the stress field in the periphery of the fold is shear-free and tensionless. The proposed equations allow for predicting both the shape and the extension of a single fold. In a

realistic situation with many folds, one should supplement the equations of motion of each fold with a global elastic energy functional of the sheet, whose minimization selects the geometrical and topological properties of the folding pattern. The latter analogy between folds and cracks relies only on the similarity between the boundary conditions induced by the folding mechanism and material separation, respectively. Therefore, we expect our conjecture to remain valid for general nonuniform loading conditions and for dynamical situations.

3.4 General conclusions

The role of boundary conditions in the wrinkling paradigm is not fully understood. We have explored the consequences of modifying the boundary conditions of the widely-studied Lamé problem in wrinkling analysis.

First, we studied a modified version of the classical Lamé problem where the outer edge is clamped and the control parameters are the inward tension T and the ratio ρ between the two radii of the disk. We showed that clamping the outer edge of the disk hinders a clear distinction between the NT and the FFT regimes. Specifically, we found that the extent of wrinkles is a function of the geometrical parameter ρ only, and thus, contrary to the classical Lamé case, it is the same in the NT and FFT regimes. Since the system is less sensitive to changes in the number of wrinkles, it would be really difficult to detect both regimes in an experiment.

Second, we address the problem of modifying the geometry of the classical Lamé problem to an elliptic hole. Specifically, we studied the stress field in a sheet with an elliptic hole subjected to a differential tension between its inner and outer boundaries. The present work aims to show how slight changes in geometry and loading can modify the usual distinction between NT and FFT regimes or result in complex wrinkled patterns. In particular, we showed that in this setup, a complex topology of regions under compression (UT or slack regions) arises and, therefore, it is not intuitive how the sheet will respond beyond the buckling instability. We have found that regions around the hole can be either in a taut, slack or UT state. This yields a rich phase diagram of different global stress states that should have an effect on the three-dimensional shape of the buckled states. These results show that slight geometrical asymmetries or inhomogeneous loading conditions might lead to complex wrinkled patterns. Our study provides a framework for experiments to probe the robustness of the wrinkling paradigm.

II

Folding induced patterns

4 Nonrigid origami

4.1 Rigid vs nonrigid origami

In recent years, the field of mechanical metamaterials has sought inspiration from origami [104, 135] in search of smart-materials with a vast range of functionality. Some applications are deployability mechanisms for large membranes [92], shape-changing structures [44, 45], and materials with tunable mechanical and thermal properties [113, 130, 15, 98], to name a few. In practice, many of these applications are limited to situations where the structures consist of an assembly of flat rigid plates connected by hingelike creases. In these cases, the space of geometrically available configurations is entirely determined by the crease network, while the structural response is a result of both the crease network and the mechanics of the creases [57, 18, 30]. However, designing such materials is not an easy task since the conditions for rigid foldability restrict the possible crease patterns in a complicated manner. By contrast, when the facets are allowed to bend and stretch, these restrictions disappear, and new behaviors emerge. Relaxing the rigidity of facets allow a crease pattern to access topologically disconnected configurations that would be inaccessible in the rigid case [80]. For example, the square twist fold [112] shown in Fig. 4.1(a) exhibits two equilibrium states–unfolded and folded–but its facets have to bend to reach its folded state. We name this class of systems *nonrigid origami*.

In a nonrigid origami system, the competition between the flexural rigidity of the panels B and the torsional rigidity of the creases k determines the elastic response of the structure. The so-called *origami length* $L^* \equiv B/k$ determines whether the mechanics of a nonrigid origami is dominated by bending or by the crease [79]. To illustrate this, let us consider the "accordion" origami shown in Fig. 4.1(b) consisting of alternating mountain-valley folds in a rectangular sheet. If l is the typical length of the facets, $l \ll L^*$ implies that the deformation is governed by the change on the folding angles while, if $l \gg L^*$, the deformation is governed by the bending of the panels [79]. Fig. 4.1(c) shows the example of a curved creased origami whose equilibrium shape is also governed by the competition between the elastic response of the creases and that of the facets.

A better understanding of nonrigid origami mechanics offers new possibilities for material design. However, suitable analytical models capturing the elastic regime of the panels remain for the most part, unexplored. In this chapter, we study the

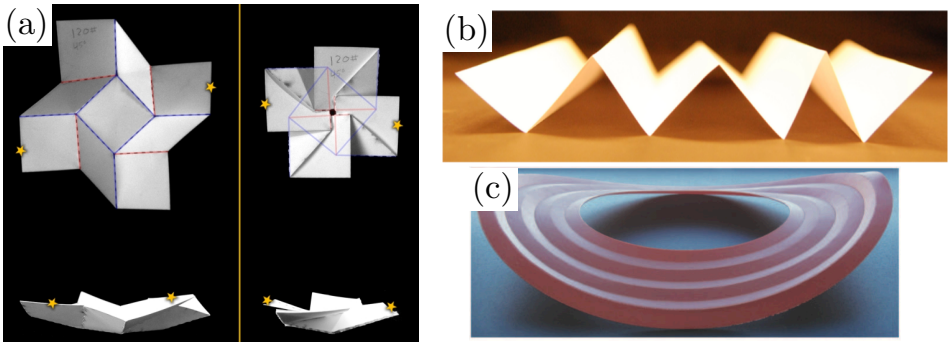

Figure 4.1 Examples of nonrigid origami. (a) The square twist fold (taken from [112]). (b) The accordionlike origami (taken from [39]). (b) Curved crease origami (taken from [44]).

properties of single-vertex nonrigid origami known as foldable cones. Before going into the details of this system, let us explore some aspects concerning the physics of folding.

4.2 Physics of folding

It is well-known that creasing a piece of paper modifies the overall mechanical response of the system. For example, a crease increases the stiffness considerably against bending deformations along the crease line. Creasing occurs when the local stress in the vicinity of the creased region surpasses the plasticity threshold, resulting in a change of the reference configuration of the material. To better understand the effects of folding on the material, let us focus on the mechanical properties of a crease, that is, its response to folding and opening. From the experimental point of view, a folding protocol must be established to obtain reproducible measurements [79]. However, the mere fact of folding a sheet does not always yield a system with reproducible mechanical properties. This process usually involves viscoelastic processes that yield a hysteretic system, that is, the crease mechanical response depends on whether the crease is folded or unfolded [120, 64]. Annealing the material along the crease line solves this issue, allowing to recover a reversible mechanical response of the fold [64].

The resulting mechanical properties of a crease are tricky to predict from first principles; however, some phenomenological models have been proposed to model folds in origami structures [18]. Let us consider a single straight point-like crease of length L modelled as the intersection of two flat panels. Fig. 4.2(a) shows that the geometry of a single straight crease can be described by its length L and three unit vectors $(\mathbf{u}, \mathbf{v}, \mathbf{w})$. The energy stored at the crease scales linearly with L and it can be expanded in powers of scalar invariants build upon these three vectors. Such invariants are $\mathbf{u} \cdot \mathbf{v}$ and $(\mathbf{u} \times \mathbf{v}) \cdot \mathbf{w}$. Therefore, at leading order, the elastic energy of a crease reads

$$E_{\text{crease}} = L\,(\sigma\,\mathbf{u} \cdot \mathbf{v} + \tau(\mathbf{u} \times \mathbf{v}) \cdot \mathbf{w}) \tag{4.1}$$

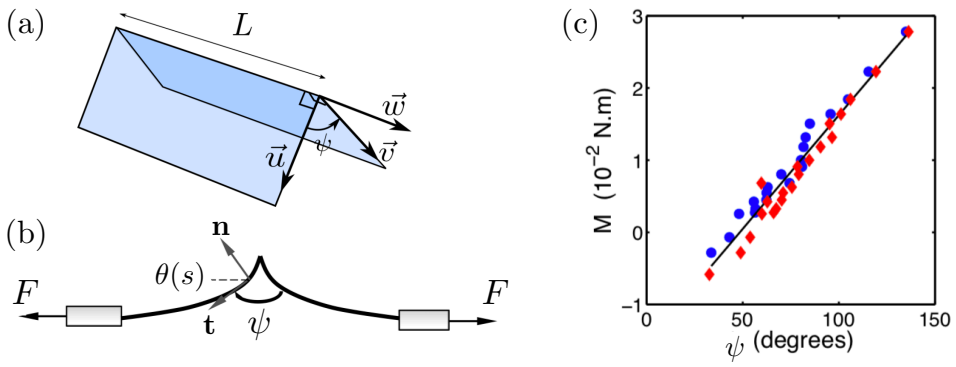

Figure 4.2 (a) The geometry of a single straight crease can be described by its length L and the three unit vectors $(\mathbf{u}, \mathbf{v}, \mathbf{w})$. (Figure adapted from [18]). (b) Experimental setup to test the mechanical response of a creased sheet and (c) applied moment M as function of the folding angle ψ (Figures (a) and (b) adapted from Ref. [79]).

where σ and τ are material constants. Note that the present approach is independent of the specific material properties of the system. When the orientation of these three vectors are defined a priori, as shown in Fig. 4.2(a), one has $\mathbf{u}\cdot\mathbf{v} = \cos\psi$ and $(\mathbf{u}\times\mathbf{v})\cdot\mathbf{w} = \sin\psi$, where the folding angle ψ is defined as the counterclockwise oriented dihedral $(\widehat{\mathbf{u},\mathbf{v}})$. We introduce the constants $k > 0$ and $\psi_0 \in [0, 2\pi]$ such that

$$\sigma = -k\cos\,\psi_0, \qquad \tau = -k\sin\,\psi_0, \tag{4.2}$$

allowing us to rewrite Eq. (4.1) as $E_{\text{crease}}(\psi) = -L\,k\,\cos\,(\psi - \psi_0)$. In the limit $\psi \simeq \psi_0$, the crease energy is well approximated by:

$$E_h = \frac{Lk}{2}(\psi - \psi_0)^2 + E_0, \tag{4.3}$$

where E_0 is a constant. Eq. (4.3) shows that the elastic behavior of a crease is analogous to that of a springy hinge with stiffness k and rest angle ψ_0. Therefore, the elastic response of a crease is characterized by a resistance to closing and opening given by a moment $M(\psi)$ given by

$$M(\psi) = \frac{dE_h(\psi)}{d\psi} = Lk(\psi - \psi_0) \tag{4.4}$$

which is a linear function of the folding angle. This theoretical observation is consistent with experimental observations in creased elastic sheets [79]. Fig. 4.2(b) shows an experimental setup used to probe the mechanical response of a creased sheet. A creased rectangular sheet is fastened at one end to a fixed clamp and the other end to a dynamometer which measures the force reaction while pulling the strip along its length. Fig. 4.2(c) shows the opening moment M as a function of the crease angle ψ evaluated by multiplying the pulling force by the height of the profile.

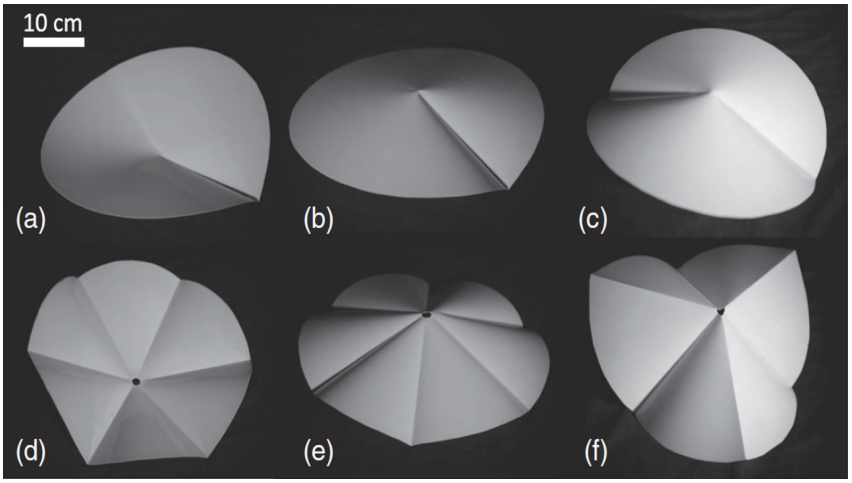

Figure 4.3 Experimental, mechanically stable f-cones in mylar-sheet disks (350 μm thick, 15 cm in radius (figure taken from reference [79]).

The stiffness and the rest angle define the behavior of a crease. How do these quantities relate to the material properties? To answer this question, let us perform some estimations assuming that creasing a sheet is governed purely by an ideally plastic behavior of the material. The elastic energy E_{el} dissipated in the fold is concentrated in a region of area Lb with curvature $1/h$, where L is the length of the fold, b is the width of the fold and h is the thickness of the plate. Assuming b scales as h, one has $E_{el} \sim BhL/h^2 = BL/h$, suggesting that the stiffness of a crease k scales as B/h [44, 39]. Recent model based on a continuous description of a fold confirms that $k = B/b$, where $b \sim h$ [64]. Other experimental studies confirm that the plastic length, where plasticity concentrates, scales linearly with h [11]. To estimate the rest angle, we assume that the irreversible deformations are localized in a region with curvature $1/h$ and characteristic angular region ϕ_p, then, the plastic strain scales as $\epsilon_p \sim h\phi_p/h = \phi_p$. Using the constitutive relation that relates the plastic strain to the yield stress σ_Y, one deduces that $\phi_p \sim \epsilon_p \sim \sigma_Y/E$, which is independent of the sample thickness. If one assumes that the rest angle ψ_0 is a univocal function of ϕ_p, then ψ_0 depends on the material properties but not on its thickness [79].

4.3 Foldable Cones

Foldable cones [78], or f-cones, are the simplest single-vertex nonrigid origami. They are made from elastic sheets decorated by straight creases meeting at a single vertex around which they are folded. This results in a family of various umbrella-like motifs (see Fig. 4.3) whose equilibrium shapes depend on the crease pattern imprinted in the flat configuration and the mechanical properties of the creases. As a first approximation, these sheets are assumed to be inextensible, implying that f-cones form developable cones, resembling d-cones [10], except that they can fold around the creases. Therefore, the equilibrium shape of the cone will be developable anywhere

except at the tip of the cone and the creases, where the curvature is not defined. In a more realistic situation, these divergencies are regularized if the inextensibility constraint is relaxed, thus leading to stretching and plastic deformations close to the vertex [21].

These structures are generically bistable in the sense that they can mechanically snap-through from one metastable configuration to another of higher elastic energy. We name the state of lower and higher energy as *rest* and *snapped*, respectively. Fig. 4.3(a) shows a single-crease *f*-cone and Fig. 4.3(b) shows its corresponding snapped configuration. Note that the structures are not flipped upside-down, but they are mechanically snapped so that all the creases preserve their initial mountain-valley assignment. This bistable behavior is observed in all foldable cones, regardless of the initial crease pattern. One of the main contributions of the present work is to understand the robustness of the bistability of *f*-cones.

4.3.1 Previous works

Huffman first noticed the bistability of single-vertex nonrigid origami in 1976. [61]. The author called these structures "general zero-curvature cones" and classified them into *convex* and *concave* vertices based on the direction of the trace generated by the surface in the Gaussian sphere[1]. Fig. 4.4 shows representations of a–according to author's terminology–convex and concave single-crease vertex corresponding to, respectively, the rest and the snapped state of a single-crease *f*-cone (Figures 4.3(a-b)). Later, foldable cones were investigated by Lechenault and Adda-Bedia [78], where the authors proposed a model describing the equilibrium shapes of these structures in the limit of small deflection and infinitely stiff creases. This model shows the existence of two equilibrium states only for particular cases: equally distributed all-valley and alternate mountain–valley creases. Nevertheless, the origin of the bistable nature of *f*-cones with arbitrary crease patterns remained unclear. We refer to their model as the *linear model* for *f*-cones, as it relies on the approximation of small deflections which allows writing the curvature of the surface as a linear function of the vertical component of the displacement.

These works have motivated the study of other closely related problems such as the bistable behavior of creased strips studied by Walker and Seffen [131] shown in Fig. 4.5. These bistrips are equivalent to a two-creases *f*-cone and can snap-through to form a vertex (see Fig. 4.3). The authors proposed a discrete model based on the Gauss map of several creases meeting at the vertex. In the limit of infinite creases, one recovers the linear version of an *f*-cone with two creases. The discrete model based on the Gauss map has limitations as it only predicts the final shape of real sheets well for small

[1] The Gaussian map maps a surface in $\mathbb{R}^3$ to the unit sphere (Gaussian sphere) such that is associates each point $\mathbf{r}$ of the surface to the normal vector $\mathbf{n}(\mathbf{r})$.

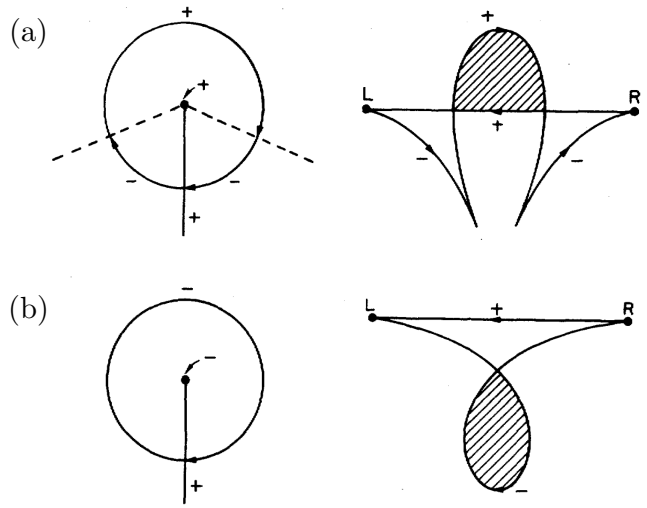

Figure 4.4 Representations of a convex (a) and a concave (b) vertex terminating a mountain crease appearing in Huffman's paper [61] and corresponding to, respectively, the rest and the snapped states of a single crease f-cone. The figures at the left represent the contours around the vertex, where $+$ $(-)$ signs denote "convexity" ("concavity") of edges, regions or vertices, as defined by the author. The figures at the right represent the trace in the Gaussian sphere, where L and R stand for the left and right side of the crease.

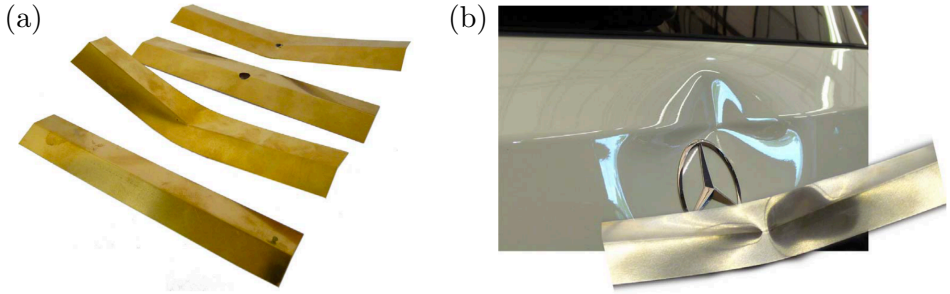

Figure 4.5 Bistable creased strips, which are equivalent to a $n = 2$ f-cone. (a) Metallic creased strips with and without a hole in their initial and inverted states. (b) A snapped strip compared to a dent in a vehicle body. The figures were adapted from [131].

deflections. Significant discrepancies with experiments appear for large deflections. Although these discrepancies may be attributed to the presence of stretching in real sheets, which in turn invalidates the inextensibility hypothesis, the inherent nonlinear nature of the system may also have a significant contribution to interpret the experimental observations.

4.3.2 Summary of the linear model

In the following, we summarize the main aspects regarding the linear model and its main results. We consider here the small deflections approach, while the nonlinear corrections can be found in Appendix A.1. Let us consider an elastic sheet with n evenly distributed straight creases meeting at a single vertex and with prescribed dihedral angles between successive panels. We adopt a cylindrical coordinate system (ρ, φ)

with the vertex located at $\rho = 0$ and $-\alpha/2 \leq \varphi \leq \alpha/2$, with $\alpha \equiv 2\pi/n$, to describe a slice of angular opening α bounded by two creases. For the sake of illustration, we only consider here the case where all the creases have the same folding angle pointing in the same direction: this configuration will be conventionally referred to as an *all-valley creases f-cone*. The position of a point in the initially planar sheet is described by the vector $\rho\mathbf{e}_\rho$, where $\mathbf{e}_\rho = -\sin\varphi\,\mathbf{x} + \cos\varphi\,\mathbf{y}$ is the radial unit vector lying in the horizontal plane. The actual position of this point in the deformed configuration reads

$$\mathbf{r} = (\rho + u_\rho(\rho,\varphi))\mathbf{e}_\rho + u_\varphi(\rho,\varphi)\mathbf{e}_\rho + w(\rho,\varphi)\mathbf{z}. \tag{4.5}$$

with u_ρ, u_φ, and z the radial, azimuth, and axial displacements, respectively. The vector $\mathbf{e}_\varphi = -\sin\varphi\,\mathbf{x} + \cos\varphi\,\mathbf{y}$ is the azimuthal unit vectors lying in the horizontal plane. We seek for conical solutions only, which imposes:

$$w(\rho,\theta) = \rho g(\varphi). \tag{4.6}$$

The condition of inextensibility requires that the stretching strains ε_{rr}, $\varepsilon_{\varphi\varphi}$, $\varepsilon_{r\varphi}$ vanish. In the moderate deflections limit, the strains ε_{rr} and $\varepsilon_{r\varphi}$ satisfy (see Eqs. (3.5)):

$$\begin{aligned} \varepsilon_{\rho\rho} &= \partial_\rho u_\rho + \frac{1}{2}(\partial_\rho w)^2 = 0, \\ \varepsilon_{\varphi\varphi} &= \frac{\partial_\varphi u_\varphi}{\rho} + \frac{u_\rho}{\rho} + \frac{1}{2\rho^2}(\partial_\varphi w)^2 = 0. \end{aligned} \tag{4.7}$$

Solving for the radial and the azimuthal displacements, one finds [21]

$$\begin{aligned} u_\rho(\rho,\varphi) &= -\frac{\rho}{2}g^2(\varphi), \\ u_\varphi(\rho,\varphi) &= -\frac{\rho}{2}\int^\varphi d\varphi[g^2(\varphi) - \dot{g}^2(\varphi)], \end{aligned} \tag{4.8}$$

where the dot denotes the derivative with respect to φ. Inextensibility in the azimuthal direction imposes[1] [78]

$$u_\varphi(\rho,\alpha/2) - u_\varphi(\rho,-\alpha/2) = 0. \tag{4.9}$$

The equilibrium shape of the surface may be determined by minimizing the elastic bending energy subjected to Eq. (4.9) (note that stretching is not considered here). The bending energy, given by Eq. (2.48), is the surface integral of the square of the surface curvature, which, for a conical surface, reads $(g(\varphi) + \ddot{g}(\varphi))/\rho$ in the limit

[1] This assumption is true only in *f*-cones with an arbitrary number of evenly distributed equal creases or with an even number of alternating mountain-valley evenly distributed creases. The general case will be discussed in a more general model presented in Section 4.5.

of small deflections (see Appendix A.1 for details). Consequently, we minimize the following augmented energy functional

$$\mathcal{L} = \frac{B}{2\rho}\left[\int_{-\alpha/2}^{\alpha/2} d\varphi[g(\varphi)+\ddot{g}(\varphi)]^2 + \bar{\lambda}\int_{-\alpha/2}^{\alpha/2} d\varphi[g^2(\varphi)-\dot{g}^2(\varphi)]\right], \tag{4.10}$$

where the first integral term is the bending energy density (per unit radius), and the second enforces the inextensibility constraint through $\bar{\lambda}$. The resulting Euler-Lagrange equation reads

$$\left(\frac{d^2}{d\varphi^2}+\mu^2\right)\left(\frac{d^2}{d\varphi^2}+1\right)g = 0, \tag{4.11}$$

where $\mu^2 \equiv 1+\bar{\lambda}$. The Lagrange multiplier $\bar{\lambda}$ is related to the hoop stress through [21]

$$\sigma_{\varphi\varphi} = -\frac{B\bar{\lambda}}{h\rho^2}, \tag{4.12}$$

where h is the thickness of the plate. Therefore $\bar{\lambda} > 0$ (respectively, $\bar{\lambda} < 0$) corresponds to a compressive (respectively, tensile) hoop stress. The sign of the hoop stress can be easily determined experimentally: if one cuts along an arbitrary radius, the structure will either open up if it is in tension ($\bar{\lambda} < 0$), or either will collapse if it is in compression ($\bar{\lambda} < 0$) [78]. The linear model proposed by Lechenault and Adda-Bedia considers infinite stiff creases, which implies the following boundary conditions:

$$\dot{g}(-\alpha/2) = -\dot{g}(\alpha/2) = p, \tag{4.13}$$

$$\mu^2\dot{g}(-\alpha/2) + g^{(3)}(-\alpha/2) = \mu^2\dot{g}(\alpha/2) + g^{(3)}(\alpha/2) = 0, \tag{4.14}$$

where p is a constant, which, in the limit of small deflections, is related to the folding angle ψ by $p = (\pi-\psi)/2$ (see Appendix A.2). For all-valley creases configurations, the solutions are given by

$$g(\varphi) = p\frac{\cos\mu\varphi}{\mu\sin\mu\alpha/2}. \tag{4.15}$$

Then, the inextensibility condition (4.9) reads

$$(1-\mu^2)\mu\alpha + (1+\mu^2)\sin\mu\alpha = 0. \tag{4.16}$$

Since $\bar{\lambda} = \mu^2 - 1$ can be arbitrarily negative, μ can be either real or purely imaginary. Solving Eq. (4.16) yields two solutions branches μ_n^{R} and μ_n^{S} for all $n \geq 1$ (see Fig. 4.6), which correspond, respectively, to deflections given by

$$\begin{aligned} g_n^{\mathrm{R}}(\varphi) &= p\frac{\cos\mu_n^{\mathrm{R}}\varphi}{\mu_n^{\mathrm{R}}\sin\mu_n^{\mathrm{R}}\alpha/2}, \\ g_n^{\mathrm{S}}(\varphi) &= p\frac{\cos\mu_n^{\mathrm{S}}\varphi}{\mu_n^{\mathrm{S}}\sin\mu_n^{\mathrm{S}}\alpha/2}. \end{aligned} \tag{4.17}$$

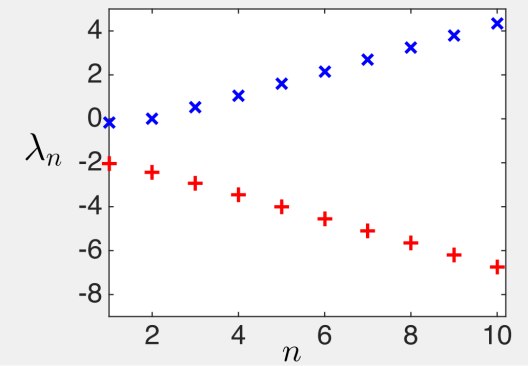

Figure 4.6 Lagrange multipliers $\bar{\lambda}_n^{\mathrm{R}}$ and $\bar{\lambda}_n^{\mathrm{S}}$ as a function of the number of faces n (Figure taken from [78]).

These solutions are referred to as *rest* and *snapped* states since the former has always lower bending energy than the latter. These states can be characterized by the sign of the Lagrange multiplier $\bar{\lambda}_n^{\mathrm{R,S}} = (\mu_n^{\mathrm{R,S}})^2 - 1$, which determines whether the structure is in azimuthal tension or compression. For $n = 1$, it is found that both states are in azimuthal tension ($\lambda_1^{\mathrm{R,S}} < 0$), while, for $n > 2$, $g_n^{\mathrm{R}}(\varphi)$ structures are in compression and $g_n^{\mathrm{S}}(\varphi)$ structures are in tension. The case $n = 2$ is marginal since its rest state corresponds to two flat facets connected by the crease and presents zero hoop stress. In the limit of large number of creases, the solutions follow the asymptotic formula:

$$\mu_n^{\mathrm{R,S}} = \frac{3^{1/4}\sqrt{n}}{\sqrt{\pi}} + O\left(\frac{1}{\sqrt{n}}\right). \tag{4.18}$$

For $n \ll 1$, the bending energy per facet is found to be quadratic in p:

$$E_n^{\mathrm{R,S}} = \frac{Bp^2}{2\rho}\left[\frac{2n}{\pi} \mp \frac{4}{\sqrt{\pi}} + O\left(\frac{1}{\sqrt{n}}\right)\right]. \tag{4.19}$$

The total bending energy scales as n^2, for large n. Note that rest states have lower bending energy than snapped ones.

The authors also solve the case when f-cones have an even number n of creases with different folding angles pointing in alternate directions, referred to as an *alternate creases f-cone*. For all configurations with $n \leq 4$, flat-facets solutions are possible with the right choice of both folding angles. When mountain and valley creases have the same folding angles, both states are obtained from one another by mirror symmetry about the $z = 0$ plane, followed by a rotation of angle α; thus, they are energetically equivalent.

Let us point out some observations regarding the linear model and its limitations:

1. It shows the existence of two families of solutions for particular cases only: all-valley and alternate creases f-cones with evenly distributed creases. However, the bistable nature of foldable-cones in the general case remains unclear.

2. The linear model is valid only for small deformations, which represents a problem when describing origami-inspired structures since their folding/unfolding mechanisms rely on exact geometrical relations between the overall deformations and their folding angles. To adequately describe such structures, it is crucial to describe the equilibrium shapes for any folding angle. Moreover, because of the scale-invariant description, the linear approximation induces errors in terms of vertical deflections that are amplified along the radial direction.
3. Lechenault and Adda-Bedia considered the limit of infinite crease stiffness only, which implies prescribing the folding angles of the entire structure. As for the elastic response of foldable-cones, a more realistic model is required; one that describes how the creases with finite stiffness behave upon external forces.

These reasons justify the need for more adequate and accurate models for a complete description of foldable cones.

In the present thesis, we propose a model for *f*-cones covering the full geometric nonlinear contributions and thus capturing the exact equilibrium shapes for arbitrary deformations. We take into account two cases, the infinitely stiff creases limit when the folding angles are prescribed, and the case with hingelike creases with controlled stiffness and rest angles. The model presented in this thesis places the *f*-cone as a framework for the study of non-rigid origami structures. Furthermore, we corroborate the predictions of the theory with the aid of finite element simulations that incorporate a model of continuous creases. These creases are narrow slices of material that self-fold when applying a temperature gradient across the thickness. The finite element analysis allows us to quantify the interplay between bending and stretching and to test the validity of the inextensibility hypothesis throughout the entire snap-through dynamics. Besides, the numerical model proves to be a useful and practical tool when studying the mechanical response of more complex origami-structures, such as a connected network of creases.

4.4 Elastic theory of conical singularities

We present an elastic theory that predicts the equilibrium shapes of any conical surface made of an inextensible elastic sheet valid for any deflection. We first introduce a general parametrization for any conical surface, and then, we introduce a Lagrangian formulation based on minimizing the bending energy of the surface subjected to inextensibility constraints.

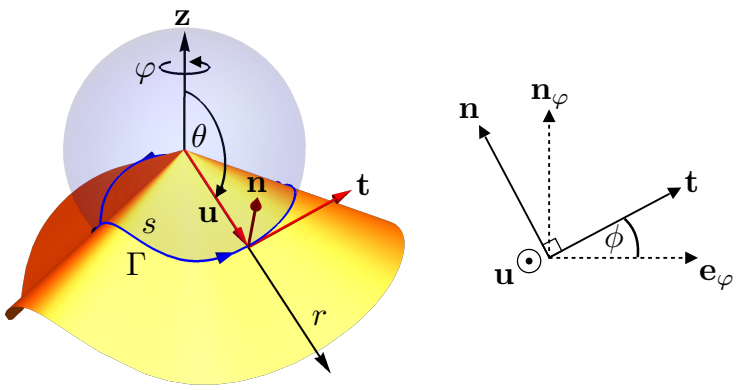

Figure 4.7 The cone geometry. A closed curve $\Gamma(s)$ on the unit sphere describes the entire conical surface. The Euler-like angles $\{\theta(s), \varphi(s), \phi(s)\}$ are shown.

4.4.1 Geometry of a developable cone

Taking advantage of the conical geometry, we implement a scale-invariant description of the problem. The most general parametrization of a conical shape is given by (see Section 2.4.1)

$$\mathbf{r}(r,s) = r\mathbf{u}(s), \tag{4.20}$$

where r is the distance to the tip, $\mathbf{u}(s)$ is a unit vector and $s \in [0, 2\pi]$ is the arc-length of a curve $\Gamma : s \to \mathbf{u}(s)$ living on the unit sphere (see Fig. 4.7). The tangent vectors adapted to the surface of the cone are $\mathbf{u}$ and $\mathbf{t} = \mathbf{u}'$, where the prime denotes derivative with respect to s. As s is the arc-length of the curve, the tangent $\mathbf{t}$ is a unit vector. Note that $\mathbf{u} \cdot \mathbf{t} = 0$ and that the normal of the surface is given by $\mathbf{n} = \mathbf{u} \times \mathbf{t}$. The metric tensor for a conical surface is given by

$$g_{\alpha\beta} = \partial_\alpha \mathbf{r} \cdot \partial_\beta \mathbf{r} = \begin{pmatrix} 1 & 0 \\ 0 & r^2 \end{pmatrix}, \tag{4.21}$$

where the Greek indices run over the material coordinates r, s. The curvature tensor is then given by

$$K_{\alpha\beta} = \partial_\alpha \mathbf{r} \cdot \partial_\beta \mathbf{n} = r \begin{pmatrix} 0 & 0 \\ 0 & \kappa \end{pmatrix}, \tag{4.22}$$

where $\kappa(s) = \mathbf{t}(s) \cdot \mathbf{n}'(s)$. The normal curvature of the surface is given by $K = g^{\alpha\beta} K_{\alpha\beta} = \kappa(s)/r$, thus, κ is the normal curvature of the surface at unit distance from the apex. It should not be confused with the Frenet curvature $\kappa_F = \|\mathbf{t}'\|$ of the curve Γ. Indeed, these two curvatures are related by $\kappa_F^2 = \kappa^2 + \kappa_g^2$, where $\kappa_g = 1$ stands for

the geodesic curvature of Γ with respect to the surface of the cone. The triad $\{\mathbf{u}, \mathbf{t}, \mathbf{n}\}$ forms a right-handed basis satisfying the structure equations [25]:

$$\mathbf{u}' = \mathbf{t} \tag{4.23a}$$

$$\mathbf{t}' = -\kappa\mathbf{n} - \mathbf{u} \tag{4.23b}$$

$$\mathbf{n}' = \kappa\mathbf{t}. \tag{4.23c}$$

Given $\kappa(s)$, the final shape of the cone can be reconstructed using Eqs. (4.23).

Alternatively, the shape can be reconstructed in terms of local angles describing rotations of the frame $\{\mathbf{u}, \mathbf{t}, \mathbf{n}\}$. To describe such, we introduce the vector $\mathbf{n}_\varphi \equiv \mathbf{u} \times \mathbf{e}_\varphi$, which together with $\mathbf{e}_\varphi$, spans a plane containing $\mathbf{t}$ and $\mathbf{n}$ (see Fig. 4.7). It is useful to describe such rotations in terms of three Euler-like angles $\{\theta(s), \varphi(s), \phi(s)\}$. The first two $\{\theta(s), \varphi(s)\}$ correspond, respectively, to the polar angle and the azimuthal angles that describe the vector $\mathbf{u}$:

$$\begin{aligned} \mathbf{u} &= \sin\theta(s)\cos\varphi(s)\mathbf{x} + \sin\theta(s)\cos\varphi(s)\mathbf{y} + \cos\theta(s)\mathbf{z} \\ &= \sin\theta(s)\mathbf{e}_\rho + \cos\theta(s)\mathbf{z}. \end{aligned} \tag{4.24}$$

The third angle $\phi(s)$ describes the tangent to the curve Γ and it is defined as the angle between $\mathbf{t}$ and $\mathbf{e}_\varphi$ (see Fig. 4.7):

$$\mathbf{t} = \cos\phi(s)\mathbf{e}_\varphi + \sin\phi(s)\mathbf{n}_\varphi, \tag{4.25a}$$

$$\mathbf{n} = -\sin\phi(s)\mathbf{e}_\varphi + \cos\phi(s)\mathbf{n}_\varphi. \tag{4.25b}$$

It can be shown that these Euler-like angles satisfy the following equations [25]

$$\theta' = -\sin\phi \tag{4.26a}$$

$$\varphi' = \frac{\cos\phi}{\sin\theta} \tag{4.26b}$$

$$\phi' = \kappa - \cot\theta\cos\phi. \tag{4.26c}$$

Knowing $\kappa(s)$, the above equations yield the shape of the structure, although we shall not make use of them.

4.4.2 Elastic energy of a conical surface

Finding the equilibrium shape of any conical singularity in inextensible elastic sheets can be done by minimizing an augmented functional consisting of the bending energy of the surface plus suitable constraints enforcing the inextensibility condition. When

an elastic sheet describes a developable surface, the bending energy Eq. (2.48) can be written as follows (recall that $K_G = 0$)

$$E_b[\mathbf{r}] = \frac{B}{2}\int dA\, K(\mathbf{r})^2, \tag{4.27}$$

where K is the surface curvature and dA is the element of area over that surface. In the case of a conical geometry, defined by the parametrization (4.20), one has $K = \kappa(s)/r$ and $dA = \sqrt{\det g_{ab}}\, dr\, ds = r dr\, ds$. Let us assume that the sheet is circular with radius R and centred at the defect. Note that, since $K \sim 1/r$, the bending energy diverges as $r \to 0$. Therefore, one needs to introduce a cutoff radius $r_0 \ll R$, to avoid the divergence of the elastic energy. In a real situation, the bending energy density becomes comparable to the cost of stretching near the vertex, resulting in stretching and plastic deformations [21, 27]. These effects are not taken into account by the theory since it considers perfectly inextensible sheets only. This cutoff radius is, in principle, arbitrary, but it can be chosen as characteristic size of the core of the defect, defined as the region where bending energy becomes comparable to stretching. In the case of the d-cone, when deformations are small, the core radius r_c has been found to scale as [27]

$$r_c = \left(\frac{B}{Eh}\right)^{1/6} R^{2/3}\epsilon^{-1/3}, \tag{4.28}$$

where $\epsilon \equiv d/R$, with d the vertical displacement at the tip.

Instead of varying the energy (4.27) directly, we follow an alternative approach introduced by Guven and Müller [53, 54]. Integrating Eq. (4.27) along the radial coordinate, we obtain the following functional of $\mathbf{u}(s)$

$$H[\mathbf{u}] = \frac{1}{2}a\oint_\Gamma ds\, \kappa(s)^2. \tag{4.29}$$

where $a = B\ln R/r_0$. Thus, $H[\mathbf{u}]$ is a functional of trajectories on the unit sphere. The condition of inextensibility along the radius is already enforced by having pre-integrated the energy before varying it. One can enforce inextensibility along the tangent of Γ by introducing local constraints in terms of the vectors $\mathbf{u}$ and $\mathbf{t}$. Recall that these vectors satisfy the following conditions:

$$\mathbf{u}^2 = 1, \quad \mathbf{t}^2 = 1, \quad \mathbf{u}' = \mathbf{t}. \tag{4.30}$$

We construct an augmented functional of $\mathbf{u}$ and $\mathbf{t}$ subjected to the above conditions. Then, by writing $\kappa(s) = \mathbf{u}\cdot(\mathbf{t}'\times\mathbf{t})$, we propose the following functional

$$F[\mathbf{u},\mathbf{t},\lambda,\Lambda,\mathbf{f}] = a\oint_\Gamma ds\left[\frac{1}{2}(\mathbf{u}\cdot\mathbf{t}\times\mathbf{t}')^2 + \frac{\lambda}{2}(\mathbf{u}^2-1) + \frac{\Lambda}{2}(\mathbf{t}^2-1) + \mathbf{f}\cdot(\mathbf{t}-\mathbf{u}')\right], \tag{4.31}$$

where $\lambda(s)$, $\Lambda(s)$ and $\mathbf{f}(s)$ are local Lagrange multipliers: $\lambda(s)$ forces $\mathbf{u}$ to be a unit vector, constraining the final trajectories to the unit sphere; $\Lambda(s)$ enforce the parameter s to be the arc-length of the curve Γ; and $\mathbf{f}(s)$ anchors the tangent vector to the embedding. These constraints enforces inextensibility of the curve Γ by fixing the arc-length of the curve: the surface does not stretch or shrink throughout deformations.

The minimization of functional (4.31) yields a second order ordinary differential equation for the dimensionless curvature $\kappa(s)$ [54]:

$$\kappa'' + (1 + c)\,\kappa + \frac{\kappa^3}{2} = 0, \tag{4.32}$$

where c is a constant related to a tension along the surface associated with the fixed area constraint which is implied by fixing the arc-length s [54]. By comparing with the linear model of f-cones, one notices that $-c$ is proportional to the hoop stress $\sigma_{\varphi\varphi}$ in the limit of small deflections, that is,

$$c \xrightarrow{\psi\to\pi} \bar{\lambda}, \tag{4.33}$$

where $\bar{\lambda}$ corresponds to the Lagrange multiplier of the linear model (see Eq. (4.12)). Therefore, for small deflections, the sign of c dictates whether the structure is in azimuthal compression ($c > 0$) or tension ($c < 0$) [78, 23].

One also finds that

$$\mathbf{f} = \left(\frac{1}{2}\kappa^2 + c\right)\mathbf{t} - \kappa'\mathbf{n}. \tag{4.34}$$

where $\mathbf{f}(s)$ can be identified as an effective force per unit length transmitted along the curve Γ [53].

Eq. (4.32) is the well-known planar *Elastica* of Euler that describes the equilibrium shape of inextensible elastic rods subjected to a tension $-(1 + c)$. Cerda *et al.* [25] noticed that finding the shape of any conical singularity in inextensible sheets reduces to solving Eq. (4.32). Remarkably, finding the shape of a 2D surface embedded in 3D space is reduced to solve a one-dimensional equation. We shall see a detailed derivation of Eq. (4.32) later for the case of an f-cone with n panels.

4.4.3 Conserved quantity

Functional (4.31) possesses a vectorial conserved quantity related to the rotational invariance of the system around the tip [54]. At equilibrium, the variation of this functional yields terms that form a total derivative:

$$\delta F = -\int ds \frac{d}{ds}\left[\mathbf{f}\cdot\delta\mathbf{u} + \kappa\mathbf{n}\cdot\delta\mathbf{t}\right]. \tag{4.35}$$

where $\mathbf{f}$ is given by Eq (4.34). Since $\delta F = 0$ for arbitrary $\delta\mathbf{u}$ and $\delta\mathbf{t}$, we can chose rotation around an arbitrary vector b, so that $\delta\mathbf{u} = \mathbf{b} \times \mathbf{u}$ and $\delta\mathbf{t} = \mathbf{b} \times \mathbf{t}$, then

$$\delta F = \oint ds \frac{d}{ds}\mathbf{b} \cdot [\mathbf{u} \times \mathbf{f} + \kappa\mathbf{u}]\,. \tag{4.36}$$

Therefore, $\mathbf{b} \cdot [\mathbf{u} \times \mathbf{f} + \kappa\mathbf{u}]$ is constant, and thus, the vector

$$\begin{aligned} \mathbf{J} &\equiv \mathbf{u} \times \mathbf{f} + \kappa\mathbf{u} \\ &= \left(\frac{1}{2}\kappa^2 + c\right)\mathbf{n} + \kappa'\mathbf{t} + \kappa\mathbf{u}. \end{aligned} \tag{4.37}$$

is a conserved quantity of the system related to the rotational invariance of the system. This vector corresponds to a normalized torque about the tip [54], which, from now on, we call J-vector. Using the frame equations (4.23) one can verify that $\mathbf{J}$ is indeed a conserved vector. Squaring Eq.(4.37), using the identity $\mathbf{f} \cdot \mathbf{u} = 0$, one finds

$$\mathbf{J}^2 = \mathbf{f}^2 + \kappa^2, \tag{4.38}$$

which can be written as follows

$$J^2 - c^2 = \kappa'^2 + (1 + c)\kappa^2 + \frac{\kappa^4}{4}. \tag{4.39}$$

Note that the quantity $J^2 - c^2$ corresponds to the first integral of the *Elastica* of Euler (4.32).

4.4.4 Shape reconstruction

To obtain the three-dimensional shape of the conical shape, we introduce spherical angles: the polar angle $\theta(s)$ and the azimuthal angle $\varphi(s)$. In terms of the spherical coordinates we may the vector $\mathbf{u}$ as

$$\mathbf{u} = \sin\theta(s)\cos\varphi(s)\mathbf{x} + \sin\theta(s)\cos\varphi(s)\mathbf{y} + \cos\theta(s)\mathbf{z}. \tag{4.40}$$

It is useful to have relations of these virtual frame rotations in terms of local angles. To this purpose, we first introduce the vectors $\mathbf{e}_\varphi = -\sin\varphi\,\mathbf{x} + \cos\varphi\,\mathbf{y}$ and $\mathbf{n}_\varphi \equiv \mathbf{u} \times \mathbf{e}_\varphi$ which span the plane containing the vectors $\mathbf{t}$ and $\mathbf{n}$ (for simplicity, we omit subscripts here). We define $\phi(s)$ as the angle between $\mathbf{t}$ and $\mathbf{e}_\varphi$. The coordinates $\theta(s)$, $\varphi(s)$, $\phi(s)$ are Euler-like angles since they describe rotations of the frame.

The coordinates $\theta(s)$ and $\varphi(s)$, as functions of the arc-length, can be obtained by using the J-vector. As it is a conserved vector, we are free to set $\mathbf{J}$ aligned along the z-axis,

then $\mathbf{J} = J\mathbf{z}$, with $J > 0$. Then, the spherical coordinates can be obtained by projecting the J-vector onto the frame $\{\mathbf{u}, \mathbf{t}\}$ [93]. Projecting $\mathbf{J}$ onto $\mathbf{u}$, one obtains

$$\mathbf{J} \cdot \mathbf{u} = J \cos\theta = \kappa, \tag{4.41}$$

then, the polar angle is given by

$$\theta(s) = \cos^{-1}\left(\frac{\kappa(s)}{J}\right). \tag{4.42}$$

If we project $\mathbf{J}$ onto $\mathbf{n}$, we obtain

$$\mathbf{J} \cdot \mathbf{n} = J\varphi' \sin^2\theta = \frac{\kappa^2}{2} + c. \tag{4.43}$$

Thus, the azimuthal angle is given by an integral formula

$$\varphi(s) = \int^s \frac{\kappa^2/2 + c}{J \sin^2\theta}\, ds = \frac{J}{2}\int^s \frac{\kappa^2 + 2c}{J^2 - \kappa^2}\, ds. \tag{4.44}$$

Note that the direction in which $\varphi(s)$ increases does not necessarily coincide with that of the arc-length s, that is to say, $\varphi'(s)$ can be either negative or positive. Knowing $\kappa(s)$, the entire shape of the conical structure can be obtained using Eqs. (4.42) and (4.44).

4.5 Elastic theory of foldable cones

In this section, we generalize the previous elastic theory to describe the equilibrium shapes of f-cones for arbitrary deformations.

4.5.1 Geometry of a foldable cone

We consider a f-cone of n creases made from a flat circular sheet of radius R which is parceled out in n circular sectors (panels) delimited by the creases (see Fig. 4.8(a)). A hole of radius $r_0 \ll R$ is cut out from the center of the sheet to avoid the divergence in the elastic energy. As the elastic sheet is inextensible, one can always find an isometrical map between the deformed shape and the flat state. Let α_i denote the sector angle of the ith panel in the flat configuration, with $\sum_{i=1}^{n} \alpha_i = 2\pi$. The value of the arc-length at the ith crease is denoted by s_i, so that, through the inextensibility condition, $\alpha_i = s_{i+1} - s_i$ in the deformed configuration. From now on, for any scalar or vector field of the form $b_i(s)$, the subscript i specifies that the domain of the function corresponds to the ith sector, where the periodic convention $b_{i\pm n} \equiv b_i$ is assumed. Moreover, we introduce the following notation: $b_i^- \equiv b_{i-1}(s_i)$ and $b_i^+ \equiv b_i(s_i)$.

In terms of spherical coordinates, the final shape is specified by a polar angle $\theta(s)$ and an azimuthal angle $\varphi(s)$ which are functions of the arc-length (see Fig. 4.8(b)). In the

deformed configuration, each crease has a folding angle (dihedral angle) ψ_i defined by the local frame in the plane perpendicular to the crease (see Fig. 4.9). The folding angle ψ_i is defined as the oriented angle $(-\widehat{\mathbf{t}_i^-, \mathbf{t}_i^+})$ which we calll *mountain* if $\psi_i \in [0, \pi]$ or a *valley* if $\psi_i \in [\pi, 2\pi]$. The projection of each panel in the xy–plan spans an azimuthal angle $\Delta\varphi_i \equiv \varphi(s_{i+1}) - \varphi(s_i)$. Note that $\Delta\varphi_i$ and α_i are not necessarily equal in the deformed configuration. However, they coincide in some specific cases: f-cones with an arbitrary number of evenly distributed identical creases or an even number of evenly distributed alternating mountain-valley creases where all the creases are mechanically identical. In such cases, we shall say in the following sections that the f-cone is *symmetrical*. Also, we use the names *all-mountain* (*all-valley*) creases f-cone if all the creases are mountain or *alternating* creases f-cone.

Closure condition: To guarantee the continuity of the elastic sheet, the curve Γ must close itself and cannot intersect itself. For the sheet to encounter itself, a closure condition must be satisfied. In particular, the curve Γ must be closed and cannot intersect itself. This closure condition can be imposed on the azimuthal spherical angle as follows

$$\sum_{i=1}^{n} \Delta\varphi_i = \begin{cases} \pm 2\pi & \text{if } \Gamma \text{ encloses the } z\text{-axis} \\ 0 & \text{if not} \end{cases}, \tag{4.45}$$

where $\pm$ indicates that $\varphi_i(s)$ can increase clockwise or counter-clockwise in the x-y plane. Although the majority of cases the curve Γ encloses the z-axis, we found a case in which the curve does not enclose. We shall discuss the details about this closure condition later.

4.5.2 Nonlinear model for f-cones

We now generalize the functional (4.31) for a f-cone with n creases. The total energy of the system is the sum of bending energies of all the n panels plus the mechanical

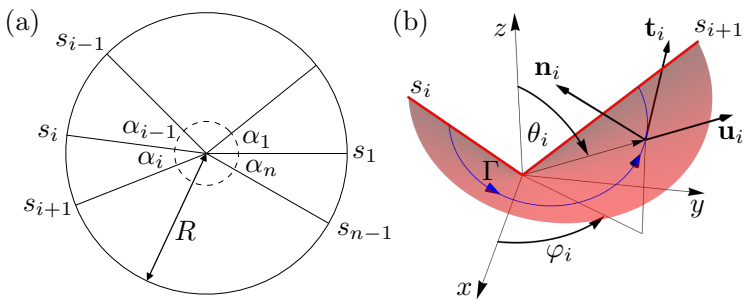

Figure 4.8 (a) Imprinted crease pattern on a flat plate. (b) Deformed state of the ith panel of a f-cone. The curve Γ, the material frame and the Euler-like angles are defined.

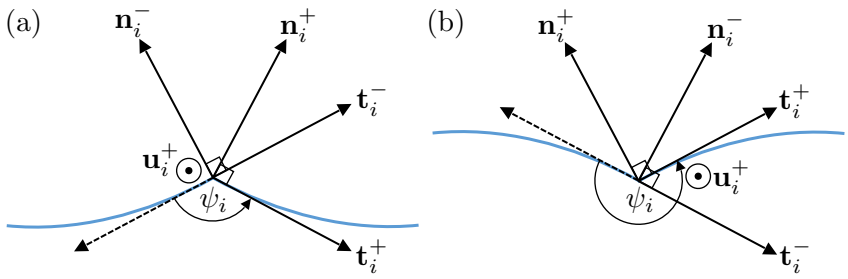

Figure 4.9 Definition of a mountain and a valley crease. The vectors $\mathbf{t}_i^{\pm}$, $\mathbf{n}_i^{\pm}$ and the crease angle ψ_i are defined.

energy stored in the creases. Therefore, the principle of virtual work is equivalent to minimizing the following functional

$$\begin{aligned} F_n[\mathbf{u},\mathbf{t}] \;=\; a\sum_{i=1}^{n}\int_{s_i}^{s_{i+1}}\Big[\frac{1}{2}(\mathbf{u}_i\cdot\mathbf{t}_i\times\mathbf{t}_i')^2+\frac{\lambda_i}{2}(\mathbf{u}_i^2-1)+\frac{\Lambda_i}{2}(\mathbf{t}_i^2-1) \\ +\mathbf{f}_i\cdot(\mathbf{t}_i-\mathbf{u}_i')\Big]ds+\sum_{i=1}^{n}g_i\left[\mathbf{t}_i^-,\mathbf{t}_i^+,\mathbf{u}_i^+\right]. \end{aligned} \tag{4.46}$$

The first term inside the brackets accounts for the bending energy of the panels, where $\mathbf{u}_i(s)\cdot(\mathbf{t}_i'(s)\times\mathbf{t}_i(s)) = \kappa_i(s)$ is the dimensionless curvature of the ith panel. The above augmented energy functional contains $3n$ local Lagrange multipliers, namely $\lambda_i(s)$, $\Lambda_i(s)$ and $\mathbf{f}_i(s)$, corresponding to the kinematical constraints enforcing the inextensibility condition.

The functions $g_i\left[\mathbf{t}_i^-,\mathbf{t}_i^+,\mathbf{u}_i^+\right]$ account for the elastic energy stored in the ith crease which is defined by local vectors $\{\mathbf{u}_i^+,\mathbf{t}_i^-,\mathbf{t}_i^+\}$ in the plane perpendicular to the crease. As said before, the crease energy can be written as an expansion of the following invariants: $\mathbf{t}_i^-\cdot\mathbf{t}_i^+$ and $\left(\mathbf{t}_i^-\times\mathbf{t}_i^+\right)\cdot\mathbf{u}_i^+$ [18]. Thus, at leading order, the elastic energy of the ith crease takes the form.

$$g_i\left[\mathbf{t}_i^-,\mathbf{t}_i^+,\mathbf{u}_i^+\right]=L\left(\sigma_i\,\mathbf{t}_i^-\cdot\mathbf{t}_i^+ +\tau_i\left(\mathbf{t}_i^-\times\mathbf{t}_i^+\right)\cdot\mathbf{u}_i^+\right), \tag{4.47}$$

where $L=R-r_0$ is the crease length, and σ_i and τ_i are material constants. The crease energy can be rewritten in terms of the folding angle ψ_i, defined as the oriented angle $(-\widehat{\mathbf{t}_i^-,\mathbf{t}_i^+})$ (see Fig. 4.9). We introduce the constants $k_i>0$ and $\psi_i^0\in[0,2\pi]$, such that

$$\sigma_i=k_i\cos\,\psi_i^0,\qquad \tau_i=k_i\sin\,\psi_i^0, \tag{4.48}$$

allows us to rewrite (4.47) as $g_i(\psi_i)=-Lk_i\,\cos\left(\psi_i-\psi_i^0\right)$. Thus, the crease energy $g_i=g_i(\psi_i)$ is a function of the folding angle which is now an unknown variable. As explained before, k_i is the crease stiffness, and ψ_i^0 is the rest angle of the crease. Note that the conical geometry implies that the folding angle is constant along the crease. For simplicity, we consider point-like creases, although the model can be

generalized to extended creases where a crease is a localized region with a non-zero natural curvature, as shown in reference [64].

4.5.3 Euler's *Elastica*

Cerda *et al.* [25] showed that finding the shape of conical singularities reduces to solve a one-dimensional equation that is equivalent to the classical planar *Elastica* of Euler, the equation that describes the shape of inextensible elastic rods. The variation of functional also yields the *Elastica* of Euler (4.31): its derivation can be found in [54]. To see how the *Elastica* equation shows up, let us compute the variation of functional (4.46):

$$\begin{aligned}\delta F_n &= a\sum_{i=1}^{n}\int_{s_i}^{s_{i+1}}\left[\left(\kappa_i^2\mathbf{u}_i-\kappa_i\mathbf{n}_i+\lambda_i\mathbf{u}_i+\mathbf{f}_i'\right)\cdot\delta\mathbf{u}_i\right.\\ &\quad\left.+\left((\kappa_i\mathbf{n}_i)'+\kappa_i^2\mathbf{t}_i+\Lambda_i\mathbf{t}_i+\mathbf{f}_i\right)\cdot\delta\mathbf{t}_i\right]ds\\ &\quad -a\sum_{i=1}^{n}(\mathbf{f}_i\cdot\delta\mathbf{u}_i+\kappa_i\mathbf{n}_i\cdot\delta\mathbf{t}_i)\Big|_{s_i}^{s_{i+1}}+\sum_{i=1}^{n}\delta g_i,\end{aligned}\tag{4.49}$$

where we have used the identities: $\mathbf{u}\cdot\mathbf{t}\times\delta\mathbf{t}'=\mathbf{n}\cdot\delta\mathbf{t}'$ and $\mathbf{u}\cdot\delta\mathbf{t}\times\mathbf{t}'=-\kappa\mathbf{t}\cdot\delta\mathbf{t}$. The term δg_i contributes to boundary terms only, which shall be treated later. Recall that we consider $\mathbf{u}_i$ and $\mathbf{t}_i$ as independent variables, therefore, the equilibrium condition $\delta F_n=0$ implies that the terms proportional to $\delta\mathbf{u}_i(s)$ and $\delta\mathbf{t}_i(s)$ vanish each. Variation with respect to $\mathbf{u}_i$ yields

$$\mathbf{f}_i'=-(\kappa_i^2+\lambda_i)\mathbf{u}_i+\kappa_i\mathbf{n}_i.\tag{4.50}$$

while variation with respect to $\mathbf{t}_i$ yields

$$\mathbf{f}_i=-\kappa'\mathbf{n}_i-2\kappa_i^2\mathbf{t}_i-\Lambda_i\mathbf{t}_i.\tag{4.51}$$

Note that

$$\mathbf{f}_i'\cdot\mathbf{t}_i = 0,\tag{4.52}$$

$$\mathbf{f}_i\cdot\mathbf{u}_i = 0.\tag{4.53}$$

Differentiating Eq. (4.51) with respect to s and using (4.52), it follows that $\Lambda_i'=5\kappa_i\kappa_i'$. Integrating once, we obtain

$$\Lambda_i=5\frac{\kappa_i^2}{2}-c_i\tag{4.54}$$

where c_i is an integration constant for each panel. Then, Eq. (4.51) can be written as follows

$$\mathbf{f}_i=\left(\frac{1}{2}\kappa_i^2+c_i\right)\mathbf{t}_i-\kappa_i'\mathbf{n}_i.\tag{4.55}$$

Note that there is an in-plane and an out-of-plane contribution to the transmitted force. Differentiating Eq. (4.55) with respect to s and projecting onto $\mathbf{u}_i$ gives

$$\mathbf{f}_i' \cdot \mathbf{u}_i = -\left(\frac{1}{2}\kappa_i^2 + c_i\right). \tag{4.56}$$

Projecting equation (4.50) onto $\mathbf{u}_i$ and equating with Eq. (4.56), one gets $\lambda_i = -\kappa_i^2/2 + c_i$. Then, Eq. (4.50) now reads

$$\mathbf{f}_i' = -\left(\frac{\kappa_i^2}{2} + c_i\right)\mathbf{u}_i + \kappa_i \mathbf{n}_i. \tag{4.57}$$

On the other hand, one can differentiate once Eq. (4.55) and obtain

$$\mathbf{f}_i' = -\left[\kappa_i'' + \kappa_i\left(\frac{\kappa_i^2}{2} + c_i\right)\right]\mathbf{n}_i - \left(\frac{\kappa_i^2}{2} + c_i\right)\mathbf{u}_i. \tag{4.58}$$

Projecting the above equation along $\mathbf{n}_i$ and using Eq. (4.57), one obtains a set of n ordinary differential equations given by

$$\kappa_i'' + (1 + c_i)\,\kappa_i + \frac{\kappa_i^3}{2} = 0, \tag{4.59}$$

where $\{c_i\}_{i=1}^n$ is the set of n integration constants. The above equations describe the dimensionless curvature of each panel of the f-cone that leads to the equilibrium shape.

In the present work we assume that all the panels have the same constant, namely, $c_i = c$ for $i = 1, \dots, n$. This hypothesis is justified as long as no external forces act on the creases, which could introduce additional tension in the panels in an unbalanced manner.

Solving the system (4.59) with the assumption of equal constants, $c_i = c$, requires $2n + 1$ conditions. We shall see that $2n$ conditions are boundary conditions to apply at each crease, which are given by the boundary terms in Eq. (4.49). The remaining condition comes from imposing the closure condition. Note that for the case of an f-cone with n panels, one has in principle n conserved vectors $\{\mathbf{J}_i\}_{i=1}^n$. We will see later how these quantities relate to each other through the boundary conditions.

4.5.4 Boundary conditions

The variation of functional (4.46) yields boundary terms corresponding to the two last terms of Eq. (4.49). These boundary terms yield the boundary conditions to apply

at each crease which allows for solving Eqs. (4.59) for each panel. In the absence of external forces, these terms must satisfy

$$\text{B.T.'s} = -a \sum_{i=1}^{n} \left[(\mathbf{f}_i \cdot \delta \mathbf{u}_i) + (\kappa_i \mathbf{n}_i \cdot \delta \mathbf{t}_i) \right] \Big|_{s_i}^{s_{i+1}} + \sum_{i=1}^{n} \delta g_i = 0, \tag{4.60}$$

where $\mathbf{f}_i$ is given by Eq. (4.55).

The boundary terms in Eq. (4.60) involve virtual rotations of the frame vectors. The folding angle is related to the Euler-like angle $\phi(s)$ by:

$$\psi_i = \pi + \phi_i^+ - \phi_i^-. \tag{4.61}$$

In Appendix A.3 we derive useful formulas (see Eq. (A.30)) that relate the Euler-like angles $\theta(s)$, $\varphi(s)$, $\phi(s)$ and the folding angles ψ_i.

At this stage, we distinguish among two cases: when the creases are infinitely stiff, so the solutions are functions of the prescribed folding angles $\{\psi_i\}_{i=1}^n$, and when the creases have finite stiffness, so the solutions are given by prescribing their stiffness $\{k_i\}_{i=1}^n$ and their rest folding angles $\{\psi_i^0\}_{i=1}^n$.

Infinitely stiff crease: Infinitely stiff creases imposes that $\delta\psi_i = 0$, which is equivalent to have $\delta g_i = 0$. Then, using the periodic convention, Eq. (4.60) can be written as follows

$$\text{B.T.'s} = \sum_{i=1}^{n} \left[\left(\mathbf{f}_i^+ - \mathbf{f}_i^- \right) \cdot \delta \mathbf{u}_i^+ + \kappa_i^+ \mathbf{n}_i^+ \cdot \delta \mathbf{t}_i^+ - \kappa_i^- \mathbf{n}_i^- \cdot \delta \mathbf{t}_i^- \right] = 0, \tag{4.62}$$

where we have used $\mathbf{u}_i^- = \mathbf{u}_i^+$. Recall that when varying our energy functional, we assume that the vectors $\mathbf{u}_i$ and $\mathbf{t}_i$ undergo independent virtual rotations. This implies that the terms accompanying $\delta \mathbf{u}_i$ must vanish, thus

$$\mathbf{f}_i^+ = \mathbf{f}_i^-. \tag{4.63}$$

This means that the transversal force $\mathbf{f}$ is continuous across the creases.

On the other hand, one can show that the condition of infinitely stiff creases $\delta\psi_i = 0$ is equivalent to imposing $\mathbf{n}_i^+ \cdot \delta \mathbf{t}_i^- = \mathbf{n}_i^- \cdot \delta \mathbf{t}_i^+$ (see Appendix A.3). Therefore, one obtains

$$\kappa_i^+ = \kappa_i^-, \tag{4.64}$$

which means that the curvature is continuous through the crease. The continuity conditions (4.64,4.63) imply that

$$\mathbf{J}_i^+ = \mathbf{J}_i^- \tag{4.65}$$

thus, the entire structure is characterized by a single vector **J**. Combining equations (4.63) and (4.64), one can show that

$$\kappa_i'^{+} = -\kappa_i'^{-}, \tag{4.66}$$

$$\kappa_i'^{+} = -\cot\left(\frac{\psi_i}{2}\right)\left(\frac{\kappa_i^{+2}}{2} + c\right), \tag{4.67}$$

thus, yielding $2n$ boundary conditions. Adding the closure condition (4.45) makes the problem well-posed.

Finite crease stiffness: Let us first compute the variation of the crease energy δg_i. Using crease energy given by Eq. (4.47), one has

$$\begin{aligned}\delta g_i = L\big[&\sigma_i\left(\delta\mathbf{t}_i^- \cdot \mathbf{t}_i^+ + \mathbf{t}_i^- \cdot \delta\mathbf{t}_i^+\right) + \tau_i\left(\left(\delta\mathbf{t}_i^- \times \mathbf{t}_i^+\right)\cdot\mathbf{u}_i^+ + \left(\mathbf{t}_i^- \times \delta\mathbf{t}_i^+\right)\cdot\mathbf{u}_i^+\right.\\ &\left.+\left(\mathbf{t}_i^- \times \mathbf{t}_i^+\right)\cdot\delta\mathbf{u}_i^+\right)\big].\end{aligned} \tag{4.68}$$

The last term on the right-hand side is zero because $(\mathbf{t}_i^- \times \mathbf{t}_i^+)|_{s_i}$ is parallel to $\mathbf{u}_i(s_i)$. Using the cyclic properties of the triple product we can write

$$\delta g_i = L\left[\sigma_i\left(\mathbf{t}_i^+ \cdot \delta\mathbf{t}_i^- + \mathbf{t}_i^- \cdot \delta\mathbf{t}_i^+\right) + \tau_i\left(\mathbf{n}_i^- \cdot \delta\mathbf{t}_i^+ - \mathbf{n}_i^+ \cdot \delta\mathbf{t}_i^-\right)\right]. \tag{4.69}$$

Using the identities (A.30) in Appendix A.3, the above equation can be written in terms of the Euler-like angles as follows

$$\delta g_i = L\left[\sigma_i \sin\psi_i\left(\delta\phi_i^+ - \delta\phi_i^-\right) + \tau_i \cos\psi_i\left(\delta\phi_i^+ - \delta\phi_i^-\right)\right]. \tag{4.70}$$

Noticing that $\delta\phi_i^+ - \delta\phi_i^- = \delta\psi_i$, and using Eq. (4.48), one recovers the form

$$\delta g_i = Lk\sin\left(\psi_i - \psi_i^0\right)\delta\psi_i = \frac{dg_i}{d\psi_i}\delta\psi_i. \tag{4.71}$$

The infinitesimal variations of the frame vectors can be translated to virtual rotations in terms of the Euler angles $\delta\theta_i^+$, $\delta\varphi_i^+$, $\delta\phi_i^+$ and $\delta\phi_i^-$. Using the results of Appendix A.3 and recalling that $\theta_i^+ = \theta_i^-$ and $\varphi_i^+ = \varphi_i^-$, we can rewrite Eq. (4.60) as follows

$$\begin{aligned}\sum_{i=1}^{n}\Bigg\{&\left(\kappa_i'^{+}\cos\phi_i^+ - \kappa_i'^{-}\cos\phi_i^- - \left(\frac{\kappa_i^{+2}}{2} + c\right)\sin\phi_i^+ + \left(\frac{\kappa_i^{-2}}{2} + c\right)\sin\phi_i^-\right)\delta\theta_i^+\\ &+\left(\kappa_i'^{+}\sin\phi_i^+ - \kappa_i'^{-}\sin\phi_i^- + \left(\frac{\kappa_i^{+2}}{2} + c\right)\cos\phi_i^+ - \left(\frac{\kappa_i^{-2}}{2} + c\right)\cos\phi_i^-\right)\sin\theta_i^+\delta\varphi_i^+\\ &+\left(\kappa_i^+ - \kappa_i^-\right)\cos\theta_i^+\delta\varphi_i^+ - \left(\kappa_i^+ - \bar{k}_i\sin\left(\psi_i - \psi_i^0\right)\right)\delta\phi_i^+\\ &+\left(\kappa_i^- - \bar{k}_i\sin\left(\psi_i - \psi_i^0\right)\right)\delta\phi_i^-\Bigg\} = 0.\end{aligned} \tag{4.72}$$

Here, we assume that the virtual rotations associated with $\delta\theta_i^+$, $\delta\varphi_i^+$, $\delta\phi_i^+$ and $\delta\phi_i^-$ are independent. Similarly to the case of infinitely stiff creases, the first two groups of terms yield $\mathbf{f}_i^+ = \mathbf{f}_i^-$. Indeed, the terms proportional to $\delta\theta_i^+$ and to $\sin\theta_i^+\delta\varphi_i^+$ correspond to projections of Eq. (4.63) along the vectors $\mathbf{e}_\varphi$ and $\mathbf{n}_\varphi$, respectively. Then, the parenthesis accompanying $\cos\theta_i^+\delta\varphi_i^+$ implies $\kappa_i^+ = \kappa_i^-$. Therefore, the structure is also characterized by a single vector $\mathbf{J}$. Conditions (4.66) and (4.67) also apply in the present case.

The terms proportional to $\delta\phi_i^+$ and $\delta\phi_i^-$ imply that

$$\kappa_i^+ = \kappa_i^- = \bar{k}_i \sin\left(\psi_i - \psi_i^0\right), \tag{4.73}$$

where

$$\bar{k}_i = \frac{Lk_i}{a} \tag{4.74}$$

is the normalized crease stiffness. The above result can be generalized to any other crease energy $g_i(\psi_i)$ to the following general condition:

$$\kappa_i^+ = \frac{1}{a}\frac{dg_i}{d\psi_i}. \tag{4.75}$$

The above equation states that the value of the curvature at each crease is given by the moment imposed by its mechanical response. Summarizing, the boundary conditions in the case of creases with finite stiffness are the same as the infinitely stiff case plus the additional condition (4.75). Note that the equilibrium shapes depend on the rest angle and the normalized crease stiffness.

4.6 Solving the *Elastica*

In this section, we present the solution of Eq. (4.59) for each of the n panels of the f-cone.

4.6.1 Generic bistability

Here, we show the existence of two families of solutions, corresponding to rest and snapped states of the f-cone, respectively. Using the J-vector, we write Eq. (4.59) in its integral form:

$$J^2 - c^2 = \kappa'^2 + (1+c)\kappa_i^2 + \frac{\kappa_i^4}{4}. \tag{4.76}$$

The above equation can be expressed in the following form:

$$\int_\Gamma ds = \int_\Gamma \frac{d\kappa_i}{\sqrt{(J^2 - c^2) - (1+c)\kappa_i^2 - \kappa_i^4/4}}. \tag{4.77}$$

This integral gives $s(\kappa)$, but one can invert this relation and obtain $\kappa(s)$ in terms of elliptic functions, whose solution depends on the sign of the quantity $J^2 - c^2$ [2]. Previous works on conical singularities have considered the case $J^2 - c^2 > 0$ only, which leads to a single family of solutions. For example, Cerda *et al.* [25, 23] considered only cases where $1 + c > 0$ (and thus $J^2 - c^2 > 0$) for d-cones. In the case of e-cones [93] or dipolar defects [55], one always has $\kappa(s^*) > 0$ for some s^*, which implies $J^2 - c^2 = \kappa'^2(s^*) > 0$. However, in the case of f-cones, one can have solutions where $\kappa(s)$ never vanishes along the panels, and with any value of c, thus, the quantity $J^2 - c^2$ can be either positive or negative. Therefore, Eq. (4.77) leads to two possible solutions:

$$\kappa_i(s) = \begin{cases} \kappa_{0i}\,\mathrm{cn}\left(\dfrac{\kappa_{0i}}{2\sqrt{m_i^{\mathrm{R}}}}s - S_{0i}\middle|m_i^{\mathrm{R}}\right), & \text{if } J^2 > c^2, \\ \kappa_{0i}\,\mathrm{dn}\left(\dfrac{\kappa_{0i}}{2}s - S_{0i}\middle|m_i^{\mathrm{S}}\right), & \text{if } J^2 < c^2, \end{cases} \tag{4.78}$$

where $\mathrm{cn}(\cdot|\cdot)$ and $\mathrm{dn}(\cdot|\cdot)$ are the cosine and the delta amplitude Jacobian elliptic functions [2], with parameters m_i^{R} and m_i^{S} given by

$$m_i^{\mathrm{R}} = \frac{1}{m_i^{\mathrm{S}}} = \frac{\kappa_{0i}^2}{2\kappa_{0i}^2 + 4(1+c)}. \tag{4.79}$$

Here, κ_{0i}, S_{0i} and c are $2n + 1$ unknown parameters that must be found such that the boundary conditions and the closure conditions are satisfied. Without loss of generality, one can define the cosine and delta amplitude functions such that $0 < m_i^{\mathrm{S}} < 1$ and $0 < m_i^{\mathrm{R}} < 1$ [2].

Let us point out some general properties about the bistability of f-cones contained in Eq. (4.79).

1. Eq. (4.79) shows the existence of two families of solutions. We identify them as the *rest* configuration (superscript R) the solutions for which $J^2 > c^2$ and the *snapped* configuration (superscript S) with $J^2 < c^2$. This choice is in agreement with the fact that we find a posteriori that the bending energy of the rest configuration is the lower one.
2. As the quantity $J^2 - c^2$ is defined for the entire structure, all the panels will be in either a rest state or a snapped state.
3. The present nonlinear approach allows us to justify the existence of two families of solutions for a given set of folding angles, regardless of whether the cone is symmetrical or not, a property that is difficult to prove in the linear model.

4.6.2 Solutions for symmetrical *f*-cones

From this point onwards, we consider a simplified situation of symmetrical *f*-cones made of all-mountain creases with the same folding angle ψ (we shall also omit the subscripts i labelling the panels). The case of alternate crease pointing in opposite directions is shown in the Appendix B. We denote n^{R} (respectively, n^{S}) as the all-mountain *f*-cones with n-creases in a rest (respectively, snapped) state. We shall here discuss the solutions for the most relevant cases, which are a semi-infinite crease ($1^{\mathrm{R,S}}$), a single infinite crease ($2^{\mathrm{R,S}}$) and two perpendicular mountain creases ($4^{\mathrm{R,S}}$).

For these symmetrical configurations, it is sufficient to solve Eq. (4.59) in a single panel where $-\alpha/2 \leq s \leq \alpha/2$ and $\alpha = 2\pi/n$. For both rest and snapped states, we proceed to find the parameters κ_0, S_0 and c that satisfy the closure condition (4.45) and the boundary conditions (4.66,4.67). As the *f*-cone is symmetrical, the solutions given by Eq. (4.78) should be even functions with respect to $s = 0$. Therefore, one has $S_0 = 0$ for the rest state and, for the snapped state there are two possibilities, either $S_0 = 0$ or $S_0 = K(m_s)$ ($K(\cdot)$ is the complete elliptic integral of the first kind and corresponds to the half period of the function $\mathrm{dn}(\cdot|m)$) [2]. We only found solutions for $S_0 = K(m_s)$ that satisfy the closure condition. Eq. (4.66) is automatically satisfied by the symmetry of the solutions. We now proceed numerically to find the parameters κ_0 and c.

The closure condition (4.45) reads now $\Delta\varphi = \pm\alpha$ or 0. For each, both rest and snapped, states, the quantity $\Delta\varphi$ is an integral that can be computed analytically as follows. In a symmetrical *f*-cone with n creases, the azimuthal angle spanned by a single panel is given by the integral

$$\Delta\varphi = \int_{-\alpha/2}^{\alpha/2} \frac{\kappa^2/2 + c}{J\sin^2\theta} ds = \int_{-\alpha/2}^{\alpha/2} \frac{J}{2}\left[\frac{J^2 + 2c}{J^2 - \kappa^2} - 1\right] ds, \tag{4.80}$$

where $\alpha = 2\pi/n$. As the deformed state will also be symmetrical, the closure condition can be written as $\Delta\varphi = \pm\alpha$ or $\Delta\varphi = 0$ according to Eq. (4.45). For rest states, Eq. (4.80) gives,

$$\Delta\varphi^{\mathrm{R}} = \left[\frac{J(J^2 + 2c)}{\kappa_0(J^2 - \kappa_0^2)}\sqrt{m_r}\,\Pi\left(\frac{\kappa_0^2}{\kappa_0^2 - J^2}, \mathrm{am}\left(\frac{\kappa_0}{2\sqrt{m_r}}s\middle|m_r\right)\middle|m_r\right) - \frac{J}{2}s\right]\Bigg|_{-\alpha/2}^{\alpha/2}, \tag{4.81}$$

and for snapped states

$$\Delta\varphi^{\mathrm{S}} = \left[\frac{c}{J}s - \frac{(J^2 + 2c)\kappa_0(m_s - 1)}{J(J^2 + (m_s - 1)\kappa_0^2)}\Pi\left(\frac{J^2 m_s}{J^2 + (m_s - 1)\kappa_0^2}, \mathrm{am}\left(\frac{\kappa_0}{2}s\middle|m_s\right)\middle|m_s\right)\right]\Bigg|_{-\alpha/2}^{\alpha/2}, \tag{4.82}$$

where the labels R, S stand, respectively, rest and snapped states and $\Pi(\cdot,\cdot|m)$ is the elliptic integral of third kind and $\mathrm{am}(\cdot|m)$ is the Jacobi amplitude with modulus m [2].

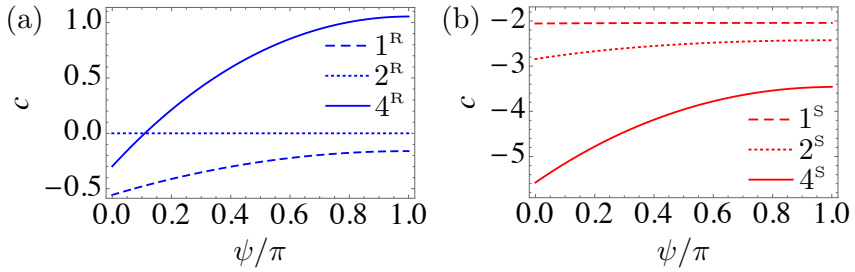

Figure 4.10 The Lagrange multiplier c as function of the folding angle ψ for (a) rest states and (b) snapped states for all-mountain f-cones with 1, 2 and 4 creases.

Eq. (4.81) (respectively, Eq. (4.82)) defines a curve in the parameter space $\{\kappa_0, c\}$ for the rest (respectively, snapped) states. This curve contains all the solutions for $0 \leq \psi \leq \pi$ and can be found numerically.

Infinitely stiff creases: We now solve the case of infinitely stiff creases, where the set of folding angles $\{\psi_i\}_{i=1}^n$ is an input of the problem. Eq. (4.67) defines a second curve in the parameter space $\{\kappa_0, c\}$ (one for the rest state and another for the snapped state). Hence, the solution for a given folding angle ψ corresponds to the intersection between this curve and that given by the closure condition. Therefore, for a given ψ one obtains the values of $\kappa_0(\psi)$ and $c(\psi)$. This procedure is performed numerically for all $\psi \in [0, \pi]$ ($\psi > \pi$ corresponds to equivalent states but vertically flipped).

Fig. 4.10 summarizes our findings regarding the integration constants as functions of the folding angle. Since $c(\psi)$ relates to the hoop stress, we shall highlight a few observations concerning this quantity. Except for the trivial case 2^{R}, one has $c \nrightarrow 0$ as $\psi \to \pi$, which suggests the existence of a residual hoop stress $c(\pi)$ as one approaches the flat state. As expected, one recovers Eq. (4.33): this hoop stress coincides with that of the linear model in the limit $\psi = \pi$ [78]. Notice that the values of $c(\pi)$ for the rest and snapped of a f-cone states are different, although both structures are flat. Therefore, the structure undergoes an abrupt jump in stress when snapping from one state to another. We attribute this residual stress to a critical load needed to observe buckling of the facets, as it happens in Euler-Bernoulli beam buckling. We notice also that, in the configuration 4^{R}, c changes sign as $\psi \to 0$. This may suggest at first sight a modification of the hoop stress from compressive to tensile as the folding angle gets sharp, a fact that the linear model does not take into account. However, this interpretation is misleading since c coincides with the hoop stress only in the small deflections regime [23].

The equilibrium shapes of the f-cones are obtained using the coordinates $\theta(s)$, $\varphi(s)$. Fig. 4.11 shows some shapes of $1^{\mathrm{R,S}}$, and $4^{\mathrm{R,S}}$ f-cones for prescribed folding angles $\psi = 0°$ and $\psi = 90°$. Note that the present model captures the limit $\psi \to 0$. For most of the cases we solved, the curve Γ encloses the z-axis for all $\psi \in [0, \pi]$, and therefore, they satisfy $\Delta\varphi^{\mathrm{R,S}} = \pm\alpha$. The 1^{R} configuration for $\psi \lesssim 14°$ are the only solutions we

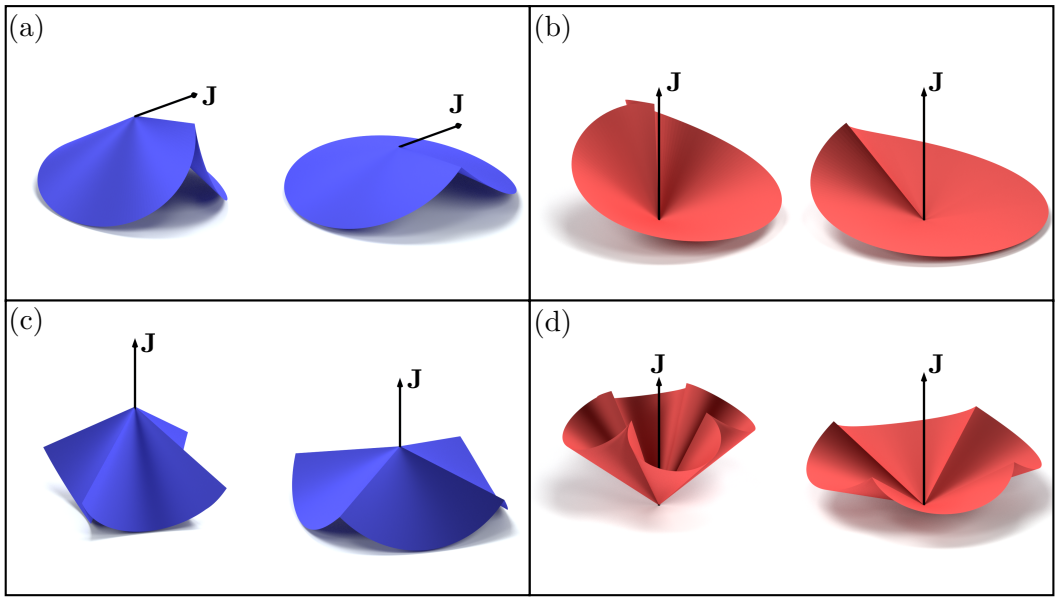

Figure 4.11 Solutions of (a-b) $1^{R,S}$ and (c-d) $4^{R,S}$ f-cones with prescribed folding angles $\psi = 0°$ and $\psi = 90°$. The arrows indicate the J-vector direction, but not its magnitude.

found in which the curve Γ does not enclose the z-axis, and therefore, $\Delta\varphi^{R,S} = 0$ (see Fig. 4.11(a)). These shapes are universal in the sense that they depend only on the folding angle ψ and not the material properties. Nevertheless, changing the bending modulus or the dimensions of the cone will modify the stresses and torques supported by the system as well as its elastic response.

Fig. 4.12 shows the relations between the folding angles and the polar angle at the creases. To quantify such deformations, we use the angle $\beta = \pi - \cos^{-1}(\mathbf{u}(0) \cdot \mathbf{u}(\pi))$ for a $1^{R,S}$ f-cone and the polar angle $\theta_c = \cos^{-1}(\mathbf{z} \cdot \mathbf{u}(\alpha/2))$ for $n^{R,S}$ f-cones ($n > 1$). The choice of ψ, instead of θ_c (or β for a $1^{R,S}$ f-cone) as a control parameter prevents finding unphysical self-intersecting solutions. A generic feature revealed by Fig. 4.12 is that the polar angle at the crease varies quasi-linearly with the folding angle for the whole range $0 < \psi < \pi$. This result is independent of the number of folds and holds for both rest and snapped configurations. Fig. 4.12(c) shows a comparison between $\theta_c(\psi)$ for the 2^S configuration and the prediction of the linear model $\theta_c = \pi/2 + 0.4386(\psi - \pi)$, which is the case of the bistable creased strips [78, 131]. The polar angle of the crease deviates slightly from the linear prediction for sharper folding angles. This deviation fits better the experimental results shown in reference [131], although there is still a significant discrepancy from the theory because of the limits of the inextensibility hypothesis.

The linear model, which is by definition valid in the limit of flat folding angles only ($\psi \to \pi$), seems to provide a fairly good prediction of $\theta_c(\psi)$ for small ψ. However, a closer look to the entire shape of the f-cone shows that this is not the case. Fig. 4.13 shows a comparison between both models of $\theta(\varphi)$ along a single panel of a 4-creases

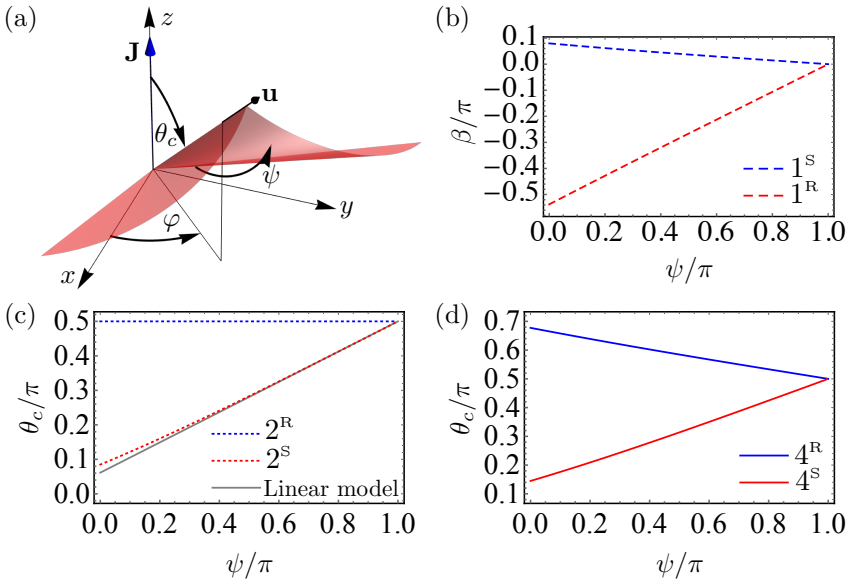

Figure 4.12 (a) Schematic definition of the polar angle θ_c for $n^{R,S}$ f-cones ($n > 1$). (b) Case $1^{R,S}$: the angle $\beta(\psi) = \pi - \cos^{-1}(\mathbf{u}(0) \cdot \mathbf{u}(\pi))$ that describes the deviation from the flat configuration. (c) Case $2^{R,S}$: the polar angle $\theta_c(\psi)$ at the creases compared with the prediction of the linear model for the snapped state. (d) Case $4^{R,S}$: the polar angle $\theta_c(\psi)$ at the creases.

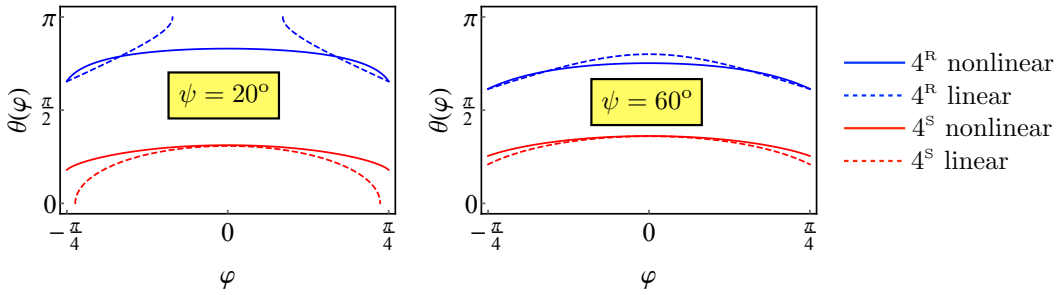

Figure 4.13 Comparison of $\theta(\varphi)$ between the nonlinear and the linear model. For small ψ the linear model fails to predict the entire shape of the structure.

f-cone. For sharp folding angles, the linear model fails to predict the shape of the whole structure: we see that for $\psi \sim 20°$, the linear model departs considerably from the exact one and touches the z-axis. Also, the linear model gives unphysical self-intersecting solutions.

Finite crease stiffness: We study again configurations with equally spaced mountain creases that share the same mechanical properties: $\bar{k}_i = \bar{k}$ and $\psi_i^0 = \psi_0$. The control parameters are then the crease stiffness $\bar{k}$ and the rest angle ψ_0. The boundary conditions are those of the infinitely stiff creases case supplemented by Eq. (4.75). Therefore, one can use the solutions found previously for the infinitely stiff creases and search the value of ψ such that Eq. (4.75) is satisfied.

Figures 4.14(a-c) show typical shapes for the cases $1^{R,S}, 2^{R,S}, 4^{R,S}$. Fig. 4.14(d) shows the final folding angle ψ as a function of $\bar{k}$ for a fixed rest angle ψ_0 of the crease. Notice that $\psi \to \pi$ as $\bar{k} \to 0$ and that $\psi \to \psi_0$ as $\bar{k} \to \infty$. For a given $\bar{k}$, the snapped state

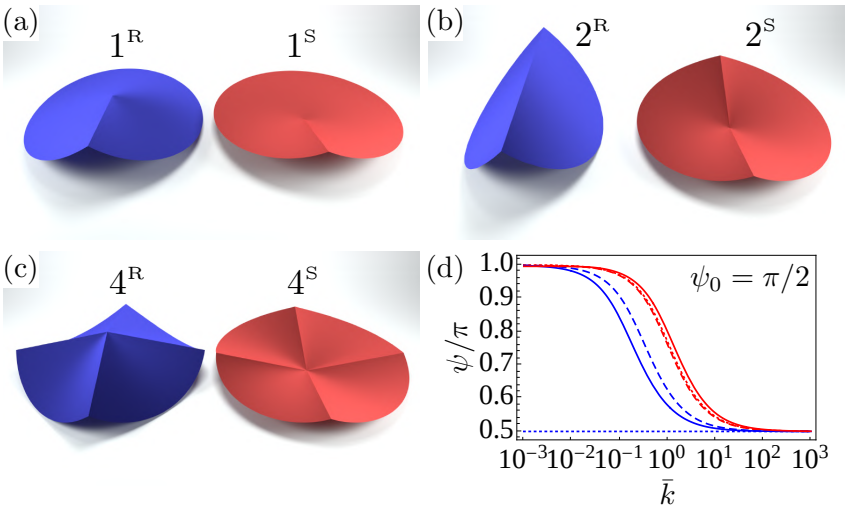

Figure 4.14 (a-c) Equilibrium shapes for $\bar{k} = 1$ and $\psi_0 = \pi/2$. (d) Final crease angles ψ as function of $\bar{k}$ for $\psi_0 = \pi/2$. Rest (blue lines) and snapped (red lines) states for all-mountain f-cones with 1, 2 and 4 creases (respectively dashed, dotted and plain lines).

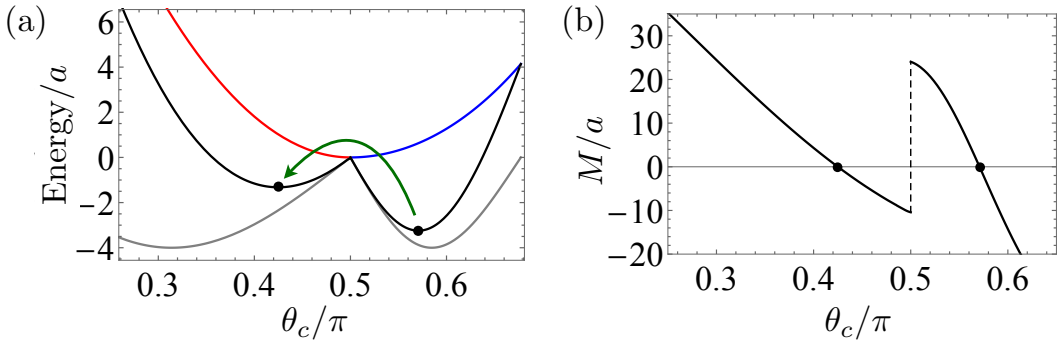

Figure 4.15 (a) Energy landscape of an all-mountain f-cone with 4 creases as function of θ_c for $\bar{k} = 1$ and $\psi_0 = \pi/2$. The blue and red curves correspond to the bending energy of the facets for the rest and snapped states, respectively. The plain gray curve is the crease energy given by Eq. (4.47). The black curve is the total elastic energy. (b) Normalized moment $M(\theta_c)$ applied on the creases. The black dots correspond to the rest and snapped states of the f-cone.

always displays a larger ψ than the rest state. This fact occurs because the hoop stress of the snapped state is always larger than its respective rest state.

4.6.3 Snap-through dynamics

The total energy consists of summing the bending energy of the facets and the energy of the creases. Fig. 4.15(a) shows an example of the energy landscape as a function of the polar angle θ_c of the crease for an all-mountain f-cone with 4 creases. While the bending energy of the facets has an asymmetric parabolic shape, the energy of the creases has a double-well potential shape whose minima are at the same energy level. The resulting shape of the total energy is an asymmetric double-well potential whose two minima corresponds to the rest and the snap states. By taking the derivative of the energy with respect to θ_c, we calculate the corresponding moment $M(\theta_c)$ applied

on the creases and the particular case associated to the 4-creases case is shown in Fig. 4.15 (b). Note that the energy has a cusp at $\theta_c = \pi/2$, which leads to an abrupt discontinuity in the mechanical response of the structure. Other similar systems, such as the waterbomb origami with rigid facets [57], show this type of snap-through behavior, although the mechanisms behind this instability in the *f*-cone and the waterbomb are different. The former is mediated by the asymmetry in the bending energy between the rest and snapped states and the latter by the asymmetrical kinematical conditions imposed by the rigid facets. For the waterbomb, the only relevant energy is the mechanical energy stored in the creases which, in addition to the kinematical constraints, accounts for an asymmetric double-well like potential.

4.7 Continuous elastic model of origami structures

Commonly, the mechanical response of origami-based metamaterials can not be reduced to elastic hinges connected to rigid or isometric panels [112]. The energy landscape of deformations generally depends on both bending and stretching energies of the panels as well as on the inherent spatially extended nature of the creases [64]. Therefore, one needs to supplement the present analysis with a more accurate description that takes into account these different contributions. When applied to the *f*-cone, such a description should be validated by the bounds given by the analytical model.

In the following, we propose a mechanical model based on a continuous description of origami structures that is suitable for numerical implementation and test it on the *f*-cone by performing Finite Element analysis (FEA). The simulations were designed in the commercial FEA software COMSOL Multiphysics 5.4. Within this software, the Structural Mechanics Module is equipped with quadratic shell elements, which have been used to our purpose. All the simulations were carried out with a linear elastic Hookean material model, and geometric non-linear kinematic relations have been included. The plate has Young's modulus $E = 3.5$ GPa, Poisson's ratio $\nu = 0.39$, and thickness $h = 300\,\mu$m. We searched for solutions with the default stationary solver, where the non-linear Newton method has been implemented. Mesh refinement studies were undertaken to ensure the convergence of the results.

4.7.1 Temperature-induced hingelike creases

In our numerical model, we develop a method to create creases that can reproduce the hingelike mechanical response of commonly folded thin sheets. Inspired by the experimental results of Ref. [64], we model creases as narrow slices of the plate undergoing thermal expansion due to a temperature gradient through the thickness of the plate, as it is schematically shown in Fig. 4.16.

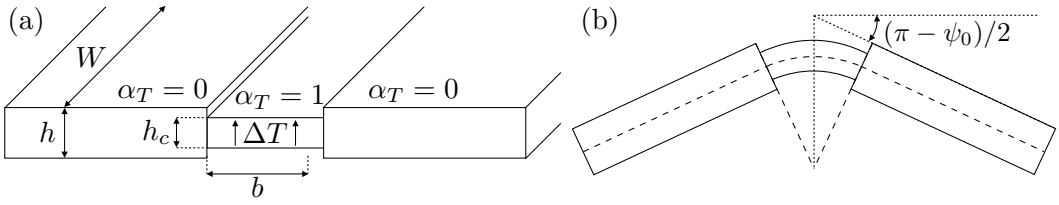

Figure 4.16 Transverse view of a plate with a narrow slice whose thermal and mechanical properties differ from those of the rest of the plate. (a) Reference configuration. (b) Curvature induced equilibrium configuration due to a linear thermal gradient across the thickness.

In order to test the mechanical response of these temperature-driven creases, we first perform a numerical test of a single fold in a hingelike geometry consisting of two facets and the crease in the middle. We consider a rectangular plate of length L, width W and thickness h. In the middle of the plate, we take a narrow transversal slice of width $b \ll W$, across the width of the plate, dividing the plate into three parts. The narrow slice corresponds to the crease, while the other two parts correspond to the facets. A linear temperature gradient ΔT is applied through the thickness of the plate. We let the creased region of the plate to undergo thermal expansion by defining an inhomogeneous coefficient of thermal expansion $\alpha_T(s)$ which is constant for $|s| < b$ and zero elsewhere, where s is the arc-length perpendicular to the creases. To simulate a more realistic crease, we add a rigid connector made of an infinitely stiff material of length W, thus preventing bending deformation in the direction of the crease line. Moreover, tuning the mechanical response of the crease is done by varying the thickness h_c and Young's modulus E_c of the crease slice. The parameters h_c, E_c, ΔT and b will define the mechanical response of the crease.

Taking advantage of the two-plane symmetry of the single fold geometry, we solve only for one quarter of the plate and then obtain the entire equilibrium shape by reflections. We perform two different studies: a heating up test and a mechanical response test. The first study is to heat the plate from the bottom while the ends of the two plates parallel to the crease are constrained to move in the xy-plane. When heating, the crease bends towards the sense of lower temperature (bottom), while the facets remain practically flat. The resulting angle between the two facets corresponds to the rest angle ψ_0 of the crease. The second study is to test the mechanical response of the crease. We add four additional rigid connectors to the sides of the facets that are perpendicular to the fold line. Two moments of opposite signs are applied respectively to each pair of rigid connectors attached to the facets so that the hingelike system can open or close. Through this mechanical test, we were able to verify the hingelike behavior of the crease.

In the following, we employ the temperature-induced creases in our numerical model of f-cones.

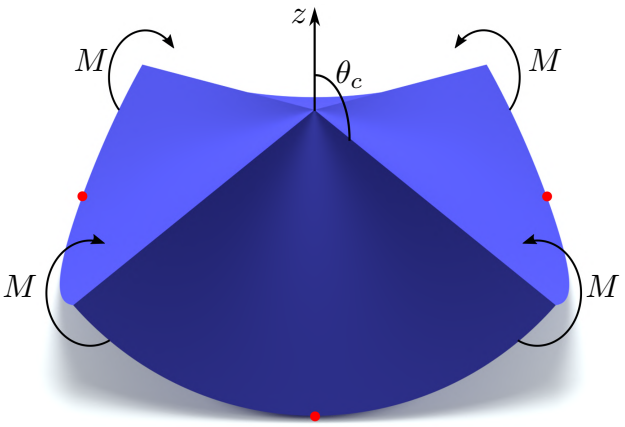

Figure 4.17 Schematics of the indentation protocol. Equal moments M are applied on each crease such that the center rim moves vertically in the downward direction, while the end points of the symmetry planes (denoted by red dots) are free to move in the xy-plane. The average displacement of the center rim is imposed and the moment M is computed as a function of the polar angle θ_c.

4.8 Numerical analysis of foldable cones

We begin with a circular planar disc of external radius $R = 100$ mm and a central hole of radius $r_0 = 1$ mm. Then, n radial narrow slices of constant width b, that correspond to the creases of the f-cone, are created. Rigid connectors along the creases are added to prevent bending along the longitudinal direction of the creases. In order to take advantage of the symmetries of the system, depending on the number of creases, only the fundamental unit cells are solved numerically, and then the complete structure is reconstructed using reflections through the symmetry planes. Because each plane of symmetry cannot coincide with a rigid connector, the $1^{R,S}$ case must be solved entirely. For $2^{R,S}$, only a half of the disk is solved so that the axis of symmetry is perpendicular to both creases. For $4^{R,S}$, a quarter of the disk is solved so that a single crease is at 45° from one plane of symmetry.

4.8.1 Snap-through dynamics

From now on, we focus only on the all-mountain f-cone with four creases, anticipating that our general conclusions also apply to more complex configurations. In order to test our analytical predictions, we study the snapping of the system through an indentation process from the rest state to the snapped state, which is carried out in two steps. Initially, we turn on the temperature to take the f-cone to its rest state with a given folding angle ψ. The endpoints of the symmetry planes are constrained to move only in the xy-plane so that the points at the inner rim rise when the temperature is activated. For all our simulations, we fix the temperature gradient in the crease such that $\alpha_T \Delta T = 0.2$. We also choose $b = 1$ mm, which is within the expected order of magnitude with respect to h according to crease formation measurements in thin sheets [11].

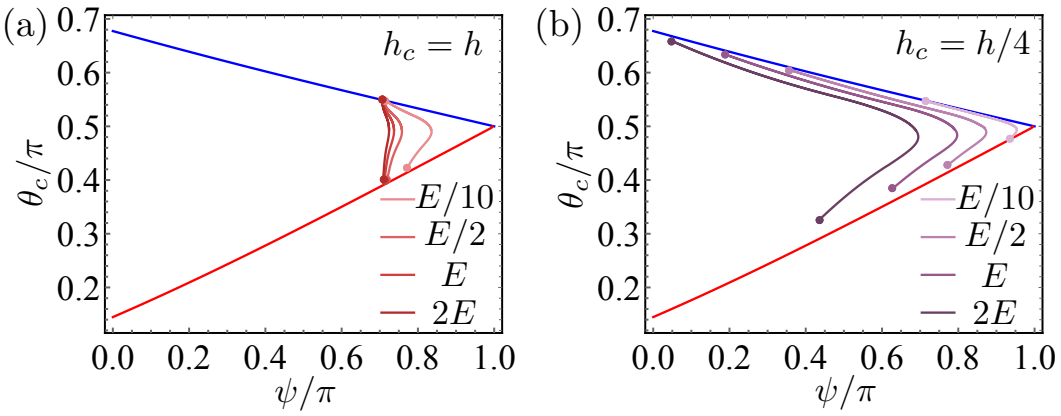

Figure 4.18 (a-b) Indentation paths $\theta_c(\psi)$ as computed by the numerical model for $h_c/h = 1, 1/4$ and $E_c/E = 2, 1, 1/2, 1/10$. The theoretical curves $\theta_c(\psi)$ for a $4^{R,S}$ f-cone are reproduced from Fig. 4.12. The dots correspond to the rest and snapped states of each indentation path.

In a second step, the inner rim is vertically lowered quasi-statically while constraining the endpoints of the symmetry planes to move freely in the xy-plane (see Fig. 4.17). Each crease is constrained to rotate only in the plane defined by its initial direction and the z-axis (as shown in Fig. 4.12(a)). Throughout indentation, the vertical displacement of the central rim is specified, and a reaction moment $M(\theta_c)$ at the creases is computed. Therefore, the mechanical response of the f-cone to the indentation process consists in the determination of the curve $M(\theta_c)$.

The folding angle ψ of the creases is also tracked during indentation. To measure ψ from the numerical results, we extract the tangent vector field of concentric curves initially defined in the flat configuration. We evaluate this vector field at each side of the crease and measure the resulting angle between them. The local folding angle is found to be not exactly constant along the crease but a function of the radial coordinate. For this reason, a representative measurement of ψ is chosen to be the average between two local folding angles measured at radial distances $r_0 + (R - r_0)/3$ and $r_0 + 2(R - r_0)/3)$. In each indentation test, we extract a curve θ_c as a function of ψ, which we call the indentation path.

The resulting curves $M(\theta_c)$ and $\theta_c(\psi)$ will be discussed in the following.

4.8.2 Numerical results

Fig. 4.18 shows the variation of $\theta_c(\psi)$ obtained numerically during the indentation test for different thicknesses and Young moduli of the crease. We compare these results with the polar angle $\theta_c(\psi)$ given by analytical f-cone calculations shown in Fig. 4.12(d). This parametric study allows us to highlight to what extent the softness of the crease affects the indentation path. Our results show that our continuous model of the crease is more sensitive to variations of h_c than those of E_c. We notice that the indentation paths do not generally follow the analytical solutions given by the

isometric constraint, meaning that the intermediate shapes throughout indentation are not perfect developable cones. If the crease is too stiff, as in the case of Fig. 4.18(a), the indentation path follows a nearly vertical line (*i.e.* approximately constant folding angle path) connecting the two stable points. However, when the crease is made softer (Fig. 4.18(b)), either by reducing its thickness or its Young's modulus, the indentation paths approach the one predicted by the isometric constraint.

While the rest states are generally well predicted by the isometric constraint, the snapped states depart from the analytical predictions when h_c is decreased. This result could be explained in terms of the crease stiffness. For a stiff crease, the folding angle is roughly constant along the crease enforcing the shape to be closer to a perfectly developable cone. On the other hand, a 4^s cone is characterized by an azimuthal tension which favors stretching deformations of the panels and thus tensile traction on the crease. This mechanism could induce a varying folding angle along the crease and yield a structure that can depart from a perfect developable cone, especially for softer creases. To verify this analysis, we plot in Fig. 4.19 one quadrant containing the lines of smallest principal curvature for stiff and soft crease cases. In a perfect developable cone, these lines coincide with the generators of a surface (*i.e.* lines of zero curvature). However, we observe that the lines curve significantly close to the vertex, where the energy is concentrated. This effect is more pronounced for the soft crease case than the stiff one.

Fig. 4.20(a) shows typical curves for the moment as a function of the polar angle θ_c during indentation for both stiff and soft crease. Notice that the unstable branch of the stiffer crease is higher than that of the soft one, which in a real experiment leads to a larger amount of energy released during a snapping process. This observation can be attributed to a larger stretching energy barrier that is required to be overcome, which is evident from the energy plots shown in Fig. 4.20(b). This stretching barrier is a result of the crease stiffness: the high stretching costs forces the cone to follow the isometric path, but at the same time, it forces the creases to become flat at the inversion point. To rationalize the interplay between stretching and crease stiffness, we define the ratio "crease-stretching" μ_{cs} of the f-cone as the ratio between energy associated with the crease energy ($\sim kR$) and the stretching energy ($\sim Eh$) associated to the panels [52]:

$$\mu_{cs} \equiv \frac{kR}{EhR^2}. \tag{4.83}$$

Assuming that the crease stiffness scale as $k \sim E_c h_c^2$, one has

$$\mu_{cs} \sim \frac{E_c h_c^2}{EhR}. \tag{4.84}$$

This value measures how "soft" or "stiff" the creases are with respect to the stretching undergone by the panels. For the indentation tests shown in Fig. 4.18(a), μ_{cs} ranges

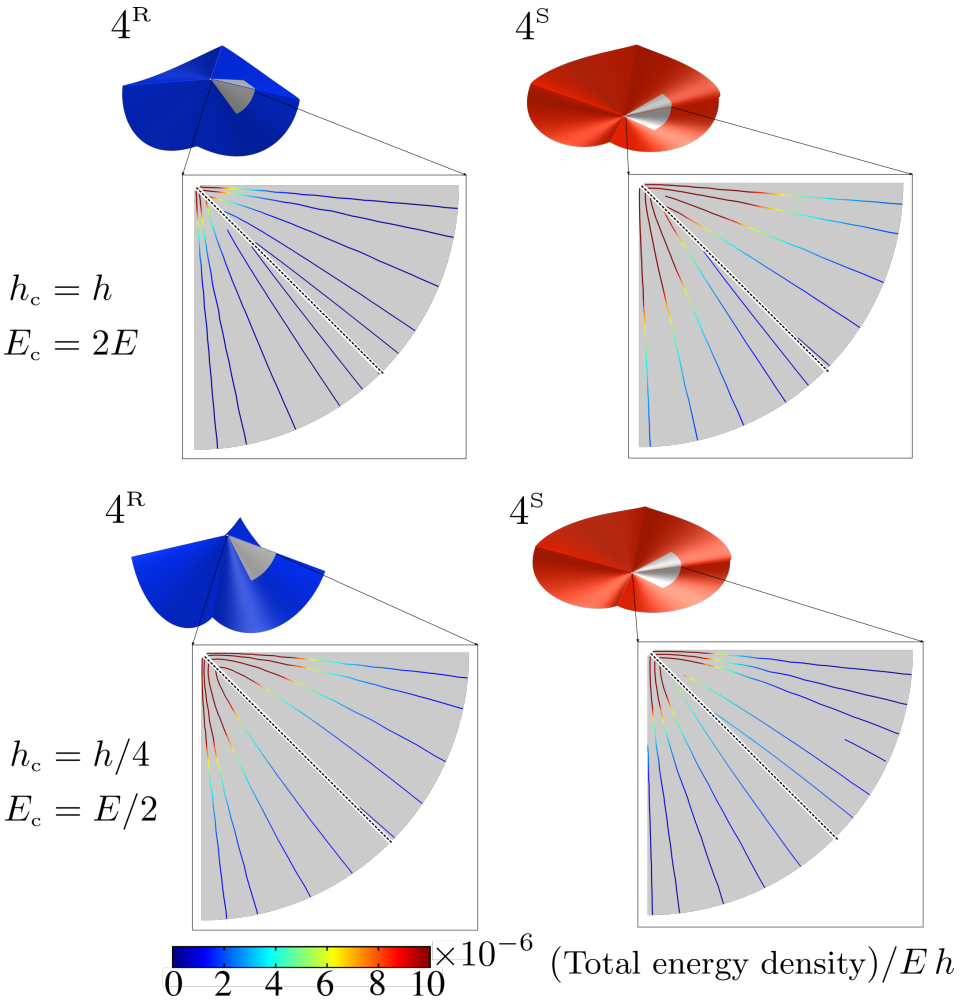

Figure 4.19 Lines of smallest principal curvature of a symmetric foldable cone with four creases. The upper (resp. lower) row corresponds to a stiff (resp. soft) crease case. The equilibrium rest (left column) and snapped (right column) states are shown. The boxes show zoomed regions next to the vertex. The black dotted line indicates the location of the crease and the color code corresponds to the elastic energy density.

between 0.1 and 2 (stiff cases), while for the curves shown in Fig. 4.18(b) μ_{cs} ranges between $\sim 10^{-3}$ and ~ 0.1 (soft cases). This parameter allows us to quantify the deviation from the isometric path during the indentation test. On the other hand, the difference in folding angle between the stable and metastable states is regulated by the competition between crease stiffness and bending of the panels, which is given by the normalized stiffness $\bar{k}$.

To compare with analytical predictions, one should focus on the Inset of Fig. 4.20(b) which shows the evolution of the bending energy of the facets throughout indentation and does not take into account the bending energy at the creases. The predicted bending energy exhibits an asymmetric parabolic shape, where the minimum corresponds to a flat solution. The bending energy of a soft crease follows closer the prediction than that of the stiff crease, which has a pronounced convex shape in the middle. As for the nature of the localisation, Fig. 4.19 shows that stretching mostly happens near the

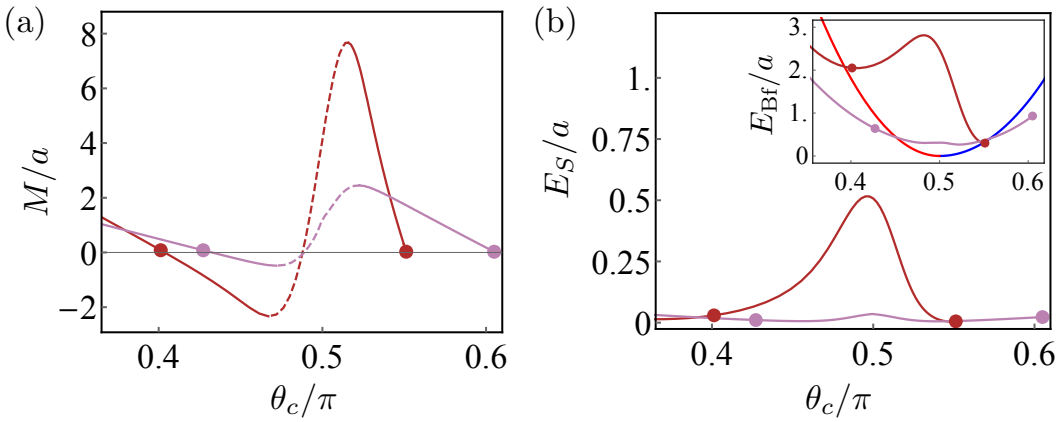

Figure 4.20 (a) Moment M as function of θ_c during the indentation of a stiff crease with $h_c = h$, $E_c = 2E$, and a soft crease, with $h_c = h/4$, $E_c = E/2$. (b) The corresponding total stretching energy. Inset. Normalized bending energy of the facets compared to the theoretical result of Fig. 4.15(a).

vertex, while bending spans over the whole plate. Therefore, one should look at the total energies between bending and stretching contributions. Fig. 4.20(b) indicates that during the indentation, as the *f*-cone passes through the unstable region, the stretching to bending ratio increases by about one order of magnitude.

4.9 General conclusions

Foldable cones are the simplest example of a single-vertex origami whose facets can bend. In the present work, we developed a theoretical model which allows us to obtain the shape of *f*-cones for any deflection. The model shows that the bistable behavior of these structures is robust, regardless of the specific properties of the creases. In particular, for symmetrical all-mountain *f*-cones, we obtained the polar angle at the crease as a function of folding angle for both rest and snapped states.

However, in more realistic situations, the geometry and mechanical response of a *f*-cone are characterized by a competition between the elasticity of the facets (both their bending and stretching behavior) and the stiffness of the creases. For a better understanding of the snap-through dynamics, we have developed a continuous numerical model accounting for both the elasticity of the creases and facets. Applying this model to the particular case of two perpendicular mountain creases, we numerically studied the role of crease stiffness and verified the snap-thorough behavior through a series of indentation tests. We studied the indentation paths in the $\theta_c(\psi)$ diagram and showed that the structures do not follow the shape of a perfect cone throughout the indentation. For stiff creases, the path followed is that of an approximately constant folding angle while the two stable states lie closely to the theoretical prediction. When the crease is made soft, the indentation paths follow closely the branches given by the isometrical constraints. However, we noticed that while the shape of the rest

state is close to the theoretical prediction, the snapped one deviates further from it. From an energetic viewpoint, not only do stiffer creases lead to indentation paths with higher stretching energy barriers, but they also enforce the preferred angle more strongly. Hence, a *f*-cone made with stiffer creases requires more stretching when passing through $\theta_c \sim \pi/2$. On the other hand, while softer creases induce large deviations of the preferred angles, they allow for low stretching during the inversion, which explains why they follow the bounds set by the analytical calculations more closely.

The present study concludes that the mechanics of real origami structures is not totally characterized by the interplay between the bending of the facets and crease stiffness, but also by the competition between stretching of the facets and crease stiffness. The presence of stretching in real structures produces a deviation from the isometrical solutions, which has to be taken into account to describe the kinematical deployment of real origami structures. The "crease-stretching" ratio defined by μ_{cs}, allows to quantify this competition by indicating how stiff the creases are and how much deviation from the isometrical solution will be observed throughout snapping. This notion can be used to study other crease networks with nonrigid panels.

The present study validates our numerical model of temperature-induced hinge-like creases, which can be applied to origami structures with more complex extended networks. In this case, a temperature-induced folding of the network would work as a phase-field model where a smooth curve replaces the sharp piecewise energy landscape. The choice of a temperature field as a trigger for crease formation is arbitrary as any other diffusion field, such as concentration [69] or swelling [67] would play a similar role. The main sought mechanism is to build up a reference configuration with a noneuclidean reference metric due to the presence of an initially imprinted crease network [137]. This approach is advantageous since one does not need to track sharp boundaries where the deformation fields are discontinuous. It renders numerical implementation tractable and less time-consuming, two crucial aspects when implementing the mechanical behavior of complex origami or crumpled structures.

5 Perspectives

In the present chapter, I would like to present some topics related to the results of Chapter 4 that I hope to develop in the near future.

5.1 Loss of bistability of foldable cones

The theoretical and numerical results of Chapter 4 showed the robustness of the bistable nature of *f*-cones. Nevertheless, *f*-cones can loose bistability by prior removal of their vertices. If a large enough hole is cut out from the vertex, the snapped state loses its stability. The removal of the vertex introduces new degrees of freedom such that the generators are not forced to meet at a single point [131]. Instead, the generators form a striction curve in space that lies outside the material. The elastic theory of *f*-cones presented in Chapter 4 cannot account for such a loss of bistability; the cutoff radius r_0 is arbitrary, and it has no role in the equations describing the equilibrium states. The *f*-cone model assumes from the beginning a conical surface, implying that generators meet at a single point.

5.1.1 Elastic ribbon theory

When a circular hole is cut out from the vertex, the *f*-cone forms a creased annular ribbon. Consequently, a complete description of the system requires to consider the system as a developable elastic ribbon. Inextensible ribbon theory was first formulated by Sadowsky [101], who derived a one-dimensional energy functional describing infinitely narrow strips. Then, Wunderlich [138] generalized this theory for ribbons with any width, where the two-dimensional variational problem is reduced to a one-dimensional integral over the centerline of the ribbon. Later, Starostin and Van Der Heijden [116] derived the Euler-Lagrange equations of the corresponding variational problem and computed the equilibrium shape of a real elastic Möbius strip. Dias and Audoly [43] proposed a description that unifies the theory of elastic ribbons with the classical theory of thin rods, deriving the equilibrium equations of ribbons with any shape and geodesic curvature.

Here, we present the set of equations describing the equilibrium shapes derived from the theory of inextensible ribbons. A detailed derivation of the equations can be found in Appendix C. We consider an annular ribbon with an outer radius R and a

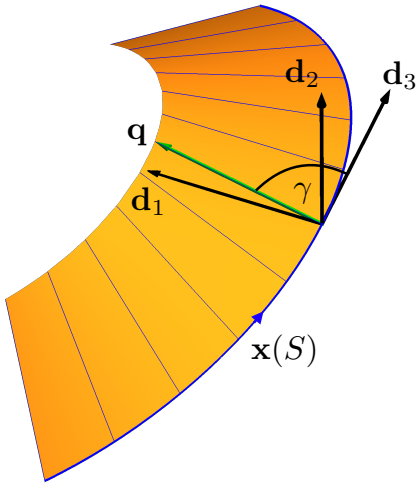

Figure 5.1 Geometry of a developable annular ribbon. The shape is parametrized by a family of straight generators that make an angle γ with $\mathbf{d}_3$. The outer edge is chosen as the directrix $\mathbf{x}(S)$ of the parametrization.

hole of radius r_0. The ribbon describes a developable surface. It is parametrized by a family of straight generators departing from a directrix $\mathbf{x}(S)$ (see Fig. 5.1). The directrix $\mathbf{x}(S)$ is chosen to be the outer edge of the annulus, where S is the arc-length of this curve (therefore, $|\mathbf{x}'(S)| = 1$). We define an orthonormal material frame $(\mathbf{d}_1(S), \mathbf{d}_2(S), \mathbf{d}_3(S))$ attached to the directrix such that $\mathbf{d}_3(S) = \mathbf{x}'(S)$, $\mathbf{d}_2(S)$ is normal to the surface, and $\mathbf{d}_1(S) = \mathbf{d}_2(S) \times \mathbf{d}_3(S)$ points towards the center of the annulus. These vectors satisfy the following equations

$$\mathbf{d}_k'(S) = \boldsymbol{\omega}(S) \times \mathbf{d}_k(S), \quad \text{for } k = 1, 2, 3, \tag{5.1}$$

where $\boldsymbol{\omega} = \omega_1 \mathbf{d}_2 + \omega_2 \mathbf{d}_2 + \omega_3 \mathbf{d}_3$ is the Darboux vector and ω_1, ω_2 and ω_3 are the normal curvature, geodesic curvature and geodesic torsion, respectively. The geodesic curvature of any curve drawn on a surface is preserved upon isometries, then, $\omega_2 = 1/R$ is constant during deformations.

Following the general equation of a ruled surface (2.61), the surface of the ribbon admits the following parametrization

$$\mathbf{y}(S, V) = \mathbf{x}(S) + v\mathbf{q}(\eta, S). \tag{5.2}$$

where,

$$\mathbf{q}(\eta, S) = \eta(S)\mathbf{d}_3(S) + \mathbf{d}_2(S), \tag{5.3}$$

defines the direction of the generatrices and v is the coordinate spanning the ribbon along a single generatrix. The function $\eta(S)$ is the cotangent of the angle γ between the generator and the positive tangent of $\mathbf{x}(S)$.

The coordinate v varies in a domain $0 \leq v \leq V(\eta, S)$, where $V(\eta, S)$ is called the *edge function* and it defines the limits of the ribbon in any deformed configuration as function of η and S. Therefore, this function is defined such that the vector $\mathbf{c}(S) = \mathbf{x}(S) + V(\eta, S)\mathbf{q}(\eta, S)$ coincides with the inner edge of the ribbon. For our annular ribbon, the edge function is given by (see Appendix C.1.1)

$$V(\eta) = R\left[\frac{1 - \sqrt{1 - (1+\eta^2)(1 - r_0^2/R^2)}}{1+\eta^2}\right]. \tag{5.4}$$

The equilibrium shape of the creased ribbon is found by minimizing a functional consisting of the bending energy of the panels, the mechanical energy stored at the creases and constraints enforcing developability. We first compute the bending energy of a section of the annular ribbon delimited by the region $S_a \leq S \leq S_b$. The mean curvature of a surface parametrized by Eq. (5.2) can be written as $H = (\omega_1(1+\eta^2))/(2(1 + v(\omega_2(1+\eta^2) - \eta')))$, and the differential area element reads $dA = (1 + v(\omega_2(1+\eta^2) - \eta'))ds\,dv$. Therefore the bending energy, can be written as follows

$$E_b = \frac{B}{2}\int_{S_a}^{S_b}\int_0^{V(\eta,s)} \frac{\omega_1^2(1+\eta^2)^2}{(1 + v(\omega_2(1+\eta^2) - \eta'))} dv\,ds \tag{5.5}$$

$$= \int_{S_a}^{S_b} e(\omega_1, \eta, \eta', S)\, ds, \tag{5.6}$$

where

$$e(\omega_1, \eta, \eta', S) = \frac{B}{2}\frac{\omega_1^2(1+\eta^2)^2}{(\omega_2(1+\eta^2) - \eta')} \ln\left(1 + V(\eta, S)(\omega_2(1+\eta^2) - \eta')\right), \tag{5.7}$$

is the bending energy density and B is the bending modulus. In the limit $R - r_0 \to 0$, energy (5.7) one recovers the Sadowsky's energy for a narrow ribbon [101]:

$$E_{\text{Sad}} = \frac{B(R - r_0)}{2}\int \omega_1^2 \left(1+\eta^2\right)^2 dS. \tag{5.8}$$

We introduce three kinematical constraints enforcing developability of the ribbon. First, we fix the arc-length S of the generatrix so that it does not change its local length during isometrical deformations. We can enforce this condition by imposing $\mathbf{d}_{3i} = \mathbf{x}_i'$. Second, we include the local constraint $\omega_2 = 1/R$ in the augmented energy. A third constraint expresses the developability of a ruled surface spanned by the generators. It can be shown in the literature that the direction of the generators with the normal curvature and the torsion of a developable surface are related by $\eta\omega_1 - \omega_3 = 0$ [114, 43].

Therefore, the final shape of the annular ribbon with n creases can be found by the minimization of the following functional

$$\begin{aligned}\mathcal{F}_n \;=\; \sum_{i=1}^{n}\Bigg\{\int_{S_i}^{S_{i+1}}\Big[-e_i(\omega_1,\eta,\eta') + \lambda_{g,i}(\omega_2 - R) + \lambda_{d,i}(\eta_i\omega_{1i} - \omega_{3i}) \\ +\mathbf{F}_i\cdot\left(\mathbf{d}_{3i} - \mathbf{x}_i'\right)\Big]\,dS\Bigg\} - \sum_{i=1}^{n} g_i. \end{aligned} \tag{5.9}$$

Here, the subscripts specify the panel corresponding to the domain of a function and follow the convention introduced in Section 4.5 for f-cones.

S_i stands for the value of the arc-length at the ith crease, $\lambda_{g,i}$, $\lambda_{d,i}$ and $\mathbf{F}_i$ are $3n$ local Lagrange multipliers enforcing developability. Similarly to the model of f-cone, g_i stands for the mechanical energy of the ith crease given by

$$g_i = (R - r_0)\left[\sigma_i\,\mathbf{d}_{3i}^{-}\cdot\mathbf{d}_{3i}^{+} + \tau_i\,(\mathbf{d}_{3i}^{-}\times\mathbf{d}_{3i}^{+})\cdot\mathbf{d}_{1i}^{+}\right]\Big|_{S_i}, \tag{5.10}$$

where we have used the convention $b_i^{-} \equiv b_{i-1}(S_i)$ and $b_i^{+} \equiv b_i(S_i)$. The parameters σ_i and τ_i are material constants. As done previously, we can define constants $k_i > 0$ and $\psi_i^0 \in [0, 2\pi]$, such that $\sigma_i = k_i \cos\,\psi_i^0$ and $\tau_i = k_i \sin\,\psi_i^0$, where k_i is associated with crease stiffness and ψ^0 with the rest folding angle.

5.1.2 Equilibrium equations and boundary conditions

Variation of the functional (5.9) leads to the following set of equations

$$\mathbf{F}_i' = \mathbf{0}, \tag{5.11a}$$
$$\mathbf{M}_i' + \mathbf{d}_{3i}\times\mathbf{F}_i = \mathbf{0}, \tag{5.11b}$$
$$\partial_{\omega_1} e_i - M_{1i} - \eta_i M_{3i} = 0, \tag{5.11c}$$
$$\partial_{\eta} e_i - (\partial_{\eta'} e_i)' - \omega_{1i} M_{3i} = 0, \tag{5.11d}$$

where $\boldsymbol{M} \equiv M_1\mathbf{d}_1 + M_2\mathbf{d}_2 + M_3\mathbf{d}_3 = (\partial_\eta e_i - \eta\lambda_d)\mathbf{d}_1 + \lambda_g\mathbf{d}_2 + \lambda_d\mathbf{d}_3$ can be interpreted as the moment along the directrix. Additionally, one obtains the following boundary conditions to apply at each crease:

$$\mathbf{F}_i^{+} - \mathbf{F}_i^{-} = \mathbf{0}, \tag{5.12a}$$
$$\left(\mathbf{M}_i^{+} - \mathbf{M}_i^{-}\right)\times\mathbf{d}_{1i}^{+} = \mathbf{0}, \tag{5.12b}$$
$$M_{1i}^{-} = M_{1i}^{+} = (R - r_0)k_i\sin\left(\psi_i - \psi_i^0\right). \tag{5.12c}$$

Similarly to f-cones, Eq. (5.12a) reflects the continuity of the force transmitted along the directrix across the creases. Then, the whole structure is characterized by a

single constant vector **F**. Eq. (5.12b) indicates the continuity of the projection of the moment in the plane perpendicular to the crease. According to Eq. (5.12c), the crease mechanics imposes a moment along the crease line.

In general, solving the ribbons equations is a difficult task since, even numerically. Note that the variable $\eta(S)$ becomes undefined when $\omega_1 = 0$, making the system stiff. Therefore, nonstandard methods have to be employed. Furthermore, if one wishes to perform a numerical continuation study, the initial solution cannot be the flat solution since it is singular degenerated (generators are not well defined if $\omega_1 = 0$). Because of the complexity of ribbons equations, we may consider an alternative approach. By performing a finite element study, similar to that used in Chapter 4, one can test the stability of the snapped state of the *f*-cone by looking at the Moment vs θ_c plots during snapping. Note that in Fig. 4.20, the curve touches three times the curve $M = 0$. If such a curve has only one zero (the rest state), it means that there is no metastable state. In this way, one can find the critical radius of the hole such that the snapped state loses stability.

5.1.3 Phase field like model of creases for origami networks

The numerical model of temperature-driven creases introduced in Chapter 4 is a suitable tool to study complex crease networks. Its implementation is straightforward since one only needs to define the crease network without the need to program the mechanical actuation of each crease individually. It is a useful tool to study the folding process of origami structures when increasing the temperature gradient, and their mechanical response for fixed temperature. Also, one can study the elastic response of nonrigid origami in terms of ratio μ_{cs} and the normalized crease stiffness $\bar{k}$ introduced in Chapter 4. These quantities account for the panel stretching vs crease stiffness, and the panel bending vs crease stiffness interplays, respectively. A similar idea was recently employed to characterize the decay of local actuation in nonrigid Miura-ori tubes *et al.* [52]. Future work is needed to calibrate the model of creases to predict with precision their mechanical properties (stiffness and rest angle) as a function of the temperature gradient ΔT, the crease width b, the crease thickness h_c and Young's modulus E_c.

5.2 The complexity of crumpled paper

Crumpling is notably inefficient: a typical crumpled paper ball is about 75% air [89]. This means that a ball of crumpled paper reacts with a large force against compression. To understand the mechanisms behind this behavior, crumpling has been widely studied theoretically [10, 82], numerically [128] and experimentally [97, 13, 7]. One

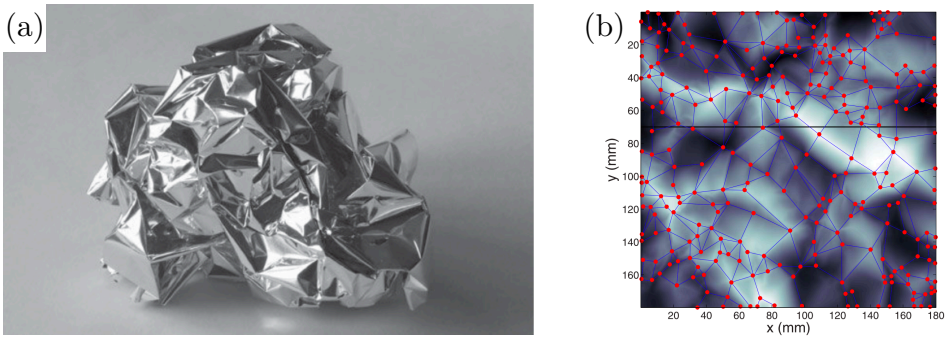

Figure 5.2 (a) A crumpled aluminum foil revealing a network of polygonal ridges. Ridges meet at vertices which are tips of conical defects (adapted from [9]). (b) Ridge network reconstruction from a real paper sheet (adapted from [7]).

possible project for the future is to implement the phase-field like model in random origami networks that mimic the properties of crumpled surfaces.

Crumpling occurs when an elastic sheet is subjected to significant compression, yielding stress focusing and energy localization. The energy localizes in point defects and ridges that connect them forming a surface consisting mostly of straight polygonal pieces (see Fig. 5.2(a)). As we have discussed in Chapter 2, these vertices correspond to d-cones since the sheet is subjected to constraints of developability. The ridges acquire a characteristic shape usually referred to as stretching ridges, which was first characterized by Lobkovsky *et al.* [83] based on scaling laws and then it was analyzed based on a boundary layer equation [81]. Since crumpling preserves the length on the surface, a crumpled configuration can be always mapped isometrically to the reference configuration. Upon unfolding a crumpled paper ball, the ridge network is revealed. This network conforms what is called in graph theory, a *random planar graph*, a network consisting of set of randomly placed vertices on the sheet and random ridges that connect them without crossing other ridges. Fig. 5.2(b) shows the ridge network reconstruction of a crumpled paper sheet by 3D scanning of the crumpled surface. From an experimental point of view, ridge networks observed in crumpled paper have been characterized by distributions of ridge length, facets area and vertex degree, vertex degree correlations and surface roughness, among other properties [97, 13, 7].

Our future goal is to generate a random planar graph that mimics the statistics of crumpled paper. There are some aspects to consider concerning the foldability of the origami network. Fig. 5.3 shows the degree distribution $p(k)$ as a function of the node degree k extracted from real crumpled sheets. Our random planar graph should display a similar degree distribution. Note that, in a rigid origami network, one must have $k \geq 4$ to guaranteeing local foldability around the vertices. Then, one may study the possible deformed configurations of the network. For instance, a deformed configuration of the structure can be characterized by the mountain–valley (M-V)

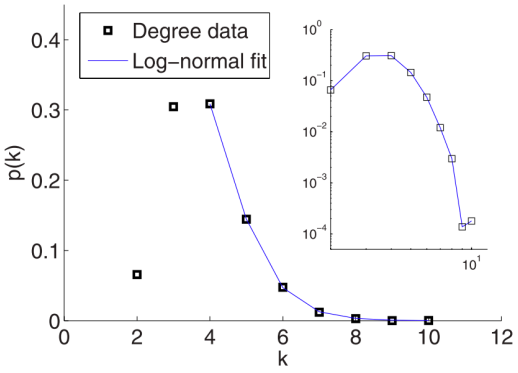

Figure 5.3 Plot of the degree distribution $p(k)$ as a function of node degree k obtained from real ridge networks. The inset shows the same data plotted on log-log scale. Note that $p(k)$ has a peak at $k = 4$. (figure adapted from [7]).

assignment of the network, that is, which creases are mountains and which ones are valleys. Also, one can characterize a deformed state of the network by its vertex sign pattern, that is, by whether a vertex "pops-up" or "pop-down". Recently, it has been shown that a randomly triangulated origami mesh can exhibit multiple solution "branches" departing from the unfolded state [28]. The number of branches depends on the number of vertices of the network. These branches are distinguished by the sign of the vertices rather than M-V assignments, since one can find configurations with equal M-V assignment but different sign vertex patterns. Besides, one may study networks with nonrigid facets through finite element analysis employing our numerical model of temperature-driven creases. In this case, one has to prescribe the M-V assignment by fixing the sign of the thermal expansion coefficient of each crease. The space of deformed configurations may be explored by varying the M-V prescription.

Appendix A

A

A.1 Corrections to the linear model of the developable cone

A.1.1 Inextensibility condition

In cylindrical coordinates, a general conical surface with the tip at the origin of the coordinate system is described by the equation $z = \rho g(\varphi)$, where ρ and φ are the polar coordinates in the horizontal plane and z is the vertical coordinate. The condition for any cylindrical surface to be a developable surface is equivalent to require a circle of radius r drawn over the surface with the center at the tip have perimeter $2\pi r$ [9]. The distance from the tip to a point on that curve is $r = \rho\sqrt{1+g^2(\varphi)}$, therefore

$$z(\varphi) = \rho(\varphi)g(\varphi) = \frac{rg(\varphi)}{\sqrt{1+g^2(\varphi)}}, \tag{A.1}$$

corresponds to the parametric equation describing the deformed circles with constant r and parameter φ. In order to express the developability condition, we compute the square of the length element along one of this circles (for r constant) is

$$dl^2 = dz^2 + d\rho^2 + \rho^2 d\varphi^2, \tag{A.2}$$

where

$$dz = \frac{r\dot{g}}{(1+g^2)^{3/2}}d\varphi, \quad d\rho = \frac{rg\dot{g}}{(1+g^2)^{3/2}}d\varphi, \quad \rho d\varphi = \frac{r}{\sqrt{1+g^2}}d\varphi, \tag{A.3}$$

Then, one obtains that

$$dl = rd\varphi\left(\frac{\sqrt{1+g^2(\varphi)+\dot{g}^2(\varphi)}}{1+g^2(\varphi)}\right). \tag{A.4}$$

Integrating along the azimuthal direction, the condition that the perimeter of this circle is $2\pi r$ reads

$$\int_{-\pi}^{\pi} d\varphi\left(\frac{\sqrt{1+g^2(\varphi)+\dot{g}^2(\varphi)}}{1+g^2(\varphi)} - 1\right) = 0. \tag{A.5}$$

At the first non-trivial order, the above equation reduces to

$$\int_{-\pi}^{\pi} d\varphi \left(g^2 - \dot{g}^2\right) \simeq 0. \tag{A.6}$$

which corresponds to the inextensibility condition of developable cones in the case of small deflections.

A.1.2 Bending energy

The bending energy of a surface is given by

$$U_B = \frac{E_b}{2} \int_A K_M^2 dA \tag{A.7}$$

where K_M is the mean curvature. For a surface in 3D space the mean curvature is given by

$$K_M = -\frac{1}{2} \nabla \cdot \mathbf{n}. \tag{A.8}$$

where $\mathbf{n}$ is the normal to the surface. The normal to the surface of a two-dimensional surface embedded in 3D space can be computed as

$$\mathbf{n} = \left(\frac{(\nabla z, -1)}{\sqrt{1 + |\nabla z|^2}} \right). \tag{A.9}$$

For a conical surface parametrized by $z(\rho, \varphi) = \rho g(\varphi)$, the normal reads

$$\mathbf{n} = \left(\frac{g\mathbf{e}_\rho + \dot{g}\mathbf{e}_\varphi - \mathbf{z}}{\sqrt{1 + g^2 + \dot{g}^2}} \right). \tag{A.10}$$

After some algebra, one finds

$$K_M = \frac{1}{2\rho} \left(\frac{(g + \ddot{g})(1 + g^2)}{(1 + g^2 + \dot{g}^2)^{3/2}} \right). \tag{A.11}$$

Note that at the first non-trivial order, one has

$$K_M \simeq \frac{1}{2\rho} (g + \ddot{g}), \tag{A.12}$$

which is the value of the curvature used in the linear model. The differential element of area dA must be taken respect to the cone surface, therefore,

$$dA = dr\, dl = r \left(\frac{\sqrt{1 + g^2 + \dot{g}^2}}{1 + g^2} \right) dr\, d\varphi. \tag{A.13}$$

Inserting the element area in (A.7) and integrating along $r_0 \leq r \leq R$, we obtain

$$U_b = \frac{B}{8} \ln\left(\frac{R}{r_0}\right) \int_{-\pi}^{\pi} \frac{(g+\ddot{g})^2(1+g^2)^2}{(1+g^2+\dot{g}^2)^{5/2}}. \tag{A.14}$$

Periodicity around the azimuthal direction implies:

$$\int_{-\pi}^{\pi} d\varphi \left(\frac{\sqrt{1+g^2(\varphi)+\dot{g}^2(\varphi)}}{1+g^2(\varphi)} - 1 \right) = 0. \tag{A.15}$$

A.1.3 Lagrangian

The Lagrangian of the system reads [27]

$$\mathcal{L}[g] = \frac{B}{8} \ln\left(\frac{R}{r_0}\right) \int_{-\pi}^{\pi} d\varphi \frac{(g+\ddot{g})^2(1+g^2)^2}{(1+g^2+\dot{g}^2)^{5/2}} + \bar{\lambda} \int_{-\pi}^{\pi} d\varphi \left(\frac{\sqrt{1+g^2+\dot{g}^2}}{1+g^2} - 1 \right). \tag{A.16}$$

The above functional yields the following differential equation for $g(\varphi)$

$$\begin{aligned}
&g^9 + g^8\left(2g^{(4)} + 5\ddot{g}\right) + 2g^{(4)}\left(\dot{g}^2+1\right)^2 + 5\left(6\dot{g}^2-1\right)\ddot{g}^3 \\
&- g^7\left(3\ddot{g}^2 - 2\dot{g}^2 + 4g^{(3)}\dot{g} + \bar{\lambda} - 5\right) \\
&- 3g^5\left(3\ddot{g}^2 - 2\dot{g}^4 - 4g^{(3)}\dot{g}^3 + 4g^{(3)}\dot{g} + \dot{g}^2\left(-18\ddot{g}^2 + \bar{\lambda} - 4\right) + \bar{\lambda} - 3\right) \\
&+ g^3\left(-9\ddot{g}^2 + 40\dot{g}^6 + 16g^{(3)}\dot{g}^5 + 24g^{(3)}\dot{g}^3 - 12g^{(3)}\dot{g} - 3\dot{g}^4\left(16\ddot{g}^2 + \bar{\lambda} - 12\right)\right. \\
&\left.-6\dot{g}^2\left(-18\ddot{g}^2 + \bar{\lambda} - 3\right) - 3\bar{\lambda} + 7\right) \\
&- g\left(3\ddot{g}^2 + (\bar{\lambda}-24)\dot{g}^6 - 16g^{(3)}\dot{g}^5 - 12g^{(3)}\dot{g}^3 + 4g^{(3)}\dot{g} + 3\dot{g}^4\left(16\ddot{g}^2 + \bar{\lambda} - 10\right)\right. \\
&\left.+\dot{g}^2\left(-54\ddot{g}^2 + 3\bar{\lambda} - 8\right) + \bar{\lambda} - 2\right) \\
&- \left(\dot{g}^2+1\right)\ddot{g}\left((\bar{\lambda}-8)\dot{g}^4 + 2(\bar{\lambda}+4)\dot{g}^2 + 20g^{(3)}\dot{g} + \bar{\lambda} - 4\right) \\
&+ g^6\left(-5\ddot{g}^3 + 4g^{(4)}\left(\dot{g}^2+2\right) - \ddot{g}\left(-14\dot{g}^2 + 20g^{(3)}\dot{g} + \bar{\lambda} - 19\right)\right) \\
&+ g^4\left(2g^{(4)}\left(\dot{g}^4 + 6\dot{g}^2 + 6\right) + 15\left(2\dot{g}^2-1\right)\ddot{g}^3\right. \\
&\left.-\ddot{g}\left(3(\bar{\lambda}-8)\dot{g}^2 + 72\dot{g}^4 + 20g^{(3)}\dot{g}^3 + 60g^{(3)}\dot{g} + 3(\bar{\lambda}-9)\right)\right) \\
&+ g^2\left(4g^{(4)}\left(\dot{g}^4 + 3\dot{g}^2 + 2\right) + 15\left(4\dot{g}^2-1\right)\ddot{g}^3\right. \\
&\left.-\ddot{g}\left(3(\bar{\lambda}+24)\dot{g}^4 + 6(\bar{\lambda}-1)\dot{g}^2 - 24\dot{g}^6 + 40g^{(3)}\dot{g}^3 + 60g^{(3)}\dot{g} + 3\bar{\lambda} - 17\right)\right) = 0.
\end{aligned}$$

The above equation must be solved together with the inextensibility condition (A.15). This highly nonlinear equation provides corrections to the linear model, however, it does not bring new insights about the bistability, neither an adequate relation.

A.2 Determination of the folding angle

The folding angle ψ_i is related to the frame by (see Fig. 4.9)

$$\mathbf{t}_i^+ \cdot \mathbf{t}_i^- = \cos(\pi - \psi_i). \tag{A.17}$$

In terms of the Euler-like angles, one may write

$$\mathbf{t} = \theta' \cos\theta\, \mathbf{e}_\rho + \varphi' \sin\theta\, \mathbf{e}_\varphi - \theta' \sin\theta\, \mathbf{z}, \tag{A.18}$$

where the prime denotes derivative with respect to s. Therefore, recalling that $\theta_i^+ = \theta_i^-$, one obtains

$$\mathbf{t}_i^+ \cdot \mathbf{t}_i^- = \theta_i'^+ \theta_i'^- + \sin^2(\theta_i)\varphi_i'^+ \varphi_i'^-. \tag{A.19}$$

The boundary conditions (4.64) and (4.66), that are valid in all f-cones, imply that

$$\theta_i'^+ = -\theta_i'^-, \quad \varphi_i'^+ = \varphi_i'^-. \tag{A.20}$$

Then, one obtains the general formula

$$\cos(\pi - \psi_i) = -\theta_i'^2 + \sin^2\theta_i \varphi_i'^2. \tag{A.21}$$

We now compute the relation between the folding angle ψ and the constant p, introduced in the linear model for the case of all-valley f-cones. Eq. (A.21) can be written as follows

$$\cos(\pi - \psi) = \left(\frac{d\varphi}{ds}\right)^2 \left[-\left(\frac{d\theta}{d\varphi}\right)^2 + \sin^2\theta\right]\Bigg|_{\varphi=-\alpha/2}. \tag{A.22}$$

For all-valley f-cones, Eqs. (4.17) give the relation $\theta(\varphi)$, through the geometrical relation

$$g(\varphi) = \cos\theta(\varphi). \tag{A.23}$$

On the other hand, the derivative $d\varphi/ds$ can be obtained using Eq. (A.4), with $dl = rds$. Then, one obtains

$$\cos(\pi - \psi_i) = \frac{(1+g^2)^2}{1+g^2+\dot{g}^2}\left[-\frac{\dot{g}^2}{1-g^2} + 1 - g^2\right]\Bigg|_{\varphi=-\alpha/2}. \tag{A.24}$$

In the small deflections limit, $\psi \simeq \pi$, and thus $\cos(\pi - \psi) \simeq 1 - (\pi - \psi)^2/2$, while the right-hand side of Eq. (A.24) approximates to $1 - 2\dot{g}^2(-\alpha/2) = 1 - 2p^2$. Hence, for small deflections one has

$$p \simeq \frac{\pi - \psi}{2}. \tag{A.25}$$

A.3 Frame virtual rotations and Euler-like angles

It is useful to compute the variation of the functional (4.46) in terms of virtual frame rotations. In terms of the Euler-like angles $\{\theta(s), \varphi(s), \phi(s)\}$, one can derive the following relations

$$\begin{aligned} \delta\mathbf{u} &= -\delta\theta\,\mathbf{n}_\varphi + \sin\theta\,\delta\varphi\,\mathbf{e}_\varphi, && \text{(A.26)} \\ \delta\mathbf{t} &= (\delta\phi + \cos\theta\,\delta\varphi)\mathbf{n} + (\sin\phi\,\delta\theta - \sin\theta\cos\phi\,\delta\varphi)\mathbf{u}. && \text{(A.27)} \end{aligned}$$

Notice that $\mathbf{u}\cdot\delta\mathbf{u} = 0$ and $\mathbf{t}\cdot\delta\mathbf{t} = 0$ as expected. The following relations are useful

$$\begin{aligned} \mathbf{n}\cdot\delta\mathbf{u} &= -\cos\phi\,\delta\theta - \sin\theta\sin\phi\,\delta\varphi, \\ \mathbf{t}\cdot\delta\mathbf{u} &= -\sin\phi\,\delta\theta + \sin\theta\cos\phi\,\delta\varphi, \\ \mathbf{n}\cdot\delta\mathbf{t} &= \delta\phi + \cos\theta\,\delta\varphi. && \text{(A.28)} \end{aligned}$$

Now, we put the subscripts back and write some useful relations. First, notice that in the plane perpendicular to a crease, the frame $\{\mathbf{t}, \mathbf{n}\}$ rotates by an angle $\psi_i - \pi$, which can be expressed as follows

$$\begin{pmatrix} \mathbf{t}_i^+ \\ \mathbf{n}_i^+ \end{pmatrix} = \begin{pmatrix} -\cos\psi_i & \sin\psi_i \\ -\sin\psi_i & -\cos\psi_i \end{pmatrix} \begin{pmatrix} \mathbf{t}_i^- \\ \mathbf{n}_i^- \end{pmatrix}. \qquad \text{(A.29)}$$

Using the relations given by Eq. (A.28) and Eq. (A.29) one obtains the following relations

$$\begin{aligned} \mathbf{n}_i^+\cdot\delta\mathbf{t}_i^+ &= \delta\phi_i^+ + \cos\theta_i^+\,\delta\varphi_i^+, \\ \mathbf{n}_i^-\cdot\delta\mathbf{t}_i^- &= \delta\phi_i^- + \cos\theta_i^+\,\delta\varphi_i^+, \\ \mathbf{t}_i^+\cdot\delta\mathbf{t}_i^- &= -\sin\psi_i\left(\delta\phi_i^- + \cos\theta_i^+\,\delta\varphi_i^+\right), \\ \mathbf{t}_i^-\cdot\delta\mathbf{t}_i^+ &= \sin\psi_i\left(\delta\phi_i^+ + \cos\theta_i^+\,\delta\varphi_i^+\right), \\ \mathbf{n}_i^+\cdot\delta\mathbf{t}_i^- &= -\cos\psi_i\left(\delta\phi_i^- + \cos\theta_i^+\,\delta\varphi_i^+\right), \\ \mathbf{n}_i^-\cdot\delta\mathbf{t}_i^+ &= -\cos\psi_i\left(\delta\phi_i^+ + \cos\theta_i^+\,\delta\varphi_i^+\right). && \text{(A.30)} \end{aligned}$$

where $\phi_i^\pm$ is the angle between $\mathbf{t}_i^\pm$ and $\mathbf{e}_\theta$. Recalling that $\delta\psi_i = \delta\phi_i^+ - \delta\phi_i^-$, the two last equations show that the condition of infinitely stiff crease $\delta\psi_i = 0$ is equivalent to imposing $\mathbf{n}_i^+\cdot\delta\mathbf{t}_i^- = \mathbf{n}_i^-\cdot\delta\mathbf{t}_i^+$

Appendix B

B

B.1 Solution for alternate crease f-cone

Here, we show the solutions for an alternate crease f-cone. For simplicity, we focus on the four alternate creases f-cone consisting of two parallel mountain creases, and two perpendicular valley creases. The solutions are then determined by two parameters: the folding angle ψ_m of the mountains and the folding angle ψ_v of the valleys. Note that, because of the symmetries of the system, the four panels are identical except for rotations and reflexions. Therefore, we solve Eq. (4.59) in a single panel where $-\alpha/2 \leq s \leq \alpha/2$. Taking into account the symmetries of the problem, we seek for solutions of the form:

$$\kappa(s) = \begin{cases} \kappa_0 \,\mathrm{cn}\left(\dfrac{\kappa_0}{2\sqrt{m}} s - \epsilon K(m) \middle| m\right), & \text{for rest states,} \\ \kappa_0 \,\mathrm{dn}\left(\dfrac{\kappa_0}{2} s - \epsilon K(m) \middle| m\right), & \text{for snapped states.} \end{cases} \tag{B.1}$$

Here, ϵ is a numerical factor and $K(m)$ is the complete elliptic integral with modulus m [2]. Note that the function $\mathrm{cn}(\cdot|m)$ (respectively, $\mathrm{dn}(\cdot|m)$) has a period $4K(m)$ (respectively, $2K(m)$) [2]. It is sufficient to consider only the range $0 \leq \epsilon \leq 1$, since configurations with other values of ϵ can always be obtained by performing the transformation $s \to -s$ and/or $\kappa \to -\kappa$ and the properties $\mathrm{cn}(x - 2K(m)|m) = -\mathrm{cn}(x|m)$ and $\mathrm{dn}(x - 2K(m)|m) = \mathrm{dn}(x|m)$. Those operations correspond to flipping the structure upside-down and rotating it around the z-axis by an angle α.

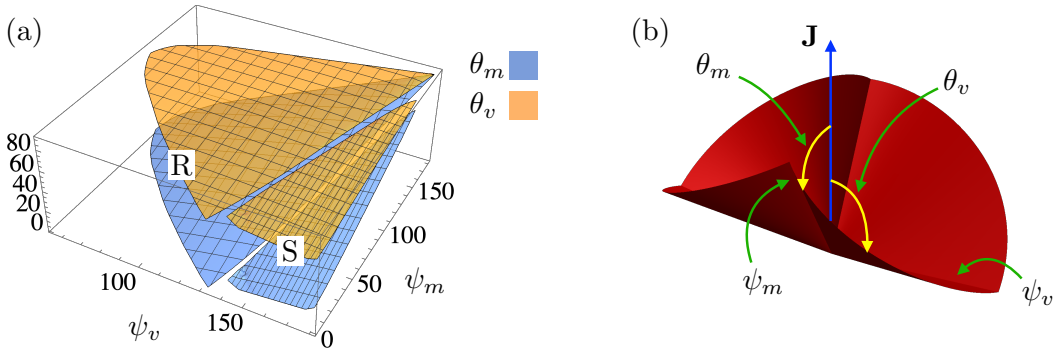

Figure B.1 (a) Family of solutions found numerically represented by the polar angles $\{\theta_m, \theta_v\}$ as function of the two folding angles $\{\psi_m, \psi_v\}$. The capital R and S denotes rest and snapped states, respectively. (b) Schematics showing the angles $\{\psi_m, \psi_v, \theta_m, \theta_v\}$.

For each rest and snapped state, we proceed with a numerical exploration for values of ϵ and m such that the closure condition (4.45) is satisfied. Once we cover the whole range $\epsilon, m \in [0, 1]$, we proceed numerically to find the mapping between the pair $\{\epsilon, m\}$ and the two folding angles ψ_m, ψ_v. The solutions are represented by the polar angles θ_m and θ_v at the mountains and valleys, respectively. Fig. B.1 shows the family of solutions found numerically as function of the two folding angles $\{\psi_m, \psi_v\}$. The solutions form four "tongues" emerging from the point $\{\psi_m = 180°, \psi_v = 180°, \theta_m = \theta_v = 90°\}$ corresponding to the flat solution. These four tongues represent the polar angles θ_m and θ_v for rest states (R) and snapped (S) states. Two pairs of tongues seem to touch at a given curve in the plane $\{\psi_m, \psi_v\}$ that is not completely captured because of numerical resolution.

Appendix C

C

C.1 Theory of elastic ribbons

C.1.1 Edge function for an annular ribbon

To compute the edge function $V(\eta, S)$ given by Eq. (5.4), we map the generatrices of a deformed configuration of the ribbon into the flat configuration. This is always possible since the ribbon is subjected to isometrical deformations only. This mapping can be expressed as

$$\Phi : \ \mathbf{y}(S, v) = \mathbf{x}(S) + v\mathbf{q}(\eta, S) \ \rightarrow \ \mathbf{Y}(S, v) = \mathbf{X}(S) + v\mathbf{Q}(\eta, S), \tag{C.1}$$

where $\mathbf{X}(S)$ is the directrix corresponding to the outer edge and the vector $\mathbf{Q}$ defines the direction of the generatrices as if drawn on the flat configuration (see Fig. C.1). This last vector can be written as $\mathbf{Q}(\eta, S) = \eta(S)\mathbf{D}_3(S) + \mathbf{D}_1(S)$, where the trihedron $\{\mathbf{D}_1(S), \mathbf{D}_2(S), \mathbf{D}_3(S)\}$ is the orthonormal frame attached to the directrix in the flat configuration. The frame is defined in such a way that $\mathbf{D}_3(S)$ is tangent to the outer edge of the annulus and $\mathbf{D}_1$ points towards the inner edge. In the reference configuration, the center of the annulus is given by $\mathbf{C} = \mathbf{X}(S) + R\mathbf{D}_1$. Thus, the edge function $V(\eta, S)$ can be found by imposing the following equation $(\mathbf{C} - \mathbf{Y}(S, V))^2 = r_0^2$. Using Eq. (C.1) and the definition of $\mathbf{Q}$, the latter equation can be written as

$$(1 + \eta^2)V^2 - 2VR + R^2 - r_0^2 = 0. \tag{C.2}$$

Solving for $V(\eta)$, one finds

$$V(\eta) = R\left[\frac{1 - \sqrt{1 - (1 + \eta^2)(1 - r_0^2/R^2)}}{1 + \eta^2}\right]. \tag{C.3}$$

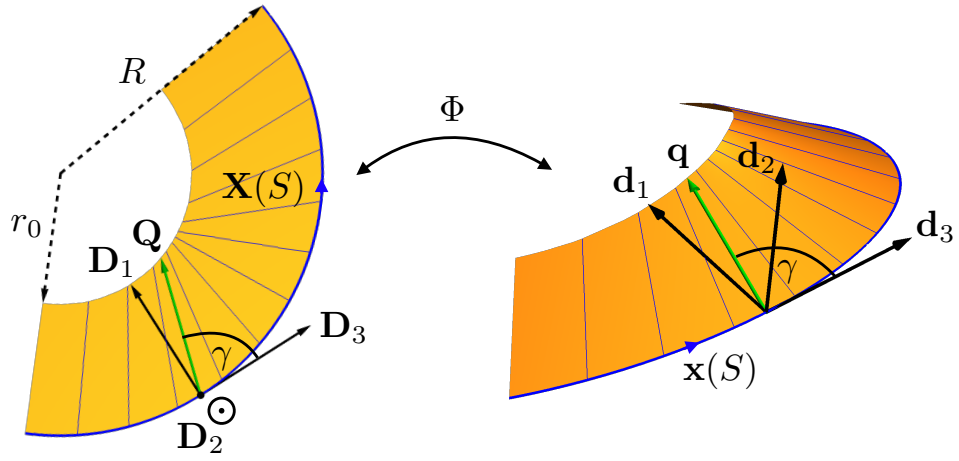

Figure C.1 Schematics of the mapping Φ between the flat configuration and the deformed configuration.

C.1.2 Derivation of equilibrium equations

The variation of functional (5.9) reads

$$\begin{aligned}
&\delta\mathcal{F}_n = \\
&\sum_{i=1}^{n}\Bigg\{\int_{S_i}^{S_{i+1}} dS\left[(\partial_{\eta'}e_i)' - \partial_\eta e_i - \lambda_d^i\omega_{1i}\right]\delta\eta_i - \left[(\partial_{\eta'}e_i)\delta\eta_i\right]_{S_i}^{S_{i+1}} \\
&+\int_{S_i}^{S_{i+1}} dS\left[\left(\mathbf{M}_i' + \mathbf{d}_{3i}^+\times\mathbf{R}_i\right)\cdot\delta\boldsymbol{\phi}_i + \mathbf{R}_i'\cdot\delta\mathbf{x}_i\right] - \left[\mathbf{M}_i\cdot\delta\boldsymbol{\phi}_i\right]_{S_i}^{S_{i+1}} - \left[\mathbf{R}_i\cdot\delta\mathbf{x}_i\right]_{S_i}^{S_{i+1}} \\
&-(R-r_0)\left[\sigma_i\left(\mathbf{d}_{3i}^-\cdot\delta\mathbf{d}_{3i}^+ + \mathbf{d}_{3i}^+\cdot\delta\mathbf{d}_{3i}^-\right) + \tau_i\left(\mathbf{d}_{2i}^+\cdot\delta\mathbf{d}_{3i}^- - \mathbf{d}_{2i}^-\cdot\delta\mathbf{d}_{3i}^+\right)\right]\Big|_{S_i}\Bigg\},
\end{aligned} \tag{C.4}$$

where

$$\mathbf{M} = M_1\mathbf{d}_1 + M_2\mathbf{d}_2 + M_3\mathbf{d}_3 = (\partial_\eta e_i - \eta\lambda_d)\mathbf{d}_1 + \lambda_g\mathbf{d}_2 + \lambda_d\mathbf{d}_3, \tag{C.5}$$

The quantity $\delta\mathbf{x}_i$ stands for virtual displacements of the directrix, while $\delta\boldsymbol{\phi} = \delta\phi_1\mathbf{d}_1 + \delta\phi_2\mathbf{d}_2 + \delta\phi_3\mathbf{d}_3$ represents virtual rotations of the material frame such that $\delta\mathbf{d}_k = \delta\boldsymbol{\phi}\times\mathbf{d}_k$.

Assuming that the virtual changes $\delta\eta_i$, $\delta\mathbf{x}_i$ and $\delta\boldsymbol{\phi}$ are arbitrary, the terms inside integrals in Eq. (C.4) and the definition Eq. (C.5) lead to Eqs. (5.11). The rest of the terms correspond to boundary terms that must vanish. The virtual changes $\delta\eta_i(S_i) = \delta\eta_i(S_{i+1})$ vanish, since the generatrices at the creases coincide with the crease direction, that is, $\eta(S_i) = 0$. Recalling the periodic convention, the rest of the boundary terms can be rewritten as follows

$$\begin{aligned}
&\sum_{i=1}^{n}\Big\{\left[\mathbf{M}_i\cdot\delta\boldsymbol{\phi}_i - \mathbf{M}_{i-1}\cdot\delta\boldsymbol{\phi}_{i-1} + \mathbf{R}_i\cdot\delta\mathbf{x}_i - \mathbf{R}_{i-1}\cdot\delta\mathbf{x}_{i-1}\right]\Big|_{s_i} \\
&+(R-r_0)\left[\sigma_i\left(\mathbf{d}_{3i}^-\cdot\delta\mathbf{d}_{3i}^+ + \mathbf{d}_{3i}^+\cdot\delta\mathbf{d}_{3i}^-\right) + \tau_i\left(\mathbf{d}_{2i}^+\cdot\delta\mathbf{d}_{3i}^- - \mathbf{d}_{2i}^-\cdot\delta\mathbf{d}_{3i}^+\right)\right]\Big\} = 0.
\end{aligned} \tag{C.6}$$

Continuity of the directrix across the fold implies that $\delta\mathbf{x}_i^+ = \delta\mathbf{x}_i^-$, so then, one obtains that $\mathbf{R}_i^+ = \mathbf{R}_i^-$. To obtain the other boundary conditions, we relate $\delta\boldsymbol{\phi}_i$ and $\delta\boldsymbol{\phi}_{i-1}$ with $\delta\mathbf{d}_{3i}^+$ and $\delta\mathbf{d}_{3i}^-$. Since $\delta\mathbf{d}_i = \delta\boldsymbol{\phi} \times \mathbf{d}_i$, it follows that $\delta\phi_1 = -\mathbf{d}_2 \cdot \delta\mathbf{d}_3$, $\delta\phi_2 = \mathbf{d}_1 \cdot \delta\mathbf{d}_3$ and $\delta\phi_3 = \mathbf{d}_2 \cdot \delta\mathbf{d}_1$. Using $\sigma_i = k_i \cos(\psi_i^0)$ and $\tau_i = k_i \sin(\psi_i^0)$, we obtain

$$\sum_{i=1}^{n} \left[\left(-M_{1i}^+ + w\kappa^i \sin(\psi_i - \psi_i^0) \right) \mathbf{d}_{2i}^+ \cdot \delta\mathbf{d}_{3i}^+ + \left(M_{1i}^- - w\kappa^i \sin(\psi_i - \psi_i^0) \right) \mathbf{d}_{2i}^- \cdot \delta\mathbf{d}_{3i}^- \right.$$
$$\left. + \left(M_{2i}^- \mathbf{d}_{3i}^- - M_{3i}^- \mathbf{d}_{2i}^- - M_{2i}^+ \mathbf{d}_{3i}^+ + M_{3i}^+ \mathbf{d}_{2i}^+ \right) \cdot \delta\mathbf{d}_{1i}^+ \right] = 0. \tag{C.7}$$

The first two parenthesis of the above equation imply that $M_{1i}^- = M_{1i}^+ = w\kappa^i \sin(\psi_i - \psi_i^0)$. On the other hand, the terms in the last parenthesis can be rewritten as

$$\sum_{i=1}^{n} \left(\mathbf{M}_i^+ - \mathbf{M}_i^- \right) \times \mathbf{d}_{1i}^+ \cdot \delta\mathbf{d}_{1i}^+ = 0. \tag{C.8}$$

Therefore, it follows that $\left(\mathbf{M}_i^+ - \mathbf{M}_i^- \right) \times \mathbf{d}_{1i}^+ = 0$. This condition expresses the continuity of the component moment perpendicular to $\mathbf{d}_{1i}^+(s_i)$ across the frame rotation at crease.

Appendix D

D

D.1 Published articles

- Pre-buckled states of a stretched sheet with an elliptic hole
  Ignacio Andrade-Silva and Mokhtar Adda-Bedia
  Published in Europhysics Letters.
- Foldable Cones as a Framework for Nonrigid Origami,
  Ignacio Andrade-Silva, Marcelo A. Dias and Mokhtar Adda-Bedia
  Published in Physical Review E.

A LETTERS JOURNAL EXPLORING THE FRONTIERS OF PHYSICS

Società Italiana di Fisica

edp sciences IOP Institute of Physics

LETTER

Pre-buckled states of a stretched sheet with an elliptic hole

To cite this article: I. Andrade-Silva and M. Adda-Bedia 2019 *EPL* **128** 14004

View the article online for updates and enhancements.

This content was downloaded from IP address 140.77.183.110 on 28/11/2019 at 14:28

A Letters Journal Exploring the Frontiers of Physics

October 2019

EPL, **128** (2019) 14004
doi: 10.1209/0295-5075/128/14004

www.epljournal.org

Pre-buckled states of a stretched sheet with an elliptic hole

I. Andrade-Silva and M. Adda-Bedia

Université de Lyon, Ecole Normale Supérieure de Lyon, Université Claude Bernard, CNRS, Laboratoire de Physique F-69342 Lyon, France

received 18 June 2019; accepted in final form 8 October 2019
published online 25 November 2019

PACS 46.32.+x – Static buckling and instability
PACS 87.10.Pq – Elasticity theory
PACS 46.70.De – Beams, plates, and shells

Abstract – It is well known that an annular sheet could wrinkle as a result of axisymmetric tensile loads applied at the edges. In this system, regions under compression appear due to Poisson effect in the azimuthal direction yielding an incompatible excess in length, so that the sheet has to buckle out of the plane. Then, radial wrinkles emerge following the direction of the tensile principal stress. This so-called Lamé configuration has been widely used as theoretical and experimental paradigms for wrinkling instabilities. In this work, we explore the consequences of changing the geometry of this model configuration by considering an elliptic hole in an infinite stretched sheet. Using the Kolosoff-Inglis solution, we analyse the stress field around the hole and identify three possible regions: taut, unidirectionally tensioned and slack regions. According to these definitions, we classify in a phase diagram the different stress states of the sheet as a function of the hole eccentricity and of the applied tensions. Finally, we quantify how the tension lines vary with the geometry of the hole and discuss possible outcomes on the emerging buckled patterns.

Copyright © EPLA, 2019

Wrinkle and fold formation in elastic thin plates has aroused a great interest due to its occurrence in a wide range of natural and manmade systems [1–9]. In biophysics, particular attention has been paid in understanding traction forces involved in cell motility on elastic substrates using the emerging wrinkling patterns [2]. For medical purposes, a better understanding of wrinkle formation would be helpful for the treatment of post-surgery scars [1,6]. In condensed-matter physics, pre-wrinkled conductive films have been proposed as stretchable electric contacts [4] and wrinkles in graphene sheets are believed to modify its electronic properties [9]. Finally, examples of wrinkled patterns are abundant in daily life: from clothes or curtains to human skin or fruit peels [6]. Wrinkles in thin elastic sheets emerge as a buckling instability triggered by in-plane compressive stresses. This compression can be induced by in-plane tensile loads so that, when the loading exceeds a critical value, the sheet buckles to relax the in-plane strain incompatibility generated by the Poisson effect, resulting in out-of-plane wavy deflections.

When wrinkling is induced by in-plane tension in sheets with zero flexural rigidity (the so-called membrane limit), the direction of wrinkles is described by tension field theory [10,11]. This theory assumes that the wrinkles occur along tension rays parallel to the direction of the largest principal stress while the smallest principal stress collapses to zero because a sheet with zero flexural rigidity cannot sustain compressive stresses. Tension field theory has been applied to predict the direction of wrinkles in some specific geometries [12], however this theory, as originally formulated, is not able to predict the fine features of wrinkled patterns such as their extension, wavelength and amplitude.

When the flexural rigidity of the sheet is small but finite, wrinkling is expected when the applied load exceeds a threshold value. In this scenario, two wrinkling regimes can be identified: a near-threshold (NT) regime which is just beyond the onset of the buckling instability [5] and a far-from-threshold (FFT) regime in which the applied loading is well in excess of this onset [7]. In the NT regime, deformations are small perturbations of the initial flat state, and thus, the fine features of the wrinkles are determined by a perturbative analysis of the Föppl-von Karman (FvK) equations around the flat state. Hence, the wavelength and extension of the wrinkles are given by the classical buckling theory. On the other hand, in the FFT regime, wrinkling induces a *complete* collapse of the stress component perpendicular to wrinkles [8], and

therefore, the selection of the wavelength and extension of the wrinkled pattern follow from a different criterion. The extension of the wrinkled region can be determined from an energy minimization technique yielding scaling laws that are different from those of the NT regime. Thus, the FFT analysis can be seen as a tension field theory for sheets with finite flexural rigidity [8].

Both NT and FFT analysis can be performed when the direction of the subsequent wrinkles is known *a priori*, which is the case of simple geometries such as rectangular [13] or annular sheets (also known as Lamé configuration) [14]. However, little is known when the lines of tension in the pre-buckled state of a sheet are not straight. Slight changes on the boundary conditions, such as nonuniform tensions or asymmetric geometries would lead to curved tension lines. The characterisation of the wrinkling instability for general geometrical and loading conditions remains an open problem [15].

The present work explores the role of geometry on the tensional wrinkling instabilities. As a natural extension of the Lamé configuration, we study the elastic problem of an infinite elastic sheet perforated by an elliptic hole and subjected to a uniform differential tension between its outer boundary and inner edge. We obtain the stress field for this configuration and compute both its principal components and principal directions as a function of the eccentricity of the hole and the ratio between the inward and outward tensions. We show that, depending on these control parameters, regions around the sheet can be either in a taut, slack or unidirectionally tensioned state. This yields a rich phase diagram of different global stress states depending on the topology of the compressed regions and on the presence (or absence) of slack regions. Finally, we compute the lines of tensions and show that as one moves away from the circular hole case towards the crack limit, lines of tensions bent considerably, making it difficult to predict wrinkling patterns beyond the buckling instability.

Lamé problem for an elliptic hole. – Figure 1 shows an infinite sheet with an elliptic hole of semi-axes a and $a\delta$, with $\delta < 1$, that is stretched through uniform tensions applied at its boundaries. For this configuration, it is suitable to use the elliptic coordinates $\xi > 0$ and $\eta \in [0, 2\pi]$ given by

$$(x, y) = (c\cosh\xi\cos\eta, c\sinh\xi\sin\eta), \tag{1}$$

where (x, y) are the Cartesian coordinates whose origin is at the centre of the hole, $c = a\sqrt{1-\delta^2}$ and the boundary of the inner hole corresponds to the ellipse $\xi = \xi_0 = \tanh^{-1}\delta$. The sheet is subjected to tensions applied at the boundaries: a uniform all-around tension T_{out} at an infinite distance from the hole and an inward tension τT_{out}, with $\tau > 0$, at the inner edge. The Lamé problem correspond to the case $\delta = 1$ [7].

In the absence of out-of-plane deformations (the so-called pre-buckled state) the linear elastic response of the plate is given by the following equilibrium equations:

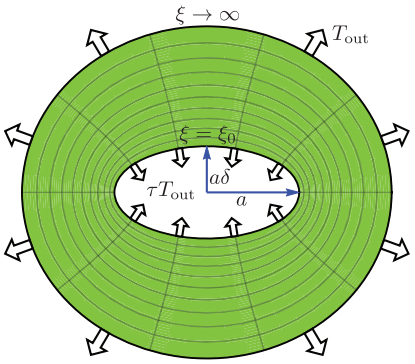

Fig. 1: Schematics of the modified Lamé problem. Lines on the sheet illustrate the elliptic coordinate system (ξ, η).

$$\nabla \cdot \overline{\overline{\sigma}} = 0, \tag{2a}$$
$$\Delta(\mathrm{Tr}\,\overline{\overline{\sigma}}) = 0, \tag{2b}$$

where ∇ and Δ are, respectively, the divergence and Laplacian operators and $\overline{\overline{\sigma}}$ is the two-dimensional stress tensor. The boundary conditions can be written in elliptic coordinates as follows:

$$\text{at } \xi \to \infty\text{: } \sigma_{\xi\xi} = \sigma_{\eta\eta} = T_{\text{out}}, \tag{3}$$
$$\text{at } \xi = \xi_0\text{: } \sigma_{\xi\xi} = \tau T_{\text{out}}, \text{ and } \sigma_{\xi\eta} = 0. \tag{4}$$

The corresponding elastic problem can be solved using the superposition principle. First, we consider the classical problem of a sheet with an elliptic hole subjected to a uniform pressure $-\Delta T$, with $\Delta T = (\tau - 1)T_{\text{out}}$, at infinity while the boundary of the hole is traction-free. The associated stress field was solved by Kolosoff and Inglis [16] and the details of the solution are reported in [17]. Then, to satisfy the boundary conditions (3), (4), we take advantage of the linearity of the system and add to the latter solution a uniformly stressed state of the sheet given by $\sigma_{\xi\xi} = \sigma_{\eta\eta} = \tau T_{\text{out}}$ and $\sigma_{\xi\eta} = 0$. One can show that the components of the resulting stress tensor are given by [17]

$$\sigma_{\xi\xi} + \sigma_{\eta\eta} = 2\tau T_{\text{out}} - 2\Delta T\ \mathrm{Re}[\coth\zeta], \tag{5a}$$
$$\sigma_{\eta\eta} - \sigma_{\xi\xi} + 2i\sigma_{\xi\eta} = \Delta T\,\frac{\cosh\bar{\zeta} - \cosh 2\xi_0\cosh\zeta}{\sinh\bar{\zeta}\sinh^2\zeta}, \tag{5b}$$

where $\zeta = \xi + i\eta$. In the following, we study the behaviour of the stress field as given by eqs. (5) and draw conclusions on the state of the sheet. To identify regions under compression, one should determine the principal stresses and their associated principal directions. After some algebraic manipulations, one computes the largest and smallest principal stresses, σ_1 and σ_2, as well as the angle β between the x-axis and the direction of the principal stresses [18]. The results are given by

see eqs. (6) *on the next page*

$$\sigma_{1,2} = \tau T_{\text{out}} - \frac{\Delta T \sinh 2\xi}{\cosh 2\xi - \cos 2\eta} \pm |\Delta T| \frac{\sqrt{(\cosh 2\xi - \cosh 2\xi_0)^2 \sin^2 2\eta + (\cosh 2\xi_0 - \cos 2\eta)^2 \sinh^2 2\xi}}{(\cosh 2\xi - \cos 2\eta)^2}, \tag{6a}$$

$$\tan 2\beta = \frac{(\sigma_{\xi\xi} - \sigma_{\eta\eta}) \sinh 2\xi \sin 2\eta + 4\sigma_{\xi\eta}(\sinh^2 \xi - \sin^2 \eta)}{2(\sigma_{\xi\xi} - \sigma_{\eta\eta})(\sinh^2 \xi - \sin^2 \eta) - 2\sigma_{\xi\eta} \sinh 2\xi \sin 2\eta}. \tag{6b}$$

Notice that β does not depend explicitly on the applied loadings and thus, is a function of the geometrical parameter δ only.

Perturbative analysis of tensional wrinkling usually focuses on the pre-buckled state of the sheet to define the regions where a single component of the diagonalised stress tensor is compressive. In the present case, both principal stresses can be either negative or positive in different regions. This leads to regions on the sheet that can be taut (tensioned in all directions), slack (compressed in all directions) or unidirectionally tensioned. In order to analyse in detail the stress, we classify regions on the sheet according to the signs of their principal stresses:

- taut region: $\sigma_1 > 0$, $\sigma_2 > 0$.
- unidirectionally tensioned (UT) region: $\sigma_1 > 0$, $\sigma_2 \leq 0$.
- slack region: $\sigma_1 \leq 0$, $\sigma_2 \leq 0$.

Figure 2 shows all the possible states of the sheet for different values of the parameters (δ, τ). Far enough from the hole, the sheet is always in a taut state. However, depending on the values of the control parameters, regions of compressive stress(es) will appear around the hole. UT regions can either concentrate at the ends of the major axis of the elliptic hole or surround it entirely (as in the Lamé case). Slack regions can also appear as small elliptical spots around the tips of the ellipse. A relevant question for a wrinkling stability analysis is whether the regions under compression that surround the hole are connected or disconnected. According to fig. 2, one can identify six possible global states that can be characterised by the values of the principal stresses at some specific locations:

- S0: the entire sheet is taut: $\sigma_2(\xi_0, \eta) > 0, \forall\, \eta \in [0, 2\pi]$.
- S1: a single UT region surrounding the hole such that each point at the edge is under compression: $\sigma_2(\xi_0, \eta) < 0$, $\forall\, \eta \in [0, 2\pi]$ and $\sigma_1 > 0$ everywhere.
- S2: there are two disconnected UT regions at both ends of the major axis of the hole, without slack regions: $\sigma_2(\xi_0, 0) < 0$ and $\sigma_2(\xi, \pi/2) > 0$, $\forall \xi \geq \xi_0$.
- S2s: similar to S2 but with the presence of slack regions around the tips of the ellipse.

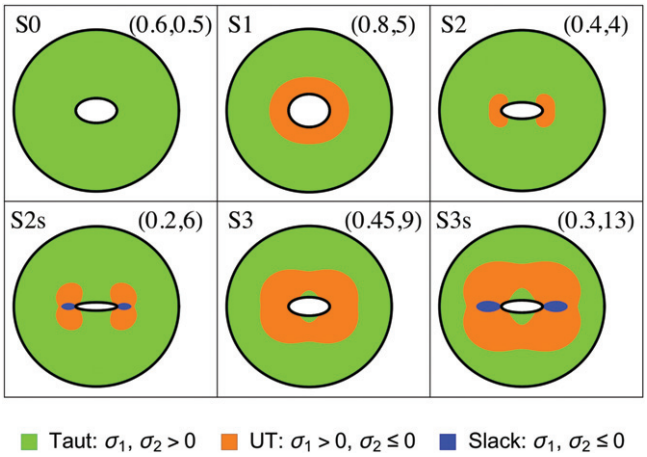

Fig. 2: Representation of the six possible states of the stretched sheet, with taut, UT and slack regions. The corresponding values of the control parameters (δ, τ) are shown in each panel.

- S3: a single connected UT region around the ellipse without slack regions and with taut regions touching both ends of the minor axis of the hole: $\sigma_2(\xi, \pi/2) \leq 0$ in a finite interval $\xi_0 < \xi_{\min} \leq \xi \leq \xi_{\max}$ and $\sigma_2(\xi, \pi/2) > 0$ elsewhere.
- S3s: similar to S3 but with the presence of slack regions around the tips of the ellipse.

Figure 3 shows the phase diagram of these different states in the parameter space (δ, τ). The critical separation curves of the phase diagram are analytically determined in the following.

Due to the symmetries of the states shown in fig. 2, the phase diagram can be retrieved by examining the principal stresses along $\eta = 0$ and $\eta = \pi/2$ only. Using eqs. (6), one has for $\tau > 1$

$$\sigma_{1,2}(\xi, 0) = \tau T_{\text{out}} - \Delta T \coth \xi \left[1 \mp \frac{\sinh^2 \xi_0}{\sinh^2 \xi}\right], \tag{7}$$

$$\sigma_{1,2}(\xi, \pi/2) = \tau T_{\text{out}} - \Delta T \tanh \xi \left[1 \mp \frac{\cosh^2 \xi_0}{\cosh^2 \xi}\right]. \tag{8}$$

Recall that $\delta = \tanh \xi_0$ and $\Delta T = (\tau - 1) T_{\text{out}}$. At the boundary of the hole, one has $\sigma_1(\xi_0, 0) = \sigma_1(\xi_0, \pi/2) = \tau T_{\text{out}}$, while $\sigma_2(\xi_0, 0) \leq \sigma_2(\xi_0, \pi/2)$. Therefore, the threshold of apparition of compressive stresses around the

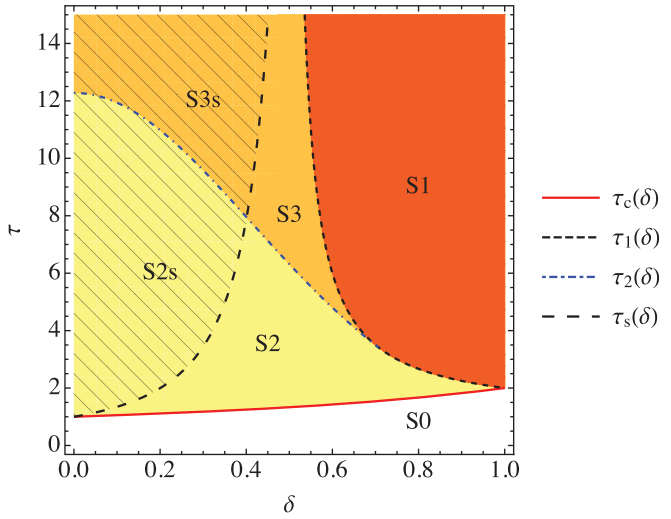

Fig. 3: Diagram showing the different states shown in fig. 2 in the parameter space (δ, τ). The critical curves $\tau_c(\delta)$, $\tau_1(\delta)$, $\tau_2(\delta)$ and $\tau_s(\delta)$ delimiting the different regions are defined in the text.

hole is given by $\sigma_2(\xi_0, 0) < 0$. Using eq. (7), this condition yields

$$\tau > \tau_c(\delta) = \frac{2}{2-\delta}. \tag{9}$$

The region S0 is defined by the condition $\tau < \tau_c(\delta)$ for which no compressive stresses occur. Notice that one recovers the threshold $\tau_c(1) = 2$ corresponding to the Lamé problem [7] and that $\tau_c(0) = 1$ for a crack-like interface. Region S1 is characterised by the existence of a UT region all around the hole. Thus the curve $\tau_1(\delta)$ bounding S1 is found by imposing the condition $\sigma_2(\xi_0, \pi/2) < 0$. Using eq. (8), we obtain

$$\tau > \tau_1(\delta) = \frac{2\delta}{2\delta - 1}. \tag{10}$$

As expected from the Lamé case, one has $\tau_1(1) = \tau_c(1) = 2$. Moreover, eq. (10) shows that τ_1 diverges as $\delta \to 1/2$.

To discriminate between the regions S2 (S2s) and S3 (S3s), one should explore the behaviour of σ_2 along the y-axis. In these regions, one has $\sigma_2(\xi_0, \pi/2) > 0$ and $\sigma_2(\infty, \pi/2) > 0$ but $\sigma_2(\xi, \pi/2)$ may not be a monotonic function of $\xi \geq \xi_0$. The critical curve $\tau_2(\delta)$ separates a region S2 (S2s) in which $\sigma_2(\xi, \pi/2) > 0$ for all $\xi \geq \xi_0$ from a region S3 (S3s) where $\sigma_2(\xi, \pi/2) \leq 0$ in a finite interval $\xi_0 < \xi_{\min} \leq \xi \leq \xi_{\max}$. The transition is given by looking at a local minimum $\xi^* \geq \xi_0$ such that

$$\frac{\mathrm{d}\sigma_2}{\mathrm{d}\xi}(\xi^*, \pi/2) = 0, \tag{11}$$

$$\sigma_2(\xi^*, \pi/2) = 0. \tag{12}$$

Using eq. (8), the condition (11) gives

$$\xi^* = \cosh^{-1}\sqrt{\frac{3}{1+\delta^2}}. \tag{13}$$

The solution given by eq. (13) should satisfy $\xi^* \geq \xi_0$. This condition holds for $\cosh\xi_0 \leq \sqrt{2}$, which is equivalent to require that $\delta \leq \delta^* = 1/\sqrt{2}$. The curve $\tau_2(\delta)$ is found by imposing condition (12). Using eqs. (8), (13) one finds

$$\tau_2(\delta) = \frac{2\sqrt{3}(2-\delta^2)^{3/2}}{2\sqrt{3}(2-\delta^2)^{3/2} - 9(1-\delta^2)}, \quad \text{with } 0 \leq \delta \leq \frac{1}{\sqrt{2}}. \tag{14}$$

One can show that the curves $\tau_2(\delta)$ and $\tau_1(\delta)$ intersect at $(\delta^* = 1/\sqrt{2}, \tau^* = 2+\sqrt{2})$. Hence, (δ^*, τ^*) corresponds to a triple point in the phase diagram linking the states S1, S2 and S3 (see fig. 3). Furthermore, notice that he slopes of $\tau_1(\delta)$ and $\tau_2(\delta)$ coincide at the triple point $(\tau_2'(\delta^*) = \tau_1'(\delta^*))$.

The critical curve $\tau_s(\delta)$ defines the transition from the states S2 and S3 to the states with slack regions S2s and S3s. As the slack regions concentrate close to the major axis of the elliptic hole (see fig. 2), it is sufficient to inspect the behaviour of $\sigma_1(\xi \geq \xi_0, 0)$ as given by eq. (7). Using the same methodology as for the determination of $\tau_2(\delta)$, one finds that the curve $\tau_s(\delta)$ is given by

$$\tau_s(\delta) = \frac{2\sqrt{3}}{2\sqrt{3} - 9\delta(1-\delta^2)}, \quad \text{with } 0 \leq \delta < \frac{1}{\sqrt{3}}. \tag{15}$$

Equation (15) shows that $\tau_s(\delta)$ diverges as $\delta \to 1/\sqrt{3}$ and $\tau_s(0) = \tau_c(0) = 1$. Therefore, slack regions occur when the elliptic hole is slender. This latter result motivates the study of the stretched sheet in the crack-like limit.

As $\delta \to 0$ the elliptic hole becomes slender and tends to a straight cut of length $2a$, resembling a crack in a stretched sheet [19]. In this case the stress field close to the elliptic hole is better represented in polar coordinates (r, θ) with origin $r = 0$ at the crack tip $x = a$. We are interested in the asymptotic behaviour of the stress field in the vicinity of the crack tip. In the appendix, we show that the limits $r \to 0$ and $\delta \to 0$ do not commute.

Let us first consider the asymptotic expansion of the stress field in powers of r/a for a given nonzero value of δ. As one approaches the crack tip ($r \to 0$) the radial stress component admits an expansion of the form (see the appendix)

$$\sigma_{rr}(r, 0) = \tau T_{\text{out}} - \frac{2\Delta T}{\delta^3}\frac{r}{a} + \mathcal{O}((r/a)^2). \tag{16}$$

Notice that $\sigma_{rr}(0, 0) = \tau T_{\text{out}}$, as dictated by the boundary conditions. On the contrary, when one takes the crack limit $\delta \to 0$ before performing the asymptotic expansion, the stress tensor admits an expansion of the form

$$\sigma_{rr}\big|_{\delta=0}(r, 0) = \tau T_{\text{out}} - \frac{\Delta T}{\sqrt{2}}\sqrt{\frac{a}{r}} + \mathcal{O}(\sqrt{r/a}). \tag{17}$$

Excepting the term τT_{out}, eq. (17) corresponds to the asymptotic expansion of the radial stress component of a stationary crack [20]. Notice that this expansion violates the original boundary conditions (4) at the hole. For

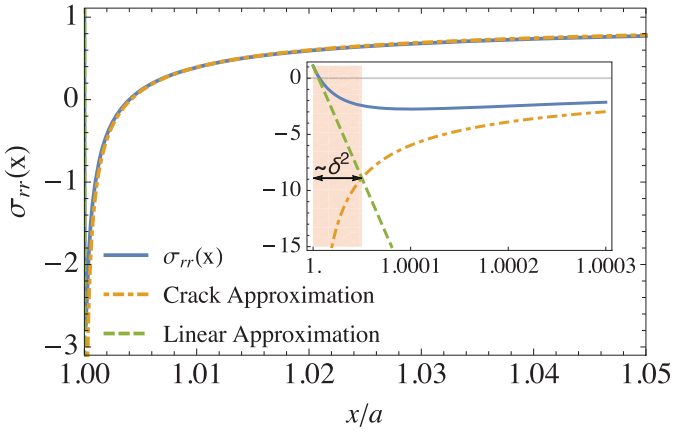

Fig. 4: Profile of σ_{rr} along the x-axis close to the hole for $\delta = 0.01$ and $\tau = 1.1$. The linear and crack approximation given by eqs. (16), (17) are also shown. The inset is a zoom in the vicinity of the tip. The shaded area represents the region where the crack approximation fails.

small $\delta \neq 0$, the crack limit approximation looses validity as one moves closer to the tip (see fig. 4). The crack approximation breaks down inside a cohesive zone-like region of typical size r_c. The radius r_c can be estimated either as the radial distance at the intersection of the linear approximation (16) with the crack approximation (17) or as the radial distance of the local minimum of $\sigma_1(r, 0)$. The two criteria yield $r_c \sim a\delta^2$ which coincides, up to proportionality factors, both with the radius of curvature at the tip of the elliptic hole and with the radius of convergence of the series expansions of the stress field given by eqs. (A.2) in the appendix.

Discussion. – Figure 3 shows the phase diagram of the different accessible global stress configurations of a stretched sheet prior to any out-of-plane deformation. To release compressive stresses, a sheet with zero flexural rigidity buckles as soon as $\tau > \tau_c(\delta)$, implying that the states S3 and S3s of the phase diagram would not be accessible. However, a sheet with finite flexural rigidity should overcome a critical compressive stress to buckle and thus, one expects the whole phase diagram to be relevant. The present study shows that a slight deviation from the original Lamé problem (a change of the geometry of the perforated hole) gives rise to a phase diagram with different global stress states that might induce a rich variety of wrinkled patterns. We believe our model problem worths experimental studies to answer fundamental questions such as: Do wrinkled regions exhibit topologies similar to those of UT regions shown in fig. 2? To what extent the phase diagram computed in fig. 3 remains relevant as τ is increased?

From a theoretical point of view, the difficulties of predicting buckled states are due to three main observations:

– UT regions exhibit complex contours which can be disconnected. Indeed, fig. 3 shows that the Lamé case $\delta = 1$ is peculiar since a small eccentricity modifies the nature of the transition to the wrinkled state. While for $\delta = 1$ a single symmetrical wrinkled state S1 exists, a new intermediate state S2 emerges for $\delta \neq 1$.

– The eccentricity of the hole may generate slack regions whose effect on the wrinkling instability is not documented neither experimentally nor theoretically.

– The tension lines are not straight curving considerably as the hole becomes slender (see fig. 5). This feature hinders any prediction about the shape of wrinkles from the pre-buckled state.

These ascertainments prevent from performing classical NT or FFT analysis. Due to the absence of axial symmetry, it is not obvious how to perform a perturbation analysis around the flat state or to find the regions of the sheet where only tensile forces take place. We believe that an accurate description of a general wrinkling problem should be considered as a step-by-step dynamical-like problem, in the sense that once the sheet starts to buckle, the stress landscape on the whole membrane is modified and the buckled zones are reshaped accordingly. In our specific problem, for $\delta < 1$ and $\tau \gtrsim \tau_c(\delta)$, compressed regions occur mainly at the tips of the ellipse, consequently, the buckling instability will be preferably located around the tips of the ellipse, much as a crack-like problem.

Specifically, wrinkles as wavy periodic structures could be peculiar patterns observed exclusively in symmetric configurations while the generic buckling instability would induce in the first place folded patterns —localised out-of-plane excursions of the sheet separated by flat regions under pure tension [21]. This assumption opens alternative approaches for the description of the post-buckling states. For example, if one considers the folding mechanism as a mean to suppress both normal and shear tractions along folds, one can envision the resulting pattern as traction-free crack lines. In this sense, one expects the physics underlying the selection of the folds pattern to be analogous to that of cracks and then must be treated as a dynamical process. The extension of a single fold should satisfy the principle of local symmetry [22] and a Griffith energy criterion [23] with vanishing fracture energy. Thus, the "equations of motion" of the fold can be written as $K_{II} = 0$ and $K_I = 0$, where K_I (resp. K_{II}) is the mode I (respectively, mode II) stress intensity factor associated to the square root singularity of the stress field at the tip of the fold. These conditions ensure that the stress field in the periphery of the fold is shear-free and tensionless. The proposed equations would allow for predicting both the shape and the extension of a single fold. In a realistic situation with many folds, one should supplement the equations of motion of each fold with a global elastic energy functional of the sheet, whose minimisation selects the geometrical and topological properties of the folding pattern. The latter analogy between folds and cracks relies only on the similarity between the boundary conditions induced by the

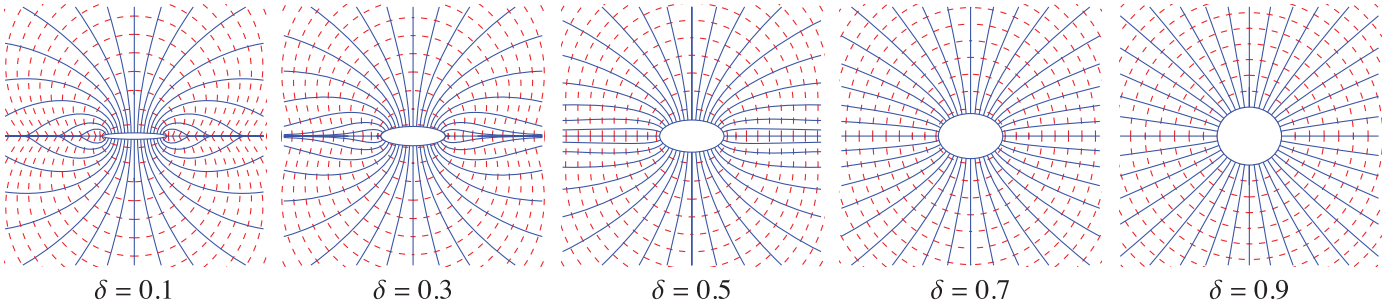

Fig. 5: The lines of tension defined by the local principal stress directions given by eq. (6b). Notice that the directions of the tension lines depend on the geometrical parameter δ only. Blue solid (respectively, red dashed) lines correspond to the largest (respectively, smallest) principal stress directions.

folding mechanism and material separation, respectively. Therefore, we expect our conjecture to remain valid for general nonuniform loading conditions and for dynamical situations.

Finally, we have studied the stress field in a sheet with an elliptic hole subjected to a differential tension between its inner and outer boundaries. We have found that regions around the hole can be either in a taut, slack or unidirectionally tensioned state. This yields a rich phase diagram of different global stress states that should have an effect on the three-dimensional shape of the sheet beyond the buckling instability. These results demonstrate that slight geometrical asymmetries or inhomogeneous loading conditions might lead to complex wrinkled patterns. Our study calls for experiments to probe the robustness of the wrinkling paradigm.

* * *

IA-S acknowledges the financial support of CONICYT DOCTORADO BECAS CHILE 2016-72170417.

Appendix: asymptotic expansion of the stress field. – The components of the stress field in polar coordinates (r,θ) can be obtained from eqs. (5) by using the following transformations:

$$\sigma_{rr}+\sigma_{\theta\theta} = \sigma_{\xi\xi}+\sigma_{\eta\eta}, \tag{A.1a}$$

$$\sigma_{rr}-\sigma_{\theta\theta}-2i\sigma_{r\theta} = e^{2i(\theta-\alpha)}(\sigma_{\xi\xi}-\sigma_{\xi\eta}-2i\sigma_{\xi\eta}). \tag{A.1b}$$

where the angle α is defined by $e^{2i\alpha} = \sinh(\xi+i\eta)/\sinh(\xi-i\eta)$. Let us define the tip $x=a$ of the elliptic hole as the origin $r=0$. Using eq. (1) and the stress field given by eqs. (5), one obtains

$$\sigma_{rr}+\sigma_{\theta\theta} = 2\tau T_{\rm out} - 2\Delta T\ \mathrm{Re}\left[\frac{a+re^{i\theta}}{\sqrt{r^2e^{2i\theta}+2rae^{i\theta}+a^2\delta^2}}\right], \tag{A.2a}$$

$$\sigma_{rr}-\sigma_{\theta\theta}-2i\sigma_{r\theta} = \Delta T\frac{2a^3\delta^2e^{2i\theta}-\left((1-\delta^2)e^{i\theta}-(1+\delta^2)e^{3i\theta}\right)a^3r}{\left(r^2e^{2i\theta}+2rae^{i\theta}+a^2\delta^2\right)^{3/2}}. \tag{A.2b}$$

The asymptotic expansion of the stress field in the vicinity of the tip of the slender ellipse can be performed in two ways: either by assuming a finite δ and taking $r\to 0$ or by taking first $\delta=0$ in and then $r\to 0$. Using eqs. (A.2), one gets for the former case

$$\begin{aligned}\sigma_{rr} &= \tau T_{\rm out} - \frac{\Delta T}{\delta}(1-\cos 2\theta)\\ &\quad+\frac{\Delta T}{2\delta^3}\frac{r}{a}\left(\left(1-\delta^2\right)\cos\theta-\left(5-\delta^2\right)\cos 3\theta\right)\\ &\quad+\mathcal{O}\left((r/a)^2\right),\end{aligned} \tag{A.3a}$$

$$\begin{aligned}\sigma_{\theta\theta} &= \tau T_{\rm out} - \frac{\Delta T}{\delta}(1+\cos 2\theta)\\ &\quad+\frac{\Delta T}{2\delta^3}\frac{r}{a}\left(3\left(1-\delta^2\right)\cos\theta+\left(5-\delta^2\right)\cos 3\theta\right)\\ &\quad+\mathcal{O}\left((r/a)^2\right),\end{aligned} \tag{A.3b}$$

$$\begin{aligned}\sigma_{r\theta} &= -\frac{2\Delta T}{\delta}\cos\theta\sin\theta\\ &\quad+\frac{\Delta T}{\delta^3}\frac{r}{a}\left(3-\delta^2+\left(5-\delta^2\right)\cos 2\theta\right)\sin\theta\\ &\quad+\mathcal{O}\left((r/a)^2\right).\end{aligned} \tag{A.3c}$$

In the crack limit case ($\delta=0$), the asymptotic expansion of eqs. (A.2) read

$$\sigma_{rr}\big|_{\delta=0} = \tau T_{\rm out} - \frac{\Delta T}{2\sqrt{2}}\sqrt{\frac{a}{r}}\cos\frac{\theta}{2}(3-\cos\theta)+\mathcal{O}\left(\sqrt{\frac{r}{a}}\right), \tag{A.4a}$$

$$\sigma_{\theta\theta}\big|_{\delta=0} = \tau T_{\rm out} - \frac{\Delta T}{\sqrt{2}}\sqrt{\frac{a}{r}}\cos^3\frac{\theta}{2}+\mathcal{O}\left(\sqrt{\frac{r}{a}}\right), \tag{A.4b}$$

$$\sigma_{r\theta}\big|_{\delta=0} = -\frac{\Delta T}{2\sqrt{2}}\sqrt{\frac{a}{r}}\cos\frac{\theta}{2}\sin\theta+\mathcal{O}\left(\sqrt{\frac{r}{a}}\right). \tag{A.4c}$$

REFERENCES

[1] Borges A. F., *Br. J. Plast. Surg.*, **13** (1960) 47.
[2] Burton K., Park J. H. and Taylor D. L., *Mol. Biol. Cell*, **10** (1999) 3745.
[3] Cerda E. and Mahadevan L., *Phys. Rev. Lett.*, **90** (2003) 074302.

[4] Lacour S. P., Wagner S., Huang Z. and Suo Z., *Appl. Phys. Lett.*, **82** (2003) 2404.
[5] Géminard J.-C., Bernal R. and Melo F., *Eur. Phys. J. E*, **15** (2004) 117.
[6] Cerda E., *J. Biomech.*, **38** (2005) 1598.
[7] Davidovitch B., Schroll R. D., Vella D., Adda-Bedia M. and Cerda E. A., *Proc. Natl. Acad. Sci. U.S.A.*, **108** (2011) 18227.
[8] Davidovitch B., Schroll R. and Cerda E., *Phys. Rev. E*, **85** (2012) 066115.
[9] Deng S. and Berry V., *Mater. Today*, **19** (2016) 197.
[10] Reissner E., *On tension field theory*, in *Proceedings of the 5th International Congress of Applied Mechanics* (J. Wiley & Sons, Inc., New York) 1939, pp. 88–92.
[11] Mansfield E. H., *The Bending and Stretching of Plates* (Cambridge University Press) 2005.
[12] Danielson D. and Natarajan S., *J. Biomech.*, **8** (1975) 135.
[13] Cerda E., Ravi-Chandar K. and Mahadevan L., *Nature*, **419** (2002) 579.
[14] Vella D., Adda-Bedia M. and Cerda E., *Soft Matter*, **6** (2010) 5778.
[15] Aharoni H., Todorova D. V., Albarrán O., Goehring L., Kamien R. D. and Katifori E., *Nat. Commun.*, **8** (2017) 15809.
[16] Inglis C. E., *Trans. Inst. Nav. Archit.*, **55** (1913) 219.
[17] Timoshenko S. and Goodier J. N., *Theory of Elasticity* (McGraw-Hill) 1969.
[18] Adda-Bedia M., Ben Amar M. and Pomeau Y., *Phys. Rev. E*, **54** (1996) 5774.
[19] Mahmood O., Audoly B. and Roux S., *Phys. Rev. Lett.*, **121** (2018) 144301.
[20] Williams M. L., *J. Appl. Mech.*, **28** (1961) 78.
[21] King H., Schroll R. D., Davidovitch B. and Menon N., *Proc. Natl. Acad. Sci. U.S.A.*, **109** (2012) 9716.
[22] Goldstein R. and Salganik R., *Int. J. Fract.*, **10** (1974) 507.
[23] Broberg K. B., *Cracks and Fracture* (Elsevier) 1999.

Foldable cones as a framework for nonrigid origami

I. Andrade-Silva* and M. Adda-Bedia
Université de Lyon, Ecole Normale Supérieure de Lyon, Université Claude Bernard, CNRS, Laboratoire de Physique, F-69342 Lyon, France

M. A. Dias
Department of Engineering, Aarhus University, 8000 Aarhus C, Denmark
and Aarhus University Centre for Integrated Materials Research–iMAT, 8000 Aarhus C, Denmark

(Received 7 June 2019; published 23 September 2019)

The study of origami-based mechanical metamaterials usually focuses on the kinematics of deployable structures made of an assembly of rigid flat plates connected by hinges. When the elastic response of each panel is taken into account, novel behaviors take place, as in the case of foldable cones (f-cones): circular sheets decorated by radial creases around which they can fold. These structures exhibit bistability, in the sense that they can snap through from one metastable configuration to another. In this work, we study the elastic behavior of isometric f-cones for any deflection and crease mechanics, which introduce nonlinear corrections to a linear model studied previously. Furthermore, we test the inextensibility hypothesis by means of a continuous numerical model that includes both the extended nature of the creases, stretching and bending deformations of the panels. The results show that this phase-field-like model could become an efficient numerical tool for the study of realistic origami structures.

DOI: 10.1103/PhysRevE.100.033003

I. INTRODUCTION

The basic premise of origami, the ancient Japanese art of paper folding, is to obtain a complex three-dimensional structure starting from a two-dimensional (2D) sheet to which a network of creases is imprinted. Despite the simplicity of this idea, in recent years, the field of mechanical metamaterials has sought inspiration from origami [1,2] in the search of smart materials with a vast range of functionality such as deployability of large membranes [3], shape changing structures [4,5], and tunable mechanical and thermal properties [6–9], just to name a few. In practice, many of these applications are constrained to situations which origami structures are made from assemblies of flat rigid plates connected by hingelike creases. In such situations, the geometrically accessible configurations are fully determined by the crease network, while the structural response is a result of the crease network and the crease mechanics [10–12]. By contrast, when the elastic response of the plates (mainly bending) is taken into account, a variety of new behaviors may emerge. In this case, the elastic response of the structure is determined by the competition between the flexural stiffness of the panels B and the torsional rigidity of the creases k. The length $L^* \equiv B/k$, called origami length, determines whether the deformation of a nonrigid origami is bending or crease dominated [13]. If l is the typical size of the facets, when $l \ll L^*$, then the deformation is governed by the change on the folding angles, while if $l \gg L^*$, then the deformation is governed by the bending of the panels.

However, suitable analytical models capturing the elastic regime of nonrigid origami still remain for the most part unexplored. Foldable cones [14], or f-cones, are the simplest single-vertex nonrigid origami in which the elasticity of the plates is relevant. f-cones are elastic sheets decorated by straight creases meeting at a single vertex around which they are folded. As a first approximation, these sheets are assumed to be inextensible. This results in a family of various umbrella-like motifs whose equilibrium shapes depend on the crease pattern imprinted in the flat configuration of the sheet and the mechanical response of the creases. Regardless of the initial crease pattern, these structures exhibit bistability in the sense that they can mechanically snap through from one metastable configuration to another of higher elastic energy.

The f-cone belongs to a larger family of singularities emerging on sheets subjected to isometrical deformations [15–17]. In many situations, the elastic energy in a thin elastic sheet can localize in a single point leading to conical dislocation. The most fundamental example is the so-called d-cone [18,19], a conical singularity observed when crumpling an elastic thin sheet. The bending energy of the defect diverges logarithmically as one gets closer to the vertex. In a more realistic situation, these divergencies are regularized if the inextensibility constraint is relaxed, thus leading to stretching and plastic deformations close to the vertex [20].

The bistable behavior of f-cones was investigated in Ref. [14] and a model was proposed to describe their equilibrium shapes in the limit of small deflection and infinitely stiff creases. We will refer to their model as the linear model for f-cones, as it relies on the approximation of small deflections which allows us to write the curvature of the surface as a linear function of the vertical component of the displacement. This system has motivated the study of other similar problems such as the bistable behavior of creased strips [21]. In this last work, the authors proposed a discrete model based on

*ignacio.andrade@ens-lyon.fr

 ©2019 American Physical Society

the Gauss map of several creases meeting at the vertex. In the limit of infinite creases, the linear version of an f-cone with two creases is recovered. The discrete model that is based on the Gauss map has limitations, as it only predicts the final shape of real sheets well for small deflections, while important discrepancies with experiments are observed for large deflections. Although these discrepancies may be attributed to the existence of stretching in real sheets, which in turn invalidates the inextensibility hypothesis, the inherent nonlinear nature of the system may also have a significant contribution to interpret the experimental observations. In the present work we propose an alternative model for f-cones that encompasses the full geometric nonlinear contributions, thus capturing any deflections—this model describes the equilibrium shapes as function of the folding (dihedral) angle of the creases. Also, the effect of crease mechanics with hingelike behaviors is incorporated into the model. Then we corroborate the predictions of the model with the aid of finite element simulations. From the numerical model we are able to quantify the stretching on the system in order to test the validity of the inextensibility hypothesis during the entire indentation process.

The manuscript is organized as follows. In Sec. II the system under study and its geometry are presented in detail. Then, in Sec. III, we present our elastic model for f-cones and the main results. The results presented here complement the predictions of the linear version of the model [14]. Subsequently, in Sec. IV, a numerical model that simulate an f-cone of four creases is proposed to study the snapping process in a finite element analysis. Then, in Sec. V the results of the numerical study are compared with the theory. The details of the analytical calculations can be found in the Appendix.

II. KINEMATICAL DESCRIPTION OF NONRIGID SINGLE VERTEX ORIGAMI

Foldable cones, or f-cones, are made from a circular elastic sheet decorated by one or more straight radial creases meeting at a single vertex [14]. These surfaces resemble those of d-cones [18], except that they can fold around the creases. When the elastic sheet is inextensible, the only possible equilibrium shapes are developable surfaces and, in this particular geometry, developable cones. This implies that the deformed shape can always be isometrically mapped to the initial flat state. The equilibrium shape of the cone will be developable anywhere except at the tip of the cone and the creases, where the curvature is not defined. In this section, we first introduce the parametrization of a general conical shape, and then we describe in detail the geometry of an f-cone.

A. Geometry of developable cones

The most general parametrization of a conical shape is given by $\mathbf{r}(r,s) = r\mathbf{u}(s)$, where r is the distance to the tip, $\mathbf{u}(s)$ is a unit vector, and $s \in [0, 2\pi]$ is the arc-length of the curve $\Gamma : s \to \mathbf{u}(s)$ on the unit sphere. The tangent vectors adapted to the surface of the cone are $\mathbf{u}$ and $\mathbf{t} = \mathbf{u}'$, where the prime denotes derivative with respect to s. As s is the arc-length of the curve, the tangent vector $\mathbf{t}$ is a unit vector. Note

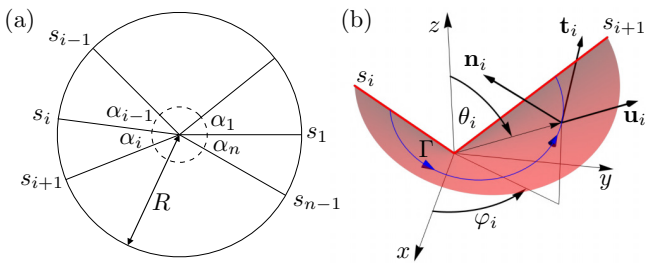

FIG. 1. (a) Imprinted crease pattern on a flat plate. (b) Deformed state of the ith panel of a f-cone. The curve Γ, the material frame, and the Euler-like angles are defined.

that $\mathbf{u} \cdot \mathbf{t} = 0$ and that the normal of the surface is given by $\mathbf{n} = \mathbf{u} \times \mathbf{t}$. Therefore, the triad $\{\mathbf{u}, \mathbf{t}, \mathbf{n}\}$ forms a right-handed basis that satisfies the following equations [22,23]:

$$\mathbf{u}' = \mathbf{t}, \tag{1a}$$

$$\mathbf{t}' = -\kappa\mathbf{n} - \mathbf{u}, \tag{1b}$$

$$\mathbf{n}' = \kappa\mathbf{t}, \tag{1c}$$

where $\kappa(s) = \mathbf{t}(s) \cdot \mathbf{n}'(s)$. The metric tensor of the conical surface is given by $g_{ab} = \partial_a\mathbf{r} \cdot \partial_b\mathbf{r}$, where the indices $a, b = r, s$. Hence, for conical geometries, the metric components are $g_{rr} = 1$, $g_{rs} = 0$, and $g_{ss} = r^2$. The extrinsic curvature tensor is defined as $K_{ab} = \partial_a\mathbf{r} \cdot \partial_b\mathbf{n}$ and its single nonvanishing component is $K_{ss} = r\kappa$. Therefore, the surface curvature is $K = g^{ab}K_{ab} = \kappa/r$. Once $\kappa(s)$ is known, the final shape of the cone can be reconstructed by integrating Eqs. (1).

B. Geometry of foldable cones

We consider an f-cone of n creases made from a flat circular sheet of radius R which is parceled out in n circular sectors (panels) delimited by the creases [see Fig. 1(a)]. A hole of radius $r_0 \ll R$ is cut out at the center in order to avoid a divergence in the elastic energy. Let α_i denote the sector angle of the ith panel in the flat configuration, with $\sum_{i=1}^{n} \alpha_i = 2\pi$. The value of the arc-length at the ith crease is denoted by s_i, so that, through the inextensibility condition, $\alpha_i = s_{i+1} - s_i$ in the deformed configuration. Hereinafter, for any scalar or vector field of the form $b_i(s)$, the subscript i specifies that the domain of the function corresponds to the $i]rmth$ sector, where the periodic convention $b_{i\pm n} \equiv b_i$ is assumed. Moreover, we introduce the following notation: $b_i^- \equiv b_{i-1}(s_i)$ and $b_i^+ \equiv b_i(s_i)$.

In the deformed configuration, each crease has a folding angle (dihedral angle) ψ_i, which we call it *mountain* if $\psi_i \in [0, \pi]$ or a *valley* if $\psi_i \in [\pi, 2\pi]$. For mountain and valley creases, Fig. 2 shows how the folding angle is defined by $\mathbf{t}_i^+$ and $\mathbf{t}_i^-$ in the plane perpendicular to the crease. In terms of spherical coordinates, the final shape is given by a polar angle $\theta(s)$ and an azimuthal angle $\varphi(s)$ which are functions of the arc-length [Fig. 1(b)]. Each angular sector will span an azimuthal angle $\Delta\varphi_i \equiv \varphi(s_{i+1}) - \varphi(s_i)$. The closure condition can be written as

$$\sum_{i=1}^{n} \Delta\varphi_i = \begin{cases} \pm 2\pi & \text{if } \Gamma \text{ encloses the } z \text{ axis} \\ 0 & \text{if not} \end{cases}, \tag{2}$$

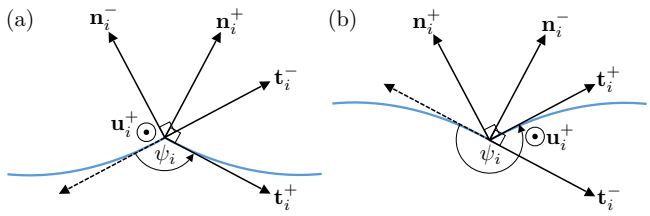

FIG. 2. Definition of (a) mountain and (b) valley creases. The vectors $\mathbf{t}_i^{\pm}$, $\mathbf{n}_i^{\pm}$ and the crease angle ψ are defined.

where $\pm$ indicates that φ_i could increase clockwise or counterclockwise in the $x-y$ plane. Notice that in principle $\Delta\varphi_i$ and α_i are not necessarily equal in the deformed configuration. However, they coincide in certain symmetrical cases: f-cones with an arbitrary number of evenly distributed mountain creases or an even number of evenly distributed alternating mountain-valley creases where all the creases are identical. In such cases, in the following sections we say that the f-cone is *symmetrical*.

III. ELASTIC THEORY OF FOLDABLE CONES

Our model is based on a generalization of the functional introduced in Ref. [24]. The total energy of an f-cone with n creases is the sum of the elastic energy over all the panels plus the mechanical energy stored in the creases. Thus, the principle of virtual work is equivalent to minimizing the following functional:

$$F_n[\mathbf{u},\mathbf{t}] = a\sum_{i=1}^{n}\int_{s_i}^{s_{i+1}}\left[\frac{1}{2}(\mathbf{u}_i\cdot\mathbf{t}_i\times\mathbf{t}_i')^2+\frac{\lambda_i}{2}\left(\mathbf{u}_i^2-1\right)+\frac{\Lambda_i}{2}\left(\mathbf{t}_i^2-1\right)+\mathbf{f}_i\cdot(\mathbf{t}_i-\mathbf{u}_i')\right]ds+\sum_{i=1}^{n}g_i[\mathbf{t}_i^-,\mathbf{t}_i^+,\mathbf{u}_i^+]. \tag{3}$$

Here $a = B\ln(R/r_0)$, where B is the flexural stiffness (bending modulus) of the sheet. The first term inside the brackets accounts for the bending energy of the facets, where $\mathbf{u}_i(s)\cdot[\mathbf{t}_i(s)\times\mathbf{t}_i'(s)] = \kappa_i(s)$ is the dimensionless curvature of the ith panel. The above augmented energy functional contains $3n$ local Lagrange multipliers, namely $\lambda_i(s)$, $\Lambda_i(s)$, and $\mathbf{f}_i(s)$, which correspond to the following kinematical constraints, respectively: $\lambda_i(s)$ enforces $\mathbf{u}_i$ to be a unit vector, thus constraining the final trajectories to the unit sphere; $\Lambda_i(s)$ enforces the parameter s to be the arc-length of the curve Γ; and, finally, $\mathbf{f}(s)$ is a force (normalized by a) that anchors the tangent vector to the embedding. The functions g_i, which depend on the frame vectors at both sides of the crease, account for the elastic energy stored in the ith crease. For simplicity, we consider pointlike creases, although the model can be generalized to extended creases where a crease is a localized regions with a given natural curvature, as shown in Ref. [25]. The variation of functional (3) yields a set of n ordinary differential equations given by (see Appendix A)

$$\kappa_i'' + (1+c_i)\kappa_i + \frac{\kappa_i^3}{2} = 0, \tag{4}$$

where $\{c_i\}_{i=1}^n$ is a set of n integration constants. The above equation describes the equilibrium shapes of Euler's elastica. In the present work we assume that all the panels have the same constant, namely $c_i = c$ for $i = 1,\ldots,n$. By comparing with the linear model of f-cones, one notices that in the limit of small deflections $-c \propto \sigma_{\varphi\varphi}$, where $\sigma_{\varphi\varphi}$ is the hoop stress [14,23]. The hypothesis of equal constants holds provided that there are no external forces acting on the creases introducing additional stresses in different panels, so that $\sigma_{\varphi\varphi}$ is continuous across the panels. From varying Eq. (3) one also obtains boundary terms that combine with terms coming from the variation of the energy stored in the creases. These boundary terms give the natural boundary conditions to solve Eq. (4) for each panel. In absence of external forces, these terms must satisfy

$$a\sum_{i=1}^{n}[-(\mathbf{f}_i\cdot\delta\mathbf{u}_i)+(\kappa_i\mathbf{n}_i\cdot\delta\mathbf{t}_i)]\big|_{s_i}^{s_{i+1}}+\sum_{i=1}^{n}\delta g_i = 0, \tag{5}$$

where $\mathbf{f}_i = \kappa_i'\mathbf{n}_i - (\kappa_i^2/2 + c_i)\mathbf{t}_i$, which can be interpreted as a normalized force per unit-length along a ray of fixed r [24].

At this point, it is convenient to introduce the vector $\mathbf{J} \equiv -\mathbf{u}\times\mathbf{f} + \kappa\mathbf{u}$ which is a conserved quantity associated with the rotational invariance of the system and can be interpreted as a torque about the vertex [24]. It can be shown that the quantity $J^2 - c^2$ corresponds to the first integral of Eq. (4). One can use the vector $\mathbf{J}$ to obtain the equilibrium shape of the f-cone by first setting it parallel to the z axis and projecting it onto the frame $(\mathbf{u},\mathbf{n})$, obtaining $\mathbf{J}\cdot\mathbf{u} = J\cos\theta = \kappa$ and $\mathbf{J}\cdot\mathbf{n} = J\varphi'\sin^2\theta = \kappa^2/2 + c$.

A. Infinitely stiff creases

In this section, we solve the case of infinitely stiff creases, so that $\delta g_i = 0$. This means that the set of folding angles $\{\psi_i\}_{i=1}^n$ is an input of the problem and that the final solutions are parameterized by these angles. In Appendix B, we show that the boundary terms (5), together with the condition $\delta\psi_i = 0$, imply the following:

$$\kappa_i^+ = \kappa_i^-, \tag{6}$$

which means that the curvature is continuous through the crease. Also, the transversal force $\mathbf{f}$ is continuous, which can be written as

$$\mathbf{f}_i^+ = \mathbf{f}_i^-. \tag{7}$$

The continuity conditions (6) and (7) imply that $\mathbf{J}_i^+ = \mathbf{J}_i^-$, and thus the entire structure is characterized by a single vector $\mathbf{J}$.

Solving the system (4) with the assumption of equal constants, $c_i = c$, requires $2n+1$ boundary conditions. Combining Eqs. (6) and (7), one can show that

$$\kappa_i'^+ = -\kappa_i'^-, \tag{8}$$

$$\kappa_i'^+ = -\cot\left(\frac{\psi_i}{2}\right)\left(\frac{\kappa_i^{+2}}{2}+c\right), \tag{9}$$

thus, yielding $2n$ boundary conditions. Adding the closure condition (2) makes the problem well posed.

Integration of Eq. (4) for each panel gives two possible solutions:

$$\kappa_i(s) = \begin{cases} \kappa_{0i}\, cn\left(\frac{\kappa_{0i}}{2\sqrt{m_i^R}} s - S_{0i} | m_i^R\right), & \text{if } J^2 > c^2, \\ \kappa_{0i}\, dn\left(\frac{\kappa_{0i}}{2} s - S_{0i} | m_i^S\right), & \text{if } J^2 < c^2, \end{cases} \tag{10}$$

where $cn(\cdot|\cdot)$ and $dn(\cdot|\cdot)$ are the cosine and delta amplitude Jacobian elliptic functions [26], with parameters m_i^R and m_i^S given by

$$m_i^R = \frac{1}{m_i^S} = \frac{\kappa_{0i}^2}{2\kappa_{0i}^2 + 4(1+c)}. \tag{11}$$

Here κ_{0i}, S_{0i}, and c are $2n+1$ unknown parameters that must be fixed such that the boundary conditions and the closure conditions are satisfied. Without loss of generality, one can define the cosine and delta amplitude functions such that $0 < m_i^S < 1$ and $0 < m_i^R < 1$ [26]. Therefore, Eq. (11) shows that there exists two families of solutions. We identify as the rest configuration (thus the superscript R) the solutions for which $J^2 > c^2$ and the snapped configuration (superscript S) with $J^2 < c^2$. This choice is in agreement with the fact that we find *a posteriori* that the bending energy of the rest configuration is the lower one. As the quantity $J^2 - c^2$ is defined for the entire structure, all the panels will be in either a rest state or a snapped state, and therefore there is no mixture of states (provided that there is a single constant c). Notice that the present nonlinear approach allows us to justify the existence of two families of solutions for a given set of folding angles, regardless of whether the cone is symmetrical or not, a property that is difficult to prove in the linear model.

The equilibrium shapes of the f-cones can be computed using the coordinates $\theta(s)$, $\varphi(s)$. As long as the concern is the geometric features, these functions are universal in the sense that they depend only on the folding angles ψ_i. Nevertheless, changing the bending modulus or the dimensions of the cone will modify the stresses and torques supported by the system as well as its elastic response. From this point forward, we consider a simplified situation of symmetrical f-cones made of all-mountain creases with same folding angle ψ (we shall also omit the subscripts i labeling the panels). We denote n^R (respectively, n^S) as the all-mountain f-cones with n-creases in a rest (respectively, snapped) state. We shall here discuss the solutions for the most relevant cases, which are a semi-infinite crease ($1^{R,S}$), a single infinite crease ($2^{R,S}$), and two perpendicular mountain creases ($4^{R,S}$).

For these symmetric configurations, it is sufficient to solve Eq. (4) in a single panel where $-\alpha/2 \leqslant s \leqslant \alpha/2$ and $\alpha = 2\pi/n$. For both rest and snapped states, we proceed to find numerically the parameters κ_0, S_0, and c that satisfy the closure condition (2) and the boundary conditions (8) and (9). The closure condition (2) reads now $\Delta\varphi = \pm\alpha$ or 0. For each state, the quantity $\Delta\varphi$ is an integral that can be computed analytically (see Appendix C). Then, for a given S_0, the closure condition defines a curve in the parameter space $\{\kappa_0, c\}$ for each state. As the f-cone is symmetrical, the solutions given by Eq. (10) should be even functions with respect to $s = 0$. Therefore, one has $S_0 = 0$ for the rest state and for the snapped state there are two possibilities, either $S_0 = 0$ or $S_0 = K(m_s)K(\cdot)$ is the complete elliptic integral of the first kind and corresponds to the half period of the function $dn(\cdot|m)$]

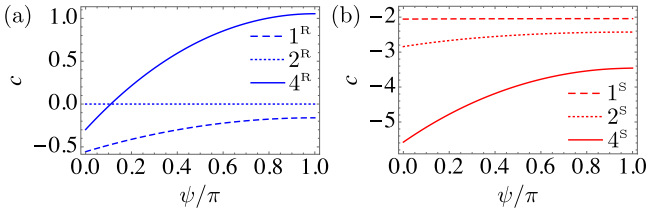

FIG. 3. The integration constant c as function of the folding angle ψ for (a) rest states and (b) snapped states for all-mountain f-cones with one, two, and four creases.

[26]. We only found solutions for $S_0 = K(m_s)$ that satisfy the closure condition. Equation (8) is automatically satisfied by the symmetry of the solutions. Then Eq. (9) defines a second curve in the parameter space $\{\kappa_0, c\}$ (one for each state). Hence, the solution for a given folding angle ψ corresponds to the intersection between these two curves, so that the values of $\kappa_0(\psi)$ and $c(\psi)$ are obtained. This procedure is done for all $\psi \in [0, \pi]$ ($\psi > \pi$ would correspond to equivalent states but vertically flipped).

Figure 3 summarizes our findings regarding the integration constants as functions of the folding angle, $c(\psi)$, and, since $c(\psi)$ relates to the hoop stress, we shall next highlight a few key observations concerning this quantity. We notice that, except for the trivial case 2^R, one has $c \nrightarrow 0$ as $\psi \to \pi$, suggesting the existence of a residual hoop stress as one approaches the flat state. We attribute this residual stress to a critical load needed to observe buckling of the facets as happens in Euler-Bernoulli beam buckling. In the configuration 4^R, c changes sign as $\psi \to 0$, suggesting at first sight a modification of the hoop stress from compressive to tensile as the folding angle gets sharper. However, this could be misleading because the interpretation of c as a hoop stress is valid only for small deformations [23].

Figure 4 shows the deviations of the structure from the flat state. To quantify such deviations, we use the angle

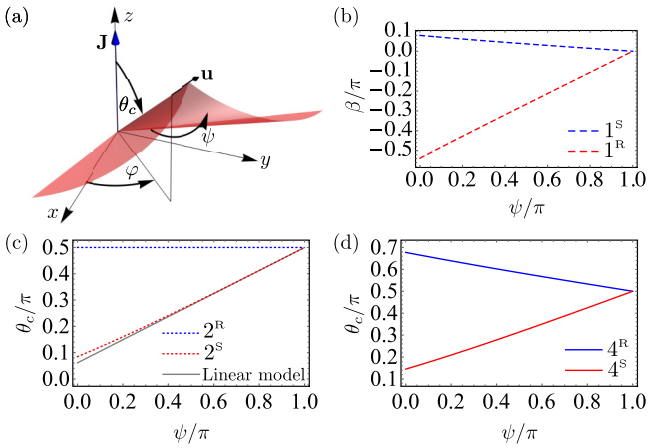

FIG. 4. (a) Schematic definition of the polar angle θ_c for $n^{R,S}$ f-cones ($n > 1$). (b) Case $1^{R,S}$: The angle $\beta(\psi) = \pi - \cos^{-1}[\mathbf{u}(0) \cdot \mathbf{u}(\pi)]$ that describes the deviation from the flat configuration. (c) Case $2^{R,S}$: The polar angle $\theta_c(\psi)$ at the creases compared with the prediction of the linear model for the snapped state. (d) Case $4^{R,S}$: The polar angle $\theta_c(\psi)$ at the creases.

$\beta = \pi - \cos^{-1}[\mathbf{u}(0)\cdot\mathbf{u}(\pi)]$ for a $1^{R,S}$ f-cone and the polar angle $\theta_c = \cos^{-1}[\mathbf{z}\cdot\mathbf{u}(\alpha/2)]$ for $n^{R,S}$ f-cones ($n > 1$). The choice of ψ, instead of θ_c (or β for a $1^{R,S}$ f-cone) as a control parameter prevents finding unphysical self-intersecting solutions. A generic feature revealed by Fig. 4 is that the polar angle at the crease varies quasilinearly with the folding angle for the whole range $0 < \psi < \pi$. This result is independent of the number of folds and holds for both rest and snapped configurations. In Fig. 4(c), we compare $\theta_c(\psi)$ for 2^S configuration with the prediction of the linear model $\theta_c = \pi/2 + 0.4386(\psi - \pi)$ [14,21], which is by definition valid in the limit of flat folding angles only, that is, for $\psi \to \pi$. These results show that polar and folding angles of the crease are related by a quasigeometrical relation that is weakly dependent on nonlinearities. However, the comparison between the linear model and the exact one should be made by considering both the polar angle and the integration constant. The fact that both these parameters deviate from the linear model as the folding angle becomes sharper yields different equilibrium shapes of the whole structure.

B. Crease mechanics

The mechanical energy of a single pointlike crease can be written as a function of invariants built from the three unit vectors that define the crease geometry: the crease vector and two vectors tangent to each facet [11]. Such invariants are $\mathbf{t}_i^- \cdot \mathbf{t}_i^+$ and $(\mathbf{t}_i^- \times \mathbf{t}_i^+)\cdot\mathbf{u}_i^+$. At leading order, the elastic energy of the ith crease takes the form [11]

$$g_i = L\,[\sigma_i\,\mathbf{t}_i^- \cdot \mathbf{t}_i^+ + \tau_i(\mathbf{t}_i^- \times \mathbf{t}_i^+)\cdot\mathbf{u}_i^+], \tag{12}$$

where $L = R - r_0$, σ_i, and τ_i are material constants associated to the crease. The crease energy can be rewritten in terms of the folding angle ψ_i, defined as the oriented angle $(\widehat{-\mathbf{t}_i^-, \mathbf{t}_i^+})$ (see Fig. 2). Introducing the constants k_i and ψ_i^0, such that

$$\sigma_i = k_i \cos\,\psi_i^0, \quad \tau_i = k_i \sin\,\psi_i^0, \tag{13}$$

allows us to rewrite (12) as $g_i(\psi_i) = -L\,k_i\,\cos(\psi_i - \psi_i^0)$. Thus the crease energy $g_i = g_i(\psi_i)$ is a function of the folding angle which is now an unknown variable. If $\psi_i \approx \psi_i^0$, then the crease energy approximates to the energy of an elastic hinge $g_i \approx L\,k_i\,(\psi_i - \psi_i^0)^2/2 + E_0$, where E_0 is a constant, k_i is the crease stiffness, and ψ_i^0 is the rest angle of the crease. The conical geometry implies that the folding angle is constant along the crease. One can show that taking into account the terms coming from the variation of the crease energy, we obtain an additional boundary condition (see Appendix B),

$$\kappa_i^+ = \frac{1}{a}\frac{dg_i}{d\psi_i}. \tag{14}$$

Equation (14) states that the value of the curvature at the crease is given by the moment imposed by its mechanical response. For a crease energy given by Eq. (12), one has $\kappa_i^+ = \bar{k}_i\,\sin(\psi_i - \psi_i^0)$, where $\bar{k}_i = Lk_i/a$ is the normalized crease stiffness.

We study again configurations with equally spaced mountain creases that have the same mechanical properties, such that $\bar{k}_i = \bar{k}$ and $\psi_i^0 = \psi_0$. The control parameters are then the crease stiffness $\bar{k}$ and the rest angle ψ_0. The boundary conditions are those of the infinitely stiff creases case supplemented by Eq. (14). Therefore, one can use the solutions found for the infinitely stiff creases and search the value of ψ such that Eq. (14) is satisfied.

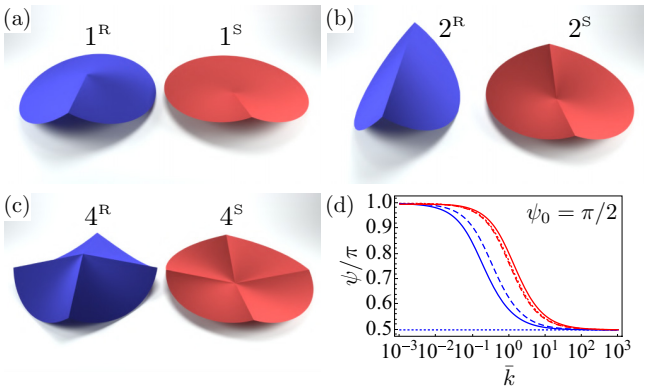

FIG. 5. [(a)–(c)] Equilibrium shapes for $\bar{k} = 1$ and $\psi_0 = \pi/2$. (d) Final crease angles ψ as function of $\bar{k}$ for $\psi_0 = \pi/2$. Rest (blue lines) and snapped (red lines) states for all-mountain f-cones with one, two, and four creases (respectively dashed, dotted, and plain lines).

Figures 5(a)–5(c) show typical shapes for the cases $1^{R,S}$, $2^{R,S}$, $4^{R,S}$. Figure 5(d) shows the final folding angle ψ as function of $\bar{k}$ for a fixed rest angle ψ_0 of the crease. Notice that $\psi \to \pi$ as $\bar{k} \to 0$ and that $\psi \to \psi_0$ as $\bar{k} \to \infty$. For a given $\bar{k}$, the snapped state always displays a larger ψ than the rest state. This observation is explained by the fact that the hoop stress of the snapped state is always larger than its respective rest state.

The total energy of the structure can be computed by summing the bending energy of the facets and the energy of the creases. Figure 6(a) shows an example of the energy landscape as function of the polar angle θ_c of the crease for an all-mountain f-cone with four creases. While the bending energy of the facets has an asymmetric parabolic shape, the energy of the creases has a double-well potential shape whose minima are at the same energy level. The resulting shape of the total energy is an asymmetric double-well potential where the two minima corresponds to the rest and the snap states. By taking the derivative of the energy with respect to θ_c, we calculate the correspondent moment $M(\theta_c)$ applied on the

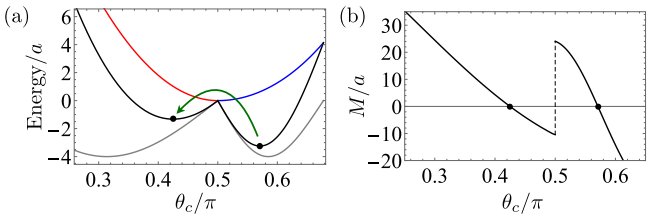

FIG. 6. (a) Energy landscape of an all-mountain f-cone with four creases as function of θ_c for $\bar{k} = 1$ and $\psi_0 = \pi/2$. The blue and red curves correspond to the bending energy of the facets for the rest and snapped states, respectively. The plain gray curve is the crease energy given by Eq. (12). The black curve is the total elastic energy. (b) Normalized moment $M(\theta_c)$ applied on the creases. The black dots correspond to the rest and snapped states of the f-cone.

creases and the particular case associated to the four-creases case is shown in Fig. 6(b). Notice that the energy has a cusp at $\theta_c = \pi/2$ which leads to a discontinuity in the mechanical response of the structure. This type of snap-through transition has been found in similar systems such as the waterbomb origami with rigid facets [10]. However, the snap-through mechanisms of the f-cone and the waterbomb are different. The former is mediated by the asymmetry in the bending energy between the rest and snapped states and the latter by the asymmetrical kinematical conditions imposed by the rigid facets. For the waterbomb, the only relevant energy is the mechanical energy stored in the creases which, in addition to the kinematical constraints, accounts for an asymmetric double-well-like potential.

IV. CONTINUOUS ELASTIC MODEL OF ORIGAMI STRUCTURES

Commonly, the mechanical response of origami-based metamaterials cannot be reduced to elastic hinges connected to rigid or isometric panels [27]. The energy landscape of deformations depends generally on both bending and stretching energies of the panels as well as on the inherent spatially extended nature of the creases [25]. Therefore, one needs to supplement the present analysis with a more accurate description that takes into account these different contributions. When applied to the f-cone, such a description should be validated by the bounds given by the analytical model.

In the following, we propose a mechanical model based on a continuous description of origami structures that is suitable for numerical implementation and test it on the f-cone by performing finite element analysis (FEA). The simulations were designed in the commercial FEA software COMSOL Multiphysics 5.4. Within this software, the structural mechanics module is equipped with quadratic shell elements, which have been used to our purpose. All the simulations were carried out with a linear elastic Hookean material model and geometric nonlinear kinematic relations have been included. The plate Young's modulus is $E = 3.5\,\mathrm{GPa}$, the Poisson's ratio is $\nu = 0.39$, and the plate thickness is $h = 300\,\mu\mathrm{m}$. We searched for solutions with the default stationary solver, where the nonlinear Newton method has been implemented. Mesh refinement studies were undertaken to ensure convergence of the results.

Temperature-induced hingelike creases

In our numerical model, we develop a method to create creases that are able to reproduce the hingelike mechanical response of commonly folded thin sheets. Inspired by the experimental results of Ref. [25], we model creases as narrow slices of the plate undergoing thermal expansion due to a temperature gradient through the thickness of the plate, as it is schematically shown in Fig. 7.

In order to test the mechanical response of these temperature driven creases, we first perform a numerical test of a single fold in a hingelike geometry consisting of two facets and the crease in the middle. We consider a rectangular plate of length L, width W, and thickness h. In the middle of the plate, we take a transversal narrow slice of width $b \ll W$

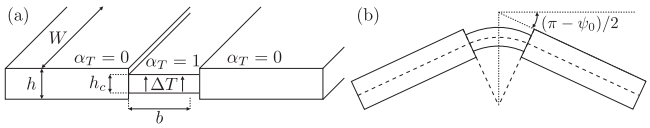

FIG. 7. Transverse view of a plate with a narrow slice whose thermal and mechanical properties differ from those of the rest of the plate. (a) Reference configuration. (b) Curvature-induced equilibrium configuration due to a linear thermal gradient across the thickness.

across the width of the plate, dividing the plate into three parts. The narrow slice corresponds to the crease while the other two parts correspond to the facets. A linear temperature gradient ΔT is applied through the thickness of the plate. We let the creased region of the plate to undergo thermal expansion by defining an inhomogeneous coefficient of thermal expansion $\alpha_T(s)$ which is constant for $|s| < b$ and zero elsewhere, where s is the arc-length perpendicular to the creases. To simulate a more realistic crease, we add a rigid connector made of an infinitely stiff material of length W, thus preventing bending deformation in the direction of the crease line. Moreover, tuning the mechanical response of the crease is done by varying the thickness h_c and the Young's modulus E_c of the crease slice. The parameters h_c, E_c, ΔT, and b will define the crease mechanical response.

Taking advantage of the two-plane symmetry of the single-fold geometry, we solve only for one quarter of the plate and then obtain the entire equilibrium shape by reflections. We perform two different studies: a heating up test and a mechanical response test. The first study consists in heating the plate from the bottom while the ends of the two plates parallel to the crease are constrained to move in the xy plane. When heating, the crease bends toward the sense of lower temperature (bottom), while the facets remain practically flat. The resulting angle between the two facets corresponds to the rest angle ψ_0 of the crease. The second study consists in a test of the mechanical response of the crease. We add four additional rigid connectors to the sides of the facets that are perpendicular to the fold line. Two moments of opposite signs are applied respectively to each pair of rigid connectors attached to the facets so that the hingelike system can open or close. Through this mechanical test, we were able to verify the hingelike behavior of the crease.

In the following, we employ the temperature-induced creases in our numerical model of f-cones.

V. NUMERICAL ANALYSIS OF FOLDABLE CONES

We begin with a circular planar disk of external radius $R = 100\,\mathrm{mm}$ and a central hole of radius $r_0 = 1\,\mathrm{mm}$. Then n radial narrow slices of constant width b, that correspond to the creases of the f-cone, are created. Rigid connectors along the creases are added so as to prevent bending along the longitudinal direction of the creases. In order to take advantage of the symmetries of the system, depending on the number of creases, only the fundamental unit cells are numerically solved and then the complete structure is reconstructed using reflections through the symmetry planes. Because each plane of symmetry cannot coincide with a rigid connector, the $1^{R,S}$

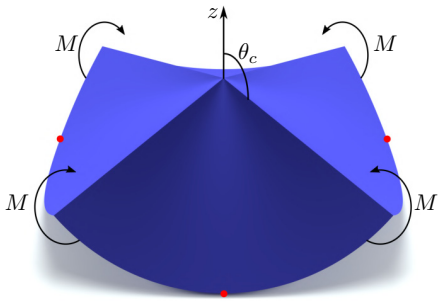

FIG. 8. Schematics of the indentation protocol. Equal moments M are applied on each crease such that the center rim moves vertically in the downward direction, while the end points of the symmetry planes (denoted by red dots) are free to move in the xy plane. The average displacement of the center rim is imposed and the moment M is computed as a function of the polar angle θ_c.

case must be solved entirely. For $2^{R,S}$, only a half of the disk is numerically solved so that the axis of symmetry is perpendicular to both creases. For $4^{R,S}$, a quarter of the disk is solved so that a single crease is at 45° from one plane of symmetry.

A. Indentation tests

Hereinafter, we focus only in the all-mountain f-cone with four creases, anticipating that our general conclusions also apply to more complex configurations. In order to test our analytical predictions, we study the snapping of the system through an indentation process from the rest state to the snapped state, which is carried out in two steps. Initially, we turn on the temperature to take the f-cone to its rest state with a given folding angle ψ. The endpoints of the symmetry planes are constrained to move only in the xy plane, so that the points at the central rim rise up when the temperature is activated. For all our simulations, we fix the temperature gradient in the crease such that $\alpha_T \Delta T = 0.2$. We also choose $b = 1$ mm, which is within the expected order of magnitude with respect to h according to crease formation measurements in thin sheets [28].

In a second step, the central rim is vertically lowered quasistatically while constraining the endpoints of the symmetry planes to move freely in the xy plane. Each crease is constrained to rotate only in the plane defined by its initial direction and the z axis [as shown in Fig. 8]. Throughout indentation, the vertical displacement of the central rim is specified and a reaction moment $M(\theta_c)$ at the creases is computed. Therefore, the mechanical response of the f-cone to the indentation process consists in the determination of the curve $M(\theta_c)$ (see movies available as supplemental material of such indentation tests in Ref. [29]).

The folding angle ψ of the creases is also tracked during indentation. To measure ψ from the numerical results, we extract the tangent vector field of concentric curves initially defined in the flat configuration. We evaluate this vector field at each side of the crease and measure the resulting angle between them. The local folding angle is found to be not exactly constant along the crease but is a function of the radial coordinate. For this reason, a representative measurement of

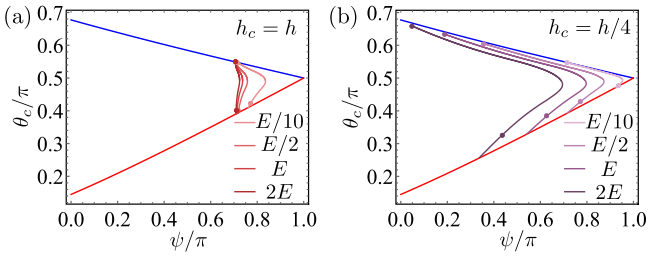

FIG. 9. [(a) and (b)] Indentation paths $\theta_c(\psi)$ as computed by the numerical model for $h_c/h = 1, 1/4$ and $E_c/E = 2, 1, 1/2, 1/10$. The theoretical curves $\theta_c(\psi)$ for a $4^{R,S}$ f-cone are reproduced from Fig. 4. The dots correspond to the rest and snapped states of each indentation path.

ψ is chosen to be the average between two local folding angles measured at radial distances $r_0 + (R - r_0)/3$ and $r_0 + 2(R - r_0)/3$. In each indentation test, we extract a curve θ_c as function of ψ which we call the indentation path.

The resulting curves $M(\theta_c)$ and $\theta_c(\psi)$ will be discussed in the following section.

B. Numerical results

Figure 9 shows the variation of $\theta_c(\psi)$ obtained numerically during the indentation test for different crease thicknesses and Young moduli. These results are compared with the polar angle $\theta_c(\psi)$ given by analytical f-cone calculations shown in Fig. 4(d). This parametric study allows us to highlight to what extent the softness of the crease affects the indentation path. Our results show that our continuous model of the crease is more sensitive to variations of h_c than those of E_c. We notice that the indentation paths do not generally follow the analytical solutions given by the isometric constraint, meaning that the intermediate shapes throughout indentation are not perfect developable cones. If the crease is too stiff, as in the case of Fig. 9(a), then the indentation path follows a nearly vertical line (i.e., approximately constant folding angle path) connecting the two stable points. However, when the crease is made softer [Fig. 9(b)], either by reducing its thickness or its Young's modulus, the indentation paths approach the one predicted by the isometric constraint.

While the rest states are generally well predicted by the isometric constraint, the snapped states depart from the analytical predictions when h_c is decreased. This result could be explained in terms of the crease stiffness. For a stiff crease, the folding angle is roughly constant along the crease enforcing the shape to be closer to a perfectly developable cone. On the other hand, a 4^S cone is characterized by an azimuthal tension which favors stretching deformations of the panels and thus tensile traction on the crease. This mechanism could induce a varying folding angle along the crease and yield a structure that can depart from a perfect developable cone, especially for softer creases. To verify this analysis, we plot in Fig. 10 one quadrant containing the lines of smallest principal curvature for stiff and soft crease cases. In a perfect developable cone, these lines coincide with the generators of a surface (i.e., lines of zero curvature), however, we observe that the lines curve significantly close to the vertex, where the stretching energy

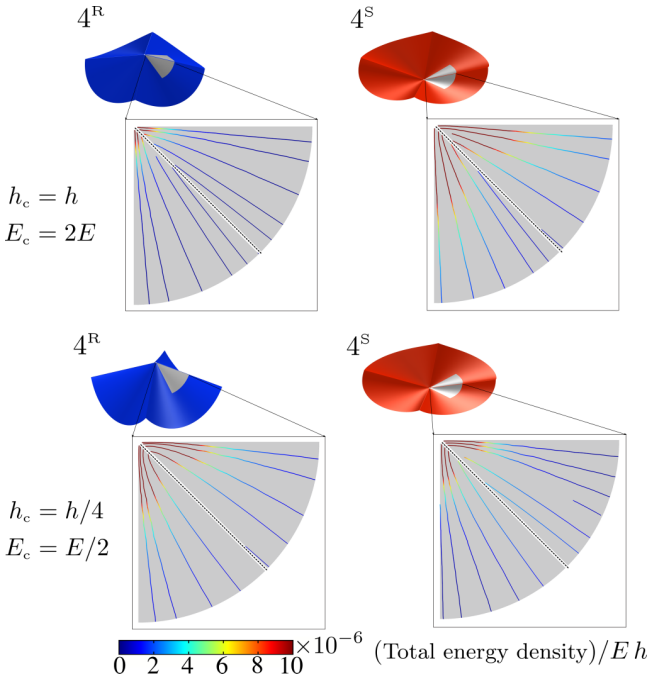

FIG. 10. Lines of smallest principal curvature of a symmetric foldable cone with four creases. The upper (respectively, lower) row corresponds to a stiff (respectively, soft) crease case. The equilibrium rest (left column) and snapped (right column) states are shown. The boxes show zoomed regions next to the vertex. Black dotted line indicates the location of the crease and the color code corresponds to the elastic energy density.

is concentrated. This effect is more pronounced for the soft crease case than the stiff one.

Figure 11(a) shows typical curves for the moment as function of the polar angle θ_c during indentation for both stiff and soft crease. Notice that the unstable branch of the stiffer crease is higher than that of the soft one, which in a real experiment leads to more energy being released during a snapping process. This observation can be attributed to a larger stretching energy barrier that is required to be overcome, which is evident from the energy plots shown in Fig. 11(b). To compare with analytical predictions, one should focus on the inset of Fig. 11(b), which shows the evolution

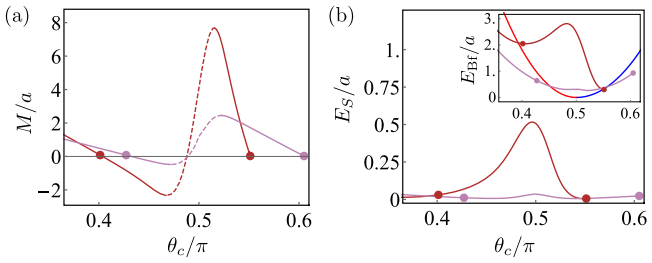

FIG. 11. (a) Moment M as function of θ_c during the indentation of a stiff crease with $h_c = h$, $E_c = 2E$ (——), and a soft crease, with $h_c = h/4$, $E_c = E/2$ (——). (b) The corresponding total stretching energy. Inset: Normalized bending energy of the facets compared to the theoretical result of Fig. 6(a).

of the bending energy of the facets throughout indentation and does not take into account the bending energy at the creases. The predicted bending energy exhibits an asymmetric parabolic shape, where the minimum corresponds to a flat solution. It is obvious that the bending energy of a soft crease follows closer the prediction than that of the stiff crease, which has a pronounced convex shape in the middle. As for the nature of the localization, Fig. 10 shows that stretching mostly happens near the vertex, while bending spans over the whole plate. Therefore, the comparison between bending and stretching contributions is made through looking at the total energies. Figure 11(b) indicates that during the indentation, as the f-cone passes through the unstable region, the stretching to bending ratio increases by about one order of magnitude.

VI. CONCLUSION

Foldable cones are the simplest example of a single-vertex origami whose facets can bend. In the present work, we developed a theoretical model which allows us to obtain the shape of f-cones for any deflection. The model shows that the bistable behavior of these structures is robust, regardless the specific properties of the creases. In particular, for symmetrical all-mountain f-cones we obtained the polar angle at the crease as function of folding angle for both rest and snapped states.

However, in more realistic situations, the geometry and mechanical response of an f-cone are characterized by a competition between the elasticity of the facets (both their bending and stretching behavior) and the stiffness of the creases. To this purpose, we have developed a continuous numerical model accounting for both the elasticity of the creases and facets. Applying this model to the particular case of two perpendicular mountain creases, we numerically studied the role of crease stiffness and verified the snap-through behavior through a series of indentation tests. We studied the indentation paths in the $\theta_c(\psi)$ diagram and showed that the structures do not follow the shape of a perfect cone throughout the indentation. For stiff creases, the path followed is that of an approximately constant folding angle while the two stable states lie closely to the theoretical prediction. When the crease is made soft, the indentation paths follow closely the branches given by the isometrical constraints; however, it is noted that while the shape of the rest state is close to the theoretical prediction, the snapped one deviates further from it. From an energetic viewpoint, not only do stiffer creases lead to indentation paths with higher stretching energy barriers, but they also enforce the preferred angle more strongly. Hence, it can be concluded that an f-cone made with stiffer creases requires more stretching when passing through $\theta_c \sim \pi/2$. On the other hand, while softer creases induce large deviations of the preferred angles, they allow for low stretching during the inversion, which explains why they follow the bounds set by the analytical calculations more closely.

The present study validates our numerical model of temperature-induced hingelike creases which can be applied to origami structures with more complex extended networks. In this case, a temperature-induced folding of the network would work as a phase-field model where the sharp piecewise energy landscape is replaced by a smooth curve. The choice of

temperature field as a trigger for crease formation is arbitrary as any other diffusion field, such as concentration [30] or swelling [31], would play a similar role. The main sought mechanism is to build up a reference configuration with a non-Euclidean reference metric due to the presence of an initially imprinted crease network [32]. This approach is advantageous since one does not need to track sharp boundaries where the deformation fields are discontinuous. It renders numerical implementation tractable and less time-consuming, two important aspects when implementing the mechanical behavior of complex origami or crumpled structures.

ACKNOWLEDGMENTS

I.A.-S. acknowledges the financial support of CONICYT DOCTORADO BECAS CHILE 2016-72170417. M.A.D. thanks the Velux Foundations for the support under the Villum Experiment program (Project No. 00023059).

APPENDIX A: DERIVATION OF THE EULER ELASTICA EQUATION

The derivation of Euler's elastica from the energy functional given by Eq. (3) can be found in Ref. [24]. Is it instructive to repeat the calculations here for the sake of completeness. The variation of the functional (3) gives

$$\begin{aligned}\delta F_n = a\sum_{i=1}^{n}\int_{s_i}^{s_{i+1}} &\big\{\big(-\kappa_i^2\mathbf{u}_i+\kappa_i\mathbf{n}_i+\lambda_i\mathbf{u}_i+\mathbf{f}_i'\big)\cdot\delta\mathbf{u}_i\\ &+\big[-(\kappa_i\mathbf{n}_i)'-\kappa_i^2\mathbf{t}_i+\Lambda_i\mathbf{t}_i+\mathbf{f}_i\big]\cdot\delta\mathbf{t}_i\,ds\big\}\\ &+a\sum_{i=1}^{n}(-\mathbf{f}_i\cdot\delta\mathbf{u}_i+\kappa_i\mathbf{n}_i\cdot\delta\mathbf{t}_i)\big|_{s_i}^{s_{i+1}}+\sum_{i=1}^{n}\delta g_i,\end{aligned}\tag{A1}$$

where we have used the identities: $\mathbf{u}\cdot\mathbf{t}\times\delta\mathbf{t}'=\mathbf{n}\cdot\delta\mathbf{t}'$ and $\mathbf{u}\cdot\delta\mathbf{t}\times\mathbf{t}'=-\kappa\mathbf{t}\cdot\delta\mathbf{t}$. The term δg_i contributes to boundary terms only and will be treated below. Taking $\mathbf{u}_i$ and $\mathbf{t}_i$ as independent variables, the terms proportional to $\delta\mathbf{u}_i$ yield

$$\mathbf{f}_i'=\big(\kappa_i^2-\lambda_i\big)\mathbf{u}_i-\kappa_i\mathbf{n}_i,\tag{A2}$$

while the terms proportional to $\delta\mathbf{t}_i$ give

$$\mathbf{f}_i=\kappa'\mathbf{n}_i+2\kappa_i^2\mathbf{t}_i-\Lambda_i\mathbf{t}_i.\tag{A3}$$

Notice that

$$\mathbf{f}_i'\cdot\mathbf{t}_i=0,\tag{A4}$$

$$\mathbf{f}_i\cdot\mathbf{u}_i=0.\tag{A5}$$

Differentiating Eq. (A3) with respect to s and using (A4), it follows that $\Lambda_i'=5\kappa_i\kappa_i'$. Integrating once, we obtain $\Lambda_i=5\kappa_i^2/2+c_i$, where c_i is an integration constant. Then, Eq. (A3) can be written as follows:

$$\mathbf{f}_i=\kappa_i'\mathbf{n}_i-\big(\tfrac{1}{2}\kappa_i^2+c_i\big)\mathbf{t}_i.\tag{A6}$$

Differentiating Eq. (A6) with respect to s and projecting onto $\mathbf{u}_i$ gives

$$\mathbf{f}_i'\cdot\mathbf{u}_i=\tfrac{1}{2}\kappa_i^2+c_i.\tag{A7}$$

Projecting equation (A2) onto $\mathbf{u}_i$ and equating with Eq. (A7), one gets $\lambda_i=\kappa_i^2/2-c_i$. Then, Eq. (A2) now reads

$$\mathbf{f}_i'=\left(\frac{\kappa_i^2}{2}+c_i\right)\mathbf{u}_i-\kappa_i\mathbf{n}_i.\tag{A8}$$

On the other hand, one can differentiate once Eq. (A6) and obtain

$$\mathbf{f}_i'=\left[\kappa_i''+\kappa_i\left(\frac{\kappa_i^2}{2}+c_i\right)\right]\mathbf{n}_i+\left(\frac{\kappa_i^2}{2}+c_i\right)\mathbf{u}_i.\tag{A9}$$

Using Eqs. (A8) and (A9), one obtains the Euler's elastica equations given by Eq. (4). In the following, the boundary terms will be treated.

APPENDIX B: BOUNDARY CONDITIONS

It is useful to compute the variation of the functional (3) in terms of virtual rotations of the frame specified by the Euler-like angles. To this purpose, we first introduce the vectors $\mathbf{e}_\varphi=-\sin\varphi\,\mathbf{x}+\cos\varphi\,\mathbf{y}$ and $\mathbf{n}_\varphi\equiv\mathbf{u}\times\mathbf{e}_\varphi$ which span the plane containing the vectors $\mathbf{t}$ and $\mathbf{n}$ (for simplicity, we omit subscripts here). If $\phi(s)$ is the angle between $\mathbf{t}$ and $\mathbf{e}_\varphi$, then

$$\mathbf{t}=\cos\phi\,\mathbf{e}_\varphi+\sin\phi\,\mathbf{n}_\varphi,\tag{B1a}$$

$$\mathbf{n}=-\sin\phi\,\mathbf{e}_\varphi+\cos\phi\,\mathbf{n}_\varphi.\tag{B1b}$$

Defining $\mathbf{e}_\rho=\cos\varphi\,\mathbf{x}+\sin\varphi\,\mathbf{y}$, one can write

$$\mathbf{u}=\sin\theta\,\mathbf{e}_\rho+\cos\theta\,\mathbf{z},\tag{B2a}$$

$$\mathbf{n}_\varphi=-\cos\theta\,\mathbf{e}_\rho+\sin\theta\,\mathbf{z}.\tag{B2b}$$

Then, one can show the following relations:

$$\delta\mathbf{u}=-\delta\theta\,\mathbf{n}_\varphi+\sin\theta\,\delta\varphi\,\mathbf{e}_\varphi,\tag{B3}$$

$$\delta\mathbf{t}=(\delta\phi+\cos\theta\,\delta\varphi)\mathbf{n}+(\sin\phi\,\delta\theta-\sin\theta\cos\phi\,\delta\varphi)\mathbf{u}.\tag{B4}$$

Notice that $\mathbf{u}\cdot\delta\mathbf{u}=0$ and $\mathbf{t}\cdot\delta\mathbf{t}=0$ as expected. The following relations are useful:

$$\begin{aligned}\mathbf{n}\cdot\delta\mathbf{u}&=-\cos\phi\,\delta\theta-\sin\theta\sin\phi\,\delta\varphi,\\ \mathbf{t}\cdot\delta\mathbf{u}&=-\sin\phi\,\delta\theta+\sin\theta\cos\phi\,\delta\varphi,\\ \mathbf{n}\cdot\delta\mathbf{t}&=\delta\phi+\cos\theta\,\delta\varphi.\end{aligned}\tag{B5}$$

Now we put the subscripts back and write some useful relations. First, notice that in the plane perpendicular to a crease, the frame $\{\mathbf{t},\mathbf{n}\}$ rotates by an angle $\psi_i-\pi$, which can be expressed as follows:

$$\begin{pmatrix}\mathbf{t}_i^+\\ \mathbf{n}_i^+\end{pmatrix}=\begin{pmatrix}-\cos\psi_i & \sin\psi_i\\ -\sin\psi_i & -\cos\psi_i\end{pmatrix}\begin{pmatrix}\mathbf{t}_i^-\\ \mathbf{n}_i^-\end{pmatrix}.\tag{B6}$$

Using the relations given by Eq. (B5) and Eq. (B6) one obtains the following relations:

$$\begin{aligned}\mathbf{n}_i^+\cdot\delta\mathbf{t}_i^+&=\delta\phi_i^++\cos\theta_i^+\,\delta\varphi_i^+,\\ \mathbf{n}_i^-\cdot\delta\mathbf{t}_i^-&=\delta\phi_i^-+\cos\theta_i^+\,\delta\varphi_i^+,\\ \mathbf{t}_i^+\cdot\delta\mathbf{t}_i^-&=-\sin\psi_i(\delta\phi_i^-+\cos\theta_i^+\,\delta\varphi_i^+),\\ \mathbf{t}_i^-\cdot\delta\mathbf{t}_i^+&=\sin\psi_i(\delta\phi_i^++\cos\theta_i^+\,\delta\varphi_i^+),\end{aligned}$$

$$\mathbf{n}_i^+ \cdot \delta\mathbf{t}_i^- = -\cos\psi_i(\delta\phi_i^- + \cos\theta_i^+\,\delta\varphi_i^+),$$
$$\mathbf{n}_i^- \cdot \delta\mathbf{t}_i^+ = -\cos\psi_i(\delta\phi_i^+ + \cos\theta_i^+\,\delta\varphi_i^+). \tag{B7}$$

where $\phi_i^\pm$ is the angle between $\mathbf{t}_i^\pm$ and $\mathbf{e}_\theta$. Notice that $\psi_i = \pi + \phi_i^+ - \phi_i^-$ and then $\delta\psi_i = \delta\phi_i^+ - \delta\phi_i^-$. At this stage, we distinguish two cases: infinitely stiff creases and finite crease stiffness.

1. Infinitely stiff crease

By taking $\delta g_i = 0$ and using the periodic convention in Eq. (5), one can write

$$\sum_{i=1}^{n}[(\mathbf{f}_i^+ - \mathbf{f}_i^-)\cdot\delta\mathbf{u}_i^+ + \kappa_i^-\mathbf{n}_i^-\cdot\delta\mathbf{t}_i^- - \kappa_i^+\mathbf{n}_i^+\cdot\delta\mathbf{t}_i^+] = 0, \tag{B8}$$

where we have used $\mathbf{u}_i^- = \mathbf{u}_i^+$. Using Eqs. (B7), the condition of infinitely stiff crease $\delta\psi_i = 0$ is equivalent to imposing $\mathbf{n}_i^+\cdot\delta\mathbf{t}_i^- = \mathbf{n}_i^-\cdot\delta\mathbf{t}_i^+$. Thus, imposing $\delta\psi_i = 0$ and letting $\delta\mathbf{u}_i^+$ undergo independent virtual rotation imply the boundary conditions (6) and (7). By projecting Eq. (7) onto $\mathbf{n}_i^+$ and $\mathbf{t}_i^+$, one obtains

$$\begin{pmatrix}\kappa_i'^+\\ \kappa_i^{+2}/2 + c\end{pmatrix} = \begin{pmatrix}-\cos\psi_i & -\sin\psi_i\\ \sin\psi_i & -\cos\psi_i\end{pmatrix}\begin{pmatrix}\kappa_i'^-\\ \kappa_i^{-2}/2 + c\end{pmatrix}, \tag{B9}$$

where we have assumed $c_i = c$. Manipulating Eq. (B9) one obtains Eqs. (8) and (9).

2. Finite crease stiffness

The variation of the crease energy given by Eq. (12) reads

$$\delta g_i = L\{\sigma_i(\delta\mathbf{t}_i^-\cdot\mathbf{t}_i^+ + \mathbf{t}_i^-\cdot\delta\mathbf{t}_i^+) + \tau_i[(\delta\mathbf{t}_i^-\times\mathbf{t}_i^+)\cdot\mathbf{u}_i^+ + (\mathbf{t}_i^-\times\delta\mathbf{t}_i^+)\cdot\mathbf{u}_i^+ + (\mathbf{t}_i^-\times\mathbf{t}_i^+)\cdot\delta\mathbf{u}_i^+]\}. \tag{B10}$$

The last term in the right-hand side is zero because $(\mathbf{t}_i^-\times\mathbf{t}_i^+)|_{s_i}$ is parallel to $\mathbf{u}_i(s_i)$. Using the cyclic properties of the triple product we can write

$$\delta g_i = L[\sigma_i(\mathbf{t}_i^+\cdot\delta\mathbf{t}_i^- + \mathbf{t}_i^-\cdot\delta\mathbf{t}_i^+) + \tau_i(\mathbf{n}_i^-\cdot\delta\mathbf{t}_i^+ - \mathbf{n}_i^+\cdot\delta\mathbf{t}_i^-)]. \tag{B11}$$

Using the identities (B7), Eq. (B11) can be rewritten as follows:

$$\delta g_i = L[\sigma_i\,\sin\psi_i(\delta\phi_i^+ - \delta\phi_i^-) + \tau_i\,\cos\psi_i(\delta\phi_i^+ - \delta\phi_i^-)]. \tag{B12}$$

Notice that the above equation has the form $\delta g_i = (dg_i/d\psi_i)\delta\psi_i$.

Using the definition for the constants introduced in Eq. (13) and recalling that $\theta_i^+ = \theta_i^-$ and $\varphi_i^+ = \varphi_i^-$, we can rewrite Eq. (5) as follows :

$$\begin{aligned}\sum_{i=1}^{n}\Bigg\{&\left[-\kappa_i'^+\cos\phi_i^+ + \kappa_i'^-\cos\phi_i^- + \left(\frac{1}{2}\kappa_i^{+2} + c\right)\sin\phi_i^+ - \left(\frac{1}{2}\kappa_i^{-2} + c\right)\sin\phi_i^-\right]\delta\theta_i^+\\ &+\left[-\kappa_i'^+\sin\phi_i^+ + \kappa_i'^-\sin\phi_i^- - \left(\frac{1}{2}\kappa_i^{+2} + c\right)\cos\phi_i^+ + \left(\frac{1}{2}\kappa_i^{-2} + c\right)\cos\phi_i^-\right]\sin\theta_i^+\delta\varphi_i^+ - (\kappa_i^+ - \kappa_i^-)\cos\theta_i^+\delta\varphi_i^+\\ &-\left[\kappa_i^+ - \bar{k}_i\sin\left(\psi_i - \psi_i^0\right)\right]\delta\phi_i^+ + \left[\kappa_i^- - \bar{k}_i\sin\left(\psi_i - \psi_i^0\right)\right]\delta\phi_i^-\Bigg\} = 0.\end{aligned} \tag{B13}$$

The infinitesimal variations of the frame vectors can be translated to virtual rotations in terms of the Euler angles $\delta\theta_i^+$, $\delta\varphi_i^+$, $\delta\phi_i^+$, and $\delta\phi_i^-$. Assuming that all these virtual rotations are independent, one obtains conditions (6), (7), and (14) with $g_i(\psi_i)$ given by Eq. (12).

APPENDIX C: CLOSURE CONDITION

In a symmetrical f-cone with n creases, the azimuthal angle spanned by a single panel is given by the integral

$$\Delta\varphi = \int_{-\frac{\alpha}{2}}^{\frac{\alpha}{2}}\frac{\kappa^2/2 + c}{J\sin^2\theta}ds = \int_{-\frac{\alpha}{2}}^{\frac{\alpha}{2}}\frac{J}{2}\left(\frac{J^2 + 2c}{J^2 - \kappa^2} - 1\right)ds, \tag{C1}$$

where $\alpha = 2\pi/n$. As the deformed state will also be symmetrical, the closure condition can be written as $\Delta\varphi = \pm\alpha$ or $\Delta\varphi = 0$ according to Eq. (2). These integrals can be computed analytically for each state:

$$\Delta\varphi^R = \left\{\frac{J(J^2 + 2c)}{\kappa_0(J^2 - \kappa_0^2)}\sqrt{m_r}\,\Pi\left[\frac{\kappa_0^2}{\kappa_0^2 - J^2}, \mathrm{am}\left(\frac{\kappa_0}{2\sqrt{m_r}}s\middle|m_r\right)\middle|m_r\right] - \frac{J}{2}s\right\}\Bigg|_{-\frac{\alpha}{2}}^{\frac{\alpha}{2}} \tag{C2}$$

and

$$\Delta\varphi^S = \left\{\frac{c}{J}s - \frac{(J^2 + 2c)\kappa_0(m_s - 1)}{J(J^2 + (m_s - 1)\kappa_0^2)}\Pi\left[\frac{J^2 m_s}{J^2 + (m_s - 1)\kappa_0^2}, \mathrm{am}\left(\frac{\kappa_0}{2}s\middle|m_s\right)\middle|m_s\right]\right\}\Bigg|_{-\frac{\alpha}{2}}^{\frac{\alpha}{2}}, \tag{C3}$$

where the labels R, S stand, respectively, for the rest and snapped states. Also, $\Pi(\cdot,\cdot|m)$ is the elliptic integral of third kind and $\mathrm{am}(\cdot|m)$ is the Jacobi amplitude with modulus m [26].

[1] M. Schenk and S. D. Guest, Proc. Natl. Acad. Sci. USA **110**, 3276 (2013).

[2] Z. Y. Wei, Z. V. Guo, L. Dudte, H. Y. Liang, and L. Mahadevan, Phys. Rev. Lett. **110**, 215501 (2013).

[3] K. Miura, *Method of Packaging and Deployment of Large Membranes in Space*, Tech. Rep. 618, The Institute of Space and Astronautical Science, Tokyo, 1985.

[4] M. A. Dias, L. H. Dudte, L. Mahadevan, and C. D. Santangelo, Phys. Rev. Lett. **109**, 114301 (2012).

[5] L. H. Dudte, E. Vouga, T. Tachi, and L. Mahadevan, Nat. Mater. **15**, 583 (2016).

[6] J. L. Silverberg, A. A. Evans, L. McLeod, R. C. Hayward, T. Hull, C. D. Santangelo, and I. Cohen, Science **345**, 647 (2014).

[7] S. Waitukaitis, R. Menaut, Bryan Gin-ge Chen, and M. van Hecke, Phys. Rev. Lett. **114**, 055503 (2015).

[8] E. Boatti, N. Vasios, and K. Bertoldi, Adv. Mater. **29**, 1700360 (2017).

[9] P. P. Pratapa, K. Liu, and G. H. Paulino, Phys. Rev. Lett. **122**, 155501 (2019).

[10] B. H. Hanna, J. M. Lund, R. J. Lang, S. P. Magleby, and L. L. Howell, Smart Mater. Struct. **23**, 094009 (2014).

[11] V. Brunck, F. Lechenault, A. Reid, and M. Adda-Bedia, Phys. Rev. E **93**, 033005 (2016).

[12] Y. Chen, R. Peng, and Z. You, Science **349**, 396 (2015).

[13] F. Lechenault, B. Thiria, and M. Adda-Bedia, Phys. Rev. Lett. **112**, 244301 (2014).

[14] F. Lechenault and M. Adda-Bedia, Phys. Rev. Lett. **115**, 235501 (2015).

[15] D. A. Huffman, IEEE Trans. Comput. **C-25**, 1010 (1976).

[16] K. A. Seffen, Phys. Rev. E **94**, 013002 (2016).

[17] J. Guven, M. M. Müller, and P. Vázquez-Montejo, J. Phys. A: Math. Theor. **45**, 015203 (2011).

[18] M. Ben Amar and Y. Pomeau, Proc. R. Soc. London, Ser. A **453**, 729 (1997).

[19] E. Cerda and L. Mahadevan, Phys. Rev. Lett. **80**, 2358 (1998).

[20] E. Cerda, S. Chaieb, F. Melo, and L. Mahadevan, Nature **401**, 46 (1999).

[21] M. G. Walker and K. A. Seffen, Thin-Walled Struct. **124**, 538 (2018).

[22] E. Cerda, L. Mahadevan, and J. M. Pasini, Proc. Natl. Acad. Sci. USA **101**, 1806 (2004).

[23] E. Cerda and L. Mahadevan, Proc. R. Soc. Lond. A **461**, 671 (2005).

[24] J. Guven and M. M. Müller, J. Phys. A: Math. Theor. **41**, 055203 (2008).

[25] T. Jules, F. Lechenault, and M. Adda-Bedia, Soft Matter **15**, 1619 (2019).

[26] M. Abramowitz and I. A. Stegun, *Handbook of Mathematical Functions: With Formulas, Graphs, and Mathematical Tables* (Dover, New York, 1964).

[27] J. L. Silverberg, J.-H. Na, A. A. Evans, B. Liu, T. C. Hull, C. D. Santangelo, R. J. Lang, R. C. Hayward, and I. Cohen, Nat. Mater. **14**, 389 (2015).

[28] A. Benusiglio, V. Mansard, A.-L. Biance, and L. Bocquet, Soft Matter **8**, 3342 (2012).

[29] See Supplemental Material at http://link.aps.org/supplemental/10.1103/PhysRevE.100.033003 for movies showing the indentation tests of soft (Movie S1) and stiff (Movie S2) all-mountain f-cones made of four creases.

[30] Y. Klein, E. Efrati, and E. Sharon, Science **315**, 1116 (2007).

[31] J. Kim, J. A. Hanna, M. Byun, C. D. Santangelo, and R. C. Hayward, Science **335**, 1201 (2012).

[32] Z. L. Wu, M. Moshe, J. Greener, H. Therien-Aubin, Z. Nie, E. Sharon, and E. Kumacheva, Nat. Commun. **4**, 1586 (2013).

Bibliography

[1] Zachary Abel et al. “Rigid origami vertices: Conditions and forcing sets”. In: *arXiv preprint arXiv:1507.01644* (2015).

[2] Milton Abramowitz and Irene A Stegun. *Handbook of mathematical functions: with formulas, graphs, and mathematical tables*. Vol. 55. Dover, 1965.

[3] Mokhtar Adda-Bedia, Martine Ben Amar, and Yves Pomeau. “Morphological instabilities of dynamic fractures in brittle solids”. In: *Physical Review E* 54.5 (1996), p. 5774.

[4] Mokhtar Adda-Bedia and Yves Pomeau. “Crack instabilities of a heated glass strip”. In: *Physical Review E* 52.4 (1995), p. 4105.

[5] Hillel Aharoni et al. “The smectic order of wrinkles”. In: *Nature Communications* 8 (2017), p. 15809.

[6] Hugo Akitaya et al. “Rigid Foldability is NP-Hard”. In: *arXiv preprint arXiv:1812.01160* (2018).

[7] Christian André Andresen, Alex Hansen, and Jean Schmittbuhl. “Ridge network in crumpled paper”. In: *Physical review E* 76.2 (2007), p. 026108.

[8] B Audoly, B Roman, and A Pocheau. “Secondary buckling patterns of a thin plate under in-plane compression”. In: *The European Physical Journal B-Condensed Matter and Complex Systems* 27.1 (2002), pp. 7–10.

[9] Basile Audoly and Yves Pomeau. “Elasticity and geometry”. In: *Peyresq Lectures On Nonlinear Phenomena*. World Scientific, 2000, pp. 1–35.

[10] M Ben Amar and Y Pomeau. “Crumpled paper”. In: *Proceedings of the Royal Society of London. Series A: Mathematical, Physical and Engineering Sciences* 453.1959 (1997), pp. 729–755.

[11] Adrien Benusiglio et al. “The anatomy of a crease, from folding to ironing”. In: *Soft Matter* 8.12 (2012), pp. 3342–3347.

[12] Marshall Bern and Barry Hayes. “The complexity of flat origami”. In: *SODA*. Vol. 96. 1996, pp. 175–183.

[13] Daniel L Blair and Arshad Kudrolli. “Geometry of crumpled paper”. In: *Physical review letters* 94.16 (2005), p. 166107.

[14] Melina K Blees et al. “Graphene kirigami”. In: *Nature* 524.7564 (2015), p. 204.

[15] Elisa Boatti, Nikolaos Vasios, and Katia Bertoldi. “Origami metamaterials for tunable thermal expansion”. In: *Advanced Materials* 29.26 (2017), p. 1700360.

[16] Albert F Borges. “Scar prognosis of wounds”. In: *British journal of plastic surgery* 13 (1960), pp. 47–54.

[17] K Bertram Broberg. *Cracks and Fracture*. Elsevier, 1999.

[18] V Brunck et al. “Elastic theory of origami-based metamaterials”. In: *Physical Review E* 93.3 (2016), p. 033005.

[19] Kevin Burton, Jung H Park, and D Lansing Taylor. “Keratocytes generate traction forces in two phases”. In: *Molecular biology of the cell* 10.11 (1999), pp. 3745–3769.

[20] Luigi Cedolin et al. *Stability of structures: elastic, inelastic, fracture and damage theories*. World Scientific, 2010.

[21] E Cerda and L Mahadevan. “Conical surfaces and crescent singularities in crumpled sheets”. In: *Physical Review Letters* 80.11 (1998), p. 2358.

[22] Enrique Cerda. “Mechanics of scars”. In: *Journal of biomechanics* 38.8 (2005), pp. 1598–1603.

[23] Enrique Cerda and L Mahadevan. “Confined developable elastic surfaces: cylinders, cones and the Elastica”. In: *Proceedings of the Royal Society of London A: Mathematical, Physical and Engineering Sciences* 461.2055 (2005), pp. 671–700.

[24] Enrique Cerda and Lakshminarayanan Mahadevan. “Geometry and physics of wrinkling”. In: *Physical review letters* 90.7 (2003), p. 074302.

[25] Enrique Cerda, Lakshminarayanan Mahadevan, and José Miguel Pasini. “The elements of draping”. In: *Proceedings of the National Academy of Sciences* 101.7 (2004), pp. 1806–1810.

[26] Enrique Cerda, K Ravi-Chandar, and L Mahadevan. “Thin films: Wrinkling of an elastic sheet under tension”. In: *Nature* 419.6907 (2002), p. 579.

[27] Enrique Cerda et al. “Conical dislocations in crumpling”. In: *Nature* 401.6748 (1999), p. 46.

[28] Bryan Gin-ge Chen and Christian D Santangelo. “Branches of triangulated origami near the unfolded state”. In: *Physical Review X* 8.1 (2018), p. 011034.

[29] Xi Chen and John W Hutchinson. “Herringbone buckling patterns of compressed thin films on compliant substrates”. In: *Journal of applied mechanics* 71.5 (2004), pp. 597–603.

[30] Yan Chen, Rui Peng, and Zhong You. “Origami of thick panels”. In: *Science* 349.6246 (2015), pp. 396–400.

[31] CD Coman. “On the applicability of tension field theory to a wrinkling instability problem”. In: *Acta Mechanica* 190.1-4 (2007), pp. 57–72.

[32] CD Coman and DM Haughton. “Localized wrinkling instabilities in radially stretched annular thin films”. In: *Acta Mechanica* 185.3-4 (2006), pp. 179–200.

[33] Ciprian D Coman and Andrew P Bassom. “On the wrinkling of a pre-stressed annular thin film in tension”. In: *Journal of the Mechanics and Physics of Solids* 55.8 (2007), pp. 1601–1617.

[34] Wikimedia Commons. *Gaussian curvature*. URL: https://commons.wikimedia.org/wiki/File:Gaussian_curvature.svg.

[35] Michael Cross and Henry Greenside. *Pattern formation and dynamics in nonequilibrium systems*. Cambridge University Press, 2009.

[36] DA Danielson and S Natarajan. “Tension field theory and the stress in stretched skin”. In: *Journal of Biomechanics* 8.2 (1975), pp. 135–142.

[37] B Davidovitch, RD Schroll, and E Cerda. “Nonperturbative model for wrinkling in highly bendable sheets”. In: *Physical Review E* 85.6 (2012), p. 066115.

[38] Benny Davidovitch et al. “Prototypical model for tensional wrinkling in thin sheets”. In: *Proceedings of the National Academy of Sciences* 108.45 (2011), pp. 18227–18232.

[39] Stephanie Deboeuf et al. “Comparative study of crumpling and folding of thin sheets”. In: *Physical review letters* 110.10 (2013), p. 104301.

[40] Erik Demaine. “Folding and unfolding”. In: (2001).

[41] Shikai Deng and Vikas Berry. “Wrinkled, rippled and crumpled graphene: an overview of formation mechanism, electronic properties, and applications”. In: *Materials Today* 19.4 (2016), pp. 197–212.

[42] Julien Dervaux and Martine Ben Amar. “Morphogenesis of growing soft tissues”. In: *Physical review letters* 101.6 (2008), p. 068101.

[43] Marcelo A Dias and Basile Audoly. “?Wunderlich, meet Kirchhoff?: A general and unified description of elastic ribbons and thin rods”. In: *Journal of Elasticity* 119.1-2 (2015), pp. 49–66.

[44] Marcelo A Dias et al. “Geometric mechanics of curved crease origami”. In: *Physical review letters* 109.11 (2012), p. 114301.

[45] Levi H Dudte et al. “Programming curvature using origami tessellations”. In: *Nature materials* 15.5 (2016), p. 583.

[46] Kenneth E Evans and Andrew Alderson. “Auxetic materials: functional materials and structures from lateral thinking!” In: *Advanced materials* 12.9 (2000), pp. 617–628.

[47] J-C Géminard, Roberto Bernal, and Francisco Melo. “Wrinkle formations in axi-symmetrically stretched membranes”. In: *The European Physical Journal E: Soft Matter and Biological Physics* 15.2 (2004), pp. 117–126.

[48] Lucas Goehring. “Evolving fracture patterns: columnar joints, mud cracks and polygonal terrain”. In: *Philosophical Transactions of the Royal Society A: Mathematical, Physical and Engineering Sciences* 371.2004 (2013), p. 20120353.

[49] Lucas Goehring. *Giant’s Causeway in Northern Ireland*. 2008. URL: https://www.physics.utoronto.ca/~nonlin/PNASpress/PNASpress.html (visited on 12/12/2008).

[50] RV Goldstein and RL Salganik. “Brittle fracture of solids with arbitrary cracks”. In: *International Journal of Fracture* 10.4 (1974), pp. 507–523.

[51] Omer Gottesman, Efi Efrati, and Shmuel M Rubinstein. “Furrows in the wake of propagating d-cones”. In: *Nature communications* 6 (2015), p. 7232.

[52] Steven W Grey, Fabrizio Scarpa, and Mark Schenk. “Strain Reversal in Actuated Origami Structures”. In: *Physical review letters* 123.2 (2019), p. 025501.

[53] Jemal Guven. “Membrane geometry with auxiliary variables and quadratic constraints”. In: *Journal of Physics A: Mathematical and General* 37.28 (2004), p. L313.

[54] Jemal Guven and Martin Michael Müller. “How paper folds: bending with local constraints”. In: *Journal of Physics A: Mathematical and Theoretical* 41.5 (2008), p. 055203.

[55] Jemal Guven et al. “Dipoles in thin sheets”. In: *The European Physical Journal E* 36.9 (2013), p. 106.

[56] Fabian Haas and Robin J Wootton. “Two basic mechanisms in insect wing folding”. In: *Proceedings of the Royal Society of London. Series B: Biological Sciences* 263.1377 (1996), pp. 1651–1658.

[57] Brandon H Hanna et al. “Waterbomb base: a symmetric single-vertex bistable origami mechanism”. In: *Smart Materials and Structures* 23.9 (2014), p. 094009.

[58] WH Horton and SC Durham. “Imperfections, a main contributor to scatter in experimental values of buckling load”. In: *International Journal of Solids and Structures* 1.1 (1965), pp. 59–72.

[59] Jiangshui Huang et al. “Capillary wrinkling of floating thin polymer films”. In: *Science* 317.5838 (2007), pp. 650–653.

[60] Jiangshui Huang et al. “Smooth cascade of wrinkles at the edge of a floating elastic film”. In: *Physical review letters* 105.3 (2010), p. 038302.

[61] David A. Huffman. “Curvature and creases: A primer on paper”. In: *IEEE Transactions on computers* 10 (1976), pp. 1010–1019.

[62] Thomas Hull. “On the mathematics of flat origamis”. In: *Congressus numerantium* (1994), pp. 215–224.

[63] Jérémy Hure, Benoı t Roman, and José Bico. “Wrapping an adhesive sphere with an elastic sheet”. In: *Physical review letters* 106.17 (2011), p. 174301.

[64] Théo Jules, Frédéric Lechenault, and Mokhtar Adda-Bedia. “Local mechanical description of an elastic fold”. In: *Soft Matter* 15.7 (2019), pp. 1619–1626.

[65] E Katzav, M Adda-Bedia, and Rodrigo Arias. “Theory of dynamic crack branching in brittle materials”. In: *International Journal of Fracture* 143.3 (2007), pp. 245–271.

[66] Toshikazu Kawasaki. “On the relation between mountain-creases and valley-creases of a flat origami”. In: *Proceedings of the First International Meeting of Origami Science and Technology, 1991*. 1991.

[67] Jungwook Kim et al. “Designing responsive buckled surfaces by halftone gel lithography”. In: *Science* 335.6073 (2012), pp. 1201–1205.

[68] Hunter King et al. “Elastic sheet on a liquid drop reveals wrinkling and crumpling as distinct symmetry-breaking instabilities”. In: *Proceedings of the National Academy of Sciences* 109.25 (2012), pp. 9716–9720. ISSN: 0027-8424. DOI: 10.1073/pnas.1201201109.

[69] Yael Klein, Efi Efrati, and Eran Sharon. “Shaping of elastic sheets by prescription of non-Euclidean metrics”. In: *Science* 315.5815 (2007), pp. 1116–1120.

[70] Hidetoshi Kobayashi, Biruta Kresling, and Julian FV Vincent. “The geometry of unfolding tree leaves”. In: *Proceedings of the Royal Society of London. Series B: Biological Sciences* 265.1391 (1998), pp. 147–154.

[71] GV Kolosoff and CE Inglis. “Solution of plate with an elliptical hole”. In: *Transactions of the Royal Institute of Naval Arch* (1913).

[72] Kazuo Kondō et al. *RAAG memoirs of the unifying study of basic problems in engineering and physical sciences by means of geometry*. Vol. 1. Gakujutsu Bunken Fukyu-kai., 1955.

[73] AP Korte, EL Starostin, and GHM Van Der Heijden. “Triangular buckling patterns of twisted inextensible strips”. In: *Proceedings of the Royal Society A: Mathematical, Physical and Engineering Sciences* 467.2125 (2010), pp. 285–303.

[74] Michael Kücken and Alan C Newell. “Fingerprint formation”. In: *Journal of theoretical biology* 235.1 (2005), pp. 71–83.

[75] Stéphanie Périchon Lacour et al. “Stretchable gold conductors on elastomeric substrates”. In: *Applied physics letters* 82.15 (2003), pp. 2404–2406.

[76] L.D. Landau et al. *Theory of Elasticity*. Course of theoretical physics. Elsevier Science, 1986. ISBN: 9780750626330. URL: https://books.google.fr/books?id=tpY-VkwCkAIC.

[77] Robert J Lang. *Origami 4*. CRC Press, 2009.

[78] F Lechenault and M Adda-Bedia. “Generic bistability in creased conical surfaces”. In: *Physical review letters* 115.23 (2015), p. 235501.

[79] Frederic Lechenault, Benjamin Thiria, and Mokhtar Adda-Bedia. “Mechanical response of a creased sheet”. In: *Physical review letters* 112.24 (2014), p. 244301.

[80] Bin Liu et al. “Topological kinematics of origami metamaterials”. In: *Nature Physics* 14.8 (2018), p. 811.

[81] Alexander E Lobkovsky. “Boundary layer analysis of the ridge singularity in a thin plate”. In: *Physical Review E* 53.4 (1996), p. 3750.

[82] Alexander E Lobkovsky and TA Witten. “Properties of ridges in elastic membranes”. In: *Physical Review E* 55.2 (1997), p. 1577.

[83] Alex Lobkovsky et al. “Scaling properties of stretching ridges in a crumpled elastic sheet”. In: *Science* 270.5241 (1995), pp. 1482–1485.

[84] Augustus Edward Hough Love. *A treatise on the mathematical theory of elasticity*. Cambridge university press, 2013.

[85] Nanshu Lu and Dae-Hyeong Kim. “Flexible and stretchable electronics paving the way for soft robotics”. In: *Soft Robotics* 1.1 (2014), pp. 53–62.

[86] O Mahmood, B Audoly, and S Roux. “Cracks in Tension-Field Elastic Sheets”. In: *Physical review letters* 121.14 (2018), p. 144301.

[87] Eric Harold Mansfield. “Load transfer via a wrinkled membrane”. In: *Proceedings of the Royal Society of London. A. Mathematical and Physical Sciences* 316.1525 (1970), pp. 269–289.

[88] Eric Harold Mansfield. *The bending and stretching of plates*. Cambridge university press, 2005.

[89] Kittiwit Matan et al. “Crumpling a thin sheet”. In: *Physical Review Letters* 88.7 (2002), p. 076101.

[90] J Clerk Maxwell. “L. on the calculation of the equilibrium and stiffness of frames”. In: *The London, Edinburgh, and Dublin Philosophical Magazine and Journal of Science* 27.182 (1864), pp. 294–299.

[91] K Miura. “Proceedings of the 31st Congress of the International Astronautical Federation”. In: (1980).

[92] Koryo Miura. “Method of packaging and deployment of large membranes in space”. In: *Title The Institute of Space and Astronautical Science Report* 618 (1985), p. 1.

[93] Martin Michael Müller, Martine Ben Amar, and Jemal Guven. “Conical defects in growing sheets”. In: *Physical review letters* 101.15 (2008), p. 156104.

[94] Nikolaı Ivanovich Muskhelishvili. *Some basic problems of the mathematical theory of elasticity*. Springer Science & Business Media, 2013.

[95] Vitor M Pereira et al. "Geometry, mechanics, and electronics of singular structures and wrinkles in graphene". In: *Physical review letters* 105.15 (2010), p. 156603.

[96] Allen C Pipkin. "The relaxed energy density for isotropic elastic membranes". In: *IMA journal of applied mathematics* 36.1 (1986), pp. 85–99.

[97] Franck Plouraboué and Stéphane Roux. "Experimental study of the roughness of crumpled surfaces". In: *Physica A: Statistical Mechanics and its Applications* 227.3-4 (1996), pp. 173–182.

[98] Phanisri P. Pratapa, Ke Liu, and Glaucio H. Paulino. "Geometric Mechanics of Origami Patterns Exhibiting Poisson's Ratio Switch by Breaking Mountain and Valley Assignment". In: *Physical Review Letters* 122 (15 Apr. 2019), p. 155501. DOI: 10.1103/PhysRevLett.122.155501. URL: https://link.aps.org/doi/10.1103/PhysRevLett.122.155501.

[99] Phanisri P Pratapa, Ke Liu, and Glaucio H Paulino. "Geometric Mechanics of Origami Patterns Exhibiting Poisson's Ratio Switch by Breaking Mountain and Valley Assignment". In: *Physical Review Letters* 122.15 (2019), p. 155501.

[100] E. Reissner. *On Tension Field Theory*. [s.n.] @, 1938. URL: https://books.google.fr/books?id=LUrNXwAACAAJ.

[101] Michael Sadowsky. *Ein elementarer Beweis für die Existenz eines abwickelbaren Möbiusschen Bandes und Zurückführung des geometrischen Problems auf ein Variationsproblem*. 1930.

[102] Thierry Savin et al. "On the growth and form of the gut". In: *Nature* 476.7358 (2011), p. 57.

[103] Mark Schenk and Simon D Guest. "Geometry of Miura-folded metamaterials". In: *Proceedings of the National Academy of Sciences* 110.9 (2013), pp. 3276–3281.

[104] Mark Schenk and Simon D. Guest. "Geometry of Miura-folded metamaterials". In: *Proceedings of the National Academy of Sciences* 110.9 (2013), pp. 3276–3281. ISSN: 0027-8424. DOI: 10.1073/pnas.1217998110. URL: https://www.pnas.org/content/110/9/3276.

[105] RD Schroll et al. "Capillary deformations of bendable films". In: *Physical review letters* 111.1 (2013), p. 014301.

[106] KA Seffen and SV Stott. "Surface texturing through cylinder buckling". In: *Journal of Applied Mechanics* 81.6 (2014), p. 061001.

[107] Keith A Seffen. "Fundamental conical defects: The d-cone, its e-cone, and its p-cone". In: *Physical Review E* 94.1 (2016), p. 013002.

[108] Keith A Seffen. “k-cones and kirigami metamaterials”. In: *Physical Review E* 94.3 (2016), p. 033003.

[109] Kyle A Serikawa and Dina F Mandoli. “An analysis of morphogenesis of the reproductive whorl of Acetabularia acetabulum”. In: *Planta* 207.1 (1998), pp. 96–104.

[110] Eran Sharon, Michael Marder, and Harry L Swinney. “Leaves, flowers and garbage bags: Making waves”. In: *American Scientist* 92.3 (2004), pp. 254–261.

[111] Eran Sharon et al. “Mechanics: Buckling cascades in free sheets”. In: *Nature* 419.6907 (2002), p. 579.

[112] Jesse L Silverberg et al. “Origami structures with a critical transition to bistability arising from hidden degrees of freedom”. In: *Nature materials* 14.4 (2015), p. 389.

[113] Jesse L Silverberg et al. “Using origami design principles to fold reprogrammable mechanical metamaterials”. In: *science* 345.6197 (2014), pp. 647–650.

[114] Michael D Spivak. *A comprehensive introduction to differential geometry*. Publish or perish, 1970.

[115] Alan Spry. “The origin of columnar jointing, particularly in basalt flows”. In: *Journal of the Geological Society of Australia* 8.2 (1962), pp. 191–216.

[116] EL Starostin and GHM Van Der Heijden. “The shape of a Möbius strip”. In: *Nature materials* 6.8 (2007), p. 563.

[117] DJ Steigmann. “Tension-field theory”. In: *Proceedings of the Royal Society of London. A. Mathematical and Physical Sciences* 429.1876 (1990), pp. 141–173.

[118] Manuel Stein. “Analysis of partly wrinkled membranes”. In: *NASA TN, 1961* (1961).

[119] Dirk Jan Struik. *Lectures on classical differential geometry*. Courier Corporation, 1961.

[120] Benjamn Thiria and Mokhtar Adda-Bedia. “Relaxation mechanisms in the unfolding of thin sheets”. In: *Physical review letters* 107.2 (2011), p. 025506.

[121] S Timoshenko and James N Goodier. *Theory of Elasticity*. McGraw-Hill, 1969.

[122] Nariya Uchida and Takuya Ohzono. “Orientational ordering of buckling-induced microwrinkles on soft substrates”. In: *Soft Matter* 6.22 (2010), pp. 5729–5735.

[123] Hugues Vandeparre et al. “Wrinkling hierarchy in constrained thin sheets from suspended graphene to curtains”. In: *Physical Review Letters* 106.22 (2011), p. 224301.

[124] Ashkan Vaziri and L Mahadevan. “Localized and extended deformations of elastic shells”. In: *Proceedings of the National Academy of Sciences* 105.23 (2008), pp. 7913–7918.

[125] Dominic Vella, Mokhtar Adda-Bedia, and Enrique Cerda. “Capillary wrinkling of elastic membranes”. In: *Soft Matter* 6.22 (2010), pp. 5778–5782.

[126] Dominic Vella et al. “The macroscopic delamination of thin films from elastic substrates”. In: *Proceedings of the National Academy of Sciences* 106.27 (2009), pp. 10901–10906.

[127] Dominic Vella et al. “Wrinkling of pressurized elastic shells”. In: *Physical review letters* 107.17 (2011), p. 174301.

[128] GA Vliegenthart and G Gompper. “Forced crumpling of self-avoiding elastic sheets”. In: *Nature materials* 5.3 (2006), p. 216.

[129] Herbert Wagner. “Ebene Blechwandtrager mit sehr dunnem Stegblech (Metal beams with very thin webs)”. In: *Zeitschrift fur Flugtechnik und Motorloftschiffahr* 20.8 (1929).

[130] Scott Waitukaitis et al. “Origami multistability: From single vertices to metasheets”. In: *Physical review letters* 114.5 (2015), p. 055503.

[131] Martin G Walker and Keith A Seffen. “On the shape of bistable creased strips”. In: *Thin-Walled Structures* 124 (2018), pp. 538–545.

[132] Patsy Wang-Iverson, Robert J Lang, and YIM Mark. *Origami 5: Fifth International Meeting of Origami Science, Mathematics, and Education*. CRC Press, 2011.

[133] Jin W Wang. “Rim curvature anomaly in thin conical sheets revisited”. In: *Physical Review E* 84.6 (2011), p. 066603.

[134] Xueshen Wang et al. “Fabrication of ultralong and electrically uniform single-walled carbon nanotubes on clean substrates”. In: *Nano letters* 9.9 (2009), pp. 3137–3141.

[135] Zhiyan Y Wei et al. “Geometric mechanics of periodic pleated origami”. In: *Physical review letters* 110.21 (2013), p. 215501.

[136] Max L Williams. “The bending stress distribution at the base of a stationary crack”. In: *Journal of applied mechanics* 28.1 (1961), pp. 78–82.

[137] Zi Liang Wu et al. “Three-dimensional shape transformations of hydrogel sheets induced by small-scale modulation of internal stresses”. In: *Nature Communications* 4 (2013), p. 1586.

[138] Walter Wunderlich. “Über ein abwickelbares Möbiusband”. In: *Monatshefte für Mathematik* 66.3 (1962), pp. 276–289.

[139] Ryan Mario Yasin. “Petit Pli: Clothes that Grow”. In: *Utopian Studies* 28.3 (2017), pp. 576–583.

[140] A Yuse and M Sano. “Transition between crack patterns in quenched glass plates”. In: *Nature* 362.6418 (1993), p. 329.

[141] Shannon A Zirbel et al. “Accommodating thickness in origami-based deployable arrays”. In: *Journal of Mechanical Design* 135.11 (2013), p. 111005.